

# Prediction by Energy Phenomenology for Harnessing Hydrokinetic Energy Using Vortex-Induced Vibrations

by

Elizabeth Maloney-Hahn Garcia

A dissertation submitted in partial fulfillment  
of the requirements for the degree of  
Doctor of Philosophy  
(Naval Architecture and Marine Engineering)  
in The University of Michigan  
2008

Doctoral Committee:

Professor Michael M. Bernitsas, Chair  
Professor J. David Allan  
Professor Philip L. Roe  
Professor Armin W. Troesch  
Associate Research Scientist Okey Nwogu



© Elizabeth Maloney-Hahn Garcia 2008  
All Rights Reserved

I dedicate this dissertation to Igor Steven Garcia, my best friend, my husband, and my sunshine,  
for never letting me give up on my dreams.

## ACKNOWLEDGEMENTS

Many people have contributed to my work, either providing guidance or support. First, thanks to everyone in the VIVACE research group. Professor Michael M. Bernitsas, thank you for inviting me to work with the VIVACE research group and providing me with guidance and flexibility. Thank you, Kamal Raghavan, Yaron Ben-Simon, Dimitri Marioulis, and Jim Chang, for helping me collect experimental results. Kamal, thank you also for helping me get started with VIV. Thank you to my committee, Professors Allan, Roe, and Troesch, and Doctor Nwogu, for your time and input. Jamie L. Szwalek, thank you for being the best mentor and a great friend. Thanks, Eleanor K. Nick, for bringing the office to life.

I never would have been able to tackle the doctoral degree without a solid educational background. Thanks to the University of Rhode Island Department of Ocean Engineering for a solid bachelors degree. Thanks to the University of Michigan Department of Naval Architecture and Marine Engineering for the opportunity to continue my education. I would not have been able to pursue the doctoral degree without financial assistance. I was supported by the Rackham Engineering Award through the University of Michigan Rackham Graduate School and the Department of Naval Architecture and Marine Engineering and later by the National Defense Science and Engineering Graduate Fellowship through the Office of Naval Research in the Department of Defense. Thank you to these institutions for making my stud-

ies possible. I completed the dissertation out-of-state, and as a result, relied heavily on the services of the University of Michigan University Library 7-FAST Document Delivery Service. This service was instrumental in my literature review, and I thank them many times over. I also have to thank the U.S. Coast Guard Academy, my current employer, for giving me the time to defend my dissertation and complete the corrections.

My family has been instrumental in getting me to this point in my life. Igor Steven Garcia, you inspired me in so many ways to pursue the doctoral degree and to never give up, providing me with support and honesty. Dad and Mom, Dan and Lisa Maloney Hahn, thank you for raising me to believe that I can do whatever I want and letting me set out on my own path while still supporting me. Thank you, Justin Maloney-Hahn, for being the big brother I aspired to equal, and to Reiko Maloney-Hahn for being a great friend and good listener. Many thanks to Grecia and Mercedes Damaso for being a very understanding and supportive extended family.

# TABLE OF CONTENTS

|   |             |
|---|-------------|
| <b>DEDICATION</b> . . . . .                     | <b>ii</b>   |
| <b>ACKNOWLEDGEMENTS</b> . . . . .               | <b>iii</b>  |
| <b>LIST OF FIGURES</b> . . . . .                | <b>viii</b> |
| <b>LIST OF TABLES</b> . . . . .                 | <b>xvi</b>  |
| <b>NOMENCLATURE</b> . . . . .                   | <b>xvii</b> |
| <b>ABSTRACT</b> . . . . .                       | <b>xx</b>   |
| <b>CHAPTER</b>                                  |             |
| <b>1. Introduction</b> . . . . .                | <b>1</b>    |
| 1.1 Thesis Problem . . . . .                    | 1           |
| 1.2 VIVACE . . . . .                            | 3           |
| 1.3 General Literature Review . . . . .         | 8           |
| 1.4 VIV of a Single Cylinder . . . . .          | 11          |
| 1.5 VIV of Multiple Cylinders . . . . .         | 15          |
| 1.6 VIV Numerical Simulations . . . . .         | 16          |
| 1.6.1 Kolmogorov Length Scale . . . . .         | 16          |
| 1.7 Extant VIV Models . . . . .                 | 20          |
| 1.7.1 Linear Single Degree-of-Freedom . . . . . | 20          |
| 1.7.2 Van der Pol Oscillator . . . . .          | 22          |
| 1.7.3 Landau Equation . . . . .                 | 24          |
| 1.7.4 Billah's Model . . . . .                  | 25          |
| 1.7.5 Hamilton's Principle . . . . .            | 26          |
| 1.8 Relevant Water Ecology . . . . .            | 28          |
| <b>2. VIV Features and Parameters</b> . . . . . | <b>42</b>   |
| 2.1 Variables . . . . .                         | 43          |
| 2.1.1 Circulation . . . . .                     | 43          |
| 2.1.2 Natural Frequency . . . . .               | 44          |
| 2.2 Dimensionless Parameters . . . . .          | 44          |
| 2.2.1 Reynolds Number . . . . .                 | 44          |
| 2.2.2 Damping Ratio . . . . .                   | 44          |
| 2.2.3 Mass Ratio . . . . .                      | 45          |
| 2.2.4 Mass-Damping Parameter . . . . .          | 45          |
| 2.2.5 Strouhal Number . . . . .                 | 46          |

|           |  |            |
|-----------|--|------------|
| 2.2.6     | Reduced Velocity . . . . .   | 47         |
| 2.3       | VIV Geometry . . . . .   | 47         |
| 2.3.1     | Stagnation Point . . . . .   | 47         |
| 2.3.2     | Separation Point . . . . .   | 47         |
| 2.3.3     | Formation Point . . . . .  | 48         |
| 2.3.4     | Boundary Layer & Shear Layer . . . . .   | 48         |
| 2.3.5     | von Kármán Vortex . . . . .  | 49         |
| 2.4       | Features . . . . .   | 49         |
| 2.4.1     | Synchronization . . . . .  | 49         |
| 2.4.2     | Lock-in . . . . .  | 50         |
| 2.4.3     | Phase Shift . . . . .  | 51         |
| 2.4.4     | Vortex Shedding Mode . . . . .   | 52         |
| 2.4.5     | Mass-Damping . . . . .   | 53         |
| <b>3.</b> | <b>Development of a Mathematical Model of VIV . . . . .</b>                          | <b>62</b>  |
| 3.1       | Hamilton's Principle . . . . .   | 63         |
| 3.2       | First-Order Approximations for Energy . . . . .                                      | 66         |
| 3.3       | Stationary Cylinder . . . . .  | 67         |
| 3.3.1     | Boundary Layer Energy . . . . .  | 67         |
| 3.3.2     | Shear Layer Energy . . . . .   | 69         |
| 3.3.3     | Attached von Kármán Vortex Energy . . . . .  | 70         |
| 3.4       | Cylinder with Single Degree-of-Freedom . . . . .                                     | 72         |
| 3.4.1     | Body Energy . . . . .  | 72         |
| 3.4.2     | Boundary Layer Energy with Body Motion . . . . .                                     | 74         |
| 3.4.3     | Shear Layer Energy with Body Motion . . . . .  | 74         |
| 3.4.4     | Attached von Kármán Vortex Energy with Body Motion . . . . .                         | 75         |
| 3.5       | Nonconservative Work . . . . .   | 76         |
| 3.6       | Derivation of the Force Equations . . . . .  | 76         |
| 3.6.1     | Body Force . . . . .   | 77         |
| 3.6.2     | Boundary Layer Force . . . . .   | 78         |
| 3.6.3     | Shear Layer Force . . . . .  | 78         |
| 3.6.4     | Attached von Kármán Vortex Force . . . . .   | 79         |
| 3.6.5     | Nonconservative Forces . . . . .   | 79         |
| 3.7       | Full Force Equation . . . . .  | 80         |
| <b>4.</b> | <b>Testing and Verifying Mathematical Model with Linear Approximations . . . . .</b> | <b>89</b>  |
| 4.1       | Numerical Simulation . . . . .   | 90         |
| 4.2       | Sinusoidal Input . . . . .   | 91         |
| 4.3       | Flow-Based Input . . . . .   | 93         |
| 4.4       | Vortex Shedding Criteria . . . . .   | 96         |
| 4.4.1     | Critical Energy . . . . .  | 96         |
| 4.5       | Analysis of Results . . . . .  | 98         |
| 4.5.1     | Qualitative Discussion . . . . .   | 98         |
| 4.5.2     | Quantitative Discussion . . . . .  | 99         |
| <b>5.</b> | <b>Mathematical Model Improvements . . . . .</b>                                     | <b>136</b> |
| 5.1       | Reynolds Number Based Inputs . . . . .   | 137        |
| 5.1.1     | Strouhal Number . . . . .  | 137        |
| 5.1.2     | Separation Point . . . . .   | 138        |
| 5.1.3     | Formation Point . . . . .  | 139        |
| 5.1.4     | Boundary Layer Thickness . . . . .   | 141        |



|           |   |            |
|-----------|---|------------|
| 5.2       | Blasius-Type Functions . . . . .                                      | 142        |
| 5.2.1     | Boundary Layer Geometry . . . . .                                     | 143        |
| 5.2.2     | Shear Layer Geometry . . . . .  | 145        |
| 5.3       | Velocity Profiles . . . . .   | 148        |
| 5.4       | Parametric Variation . . . . .  | 149        |
| 5.4.1     | Energy Dissipation . . . . .  | 149        |
| 5.5       | Other Examined Factors . . . . .                                      | 151        |
| 5.6       | Final Force Equations . . . . .                                       | 152        |
| <b>6.</b> | <b>Comparison to Experimental Results and Extant Models . . . . .</b> | <b>196</b> |
| 6.1       | Comparison to Experimental Results . . . . .                          | 196        |
| 6.2       | Comparison to Extant Models . . . . .                                 | 198        |
| 6.2.1     | Linear Single Degree-of-Freedom Equation . . . . .                    | 198        |
| 6.2.2     | van der Pol Oscillator . . . . .                                      | 198        |
| 6.3       | Comparison to Baselines . . . . .                                     | 200        |
| <b>7.</b> | <b>VIVACE Design . . . . .</b>  | <b>225</b> |
| 7.1       | Cylinder Spacing . . . . .  | 225        |
| 7.1.1     | Length from Aspect Ratio . . . . .                                    | 226        |
| 7.1.2     | Vertical Spacing . . . . .  | 227        |
| 7.2       | Energy Extraction . . . . .   | 228        |
| 7.3       | Ecological Implications of VIVACE . . . . .                           | 229        |
| 7.3.1     | General Ecological Review of VIVACE . . . . .                         | 231        |
| 7.3.2     | Sediment transport . . . . .  | 234        |
| 7.3.3     | Distance from the free surface . . . . .                              | 234        |
| 7.3.4     | Distance from the bottom . . . . .                                    | 236        |
| 7.3.5     | Measures of Regime Change . . . . .                                   | 236        |
| <b>8.</b> | <b>Conclusion . . . . .</b>   | <b>241</b> |
| 8.1       | Math Model Overview . . . . .   | 241        |
| 8.1.1     | Qualitative Overview . . . . .  | 242        |
| 8.1.2     | Quantitative Overview . . . . .                                       | 243        |
| 8.2       | VIVACE Overview . . . . .   | 244        |
| 8.3       | Future Work . . . . .   | 244        |
|           | <b>BIBLIOGRAPHY . . . . .</b>   | <b>250</b> |

## LIST OF FIGURES

**Figure**

|     |  |    |
|-----|--|----|
| 1.1 | A VIVACE single cylinder schematic, where the side struts contain the generator (dampers) and springs (Bernitsas, Raghavan, Ben-Simon, and Garcia 2006). . . . .   | 32 |
| 1.2 | VIVACE cylinder array schematic. Cylinders are staggered in a hexagonal shape (Bernitsas, Raghavan, Ben-Simon, and Garcia 2006). . . . .   | 33 |
| 1.3 | Lift and drag coefficients as a function of Reynolds number (Zdravkovich 1997). . .  | 36 |
| 1.4 | Lift and drag coefficients as a function of Reynolds number for the Reynolds number area of interest in the transition region (Zdravkovich 1997; Raghavan 2007). . . . .   | 37 |
| 1.5 | The destructive nature of VIV is best exemplified by the Tacoma Narrows Bridge Disaster in Tacoma, Washington, 1940. . . . .   | 38 |
| 1.6 | Sketch by Leonardo da Vinci in 1513 showing the wake behind a piling in a river. .   | 39 |
| 1.7 | A schematic of the Gerrard theory of vortex shedding, showing the vortex being drawn across and cutting off the opposite vortex from the feeding sheet (Gerrard 1966). . . . .   | 40 |
| 1.8 | Experimental, (a), and analytical, (b), output for extended Hamilton’s principle for fluid control-volume approach (Benaroya, Wei, Kuchnicki, and Dong 2003). . .  | 41 |
| 2.1 | Schematic of important parameters from the geometry of the body and attached flow with first order approximations. . . . .   | 55 |
| 2.2 | A generalized plot of the range of synchronization with the typical initial, upper, and lower branches, where a hysteresis typically occurs between the initial and upper branches and the upper and lower branches (Williamson and Govardhan 2004). . . . . | 56 |
| 2.3 | The effect of the mass ratio on the frequency of response for the cylinder during lock-in from experiments (Govardhan and Williamson 2000). . . . .  | 57 |
| 2.4 | A schematic of the approximate nature of the phase shift between fluid forcing and cylinder displacement at lock-in (Sumer and Fredsøe 1997). . . . .  | 58 |
| 2.5 | The regimes of the vortex patterns for a forced oscillating cylinder with non-dimensional velocity and amplitude for the axes (Williamson and Roshko 1988). . .  | 59 |

|      |   |     |
|------|---|-----|
| 2.6  | The vortex patterns identified using a forced oscillating cylinder (Williamson and Roshko 1988). . . . .  | 60  |
| 2.7  | The modified Griffin plot, with Skop-Griffin parameter plotted against a non-dimensional amplitude (Govardhan and Williamson 2006). . . . .   | 61  |
| 3.1  | Schematic of body and attached fluid region, showing area of energy into and out of the system, including dissipation into the wake at the end of the shear layer. . .  | 86  |
| 3.2  | Rankine approximation compared to the nature of a real vortex. . . . .  | 87  |
| 4.1  | The axes for the plots that are used for examining numerical results of the developed model. . . . .  | 103 |
| 4.2  | Sinusoidal time inputs for the stagnation point, top and bottom separation points, top and bottom formation points, and top and bottom attached vortex radii, where $m^* = 1$ , $\zeta = 1$ , $f_n = 1$ , $D = 0.1m$ , and $2 \times 10^3 < Re < 4 \times 10^5$ . . . . .     | 104 |
| 4.3  | Cylinder displacement output from a sinusoidal time input for various reduced velocities, where $m^* = 1$ , $\zeta = 1$ , $f_n = 1$ , $D = 0.1m$ , and $2 \times 10^3 < Re < 4 \times 10^5$ . . . . .   | 105 |
| 4.4  | Cylinder displacement frequency energy spectrum from a sinusoidal time input for various reduced velocities, where $m^* = 1$ , $\zeta = 1$ , $f_n = 1$ , $D = 0.1m$ , and $2 \times 10^3 < Re < 4 \times 10^5$ . . . . .  | 106 |
| 4.5  | Cylinder displacement versus velocity phase plots from a sinusoidal time input for various reduced velocities, where $m^* = 1$ , $\zeta = 1$ , $f_n = 1$ , $D = 0.1m$ , and $2 \times 10^3 < Re < 4 \times 10^5$ . . . . .  | 107 |
| 4.6  | Cylinder amplitude response from a sinusoidal time input with varying damping coefficients for various reduced velocities, where $m^* = 1$ , $f_n = 1$ , $D = 0.1m$ , and $2 \times 10^3 < Re < 4 \times 10^5$ . . . . .  | 108 |
| 4.7  | Cylinder phase-shift response from a sinusoidal time input with varying damping coefficients for various reduced velocities, where $m^* = 1$ , $f_n = 1$ , $D = 0.1m$ , and $2 \times 10^3 < Re < 4 \times 10^5$ . . . . .  | 109 |
| 4.8  | Cylinder peak-frequency response from a sinusoidal time input with varying damping coefficients for various reduced velocities, where $m^* = 1$ , $f_n = 0.5679$ and $D = 0.1m$ . . . . .   | 110 |
| 4.9  | Cylinder amplitude response from a sinusoidal time input with varying damping coefficients for various reduced velocities. . . . .  | 111 |
| 4.10 | Cylinder phase-shift response from a sinusoidal time input with varying damping coefficients for various reduced velocities. . . . .  | 112 |
| 4.11 | Cylinder peak-frequency response from a sinusoidal time input with varying damping coefficients for various reduced velocities. . . . .   | 113 |
| 4.12 | Square-root of time inputs for the stagnation point, top and bottom separation points, top and bottom formation points, and top and bottom attached vortex radii, where $m^* = 1$ , $\zeta = 1$ , $f_n = 1$ , $D = 0.1m$ , and $2 \times 10^3 < Re < 4 \times 10^5$ . . . . . | 114 |

|      |   |     |
|------|---|-----|
| 4.13 | Cylinder displacement output from a square-root of time input for various reduced velocities, where $m^* = 1$ , $\zeta = 1$ , $f_n = 1$ , $D = 0.1m$ , and $2 \times 10^3 < Re < 4 \times 10^5$ . . .   | 115 |
| 4.14 | Cylinder-displacement frequency-energy spectrum from a square-root of time input for various reduced velocities, where $m^* = 1$ , $\zeta = 1$ , $f_n = 1$ , $D = 0.1m$ , and $2 \times 10^3 < Re < 4 \times 10^5$ . . . . .  | 116 |
| 4.15 | Cylinder displacement versus velocity phase plots from a square-root of time input for various reduced velocities, where $m^* = 1$ , $\zeta = 1$ , $f_n = 1$ , $D = 0.1m$ , and $2 \times 10^3 < Re < 4 \times 10^5$ . . . . .  | 117 |
| 4.16 | Cylinder amplitude response from a square-root of time input with varying damping coefficients for various reduced velocities, where $m^* = 1$ , $f_n = 1$ , $D = 0.1m$ , and $2 \times 10^3 < Re < 4 \times 10^5$ . . . . .  | 118 |
| 4.17 | Cylinder phase-shift response from a square-root of time input with varying damping coefficients for various reduced velocities, where $m^* = 1$ , $f_n = 1$ , $D = 0.1m$ , and $2 \times 10^3 < Re < 4 \times 10^5$ . . . . .  | 119 |
| 4.18 | Cylinder peak-frequency response from a square-root of time input with varying damping coefficients for various reduced velocities, where $m^* = 1$ , $f_n = 1$ , $D = 0.1m$ , and $2 \times 10^3 < Re < 4 \times 10^5$ . . . . .   | 120 |
| 4.19 | Cylinder amplitude response from a square-root of time input with varying damping coefficients for various reduced velocities. . . . .  | 121 |
| 4.20 | Cylinder phase-shift response from a square-root of time input with varying damping coefficients for various reduced velocities. . . . .  | 122 |
| 4.21 | Cylinder peak-frequency response from a square-root of time input with varying damping coefficients for various reduced velocities. . . . .   | 123 |
| 4.22 | Square-root of time with critical energy shedding inputs for the stagnation point, top and bottom separation points, top and bottom formation points, and top and bottom attached vortex radii, where $m^* = 1$ , $\zeta = 1$ , $f_n = 1$ , $D = 0.1m$ , and $2 \times 10^3 < Re < 4 \times 10^5$ . . . . . | 124 |
| 4.23 | Cylinder displacement output from a square-root of time with critical energy shedding input for various reduced velocities, where $m^* = 1$ , $\zeta = 1$ , $f_n = 1$ , $D = 0.1m$ , and $2 \times 10^3 < Re < 4 \times 10^5$ . . . . .   | 125 |
| 4.24 | Cylinder-displacement frequency-energy spectrum from a square-root of time with critical energy shedding input for various reduced velocities, where $m^* = 1$ , $\zeta = 1$ , $f_n = 1$ , $D = 0.1m$ , and $2 \times 10^3 < Re < 4 \times 10^5$ . . . . .  | 126 |
| 4.25 | Cylinder displacement versus velocity phase plots from a square-root of time with critical energy shedding input for various reduced velocities, where $m^* = 1$ , $\zeta = 1$ , $f_n = 0$ , $D = 0.1m$ , and $2 \times 10^3 < Re < 4 \times 10^5$ . . . . .  | 127 |
| 4.26 | Cylinder amplitude response from a square-root of time with critical energy shedding input with varying damping coefficients for various reduced velocities, where $m^* = 1$ , $f_n = 1$ , $D = 0.1m$ , and $2 \times 10^3 < Re < 4 \times 10^5$ . . . . .  | 128 |

|      |  |     |
|------|--|-----|
| 4.27 | Cylinder phase-shift response from a square-root of time with critical energy shedding input with varying damping coefficients for various reduced velocities, where $m^* = 1$ , $f_n = 1$ , $D = 0.1m$ , and $2 \times 10^3 < Re < 4 \times 10^5$ . . . . .           | 129 |
| 4.28 | Vortex-shedding peak-frequency response from a square-root of time with critical energy shedding input with varying damping coefficients for various reduced velocities, where $m^* = 1$ , $f_n = 1$ , $D = 0.1m$ , and $2 \times 10^3 < Re < 4 \times 10^5$ . . . . . | 130 |
| 4.29 | Cylinder peak-frequency response from a square-root of time with critical energy shedding input with varying damping coefficients for various reduced velocities, where $m^* = 1$ , $f_n = 1$ , $D = 0.1m$ , and $2 \times 10^3 < Re < 4 \times 10^5$ . . . . .        | 131 |
| 4.30 | Cylinder amplitude response from a square-root of time with critical energy shedding input with varying damping coefficients for various reduced velocities. . . . .   | 132 |
| 4.31 | Cylinder phase-shift response from a square-root of time with critical energy shedding input with varying damping coefficients for various reduced velocities. . . . .   | 133 |
| 4.32 | Vortex-shedding peak-frequency response from a square-root of time with critical energy shedding input with varying damping coefficients for various reduced velocities. . . . .   | 134 |
| 4.33 | Cylinder peak-frequency response from a square-root of time with critical energy shedding input with varying damping coefficients for various reduced velocities. . . . .  | 135 |
| 5.1  | The non-dimensional Strouhal number over Reynolds number for a stationary cylinder (Sumer and Fredsøe 1997). Other experiments have not agreed with the smooth jump shown during Boundary Layer Transition. . . . .  | 157 |
| 5.2  | Comparison of the amplitude response for the implementation of a Reynolds-number-based Strouhal number to a constant Strouhal number. . . . .  | 158 |
| 5.3  | Comparison of the phase-shift response for the implementation a Reynolds-number-based Strouhal number to a constant Strouhal number. . . . .   | 159 |
| 5.4  | Comparison of the vortex-shedding frequency response for the implementation of a Reynolds-number-based Strouhal number to a constant Strouhal number. . . . .  | 160 |
| 5.5  | Comparison of the cylinder frequency response for the implementation of a Reynolds-number-based Strouhal number to a constant Strouhal number. . . . .   | 161 |
| 5.6  | The position of the separation point over Reynolds number for a stationary cylinder with points originally from Achenbach (1968) (Sumer and Fredsøe 1997). . . . .   | 162 |
| 5.7  | Comparison of the amplitude response for the implementation of a Reynolds-number-based separation point to a constant separation point. . . . .  | 163 |
| 5.8  | Comparison of the phase-shift response for the implementation of a Reynolds-number-based separation point to a constant separation point. . . . .  | 164 |
| 5.9  | Comparison of the vortex-shedding frequency response for the implementation of a Reynolds-number-based separation point to a constant separation point. . . . .  | 165 |
| 5.10 | Comparison of the cylinder frequency response for the implementation of a Reynolds-number-based separation point to a constant separation point. . . . .   | 166 |

|      |   |     |
|------|---|-----|
| 5.11 | The formation length (formation point) from center of a stationary cylinder over Reynolds number (Norberg 1987b). . . . .   | 167 |
| 5.12 | Comparison of the amplitude response for the implementation of a Reynolds-number-based formation point to a constant formation point. . . . .   | 168 |
| 5.13 | Comparison of the phase-shift response for the implementation of a Reynolds-number-based formation point to a constant formation point. . . . .   | 169 |
| 5.14 | Comparison of the vortex-shedding frequency response for the implementation of a Reynolds-number-based formation point to a constant formation point. . . . .   | 170 |
| 5.15 | Comparison of the cylinder frequency response for the implementation of a Reynolds-number-based formation point to a constant formation point. . . . .  | 171 |
| 5.16 | Comparison of the amplitude response for the implementation of a Reynolds-number-based maximum boundary-layer thickness to a constant maximum boundary-layer thickness. . . . .   | 172 |
| 5.17 | Comparison of the phase-shift response for the implementation of a Reynolds-number-based maximum boundary-layer thickness to a constant maximum boundary-layer thickness. . . . .   | 173 |
| 5.18 | Comparison of the vortex-shedding frequency response for the implementation of a Reynolds-number-based maximum boundary-layer thickness to a constant maximum boundary-layer thickness. . . . .                             | 174 |
| 5.19 | Comparison of the cylinder frequency response for the implementation of a Reynolds-number-based maximum boundary-layer thickness to a constant maximum boundary-layer thickness. . . . .                                    | 175 |
| 5.20 | Comparison of the amplitude response for the implementation of a Reynolds-number-based Strouhal number, separation point, formation point, and maximum boundary-layer thickness to constant inputs. . . . .                 | 176 |
| 5.21 | Comparison of the phase-shift response for the implementation of a Reynolds-number-based Strouhal number, separation point, formation point, and maximum boundary-layer thickness to constant inputs. . . . .               | 177 |
| 5.22 | Comparison of the vortex-shedding frequency response for the implementation of a Reynolds-number-based Strouhal number, separation point, formation point, and maximum boundary-layer thickness to constant inputs. . . . . | 178 |
| 5.23 | Comparison of the cylinder frequency response for the implementation of a Reynolds-number-based Strouhal number, separation point, formation point, and maximum boundary-layer thickness to constant inputs. . . . .        | 179 |
| 5.24 | Comparison of the amplitude response for the implementation of a Reynolds-number-based boundary-layer growth (square-root of arc-length) to a linear boundary-layer growth. . . . .   | 180 |

|      |   |     |
|------|---|-----|
| 5.25 | Comparison of the phase-shift response for the implementation of a Reynolds-number-based boundary-layer growth (square-root of arc-length) to a linear boundary-layer growth. . . . .   | 181 |
| 5.26 | Comparison of the vortex-shedding frequency response for the implementation of a Reynolds-number-based boundary-layer growth (square-root of arc-length) to a linear boundary-layer growth. . . . .   | 182 |
| 5.27 | Comparison of the cylinder frequency response for the implementation of a Reynolds-number-based boundary-layer growth (square-root of arc-length) to a linear boundary-layer growth. . . . .  | 183 |
| 5.28 | Comparison of the amplitude response for the implementation of a Reynolds-number-based boundary-layer growth (square-root of arc-length) to a linear boundary-layer growth with the same maximum boundary layer thickness. . . . .  | 184 |
| 5.29 | Comparison of the phase-shift response for the implementation of a Reynolds-number-based boundary-layer growth (square-root of arc-length) to a linear boundary-layer growth with the same maximum boundary layer thickness. . . . .  | 185 |
| 5.30 | Comparison of the vortex-shedding frequency response for the implementation of a Reynolds-number-based boundary-layer growth (square-root of arc-length) to a linear boundary-layer growth with the same maximum boundary layer thickness. . . . .  | 186 |
| 5.31 | Comparison of the cylinder frequency response for the implementation of a Reynolds-number-based boundary-layer growth (square-root of arc-length) to a linear boundary-layer growth with the same maximum boundary layer thickness. . . . .   | 187 |
| 5.32 | Comparison of the amplitude response for the implementation of a linear shear-layer growth with Reynolds number based maximum shear layer thickness with a constant shear layer thickness both with Reynolds number based maximum boundary layer thickness. The gap around reduced velocity 10 is the result of the response amplitude going to infinity. . . . .                         | 188 |
| 5.33 | Comparison of the phase-shift response for the implementation of a linear shear-layer growth with Reynolds number based maximum shear layer thickness with a constant shear layer thickness both with Reynolds number based maximum boundary layer thickness. . . . .   | 189 |
| 5.34 | Comparison of the vortex-shedding frequency response for the implementation of a linear shear-layer growth with Reynolds number based maximum shear layer thickness with a constant shear layer thickness both with Reynolds number based maximum boundary layer thickness. . . . .   | 190 |
| 5.35 | Comparison of the cylinder frequency response for the implementation of a linear shear-layer growth with Reynolds number based maximum shear layer thickness with a constant shear layer thickness both with Reynolds number based maximum boundary layer thickness. The frequency response points of zero correspond to infinite amplitude response, an inaccuracy of the model. . . . . | 191 |
| 5.36 | Comparison of the amplitude response for various values of the dissipation/amplification parameter $\alpha$ . . . . .   | 192 |

|      |   |     |
|------|---|-----|
| 5.37 | Comparison of the phase-shift response for various values of the dissipation parameter $\alpha$ , with testing for energy entrainment in place of dissipation. . . . .  | 193 |
| 5.38 | Comparison of the vortex-shedding frequency response for various values of the dissipation/amplification parameter $\alpha$ . . . . .   | 194 |
| 5.39 | Comparison of the cylinder frequency response for various values of the dissipation/amplification parameter $\alpha$ . . . . .  | 195 |
| 6.1  | Comparison of the amplitude response of the developed math model to the high mass ratio experimental data sets from Feng (1968) and Govardhan and Williamson (2000), data received via private communication from Williamson. . . . .                 | 205 |
| 6.2  | Comparison of the phase-shift response of the developed math model to the high mass ratio experimental data sets from Feng (1968) and Govardhan and Williamson (2000), data received via private communication from Williamson. . . . .               | 206 |
| 6.3  | Comparison of the vortex-shedding frequency response of the developed math model to the high mass ratio experimental data sets from Feng (1968) and Govardhan and Williamson (2000), data received via private communication from Williamson. . . . . | 207 |
| 6.4  | Comparison of the cylinder frequency response of the developed math model to the high mass ratio experimental data sets from Feng (1968) and Govardhan and Williamson (2000), data received via private communication from Williamson. . . . .        | 208 |
| 6.5  | Comparison of the amplitude response of the developed math model to the low mass ratio experimental data set from Govardhan and Williamson (2000), data received via private communication from Williamson. . . . .                                   | 209 |
| 6.6  | Comparison of the phase-shift response of the developed math model to the low mass ratio experimental data set from Govardhan and Williamson (2000), data received via private communication from Williamson. . . . .                                 | 210 |
| 6.7  | Comparison of the cylinder frequency response of the developed math model to the low mass ratio experimental data set from Govardhan and Williamson (2000), data received via private communication from Williamson. . . . .                          | 211 |
| 6.8  | Comparison of the amplitude response of the developed math model to the experimental data set from Anagnostopoulos and Bearman (1992), data taken from points on plots. . . . .   | 212 |
| 6.9  | Comparison of the vortex-shedding frequency response of the developed math model to the experimental data set from Anagnostopoulos and Bearman (1992), data taken from points on plots. . . . .   | 213 |
| 6.10 | Comparison of the cylinder frequency response of the developed math model to the experimental data set from Anagnostopoulos and Bearman (1992), data taken from points on plots. . . . .  | 214 |
| 6.11 | Comparison of the amplitude response of the developed math model to the van der Pol oscillator from Facchinetti, de Langre, and Biolley (2004) with acceleration coupling. . . . .  | 215 |



|      |   |     |
|------|---|-----|
| 6.12 | Comparison of the phase-shift response of the developed math model to the van der Pol oscillator from Facchinetti, de Langre, and Biolley (2004) with acceleration coupling. . . . .  | 216 |
| 6.13 | Comparison of the vortex-shedding frequency response of the developed math model to the van der Pol oscillator from Facchinetti, de Langre, and Biolley (2004) with acceleration coupling. . . . .  | 217 |
| 6.14 | Comparison of the cylinder frequency response of the developed math model to the van der Pol oscillator from Facchinetti, de Langre, and Biolley (2004) with acceleration coupling. . . . .   | 218 |
| 6.15 | Comparison of the phase-shift response of the developed math model to the empirically based results as shown in Sumer and Fredsøe (1997). . . . .   | 219 |
| 6.16 | Comparison of the amplitude response of the developed math model for high mass ratio to the empirically based range of synchronization as taken from Williamson and Govardhan (2004). . . . .   | 220 |
| 6.17 | Comparison of the amplitude response of the developed math model for low mass ratio to the empirically based range of synchronization as taken from Williamson and Govardhan (2004). . . . .  | 221 |
| 6.18 | Comparison of the approximate number of vortices shed per cycle from the developed math model to the empirically based vortex shedding modes as taken from Williamson and Roshko (1988). Many experimental results show mode $2S$ present up to around $U^* = 5$ and then mode $2P$ takes over. . . . . | 222 |
| 6.19 | Comparison of the cylinder frequency response of the developed math model to the empirically based frequency response for low mass ratios as taken from Govardhan and Williamson (2000). . . . .  | 223 |
| 6.20 | Comparison of the modified Griffin amplitude response of the developed math model to the empirically based modified Griffin plot as taken from Govardhan and Williamson (2006). . . . .   | 224 |
| 7.1  | Flow chart for the effect of flow regime on ecological integrity (Allan and Castillo 2007). . . . .   | 239 |
| 7.2  | Definitions of basic multiple cylinder arrangements (Blevins 1990). . . . .   | 239 |
| 7.3  | Side-by-side and tandem cylinder wakes as a function of separation (Blevins 1990). . . . .  | 240 |
| 8.1  | Flow chart for derivation of the VIV energy math model. . . . .   | 249 |
| 8.2  | Shear layer transition frequency in comparison to von Kármán vortex shedding frequency as a function of Reynolds number (Prasad and Williamson 1997). . . . .   | 249 |

## LIST OF TABLES

### Table

|     |   |     |
|-----|---|-----|
| 1.1 | Characteristic flow regimes in the wake of a stationary circular cylinder, taken from Zdravkovich (1997), Sumer and Fredsøe (1997), and Raghavan (2007). . . . .  | 34  |
| 1.2 | Sketches of the characteristic flow regimes in the wake of a stationary circular cylinder, taken from Sumer and Fredsøe (1997). Solid lines represent laminar flow and dashed lines represent turbulent flow. . . . . | 35  |
| 3.1 | Assumptions used in the development of the first-order approximations for inputs into the derived energy model. . . . .   | 88  |
| 5.1 | Final math model inputs and outputs. . . . .  | 195 |
| 6.1 | Selected experimental data sets for comparison against developed mathematical model. . . . .  | 204 |

## NOMENCLATURE

### Symbol    Definition

#### Latin Alphabet

|               |  |
|---------------|--|
| $A$           | Cross-sectional area per unit length                             |
| $a_*$         | Dimensional inertia coefficient                                  |
| $c$           | Dimensional damping coefficient                                  |
| $C_a$         | Dimensionless fluid added mass                                   |
| $c_y$         | Dimensionless lift coefficient                                   |
| $D$           | Cylinder diameter  |
| $E$           | Energy   |
| $F$           | Force  |
| $f$           | Frequency  |
| $f_n$         | Natural frequency  |
| $f_r$         | Response frequency of cylinder motion                            |
| $f_s$         | Strouhal frequency   |
| $k$           | Dimensional spring stiffness coefficient                         |
| $\mathcal{L}$ | Lagrange energy operator   |
| $l$           | Formation length   |
| $m$           | Dimensional cylinder mass per unit length                        |
| $m_a$         | Dimensional fluid added mass                                     |
| $Q$           | Volume flow rate per unit length, same as $\dot{m}/\rho$         |
| $R$           | Cylinder radius  |
| $r$           | radius coordinate, zero at the stationary center of the cylinder |
| $Re$          | Reynolds number  |
| $St$          | Strouhal number, 0.21 unless noted otherwise                     |
| $T$           | System kinetic coenergy  |
| $u$           | velocity magnitude, function of x,y, and t                       |
| $U$           | Steady free stream velocity                                      |

|     |                                     |
|-----|-------------------------------------|
| $V$ | System potential energy             |
| $v$ | Body velocity as a function of time |
| $w$ | Wake variable                       |
| $y$ | Body-displacement variable          |

### Greek Alphabet

|            |  |
|------------|--|
| $\alpha$   | Fraction of energy transferred from shear layer to attached vortex |
| $\Gamma$   | Total net circulation  |
| $\gamma$   | Dimensional fluid stiffness coefficient                            |
| $\Delta$   | Maximum boundary layer thickness                                   |
| $\delta$   | Boundary layer thickness ( $u = 0.99U$ )                           |
| $\zeta$    | Dimensionless damping coefficient                                  |
| $\eta$     | Radius of Rankine vortex core                                      |
| $\Theta$   | Amplitude of oscillation for an angle                              |
| $\theta$   | Angle coordinate in radians, zero at upstream center line          |
| $\nu$      | Kinematic fluid viscosity  |
| $\Xi$      | Nonconservative forces   |
| $\rho$     | Fluid density  |
| $\omega_n$ | Rotational natural frequency                                       |
| $\omega_s$ | Rotational Strouhal frequency                                      |

### Subscripts

|          |   |
|----------|---|
| $o_b$    | The bottom fluid rotating counterclockwise from the mean stagnation point |
| $o_{BL}$ | The boundary layer effect on the system                                   |
| $o_{fp}$ | At the formation point  |
| $o_{KV}$ | The attached von Kármán vortex effect on the system                       |
| $o_{SL}$ | The shear layer effect on the system                                      |
| $o_{st}$ | At the stagnation point   |
| $o_{sp}$ | At the separation point   |
| $o_t$    | The top fluid rotating clockwise from the mean stagnation point           |

### Style

|                     |  |
|---------------------|--|
| $\dot{\phantom{x}}$ | Time-derivative  |
| <i>italics</i>      | Assumption or limitation being imposed on method development |

### Acronyms

|     |                              |
|-----|------------------------------|
| CFD | Computational Fluid Dynamics |
|-----|------------------------------|

|        |  |
|--------|--|
| DNS    | Direct Numerical Simulation                        |
| FSI    | Fluid-Structure Interaction                        |
| LES    | Large-Eddy Simulation                              |
| PIV    | Particle Image Velocimetry                         |
| RANS   | Reynolds-Averaged Navier-Stokes                    |
| RK4    | Runge-Kutta Method of Order Four                   |
| VEM    | Vortex-Elements Method                             |
| VIV    | Vortex-Induced Vibrations                          |
| VIVACE | Vortex-Induced Vibrations for Aquatic Clean Energy |

## ABSTRACT

This dissertation studies harnessing of the hydrokinetic energy of water-currents by utilizing single degree-of-freedom Vortex-Induced Vibrations (VIV) of a circular cylinder. A mathematical model is developed based on a novel approach of energy phenomenology supported by experimental measurements of harnessed energy. VIV is a complex fluid-structure interaction. Computational fluid dynamics has limited success due to the necessity to resolve the smallest scales. Phenomenological models are based on linear, mass-spring-dashpot equations or van der Pol oscillators with experimentally defined sinusoidal forcing missing the underlying physics of VIV. Van der Pol oscillators do not model VIV, just classical flutter. In all models, the vortex-shedding mode is limited to 2-Single vortices per cylinder cycle, while experiments show broad variety of vortex structures. In this dissertation, a new math model is developed through rigorous derivation of the energy of a cylinder, boundary layer, shear layer, and attached vortices, allowing for small-scale variations to be smoothed out, leaving the large-scale variations as the drivers for VIV. Due to the rigorous derivation, all parameters are physically meaningful and experimentally measurable. No curve-fitting is used to develop the model and there was no intended final form of the equation. Hamilton's principle is used to develop the force equation. The developed model has high level of qualitative and quantitative success capturing:

(a) The phase-shift between the lift force and the cylinder displacement at synchro-

nization lock-in.

- (b) The cylinder frequency lock-in response around the natural frequency.
- (c) The higher cylinder frequency response for very low mass ratio.
- (d) Lock-out at desynchronization.
- (e) The vortex-shedding frequency not locking in at synchronization. This allows for the model to respond to various vortex shedding modes, with both the traditional 2-Single and 2-Pair modes documented, along with even higher modes observed in the output.
- (f) The amplitude response, qualitatively, in the representation of initial, upper, and lower branches within the range of synchronization, followed by desynchronization.

The model yet fails to capture the actual amplitudes, but small changes in energy have nonlinearly large effects on the amplitude. In future research, the model will be updated to capture all of the energy affecting the system.

## CHAPTER 1

### Introduction

“The renewable energy era has begun (Sims 2004).” In an innovative approach, a concept for extracting energy from water was invented by Bernitsas and Raghavan in the Department of Naval Architecture and Marine Engineering and patented through the University of Michigan (Bernitsas and Raghavan 2004; Bernitsas and Raghavan 2005a; Bernitsas and Raghavan 2005b; Bernitsas and Raghavan 2005c). The concept has been named VIVACE (Vortex-Induced Vibrations for Aquatic Clean Energy), and in its simplest form consists of a single rigid cylinder mounted on elastic supports. The cylinder is connected to a power take-off system and placed in a steady, uni-directional current, causing excitation through VIV (Vortex-Induced Vibrations) (Bernitsas, Raghavan, Ben-Simon, and Garcia 2006) (Figure 1.1). The single cylinder can be expanded to an array of cylinders for optimal energy extraction (Figure 1.2).

#### 1.1 Thesis Problem

The essential problem of this thesis is to analytically predict vortex-induced vibrations of a single degree-of-freedom cylinder in water currents in order to calculate the energy that can be extracted. Due to the complex nature of the VIV phenomenon, Navier-Stokes equations cannot be analytically solved, and extant VIV models fail



to model the actual phenomenon when trying to seam desired characteristics with known mathematical equations. Therefore, a mathematical model is developed using a new model for the predictions. This model is required to be fairly robust with few user-defined parameters, and all the parameters are to be physically meaningful and experimentally measurable. The robustness of the model includes applicability to a wide range of Reynolds numbers. Since energy extraction is of paramount importance in the problem at hand, the desired Reynolds number range is on the order of  $10^5$ , placing the problem out of the realm of direct numerical simulation and requires use of numerical turbulence models for computational fluid dynamics.

Traditional models tend either to not be robust over a wide range of flow velocities, or to not be physically meaningful. This is why a new model is developed, using an energy phenomenological approach. The energy approach allows for small-scale variations to be smoothed out, while focusing on the large-scale variations as the drivers for VIV. Working at the integral level of energy, many errors are smoothed out, and the cylinder and attached fluid becomes a single system with a single degree-of-freedom for the motion of the cylinder. Hamilton's principle is then applied to derive the force equations. The model is then used in combination with available experimental data and tests at the Marine Renewable Energy Laboratory at the University of Michigan (Bernitsas, Raghavan, Ben-Simon, and Garcia 2006; Bernitsas, Ben-Simon, Raghavan, and Garcia 2006) to predict the energy extraction available for one and then multiple cylinders. In addition, ecological impacts are also considered based on the anticipated flow regime change.

The developed model predicts three key parameters: the synchronization of the cylinder motion over a range of reduced velocities, the ability for the model to have different vortex shedding modes, and the lock-in of the cylinder motion frequency

with the natural frequency within the range of synchronization. With these three criteria met, the model far exceeds any extant VIV model. Parameter inputs using physically meaningful quantities can then be used to allow the amplitudes of oscillation to match experimental results.

## 1.2 VIVACE

In order for any device to be justified as effective at harnessing renewable energy from water, six criteria must be met: there must be a high density of energy that is captured; the device must be unobtrusive; the maintenance on the device must be minimal; the device must be robust in the environment; the cost must be below targets for the entire life-cycle; the lifetime of the device must be on the order of ten to twenty years (Bernitsas, Raghavan, Ben-Simon, and Garcia 2006). Preliminary calculations based on prototype model tests show that VIVACE is expected to reach all of these criteria. In further detail, VIVACE extracts kinetic energy from the body of water, either an ocean, river, or other moving water, through the low-pressure, low-speed currents that are naturally occurring in the water with predictability. The manner in which the kinetic energy is extracted is by VIV. VIV converts kinetic energy from the current to transverse mechanical motion of the cylinder. The energy can then be converted from mechanical to electrical through a variety of generator types.

VIVACE has tested well in early experiments, with peak cross-sectional energy extraction reaching 30.8% and integrated power extraction as high as 22%. An estimate of the upper limit for extraction of energy from currents by VIV has been calculated at 36.63% (Bernitsas, Ben-Simon, Raghavan, and Garcia 2006). From these early test results, it appears that VIVACE is efficient and cost-effective at extracting energy from what can only be considered an abundant, predictable, and

renewable alternative energy resource. From the early measurements, it can be speculated that the device may even be competitive with conventional energy generation technologies in addition to alternative technologies (Bernitsas, Allan, Webb, and Lyon 2006). Further work is needed to compute the energy extraction rates for any flow regime, as each installation cannot be modeled experimentally. It is also speculated that VIVACE has the potential to generate clean renewable energy without disrupting what can only be described as the fragile water environments.

As stated above and as the name indicates, VIVACE uses the extensively studied phenomenon of VIV to extract energy from water currents. VIV is included in a particular group of Fluid-Structure Interactions (FSI) in which the structure vibrates with a certain number of degrees of freedom due to some relationship with the natural frequency of the system. Other FSI include galloping, flutter, and buffeting. The VIV phenomenon occurs over a wide range of flow speeds, defined by the Reynolds number ( $Re$ ) for a variety of bluff bodies, although the cylinder is the most commonly studied. VIV has been shown to occur at  $Re$  as low as 400 and as large as  $10^{10}$ . The complexity of VIV comes in the form that it is a highly nonlinear phenomenon. The word highly is used because there are several manifestations of nonlinearity involved. One nonlinearity results from the vortex shedding synchronization with the bluff-body vibrations over a broad range of current velocities. Another is due to the self-limiting amplitudes of oscillations. Other nonlinearities appear due to the dynamic nature of the added mass, and the inherent nonlinearities in real-world dampers and springs.

In order to further illustrate the importance of VIV in the scientific community, the example of the Tacoma Narrow Bridge Disaster in Tacoma, Washington on November 7, 1940 cannot go without mention. Just after completion, a particular

wind velocity blew across the bridge, sending it into VIV, until the bridge collapsed. This outlines a key difference in the approach to VIV between VIVACE and all other applications. Typically, research attempts to inhibit or suppress VIV, so as to avoid oscillations in the structure from the fluid. VIVACE, however, enhances the vibrations in order to convert the motion to electricity (Bernitsas, Allan, Webb, and Lyon 2006). The problem in VIVACE then becomes how to optimally dampen the system for extracting energy while not over dampening to the point of suppressing the vibrations.

There are two additional parameters that make a study of the VIVACE concept unique from other VIV studies. They are the fact that the damping is much higher than in other studies due to the harnessing of the kinetic energy for conversion to electricity and that  $Re$  range of interest for maximum energy extraction is significantly higher than past VIV studies. This range of  $Re$  is more realistic to operating conditions, and it increases the lift forces, amplitude of oscillations, and the range of synchronization on the cylinder. VIVACE is estimated to operate at an efficient level for flow velocities as low as  $0.25m/s$ , more than an order of magnitude lower than what most hydrokinetic devices need for operation (Bernitsas, Raghavan, Ben-Simon, and Garcia 2006). Currently, there is a plan for a VIVACE installation in the Detroit River in Detroit, Michigan. In the proposed area of the installation, the flow varies between  $0.3m/s$  and  $1m/s$ , with an average velocity of  $0.75m/s$ . Other hydrokinetic devices, such as turbines, require relatively high flow velocities (typically around  $3m/s$  for reasonable energy extraction rates).

This leads to the four principles of VIVACE that are all interconnected.

- The first is VIV itself, where the cylinder naturally oscillates perpendicular to its axis and to the flow direction.

- The second is the nonlinearity of the vibrations, as mentioned before, partly due to the self-limiting amplitude of oscillations and the synchronization of vortex shedding.
- The third principle is the correlation length. The correlation length is the average length of a cell of in-phase vortex shedding. Turbulence or a large aspect ratio of the cylinder length to diameter often lead to cells of vortices with different phases, leading to opposite signs of lift forces. In order to keep the correlation length equal to the length of the cylinder (one cell), recommendations must be made for the aspect ratio, enhancing the lift force.
- The fourth principle of VIVACE is the generation of energy, which induces mechanical damping on the structures. A careful balance must be found so as to optimally extract energy without over damping.

The parameters to be considered for a single cylinder are the mass ratio of the mass of the oscillating parts to the displaced fluid mass, the  $Re$ , the current flow velocity, and the damping. The complexities of the problem are in the wake structures, the range of synchronization, the appearance on initial, upper, and lower branches over the range of synchronization when referring to the amplitude of oscillation, and the distinct flow regimes both upstream and downstream of the cylinder. The problem is further complicated when an array of cylinders is considered for maximizing the energy extraction in a given volume. In fact, the variety of configurations of the array is further indicative of the impossibility of experimental tests or Computational Fluid Dynamic (CFD) simulations in all cases.

To date, no VIV work has addressed the area of high damping nor high  $Re$ , where VIVACE will operate. Only low damping and subcritical  $Re$  have been studied,

although extensively. The first publication dealing with high damping came from the VIVACE group in 2006. The highest  $Re$  for experimental work reported in literature as of 2004 was 40,000, and the highest  $Re$  for numerical work was 3800 for a two-dimensional model, and 1,000 for a three-dimensional model (Williamson and Govardhan 2004). Other works have reported singular points at higher  $Re$  (Ding, Balasubramanian, Lokken, and Yung 2004), but no comprehensive data sets are available.

In fact, there is literature as recent as the year 2008 supporting the idea the VIV has no  $Re$  dependence. This assertion is unproven and unfounded. Early VIVACE work strongly contradicts this idea, showing a high dependence on  $Re$ . The  $Re$  range studied in this thesis is from  $8 \times 10^3$  to  $2 \times 10^5$ . Another important parameter incorporated into the mathematical model is the mass ratio (the mass of the oscillating parts divided by the mass of the displaced fluid). The range of synchronization of flow speed over which the cylinder oscillates largely depends on the mass ratio. VIVACE prototypes have mass ratios in the range of 1.0 to 3.0, which is considered high. The spring stiffness also largely affects the range of synchronization as it defines the natural frequency. The free stream velocity is also important, not just to  $Re$ , but also to define a reduced velocity for the range of synchronization. VIVACE operates in free stream velocities as low as 0.25 meters per second. Finally, the cylinder diameter is also important as a design parameter to normalize the amplitude of oscillation and define  $Re$ .

A final component of the thesis will be to assess the environmental impact of VIVACE on a water system. Incontrovertibly, the nature of a body of water is defined by the flow. Any human invasion affects the flow, which in turn affects the marine organisms. The initial mind set is that VIVACE can be considered a benign invasion,

but evidence must be shown to support this in order to move forward with prototypes and commercialization. Site specific, general guidelines and recommendations can be drawn from flow regime change examination, indicating the impact on fish, sediment, and other environmental components. An investigation of the proximity to the free surface and the bottom can easily be performed. Conclusions can then be drawn as to how far from the interfaces the cylinder must be in order to avoid disturbing the nutrient film on the free surface integral to water life, and to avoid disturbing contaminants in soft sediments on the bottom. An environmental assessment of VIVACE will also improve the understanding of the impact of placing any man-made objects in a body of water.

There are several major assumptions that will be used to derive the mathematical model in this thesis. *The first and most important assumption is that the fluid-structure interaction of VIV can be effectively modeled in two-dimensions for VIVACE.* This enforces a correlation length equal to the length of the structure, where the entire vortex sheet is in-phase. This also ignores the effects of the endplates of the finite cylinder. The two-dimensionality also suppresses any three-dimensional instabilities that may be occurring. Computational fluid dynamics has shown that, not working on an integrated energy level, the small-scale instabilities are necessary to properly model VIV. With the integration of the energy, many of these small three-dimensional instabilities are integrated out, as the two-dimensional effects are much larger, and the two-dimensional assumption holds.

### **1.3 General Literature Review**

A search on Google.com online for “vortex induced vibrations” turns up over 43,000 results. To say the least, the study of VIV is extensive, although not exhaustive. With so many intrinsic complexities, VIV may never be fully understood. There

has been documentation on the phenomenon beginning with the rabbinic records from thousands of years ago, where King David hung a stringed instrument over his bed at night and the wind would cause the strings to sound. Formally examining vortices and the resulting vibrations, however, is much newer than this. Leonardo da Vinci drew a sketch of the vortex street behind a piling in a river in 1513 (Figure 1.6). Strouhal in 1878, however, was the first to document the observation that the frequency of vibration of a string was proportional to the wind speed divided by the thickness of the string (Blevins 1990). This introduces the non-dimensional Strouhal number, which is still the predominant characteristic of any vortex shedding flow, although not to be labeled a “unique identifier” (Sarpkaya 2004). A series of scientists soon followed Strouhal in studying VIV, with Lord Rayleigh in 1879 noting that the vibrations were in fact in the transverse direction, Benard in 1908 noting that the vortices were related to the periodicity of the wake, and finally, von Kármán in 1912 noting the stable street of alternating vortices in the wake (Blevins 1990).

Since early pioneers in the field like Strouhal and von Kármán, much more work has been done in the field, with reviews appearing with increasing frequency, particularly as controversy in analyses arise (Bearman 1984; Williamson 1996; Williamson and Govardhan 2004; Sarpkaya 2004). Several texts are entirely devoted to the subject of flow around cylinders (Zdravkovich 1997; Zdravkovich 2003), while there are even texts devoted just to VIV (Blevins 1990; Chen 1987; Sumer and Fredsøe 1997). The quantity of books available on the subject is a good indication of the complexity of the phenomenon, and, as noted in the introduction, all work so far published is for low  $Re$  and low damping. It is recommended that anyone seeking to understand the basic phenomenon peruse any one of these texts, as a brief description is all that will be included below. For the case of water flow, which does have subtle,



quantifiable differences from air flow, the text by Sumer and Fredsøe (1997) is recommended. One important factor that all should be aware of is that VIV occurs not only near the natural frequency of the system, nor near the Strouhal frequency, but over a wide range of flow velocities, including super-harmonics of the natural frequency (Sarpkaya 2004).

In order to familiarize the reader with VIV, a very simple explanation will now be presented. For a cylinder, when  $Re$  is greater than 40, vortex shedding occurs. The vortices will shed with opposite orientation from opposite sides of the cylinder. This is because flow separation occurs and the shear layer will roll up into a vortex. The only stable arrangement is for the vortices to alternate as was shown mathematically by von Kármán, making one larger than the other at all times. The actual mechanism of vortex shedding is not known for certain. However, a generally accepted theory is that the larger vortex draws the smaller vortex across the wake, causing the shear layers to interact, which effectively cuts off the supply to the larger vortex and it is then shed and carried downstream. The smaller vortex is now the larger one and the process continues, as represented in Figure 1.7. This theory was first developed because it was found when a splitter plate was placed on the downstream side of the cylinder, the vortices remained attached to the cylinder, supposedly because they did not interact as described. This is also shown in Figure 1.7.

Vortex shedding leads to periodic variations in the lift and drag forces. The lift force has a period equal to the vortex shedding frequency. When a degree of freedom is allowed in the cross-flow direction, these variations in the lift force induce vibrations, or VIV. The preceding description of VIV is named the Gerrard model, as outlined by Gerrard (1966). Two key instability regions have been identified in the description: the vortex and the shear layer. Prasad and Williamson (1997) defined

the vortex instability to be a Hopf bifurcation and to be of the order of the diameter of the cylinder. The shear layer instability, they argued, is a Kelvin-Helmholtz type instability of the order of the shear layer thickness. This argument of two distinct instabilities can aid in the modeling of VIV.

#### 1.4 VIV of a Single Cylinder

VIV can occur with any elastic bluff body. The area of interest here is for a rigid circular cylinder with a single degree of freedom in the transverse direction resulting from elastic mountings. This therefore excludes work done for any non-circular and non-cylindrical structure, any elastic structure, and any rigid structure with more than one degree of freedom. In general, literature on these excluded topics will be avoided except where pertinent due to the large discrepancies and further complications in their fluid-structure interactions. It was noted by Sarpkaya (2004) that only short cylinders eliminated two degree-of-freedom interaction, enabling single-mode lock-in for vibrations. For this reason, VIVACE has a specified aspect ratio of finite length.

The complexity of the problem begins with the numerous parameters needed to define VIV. These parameters are fluid density, dynamic viscosity, free stream velocity, cylinder diameter, cylinder length, spring stiffness, cylinder roughness, structural damping, mean shear stress, body mass, turbulence intensity, etc. (Sarpkaya 2004; Sumer and Fredsøe 1997). In this work, VIVACE uses only smooth cylinders, so roughness may be excluded, only slightly simplifying the problem. The  $Re$  was often thought to be unimportant in a variety of variables (amplitude of oscillation, range of synchronization). It was not until recently that the large effect of  $Re$  was in fact substantial. Govardhan and Williamson (2006) published an entire paper on the subject, although the experimental data is still incomplete to validate their conclu-

sions of the exact  $Re$  effect. The  $Re$  effect was noted in the amplitude of oscillation, where the amplitude was found to increase with increasing  $Re$ . A modified amplitude in the Skop-Griffin plot, a plot often used to show the relationship between a combined mass-damping parameter and the amplitude of oscillation (Williamson and Govardhan 2004), shows preliminary results with all current experimental data collapsing “beautifully” onto one line (Figure 2.7). VIVACE, however, has shown to have results that still lay outside this line, indicating the  $Re$  effect on amplitude is still not satisfied analytically. Raghavan, M., and Maroulis (2007) prove the  $Re$  dependence of VIV for the first time.

Williamson (1996) outlined the three-dimensionality of VIV. The three-dimensional aspects include cellular shedding, as discussed above in the correlation length, vortex dislocations, oblique shedding, phase shocks and expansions, vortex loops, and end boundary conditions influencing the flow inside the ends. These aspects can be broken into extrinsic and intrinsic categories, where the end conditions would be extrinsic, and the natural instabilities intrinsic. The actual effect of all the three-dimensionality on the fluid forces on the cylinder, however, is still not known.

The emphasis on very low mass and very low damping in VIV work has been acknowledged (Williamson and Govardhan 2004). As with any complex phenomenon, the initial work was done in these ranges in order to further the information about the simplest form of the phenomenon. The highest  $Re$  done in experimental work for VIV on an single-degree-of-freedom, elastically-mounted rigid cylinder is  $4 \times 10^4$ , and computational work has only gone as high as  $3.8 \times 10^3$  (Williamson and Govardhan 2004). The result is that most conclusions in recent works call for increased information to be collected on VIV for  $Re$  greater than  $2 \times 10^4$  (Sarpkaya 2004). It has been acknowledged that general phenomenon of VIV at higher  $Re$  is still unknown, and

different wake structures may exist. Also, the maximum amplitude possible, which has been found to increase with  $Re$ , is still unknown, and there may be more general characteristics of the flow that change with  $Re$  (Williamson and Govardhan 2004). All of the complexities of VIV at higher  $Re$  are left open for questioning. Studying VIVACE and simulating the flows will help answer these unknowns.

There are also several topics of debate within the VIV phenomenon. It has been proposed that there is a critical mass ratio at which point the range of synchronization would be infinite, or VIV would exist to infinite flow velocity (Williamson and Govardhan 2004). Intuitively, this appears impossible and there is not yet any data to substantiate this conclusion. Additional debate exists of the decomposition of the forces on the body. Many have proposed that the added mass force can be considered entirely inviscid, separating it from all other forces. However, Sarpkaya (2004) points out that even Stokes in 1851 showed that the added mass has a viscous component that changes in magnitude and position with time. An additional parameter, referred to as the Skop-Griffin parameter, is proportional to the mass ratio multiplied by the damping. This parameter is also under dispute; where many now use it to plot data, and others identify it as unsupported (Sarpkaya 2004).

Other debates also exist about the relevance of the simple single-degree-of-freedom elastically-mounted rigid cylinder as a model for more complex systems. The relationship between forced and free vibrations has not been established, either, as much work has been done to define the problem using forced, often linear, vibrations in order to gather data otherwise difficult to obtain with free oscillations. The application of forced oscillation data to the free vibration problem has not been entirely substantiated.

The highly nonlinear nature of VIV is emphasized in most review papers. Sarp-

kaya (2004) describes VIV in the following way: “It is an inherently nonlinear, self-governed or self-regulated, multi-degree-of-freedom phenomenon. It presents unsteady flow characteristics manifested by the existence of two unsteady shear layers and large-scale structures.”

At this point, key data reporting plots will be identified. There are two main plots for reference: the range of synchronization and the Griffin plot. The range of synchronization plots the non-dimensional amplitude of oscillation as a function of non-dimensional free-stream flow (Williamson and Roshko 1988). The new, modified Griffin plot is shown in Govardhan and Williamson (2006) and in Chapter 2. This plots a mass-damping parameter against a modified non-dimensional amplitude. Both plots are key because the VIVACE data sets to date are proving to be very different in nature from these plots, and they will become a key comparison between past data sets and the work done by VIVACE at high  $Re$  and high damping (Bernitsas, Raghavan, Ben-Simon, and Garcia 2006; Bernitsas, Ben-Simon, Raghavan, and Garcia 2006).

The range of synchronization plot shows three branches: initial, upper, and lower, with a discontinuity between the initial and upper, and a hysteresis between the upper and lower. The hysteresis indicates a memory effect on VIV, another source for nonlinearity. With increasing  $Re$ , it has been found that the upper branch extends while the lower branch is cut off. VIVACE is finding an even more prominent difference, with no lower branch, and a continually increasing upper branch. It has already been suggested that the jump to the upper branch may be an effect of  $Re$  (Sarpkaya 2004), but VIVACE results are going beyond this concept (Bernitsas, Raghavan, Ben-Simon, and Garcia 2006; Bernitsas, Ben-Simon, Raghavan, and Garcia 2006).

While on the topic of Reynolds number, it has been shown in the past that the

phase angle between lifting and vortex shedding, and the lift coefficient both significantly increase with increasing  $Re$ . The effect on increasing  $Re$  on the amplitude of oscillation and the frequency of excitation was considered unknown (Sarpkaya 2004) but was reported for the first time by Raghavan, M., and Maroulis (2007).

### 1.5 VIV of Multiple Cylinders

There has been a large quantity of work done for two or more cylinders coupled by the fluid flow. This is due to the fact that VIV can occur in a wide range of real world applications. It occurs for riser cables and structural supports of offshore structures as well as for heat exchangers. Both of these applications involve multiple bodies affected by the flow of their neighbors. Zdravkovich (1997, Zdravkovich (2003) outlines the further complexities of multiple stationary cylinders, and Blevins (1990) dedicates an entire chapter to introduce the complexities of multiple cylinders in VIV. A common occurrence is that VIV is not the only vibratory Fluid Structures Interaction present. Galloping, and sometimes flutter, enter into the problem for the downstream cylinders.

For two cylinders in tandem, it has been shown that the upstream cylinder behaves independent of the downstream cylinder, while the downstream cylinder has a high dependence on the separation distance between the two cylinders. Coupling with the second cylinder is caused by the fluid flow, and the turbulence intensity in the flow greatly affects the response of the cylinders. The maximum amplitude of oscillation and the synchronization region for the second cylinder is decreased with increasing separation distance between the cylinders (Laneville and Brika 1999). However, if the cylinders are placed one atop another rather than tandem, or even at an angle from one another, neither cylinder can be considered independently. It is obvious from a brief overview that the complexity is greatly increased by having more than one

cylinder present in the fluid. Additionally, the literature review could become very extensive if all cases were considered herein. For brevity, it will be concluded that the FSI of multiple cylinders is highly dependent on the arrangement of the cylinders, and no universal conclusions can be drawn as to what the effect of altering an arrangement may be. For this reason, it is important to have experimental information available for the simulations of a VIVACE array.

## 1.6 VIV Numerical Simulations

Numerical simulations have been used mostly only in the laminar flow regime. Numerical simulations have always been measured against experimental visualization. For VIV, it is particularly important to obtain measurements and flow visualization with non-intrusive techniques, such as Particle Image Velocimetry (PIV). A variety of flow simulation methods have already been applied to the VIV problem, including Direct Numerical Simulation (DNS), Reynolds-Averaged Navier-Stokes (RANS), Large-Eddy Simulation (LES), and Vortex Element Methods (VEM), all of which involve some form of the Navier-Stokes equations (Sarpkaya 2004). DNS is typically the preference, but due to exorbitant computational cost and unacceptable computational time, it is not even considered an option for flows with any complexities. DNS has recently been applied to a stationary and forced rigid cylinder at a  $Re$  of  $1 \times 10^4$ . This is within the turbulent regime. Multilevel-type parallel algorithms within a spectral element framework were used (Dong and Karniadakis 2005). This work, however, did not allow for free vibrations of the cylinder.

### 1.6.1 Kolmogorov Length Scale

In determining the necessary resolution of DNS, the smallest scale present in a simulation should be predicted. In 1941, the Russian mathematician Kolmogorov developed an equation to accurately predict the smallest scale present in a fluid flow

problem,  $L$  (White 1991).

$$L = \left( \frac{\nu^3 \delta}{U^3} \right)^{1/4} \quad (1.1)$$

In this equation,  $\delta$  is the shear layer thickness. In the case of the flow around a cylinder, the shear layer thickness can be approximated from the Blasius equation for a flat plate, assuming the boundary layer thickness is much smaller than the radius of the cylinder, and substituting the length with the arc length (Schlichting 1968).

$$\delta = 5 \sqrt{\frac{\nu R \theta}{U}} \quad (1.2)$$

Combining the two above equations and using the definition of the Reynolds number for a cylinder,  $Re = UD/\nu$ , where  $D = 2R$ , the following relationship between the Kolmogorov length scale and the Reynolds number for flow around a cylinder is found.

$$L = R \left( \frac{5\sqrt{128}\theta^{1/2}}{Re^{7/2}} \right)^{1/4} \quad (1.3)$$

The boundary layer will reach it's maximum around  $\pi/2$ , just around the separation point (see Chapter 2 for discussion of separation point), and then the relationship can be approximated as follows.

$$L \approx 2.9 \frac{R}{Re^{7/8}} \quad (1.4)$$

In order to determine the Kolmogorov length scale that would be typical for simulating the results of VIVACE, numbers for the Reynolds number and radius of the cylinder are taken from Bernitsas, Raghavan, Ben-Simon, and Garcia (2006). The diameter of the cylinder in these published experiments was on the order of  $0.1m$  ( $R \approx 0.05$ ), and the Reynolds number was on the order of  $1 \times 10^5$ . This results in a Kolmogorov length scale of approximately  $6 \times 10^{-6}$ , while the thickness of the boundary layer itself will be  $\delta \approx 1 \times 10^{-3}$ . The smallest scale is three orders of



magnitude smaller than the boundary layer thickness. Now that the smallest scale is known, estimates of the number of grid points for a direct numerical simulation can be made. To solve the flow just within the boundary layer  $\delta$  in three dimensions, there will need to be  $1000 \times 1000 \times 1000 = 1 \times 10^9$  grid points in order to resolve the smallest scales. The time scale follows the same argument, where it will take three orders of magnitude smaller resolution in the time scale to resolve the time variation of the smallest scales.

To solve the entire flow regime, there would need to be many cells of the size of  $\delta$ , on the order of  $10^4$ , or  $10^{13}$  total grid points. Most simulations require about 20 periods to pass, which would be order  $10^4$  total timesteps. For the entire simulation, the total steps in time and space would be  $10^{13} \times 10^4 = 10^{17}$  computations. Current supercomputers require approximately  $20\mu s$  per computation, so the total time to compute this simulation on a supercomputer would take  $2 \times 10^{15} s$  or over  $6 \times 10^7$  years, which is obviously not reasonable nor attainable. Even if at some point in the future computers can perform computations as the speed of light through a hydrogen atom, which is theoretically the fastest possible, the computer would take  $3 \times 10^{-19}$  per computation, so this simulation would take  $20 \times 10^{-6} s$ , and this is at the minimum. Therefore, until the theoretical limits of computers can be obtained, fully turbulent DNS is not possible for the problem at hand.

This is an extreme example, however, showing the requirements to show every detail of the flow. The Kolmogorov scale resolves only unrepeatable events that are only of statistical interest. In actuality, accurate results can be obtained within a reasonable computation time, particularly with a turbulence model, as found from RANS and LES. Although many turbulence models have been developed as a result, it is preferred by the author to look for a simpler, more robust and meaningful

analytical answer to the problem at hand, since the entire flow does not need to be described in such detail, allowing for faster calculations from a mathematical model.

In an industrial application, Halkyard, Srinivas, Holmes, Constantinides, Oakley, and Thiagarajan (2005) found that a commercially available Computational Fluid Dynamics (CFD) package showed potential for solving their VIV problem, but it overestimated the magnitude of response, and difficulties arose from many intrinsic and extrinsic properties of VIV. Kallinderis and Ahn (2005) found that the RANS equations with a Spalart-Allmaras scheme for turbulent viscosity allowed larger time steps with fairly accurate results, and Lam, Jiang, Liu, and So (2006) found that a surface vorticity method (under the category of VEM) was in good agreement with experimental data for a  $Re$  of  $2.67 \times 10^4$ . There is no agreement on one method to be superior for application to the VIV problem, and work continues on these and other flow models.

The author evaluated different available numerical simulators as an approach to the thesis problem. Based on the Kolmogorov scale used to estimate the smallest scale fluctuation in a flow, DNS would be computationally impossible at any reasonably high Reynolds number, where current supercomputers could not even handle the number of flops needed to compute a single timestep of the flow field in a reasonable timeframe, as was shown above. Although Dong and Karniadakis (2005, Halkyard et al. (2005, Kallinderis and Ahn (2005) all found reasonable approximations through numerical simulation of the Navier-Stokes equations, all simulations required calibration. These calibrations do not carry much physical meaning and often require a large amount of effort through trial and error, increasing the computational cost. It was determined that VEM could serve as the most robust simulator for a wide range of  $Re$  for VIV, particularly a mesh-free approach. However, as there

are no commercially available codes of VEM at this time, it was found that analytical modeling would create the best fast predictor of VIV for the VIVACE system.

## 1.7 Extant VIV Models

The extant models range from simple single degree-of-freedom models, typically used in engineering practice for rough estimates, to multi degree-of-freedom models that can only be examined using numerical methods. In fact, the numerical simulations of the Vortex Element Method arose from what started as a simple mathematical model. It is part of the nature of this problem to start simple and become complex very quickly while trying to correctly model each of the flow characteristics.

### 1.7.1 Linear Single Degree-of-Freedom

As indicated above, there are many parameters which play into the VIV phenomenon. For the case of the single degree-of-freedom cylinder, a simplified mathematical model has been presented in the literature. This linear, single degree-of-freedom model does not truly model VIV, but for engineering purposes, it is considered acceptable at approximating the maximum response at resonance. We already know that VIV has a range of synchronization extending well beyond the point of resonance. Although acceptable for engineering practice, there is still the necessity to calibrate the lifting force for each case (any variation of mass  $m$ , damping  $c$ , spring stiffness  $k$ , or flow velocity  $U$  is a different case). Therefore, although acceptable in engineering practice, it is not practical to rely upon such a model, especially when there is no experimental data available at a specific point. Interpolation and extrapolation of data for VIV can lead to very incorrect approximations. In addition to the limitations of the single degree-of-freedom model, even the nature of the terms in the model are highly contentious. In particular, the splitting of terms into viscous and inviscid contributions has led to wide-spread disagreement even by the most notable

researchers in VIV for the last several decades, and no agreement on the handling of the terms has been reached (Sarpkaya 2001). Bernitsas, Ben-Simon, Raghavan, and Garcia (2006) provides an approach of a single degree-of-freedom model as follows. The model is based on a simple mass-damper-spring equation.

$$m\ddot{y} + c\dot{y} + ky = F \quad (1.5)$$

$$m\ddot{y} + c\dot{y} + ky = F_{viscous} + F_{inviscid} \quad (1.6)$$

Although the division of forces into viscous and inviscid is considered controversial, in the simplest form of the mathematical model, it is appropriate since model tests are required to estimate the hydrodynamic forces. The inviscid force is proportional to the added mass of the accelerated fluid, and the viscous force is proportional to the lift force. This modifies the equation to the following form (equation 1.7) where the coefficient on the right-hand side is the lift coefficient, and the mass is the displaced fluid mass. This equation then can be non-dimensionalized to the form given in equation 1.8.

$$(m + m_a)\ddot{y} + c\dot{y} + ky = \frac{2}{\pi D}c_y(t)m_dU^2 \quad (1.7)$$

$$(m^* + C_a)\left(\frac{\ddot{y}^*}{f_n^2} + \frac{4\pi\zeta\dot{y}^*}{f_n} + ky^*\right) = \frac{2}{\pi}c_y(t)U^{*2} \quad (1.8)$$

An assumed linear form for the amplitude of oscillation and lift coefficient can then be written as in equations 1.9 and 1.10.

$$y^* = y_{max}^* \sin(2\pi f_{fluid}t) \quad (1.9)$$

$$c_y(t) = C_y \sin(2\pi f_{fluid}t + \phi) \quad (1.10)$$

Equations 1.9 and 1.10 allow for estimates of the power available in the water (equation 1.11) and power available due to damping (equation 1.12). An upper limit for the maximum rate of power harnessing can then be found, as given in equation

1.13. The actual efficiency for the VIVACE converter is measured experimentally as the power harnessed.

$$P_{fluid} = \frac{1}{2}\rho\pi C_y U^2 f_{cyl} y_{max} DL \sin(\phi) \quad (1.11)$$

$$P_{mech} = 8\pi^3 (m + m_a) \zeta (y_{max} f_{cyl})^2 f_{n_{water}} \quad (1.12)$$

$$\begin{aligned} \eta_{UL} &= \frac{P_{fluid}}{\text{Power in the fluid}} \\ &= \frac{\frac{1}{2}\rho\pi C_y U^2 f_{cyl} y_{max} DL \sin(\phi)}{\frac{1}{2}\rho U^3 DL} \end{aligned} \quad (1.13)$$

This mathematical model is the simplest form for solving quantities for the forces experienced by a cylinder in VIV. However, the hydrodynamic forces are not so simply modeled.

### 1.7.2 Van der Pol Oscillator

The van der Pol oscillator has been used several times in VIV mathematical models (Facchinetti, de Langre, and Biolley 2004; Sarpkaya 1979; Blevins 1974), particularly in two degree-of-freedom models (one for the cylinder, and one for a wake parameter). However, as clearly outlined in Billah (1989), the use of the van der Pol oscillator in VIV originates from using a well-known mathematical equation to model something with similar results, rather than the result of rigorous derivation. As a mathematical equation, the van der Pol oscillator represents self-excited oscillations, introduced through the nonlinearity of the damping term, as can be seen in the generalized form of the equation as follows. As a result, the damping is negative in response to certain motions. The resulting output is a limit cycle (Kelly 1993). The self-excitation and limit cycling are two of the characteristics of the oscillator that lead to it being selected to model VIV, despite no physical connection of the parameters,

except for reverse reasoning after the equation has been implemented.

$$\begin{aligned} \ddot{y} + 2\xi\dot{y} + y &= a\Omega^2 C_L \\ \ddot{C}_L - \alpha\Omega\dot{C}_L + \frac{\gamma}{\Omega}C_L^3 + \Omega^2 C_L &= b\dot{y} \end{aligned} \tag{1.14}$$

In fact, the forced van der Pol oscillator is very clearly defined to model a phenomenon where two frequencies coalesce. In vibratory fluid-structures interactions, this is known as classical flutter, a very different phenomenon from VIV. Therefore, although it is known that the van der Pol oscillator has a similar “shape” to VIV, it in fact models something quite different, and for that reason can never be expected to align with VIV experimental results.

One of the more famous and semi-physical developments of a coupled van der Pol oscillator system was done in the dissertation of Blevins (1974). However, when Blevins developed the model, there was a leap away from the physics of a fluid momentum approach when deriving the force through the control surface “correction terms”. This forced the equation to look like the van der Pol oscillator, and it was in this leap that the Blevins model became incorrect for modeling VIV. The Blevins nondimensionalized model is written below with notation changed only for consistency.

$$\begin{aligned} \ddot{y} + 2\xi_T\omega_n\dot{y} + \omega_n^2 y &= a_3''\dot{z} + a_4''z \\ \ddot{z}K'\frac{u_t}{U}\frac{U^\circ}{D}\omega_z^\circ z &= (a_1' - a_4')\frac{U}{D}\dot{z} - a_2'\frac{\dot{z}^3}{UD} + a_3'\dot{y} + a_4'\frac{U}{D}\dot{y} \end{aligned} \tag{1.15}$$

The nomenclature of the above terms will not be outlined here. The purpose of seeing the analytical model is to notice that in the second line on the right-hand side, there is a nonphysical term with  $\dot{z}^3$ , the result of forcing the momentum equation to look like the van der Pol oscillator. In addition, all terms beginning with  $a$  are coefficients that need to be determined experimentally. Not all of these coefficients have a straight forward, measurable value, however, and a certain amount of calibration and trial

and error must be used. Therefore, in addition to a departure from physics in the derivation of the model, the requirement for rigorous model development of having all coefficients being meaningful and measurable can not met by this model.

### 1.7.3 Landau Equation

Similar to the van der Pol oscillator is the Landau equation (Equation 1.16) , refined both by Stuart and by Ginzberg. Equation 1.17 shows a form of the Ginzberg-Landau equation used in a numerical simulation of a long, flexible cylinder used in Aranha et al. (2005). It is a simple exercise to show that with just one more simplification of the Landau equation, the van der Pol oscillator is recovered. The Landau equation is intriguing due to the fact that it is derived directly from the Navier-Stokes equation, although it is derived for the onset of turbulent instability. This is exciting, since it is the intention to always maintain some semblance of the Navier-Stokes equations in modeling fluid flow. However, in this excitement, the assumptions used to derive the Landau equation cannot be overlooked. In fact, the assumptions very quickly diverge from what we know about VIV. The assumption of the Landau equation is that there is only one frequency present, and only a short period of time has passed since a disruption, close to a critical  $Re$ , or the onset of instability, occurs in a steady flow. Additionally, the velocity of the disruption must be considered small in comparison with the steady flow.

$$v_1 = A(t)f(x, y, z)$$

$$A(t) = ce^{\gamma_1 t} e^{-i\omega_1 t} \tag{1.16}$$

$$\frac{d|A|^2}{dt} = 2\gamma_1|A|^2 - \alpha|A|^4$$

$$\frac{\partial A}{\partial t} + \sigma A - \gamma_R(1 + ic_1)\frac{\partial^2 A}{\partial z^2} + \mu_R(1 + ic_2)|A|^2 A = 0 \tag{1.17}$$

This leads to several inconsistencies with VIV. First, VIV models need to be accurate particularly after a long period of time, violating the Landau equation.

Second, the model must work for a wide variety of  $Re$ , where as the Landau equation only works within a small region just above the critical value. Additionally, as  $Re$  is increased above this critical value, additional equations must be added for additional frequencies, going to infinity as  $Re$  goes to infinity, quickly making the Landau equation impractical even if the assumptions were considered acceptable (Landau and Lifshitz 1995). It was shown that the Landau equation was an inappropriate choice for VIV more rigourously in Le Gal, Nadim, and Thompson (2001).

There has been a successful application of the Landau Equation to VIV, but not coupled for the motion of the body. Williamson (1996) showed a reasonable argument for using the Ginzburg-Landau equation to model the instability in the third dimension for VIV, although rigorous development of such a model was again a leap of known physical characteristics of the third dimesion instability and known mathematical characteristics of the Ginzburg-Landau equation.

#### **1.7.4 Billah's Model**

In 1989, Billah introduced a new model in his dissertation that took the approach of developing the Hamilton energy equations, which could then be translated into a nonlinearly coupled, two degree-of-freedom model. This is the only case where energy was the starting point of the system of equations. However, Billah did not include the physical information necessary to develop a complete VIV model. Billah does not take into account the experiments of Williamson and Roshko (1988), and therefore a large amount of information about vortex shedding modes and separation points is not covered by the model.

Billah's model is shown below, although notation has been changed in order to ease the comparison to the current thesis model. Billah begins by arguing a development of the system energy for use in Hamilton's principle, but without rigorous



development, particularly for the degree of freedom  $w$ . Dissipative forces like the mechanical damping are added later.

$$\mathcal{L} = \frac{1}{2}m\dot{y}^2 + \frac{1}{2}a_0\dot{w}^2 - \frac{1}{2}a_1y^2\dot{w}^2 - \frac{1}{2}a_2y^4\dot{w}^2 - \frac{1}{2}ky^2 - \frac{1}{2}c_1y^2w - \frac{1}{2}c_2y^4w - \frac{1}{2}\gamma w^2 \quad (1.18)$$

The above Lagrangian equation then undergoes the Hamilton's principle to develop the two force equations. The result of the derivation is as follows. Billah dropped the higher order wake parameter acceleration terms, slightly simplifying the wake equation.

$$m\ddot{y} + ky + a_1y\dot{w}^2 + 2a_2y^3\dot{w}^2 + c_1yw + 2c_2y^3w = \Xi_1 \quad (1.19)$$

$$a_0\ddot{w} + \gamma w - 2a_1y\dot{y}\dot{w} - 4a_2y^3\dot{y}\dot{w} + \frac{1}{2}c_1y^2 + \frac{1}{2}c_2y^4 = \Xi_2 \quad (1.20)$$

Billah uses a wake variable  $w$ , that at the point of developing the equation has no meaning. Later, he connected the degree-of-freedom with the vortex formation length. However, such connections formed after the model has been derived again leads to a physically meaningless model as was done in Blevins (1974) and other previous works. A single incorrect, all-encompassing assumption invalidates an entire method.

### 1.7.5 Hamilton's Principle

Others have taken notice of the work of Billah (1989), some only slightly reworking it (Goswami, Scanlan, and Jones 1993b), and others using it to develop Navier-Stokes-based equation that requires averaging of information on the entire control volume at every instant in time (Benaroya and Wei 2000; Benaroya, Wei, Kuchnicki, and Dong 2003).

Benaroya and Wei (2000) derived an extended Hamilton's Principle for external viscous flow in a fluid-structure interaction using McIver's extension to show how

Hamilton's principle applies to fluid. Initial results with an application to a cylinder pinned at one end in water experiencing VIV. First, a complete data set was collected using Particle Image Velocimetry (PIV). The results were then averaged over the control surface and volume, and averaged signal was then used as the input for the equation derived from Hamilton's principle. Benaroya, Wei, Kuchnicki, and Dong (2003) summarized the work from the previous paper and showed further proof of it's applicability to a cylinder acting like a pendulum in water. This is a very significant result, because it shows that Hamilton's principle can be successfully applied to the fluid-structure problem of VIV. It is safe to assume that an integral value of the energy in the system can properly influence the body in order to produce the phenomenon of VIV. This has been shown with these references. The below equation comes from Benaroya, Wei, Kuchnicki, and Dong (2003), and shows the form of the equation for the case of a translating cylinder with a stationary outer control volume. No results are given for this equation since all their experimental work was for the cylinder acting like a pendulum. However, this is the most relevant equation for this thesis. The equations resulting from this reference are all in units of power, and are therefore not identical to the force equations that are sought herein.

$$\begin{aligned} \dot{y} (m_{cylinder}\ddot{y} + ky) + m_{fluid}U\dot{U} = \int_{CS_{closed}} (-p\vec{n} + \vec{\tau}_c) \cdot \vec{U} ds \\ + \int_{CS_{open}} \left[ -\frac{\rho}{2}U^2\vec{U} \cdot \vec{n} + (-p\vec{n} + \vec{\tau}_o) \cdot \vec{U} \right] ds \end{aligned} \quad (1.21)$$

Although using a control-volume approach like that used by Benaroya and Wei is in fact physically meaningful, it requires that there already be a complete data set for the input, such as can only be gotten from PIV experiments. Therefore, it is in fact a matter of performing the simulation twice: once experimentally and then once numerically, thus defeating the purpose of numerical simulation. However, it does indicate that using an energy method can lead to reasonable results. In fact, the

validation of the theory comes from the same data set as the input for the analytical result, as shown in Figure 1.8. This figure shows that the analytical output for the displacement pendulum cylinder is very closely related to the experimental output, being placed on the same sized axes. It is proposed that a simplified system approach can be used in place of the fluid control volume approach with a high relative degree of success without using Reynolds transport theorem as this example did. In this sense, the system can be modeled as simply as possible, and the results should be significant.

## **1.8 Relevant Water Ecology**

When referring to water ecology, a particular phrase becomes integral: dynamic equilibrium. “The concept that each individual river has a natural (flow) regime on which its ecological integrity depends has become firmly established (Allan and Castillo 2007).” Any change to the flow regime, discussed further in Chapter 7, has a direct impact on the system ecology. The flow regime establishes the water quality, food sources and habitat available to biota, and the interactions between biota. Changing any of these features will further impact the ecological integrity as well. These types of flow regime changes have been studied with the placement and removal of dams in a river system, as well as for less-extreme cases such as log jams (Allan and Castillo 2007).

It was put best by Pelc and Fujita (2002) when they stated: “Any energy technology has some environmental impact.” With renewable energy struggling to hold onto a mere 2% of the global consumer energy market (Sims 2004), it is important to identify the environmental impacts of an installation before deployment to avoid barriers to technology development. It has been stated in many mainstream articles recently the importance in investing in a wide variety of sustainable energy sources.

It is hypothesized that VIVACE can be a contributor to the global energy market.

One important thing to note about environmental impact and ecology is that the impacts are highly site specific and scale dependent. Therefore, sites must be carefully chosen with the water environment held as a priority over the desire for renewable energy (Pelc and Fujita 2002). Gill (2005) made a generalization as to the selection device sites in order to minimize the impact on the biology in oceans, stating that: “Soft sediment communities are typically low in diversity and have species that are adapted to naturally unstable habitat conditions. However, locations that are used as a migratory or periodic habitat essential for life-history completion should be avoided.” This statement does not take into account the fact that soft sediments often contain contaminants that would then be released into the environment, extending beyond the immediate area. Therefore, even general statements have erroneous claims, further emphasizing the site specific impacts. As for the river environment, “streams with more variable flows tended to support resource generalists, and streams with more stable flows had a higher proportion of specialist species (Allan and Castillo 2007).” A river that already has a highly variable flow is more likely to be able to adapt to an installation that will cause flow variations.

When an environment is changed, the organisms present are tested for adaptability and the ability to survive. In the river system, the dynamic equilibrium is sought between the supplies of water and sediments. The quantification of this equilibrium is in its infancy, but further work will deepen the understanding of the effect man has on changing river ecology. It has already been found that large intrusions, such as dams and channels, reduce the richness of the biology of the river. It is important to “view the entire river basin as an integrated unit (Allan and Castillo 2007).”

With a system such as VIVACE, there will be both direct and indirect effects.

The direct effects will arise from the fact that energy is being removed from the ecosystem, reducing the net flow speed and changing the shear forces at the free surface and bottom interfaces. This will result in eddy formation which in turn will alter the energy distribution in the flow downstream of the device (Bernitsas, Allan, Webb, and Lyon 2006).

While any water energy installation must consider the impact on the environment, the impact could also be considered positive rather than negative in some cases. The changes in a river bottom from new sediment deposits can increase local diversity, or it could cause the bottom to become unsuitable for certain organisms. Additionally, increasing the turbulence intensity in a river, such as will occur from the turbulent wake structures of VIVACE, can either provide opportunities for station holding that can attract fish or can cause fish to avoid the area (Bernitsas, Allan, Webb, and Lyon 2006). It is important to note, however, that “the flow of water in rivers generally is turbulent (Allan and Castillo 2007).” The increased turbulence introduced by VIVACE may therefore be negligible.

It is therefore very important to understand the flow in an area and its effects on the physical, chemical, and biological conditions of rivers. Water ecosystems naturally have a wide range of variability in quantity, quality, timing, and temporal water flow. The flow rate of a river varies over all time scales, from hourly to annual to geologic time. Rivers act both as a storage and a transfer mechanism for water and are therefore important to not just the immediate biology but the global biology (Allan and Castillo 2007).

Within the contiguous USA, ten distinctive flow regimes have been identified in rivers, seven permanent and three intermittent. For every stream, the velocity varies considerably throughout the cross-section. There is friction along the sides and bot-

tom, and obstructions and meandering also contribute to the variation. Upon site selection for a VIVACE installation, the first step will be to identify the ecological current flow regime, therefore allowing ecologists to qualitatively and quantitatively assess the flow regime change that will result. This provides both the information for installation licensing as well as allowing VIVACE to be designed to be as environmentally benign as possible, enhancing its “green” energy rating. A math model that can provide large-scale flow information useful for the ecological impact assessment. This is another motivation for the model, in addition to advancing the scientific understanding of VIV for the entire science community and designing VIVACE for optimum power extraction.

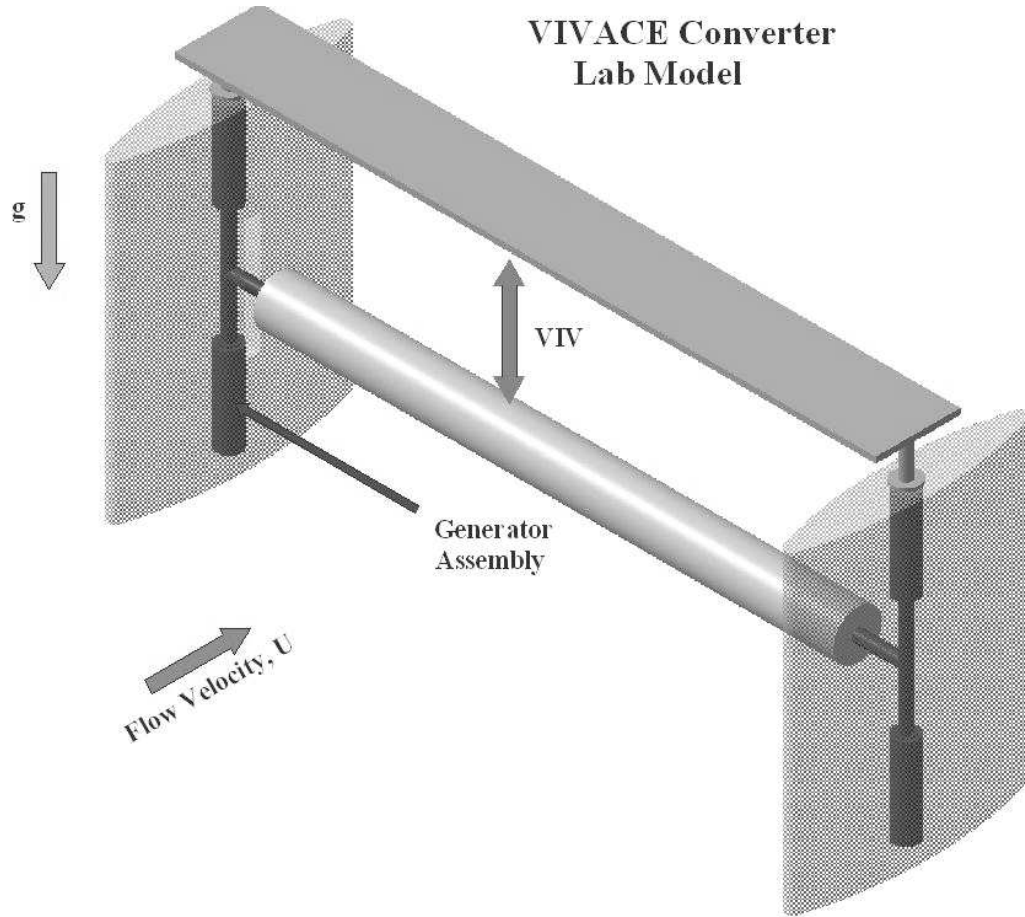


Figure 1.1: A VIVACE single cylinder schematic, where the side struts contain the generator (dampers) and springs (Bernitsas, Raghavan, Ben-Simon, and Garcia 2006).

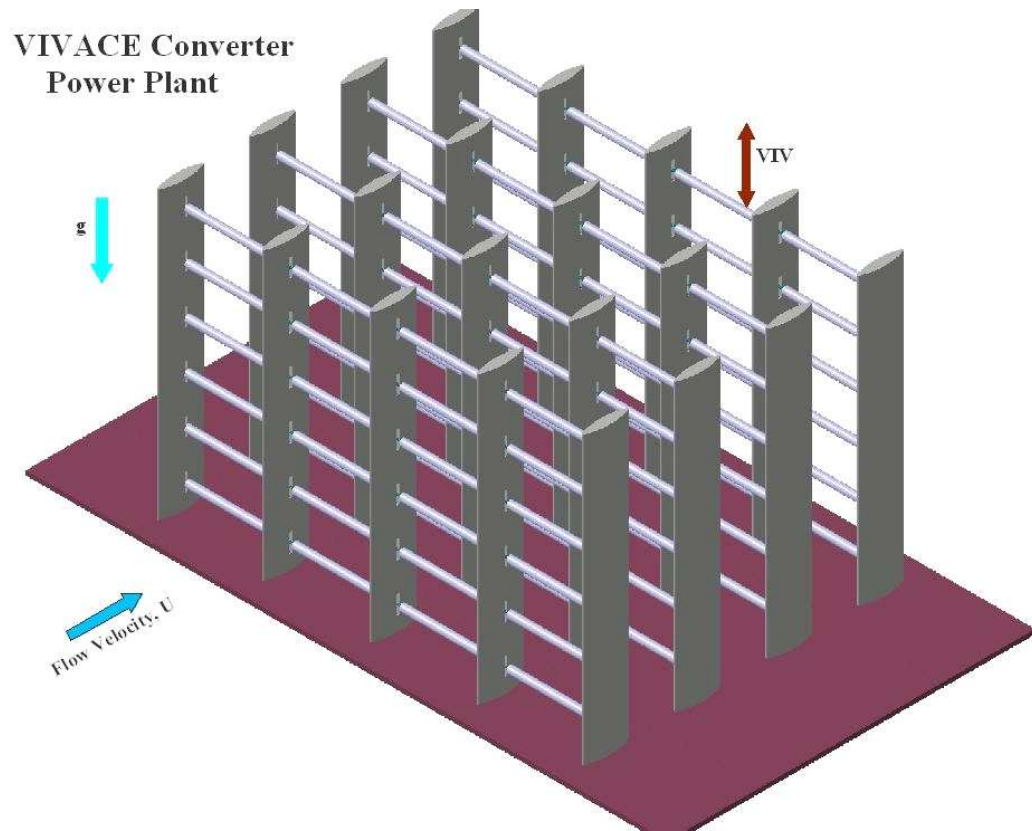


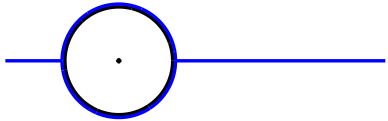
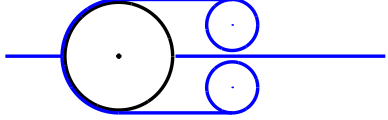
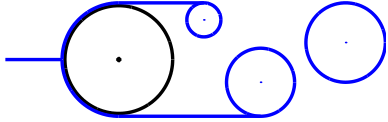
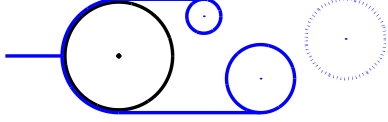
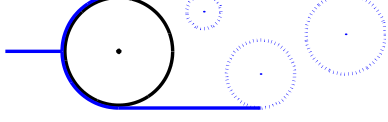
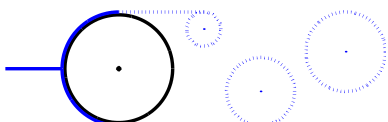
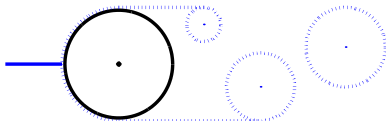
Figure 1.2: VIVACE cylinder array schematic. Cylinders are staggered in a hexagonal shape (Bernitsas, Raghavan, Ben-Simon, and Garcia 2006).

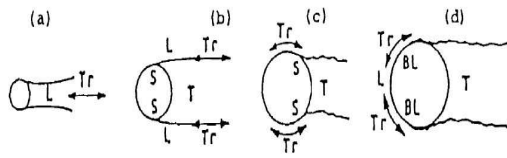


Table 1.1: Characteristic flow regimes in the wake of a stationary circular cylinder, taken from Zdravkovich (1997), Sumner and Fredsøe (1997), and Raghavan (2007).

| <i>Re Range</i>  | <i>Name</i> | <i>Characteristic Feature</i>                                   | <i>Regime</i>               |
|--|-------------|---|-----------------------------|
| $Re < 1$   |             | Creeping flow (no separation)                                   |                             |
| $3 - 5 < Re < 30 - 40$   | L1          | Steady separation (fixed pair of symmetric vortices)            | Laminar                     |
| $30 - 40 < Re < 150 - 300$   | L2          | Periodic laminar shedding (vortex street)                       |                             |
| $150 - 200 < Re < 200 - 300$   | TrW1        | Transition from laminar to turbulent vortices in wake           |                             |
| $200 - 250 < Re < 350 - 500$   | TrW2        | Transition of irregular vortex during formation                 |                             |
| $350 - 500 < Re < 1 \times 10^3 - 2 \times 10^3$                           | TrSL1       | Development of transition waves in free shear layer             |                             |
| $1 \times 10^3 - 2 \times 10^3 < Re < 2 \times 10^4 - 4 \times 10^4$       | TrSL2       | Formation of transition vortices in free shear layer            | Subcritical                 |
| $2 \times 10^4 - 4 \times 10^4 < Re < 1 \times 10^5 - 2 \times 10^5$       | TrSL3       | Fully turbulent shear layer, laminar boundary layer separation  |                             |
| $1 \times 10^5 - 2 \times 10^5 < Re < 3 \times 10^5 - 3.1 \times 10^5$     | TrBL0       | Onset of transition at separation point, laminar boundary layer | Critical (Lower Transition) |
| $3 \times 10^5 - 3.1 \times 10^5 < Re < 3.3 \times 10^5 - 3.4 \times 10^5$ | TrBL1       | Single separation bubble regime                                 | Supercritical Upper         |
| $3.3 \times 10^5 - 3.4 \times 10^5 < Re < 5 \times 10^5 - 1 \times 10^6$   | TrBL2       | Two-bubble regime, turbulent boundary layer separation          | Transition                  |
| $5 \times 10^5 - 1 \times 10^6 < Re < 3.5 \times 10^6 - 6 \times 10^6$     | TrBL3       | Fragmented separation bubble                                    |                             |
| $3.5 \times 10^6 - 6 \times 10^6 < Re < 6 \times 10^6 - 8 \times 10^6$     | TrBL4       | Partial transition, boundary layer turbulent an one side        |                             |
| $Re > 8 \times 10^6$   | T           | Complete transition to turbulence                               | Turbulent (Transcritical)   |

Table 1.2: Sketches of the characteristic flow regimes in the wake of a stationary circular cylinder, taken from Sumer and Fredsøe (1997). Solid lines represent laminar flow and dashed lines represent turbulent flow.

| <i>Sketch</i>   | <i>Range</i>                             |
|---|--|
|    | Creeping                                 |
|    | L1                                       |
|   | L2                                       |
|  | TrW1                                     |
|  | TrW2                                     |
|  | TrSL1, TrSL2, and TrSL3                  |
|  | TrBL0, TrBL1, TrBL2, TrBL3, TrBL4, and T |



Transition States (schematic); BL -- Boundary Layer, L-Laminar, S-Separation, T-Turbulent and Tr-Transition L to T.

Drag and lift coefficients

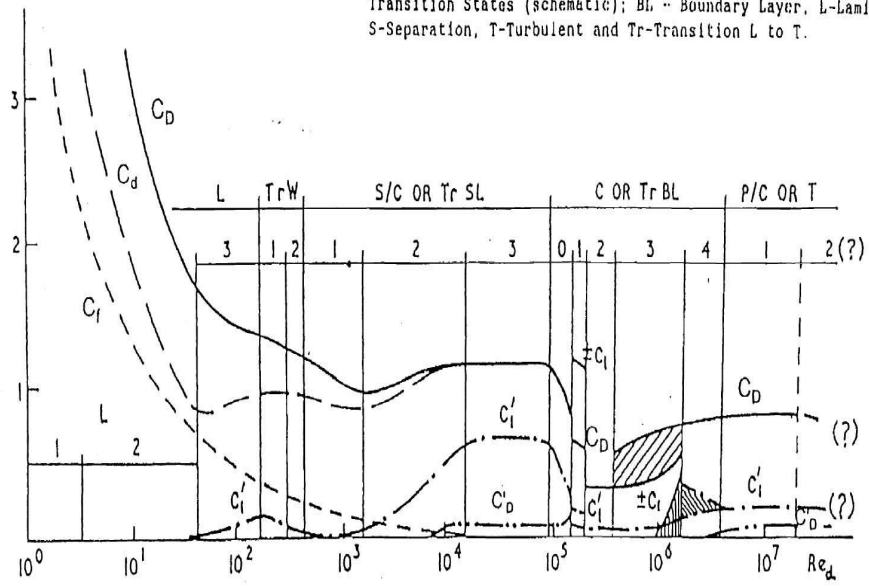


Figure 1.3: Lift and drag coefficients as a function of Reynolds number (Zdravkovich 1997).

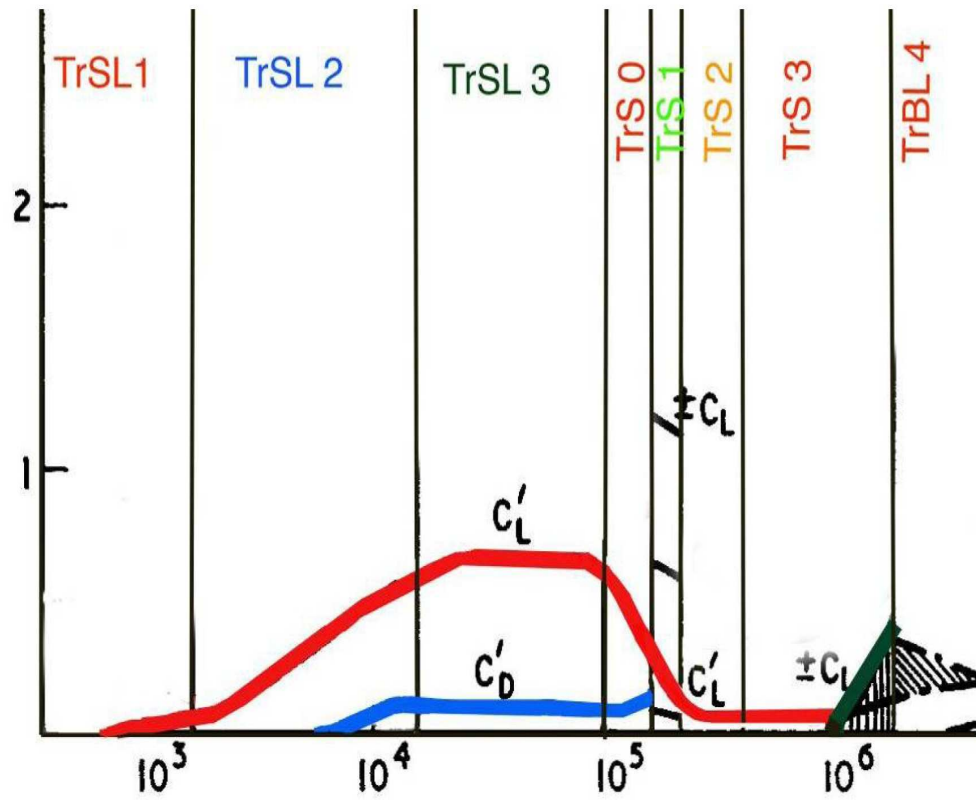


Figure 1.4: Lift and drag coefficients as a function of Reynolds number for the Reynolds number area of interest in the transition region (Zdravkovich 1997; Raghavan 2007).



Figure 1.5: The destructive nature of VIV is best exemplified by the Tacoma Narrows Bridge Disaster in Tacoma, Washington, 1940.



Figure 1.6: Sketch by Leonardo da Vinci in 1513 showing the wake behind a piling in a river.

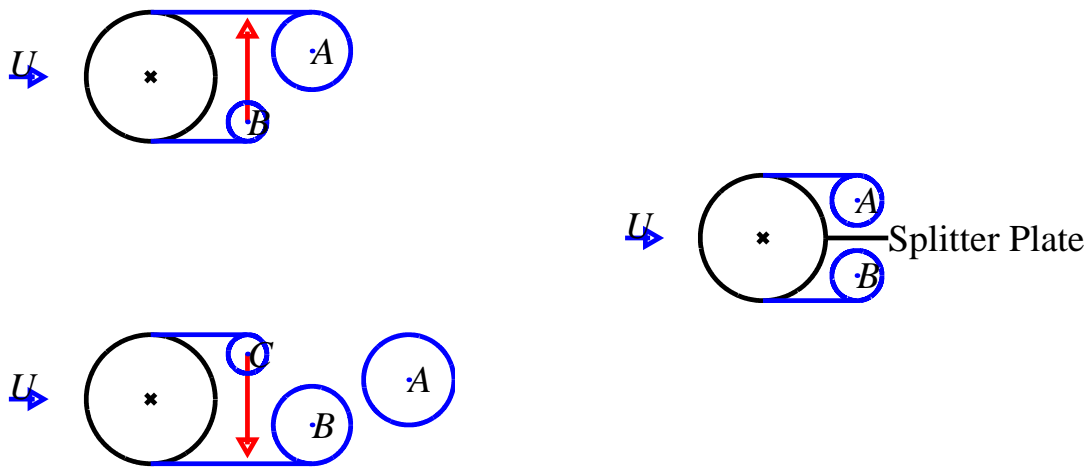
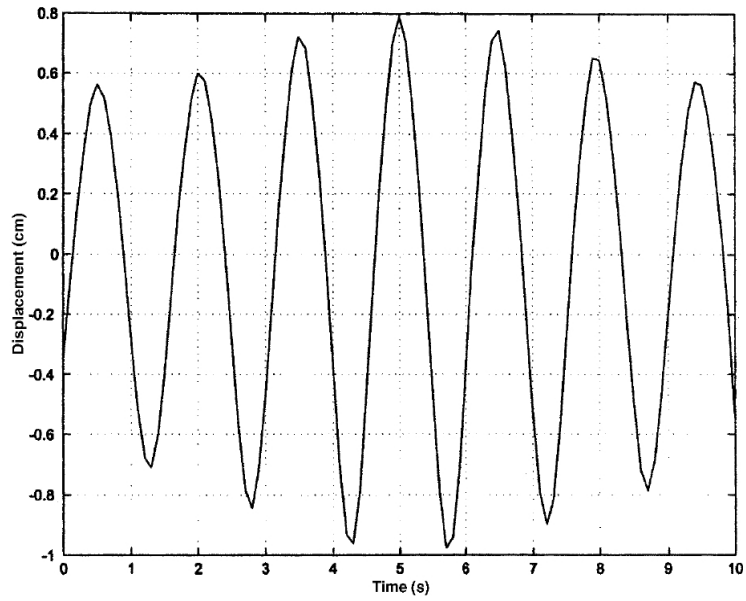
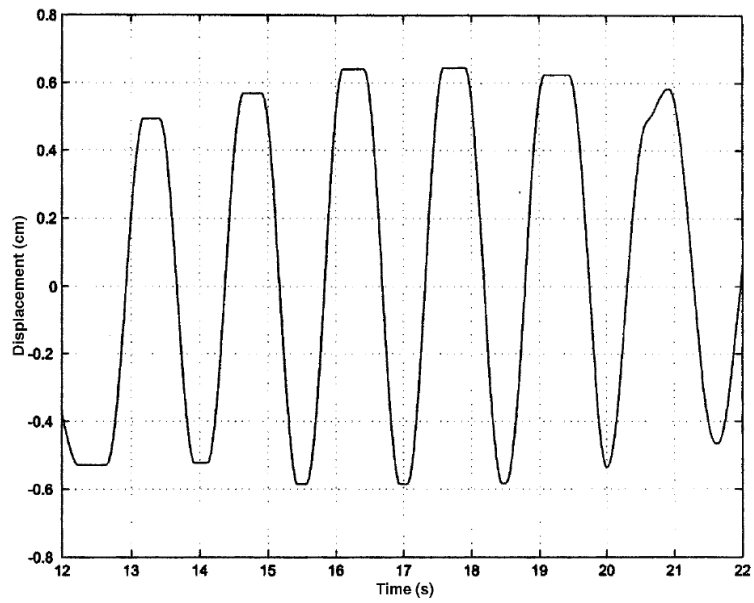


Figure 1.7: A schematic of the Gerrard theory of vortex shedding, showing the vortex being drawn across and cutting off the opposite vortex from the feeding sheet (Gerrard 1966).



(a)



(b)

Figure 1.8: Experimental, (a), and analytical, (b), output for extended Hamilton's principle for fluid control-volume approach (Benaroya, Wei, Kuchnicki, and Dong 2003).



## CHAPTER 2

### VIV Features and Parameters

The approach of this thesis will be a phenomenological model. Approximations to the energy present in the body and the effecting fluid will be integrated to find the energy present. The process of integrating to the energy level is believed to be very advantageous as it reduces the effects of approximations and their errors, leading to a more generalized model. Many of the physical parameters can either be measured directly from experiments or approximated based on phenomenological observations. Due to the complexity of the Navier-Stokes equations and the ability to solve them only for a few potential flow and basic viscous flow problems, they will not be applied here. Perhaps in the near future a full Navier-Stokes model can be used, but it is of the opinion of the author that it would lead to a system of equations that are impossible to model if applied here. Therefore, the effecting fluid will be modeled part of a system with the body rather than a fluid continuum. It is considered a reasonable approximation for VIV, particularly in order to not take the model to the level of needing to carry out complete numerical simulations where computational power becomes the limiting factor. Instead, it will be a single degree-of-freedom system that can be stepped in time using simple methods.

In order to develop a new model that can accomplish what is necessary in this

thesis, the important parameters must be identified, and some insight into their role in the model must also be established. Certain parameters are important as input variables, while others are the output necessary to validate and use the model. The obvious parameters come from the traditional mass-spring-damper equation, where we want to develop the most appropriate forcing. The model is an energy model where the energy equation is first derived, and the single degree-of-freedom force equation is then derived using properties of Hamilton's principle.

## 2.1 Variables

Time is the independent variable for the final system of equations. The stagnation point, separation point, formation point, and the attached vortices are all dependent upon time. However, there is only one dependent variable output in the final equations, and this will be the degree-of-freedom given to the system:  $y$  for the displacement of the body. Variable  $y$  is applied to the cylinder and the attached fluid, where  $y$  is perpendicular to the axis of the cylinder and perpendicular to the flow direction.

### 2.1.1 Circulation

The next quantity to be considered is the lifting force. The lifting force, defined as perpendicular to the stream direction, is the main output in engineering studies of VIV. As an output property, it is dependent on all the input quantities. For inviscid theory, the Kutta-Joukowski theorem can be applied with great accuracy. This would imply a  $Re = \infty$ , which is a good approximation for the fully turbulent case, but not for practical applications. The Kutta-Joukowski theorem is as follows.

$$L = \rho U \Gamma \tag{2.1}$$

$$m\ddot{y} + c\dot{y} + ky = L \tag{2.2}$$

### 2.1.2 Natural Frequency

As mentioned before, the traditional mass-spring-damper equation contains several important parameters, namely the mass ( $m$ ), damping ( $c$ ), and spring stiffness ( $k$ ). Derived from these parameters, the natural frequency is found as follows.

$$\omega_n = \sqrt{\frac{k}{m}} \quad (2.3)$$

$$f_n = \frac{\omega_n}{2\pi} \quad (2.4)$$

The damped natural frequency can also be found. With the addition of damping, the peak response frequency is shifted and the amplitude of response is decreased.

$$\omega_d = \sqrt{\frac{k}{m} - \left(\frac{c}{2m}\right)^2} \quad (2.5)$$

## 2.2 Dimensionless Parameters

### 2.2.1 Reynolds Number

The first important parameter, and perhaps the most important parameter for this fluid-structures interaction is the Reynolds Number ( $Re$ ), defined by the cylinder diameter as shown below. The  $Re$  is an input parameter, implying the level of turbulence in flow, the approximate location of the separation point, and the strength of the stationary lift coefficient. By definition, we know it to be the ratio of the inertial forces to the viscous forces.

$$Re = \frac{UD}{\nu} \quad (2.6)$$

### 2.2.2 Damping Ratio

Along the lines of the damped natural frequency is the damping ratio. When the damping ratio,  $\zeta$ , is within a certain range, characteristics of the unforced, or free vibrations of a system can be known. When  $\zeta = 0$ , the system is undamped, and the response should not vary in amplitude or frequency,  $f_n$ . When  $\zeta < 1$ , the

system is underdamped, and the amplitude undergoes a logarithmic decay with the damped frequency. When  $\zeta = 1$ , the system is critically damped, and there is a particular solution to the spring-mass-dashpot equation. When  $\zeta > 1$ , the system is overdamped, and no oscillations can take place for free vibrations. The response will just decay to zero without oscillating (Kelly 1993).

$$\zeta = \frac{c}{2m\omega_n} = \frac{c}{2\sqrt{mk}} \quad (2.7)$$

To differentiate the damping from the structure from the damping that may result from the fluid, the structural damping will often carry an 's' for a subscript,  $\zeta_s$ .

### 2.2.3 Mass Ratio

Since this is a fluids-structure problem, often the mass has little meaning in dimensional form. The meaning becomes more significant when divided by the displaced fluid mass, relating to buoyancy. This division results in the mass ratio. There has even been work suggesting that at a particular mass ratio of  $m^* = 0.54$ , VIV oscillations can occur “forever” (Govardhan and Williamson 2002), rather than desynchronizing around the first superharmonic. For the case that is used throughout this dissertation of a two-dimensional cylinder, the mass ratio is defined as follows.

$$m^* = \frac{m}{\pi\rho R^2} \quad (2.8)$$

### 2.2.4 Mass-Damping Parameter

At this point, it is relevant to mention the mass-damping parameter. Although unjustified, it has been found that multiplying the damping ratio with the mass ratio plus added mass results in a very nice curve for the amplitude of oscillation for each individual experimental data set. Although highly contested (Sarpkaya 2004), some success has been made plotting this mass-damping parameter against the amplitude ratio (Govardhan and Williamson 2006). However, the success of any

simplification of the parameters in order to collapse onto a single curve have been unsuccessful, as was demonstrated by the VIVACE model at high Reynolds numbers ( $Re \propto 10^5$ ) (Raghavan 2007). As a result, the mass-damping parameter will not be used extensively here. The mass-damping parameter, denoted as  $\alpha$  here, first arose from the studies of Griffin and Skop in the 1970s (Skop and Griffin 1973; Griffin and Koopmann 1977), and a similar parameter has been named Skop-Griffin as a result. The Skop-Griffin parameter calls upon the Strouhal number, outlined next.

$$\alpha = (m^* + c_a)\zeta \quad (2.9)$$

$$S_G = 2\pi^3 St(m^*\zeta) \quad (2.10)$$

### 2.2.5 Strouhal Number

Another important frequency is the Strouhal frequency. This frequency is so fundamental to VIV, it was defined in conjunction with research on VIV, even though it applies to stationary bodies only. The nondimensional number that results is called the Strouhal number. It incorporates the free-stream velocity and the cylinder diameter, and has a heavy dependence on  $Re$ .

$$St = \frac{f_s D}{U} \quad (2.11)$$

Often, the Strouhal frequency can be approximated by a constant value. Unless stated otherwise, the Strouhal frequency is given as  $St = 0.21$ , a good approximation for a large range of Reynolds number for a cylinder.

The next few quantities that are considered important to the development of a VIV mathematical model relate directly to the physical features of the flow over the body. They are the stagnation point, separation point, formation point, boundary layer, shear layer, and vortex shedding. The stagnation point and separation point are denoted in radians with zero radians being the potential flow stagnation point.

### 2.2.6 Reduced Velocity

The reduced velocity has sometimes been referred to as the velocity ratio, as it is a non-dimensional quantity. In the past when it was believed that only one vortex shed from each side during each cycle of motion of the body, the Strouhal Frequency was used to normalize the freestream velocity. However, the most recent and more proper trend in VIV data analysis has been to use the natural frequency of the system instead. This parameter is often used as the x-axis on many plots since it properly collapses many test cases onto the same plot.

$$U^* = \frac{U}{f_n D} \quad (2.12)$$

## 2.3 VIV Geometry

### 2.3.1 Stagnation Point

The stagnation point,  $\theta_{st}$ , from potential flow theory is the point of zero velocity on the body, and the only place where a streamline diverges. In viscous fluid flow, the stagnation point still exists, but is defined as the point of highest pressure. There is no streamline intersection in viscous fluid flow, and the point is not directly on the body. However, it is reasonable to assume that the *stagnation point is directly on the body* for most cases, and is considered as such here. The stagnation point moves with the motion of the body as well as with the growth and shedding of the vortices during VIV (see Figure 2.1). *This motion has been observed to be periodic, and will be assumed to be periodic with the Strouhal frequency,  $f_s$ .* The amplitude of the motion of the stagnation point will be denoted by  $\Theta_{st}$ .

$$\theta_{st} = \Theta_{st} f(t) \quad (2.13)$$

### 2.3.2 Separation Point

The separation point is defined as the point where the wall shear stress is exactly zero, after which point there is flow reversal. In viscous fluid flow this can be difficult

to define, particularly if the separation point experiences excursions towards the stagnation point. In experimental fluid flow, the separation point is the point where fluid particles leave the wall. This is still hard to identify, but easier than finding the point of flow reversal. There is a separation point both on the top and the bottom of the cylinder. The separation point mean position is very strongly dependent on  $Re$ . For example, in laminar flow, the mean position of the separation point has been measured to be around  $82^\circ$  from the potential-flow stagnation point, but is pushed back to around  $120^\circ$  for turbulent flow, creating a much narrower wake (White 1994). *The separation point also moves (see Figure 2.1), and is also assumed to be periodic with  $f_s$ .*

$$\theta_{sp} = \Theta_{sp} f(t) \quad (2.14)$$

### 2.3.3 Formation Point

The formation point, denoted  $x_{fp}$ , is a point in the near wake at which the shear layer saturates and begins to form the von Kármán vortex. It moves away from the body during vortex growth and quickly snaps back towards the body at the moment the vortex sheds (see Figure 2.1). There is a very large dependence on  $Re$  due to the fact that this is an instability region, and the number of vortices within the formation point has been measured experimentally (Prasad and Williamson 1997), proving the  $Re$  dependence. Additionally, *the formation point has a dependence on the motion of the body as well. This is assumed to be due to the fact that the formation region becomes exposed to the flow due to the motion of the body.*

### 2.3.4 Boundary Layer & Shear Layer

The boundary layer exists between the stagnation point,  $\theta_{st}$ , and each respective separation point,  $\theta_{sp}$ . It is highly dependent on  $Re$  since viscous forces dominate in this region. Any term that is the result of the effect of the boundary layer on the

system will have the subscript  $_{BL}$ . The shear layer exists between the separation point,  $\theta_{sp}$  and the formation point,  $x_{fp}$ , and has an  $Re$  dependence as stated above in the formation point discussion. The shear layer is also known as the feeding layer in the case of VIV since it feeds energy or vorticity into the vortex. Any term that is the result of the effect of the shear layer on the system will have the subscript  $_{SL}$ .

### 2.3.5 von Kármán Vortex

Finally, the von Kármán vortex shedding is an important parameter. Past definitions of VIV assumed that there was only one mode of vortex shedding, where a single vortex sheds from each side of the cylinder during one cycle of motion. However, Williamson and Roshko (1988) thoroughly investigated the vortex shedding modes and have shown that there is a multitude of modes involving not just single vortices from each side of the cylinder (2S), but two (2P) and three (2T) vortices from each side of the cylinder. In VIVACE preliminary visualizations, as many as five vortices are shed from each side of the cylinder during one cycle. It would be advantageous to have a model that could incorporate this. Based on the properties of coupling the cylinder and the attached fluid, we believe that the coupling between the body motion and the vortex parameter could potentially incorporate multiple vortex shedding modes. Any term that is the result of the effect of the attached vortex on the system will have the subscript  $_{KV}$ .

## 2.4 Features

### 2.4.1 Synchronization

One of the most intriguing and significant features of VIV that separates it from other fluid-structure interactions is the “range of synchronization” and the inherent characteristics of the range of synchronization. This range of synchronization has been extensively analyzed and described over several decades. Sumer and Fredsøe



(1997) describe the range of synchronization. Plotting the amplitude of oscillation divided by the diameter of the cylinder versus the reduced velocity is the most common way to illustrate the range of synchronization.

Synchronization is comprised of three sections: (1) initial branch, (2) upper branch, (3) lower branch. Figure 2.2 shows the approximate nature of these three branches followed by desynchronization. The amplitudes  $A/D$  are typically around the order of one. The three branches do vary in nature depending on the parameters described above for a particular scenario. The initial branch will typically have the lowest amplitude oscillations, while the upper branch will have the highest amplitude. Depending on the mass ratio or the damping, the upper branch may not exist over a range but only at a point, and the lower branch may lead directly to desynchronization rather than existing over a large range as well, as was shown in Feng (1968).

The effect of the Reynolds number must also be considered in addition to the mass and damping ratios. Bernitsas, Raghavan, Ben-Simon, and Garcia (2006) showed experiments in the critical Reynolds number range, where the upper branch seemed to extend from  $U^* \approx 5$  to  $U^* \approx 10$ , increasing in amplitude with increasing  $U^*$ , and then directly into desynchronization. This could also be described as the lower branch being raised up to the upper branch. Further experimentation in this range is needed to determine what is causing the change in the range of synchronization in the critical  $Re$  regime.

#### **2.4.2 Lock-in**

Another key feature unique to VIV is the frequency lock-in. This corresponds to the vortex shedding frequency locking into the natural frequency of the cylinder, where the cylinder is also responding at the natural frequency. Lock-in typically

occurs over most of the range of synchronization. The frequency of vortex shedding may not always be equal to the natural frequency, but the frequency of response of the cylinder versus the frequency response of vortex shedding will be approximately equal within the range of synchronization.

Figure 2.3 shows the different frequency lock-on behaviors based on the mass ratio. For most real-world applications, the mass ratio is above 1 and often above 10, so the frequency ratios,  $f_C/f_n$  typically falls around unity.

There is a large amount of confusion presented in the literature for the frequency lock-in plots. Although almost always written  $f/f_n$ , it is not always clear what frequency  $f$  represents. Sometimes the frequency is the frequency of vortex shedding, while other times it represents the frequency of oscillation of the cylinder. The frequency plot shown in Figure 2.3 shows the frequency of oscillation of the cylinder. However, before  $U^* \approx 5$  and after lock-out at desynchronization, it has been shown in many experiments that the frequency of oscillation of the cylinder remains around the natural frequency. The frequency of vortex shedding is what has been clearly found to lock-in and then lock-out. It is important that attention be paid when reading frequency lock-in plots and caution in interpreting the results. The vortex shedding frequency and the cylinder oscillation frequency are not the same. This is further emphasized in the discussion of vortex shedding modes.

### **2.4.3 Phase Shift**

This phase refers to the phase difference between the forcing, or vortex shedding, and the motion of the cylinder. The forcing always leads the displacement, as stated in the cliché “the donkey leads the cart”. This is stated because in some equations for the lifting and displacement of VIV, the phase has been attached to the lifting

term. However, it should be attached to the displacement.

$$\begin{aligned}L &= C_L \sin(\omega t) \\ y &= A \sin(\omega t + \phi)\end{aligned}\tag{2.15}$$

The phase shift or jump refers to the change in the phasing at the initiation of lock-in, when the initial branch jumps to the upper branch. At reduced velocities less than that at lock-in, the phase typically is around zero, while just after lock-in, the phase typically jumps up. The actual value varies depending on the damping and mass ratio, but can be as much or slightly more than a phase of  $180^\circ$ , for a total phase shift of  $180^\circ$ .

This is a characteristic of the nonlinear, unforced nature of VIV; a further indication that a linear math model will not properly model the phenomenon.

#### 2.4.4 Vortex Shedding Mode

It was originally thought that there was only one mode of vortex shedding. Since the assertion by Bénard and von Kármán that vortices shed in an alternating pattern from a stationary cylinder, this concept crossed over to VIV with the idea that a single vortex sheds from the top and the bottom within one cycle of the cylinder motion. However, this led to inconsistencies in the analysis of vortex shedding frequency response versus cylinder frequency response. Later, with laser visualization techniques, Williamson and Roshko (1988) were able to complete a map of vortex shedding modes for forced oscillations of a cylinder. It was found that, for forced oscillations, different vortex shedding modes resulted based on different reduced amplitudes and reduced velocities. It was later proposed by Bernitsas, Raghavan, and Duchene (2007) that there may be even more vortex shedding modes based on the Reynolds number as well, or a sort of three-dimensional mapping.

Unfortunately, the most extensive work on vortex shedding modes has been done

for forced oscillations, and there are inherent problems with attempting to extrapolate the vortex shedding mode of natural oscillations from forced oscillations. However, it is important to note that the vortex shedding mode will not always be two single vortices from each side, and that the frequency of vortex shedding is an important parameter to record.

Figure 2.5 shows a plot of the vortex patterns for a forced oscillating cylinder, where several patterns have been identified unique to amplitude and flow speed. These vortex shedding modes are described in Figure 2.6 It is important to note that this is for forced oscillations, and many of the regions will never be crossed by free vibrations. The switching between interfaces and the phasing with respect to oscillations is not abrupt, but occurs over several cycles of oscillation.

One thing that has been found by the VIVACE group is the possible existence of higher vortex shedding modes. VIV research has begun to refer to triple vortices from each side,  $2T$ . This could be interpreted as the same as what is referred to in Figures 2.5 and 2.6 as  $2P+2S$ , where a pair,  $P$ , and single  $S$ , from one side is a triple  $T$ . VIVACE has initial visualizations suggesting quadruple and possibly quintuplet vortices from each side for the higher  $Re$ . This corresponds to the proposal of more vortex shedding modes based on  $Re$  from Bernitsas, Raghavan, and Duchene (2007).

#### 2.4.5 Mass-Damping

Above, the mass-damping parameter was defined under the dimensionless parameters. The parameter,  $\alpha = (m^* + c_a)\zeta$ , has been shown to be useful under certain contexts. In addition to introducing the parameter, Griffin (1978) found that when the mass-damping parameter is used as the horizontal axis against the maximum possible amplitude divided by diameter,  $A/D$ , many points fell into a smooth curve. More recently, it has been shown that over certain ranges of Reynolds numbers,

many points can be collapsed onto a single line with additional modifications to this Skop-Griffin parameter,  $\alpha$  (Govardhan and Williamson 2006). However, it has been shown that this does not hold over all Reynolds numbers (Bernitsas, Raghavan, and Duchene 2007). Figure 2.7 shows the modified Griffin plot, where most subcritical Reynolds numbers collapse onto a single line. However, for higher subcritical and critical Reynolds numbers, the current modified Griffin plot no longer holds and the current state of the mass-damping behavior is questionable (Bernitsas, Raghavan, and Duchene 2007).

It is proposed that the actual relationship is the result of the damping multiplied by the natural frequency, as this does appear in the dimensionless version of the mass-spring-damping equation. It would be interesting to see how the plots are modified when the parameter is  $\omega_n\zeta$  rather than  $m^*\zeta$ .

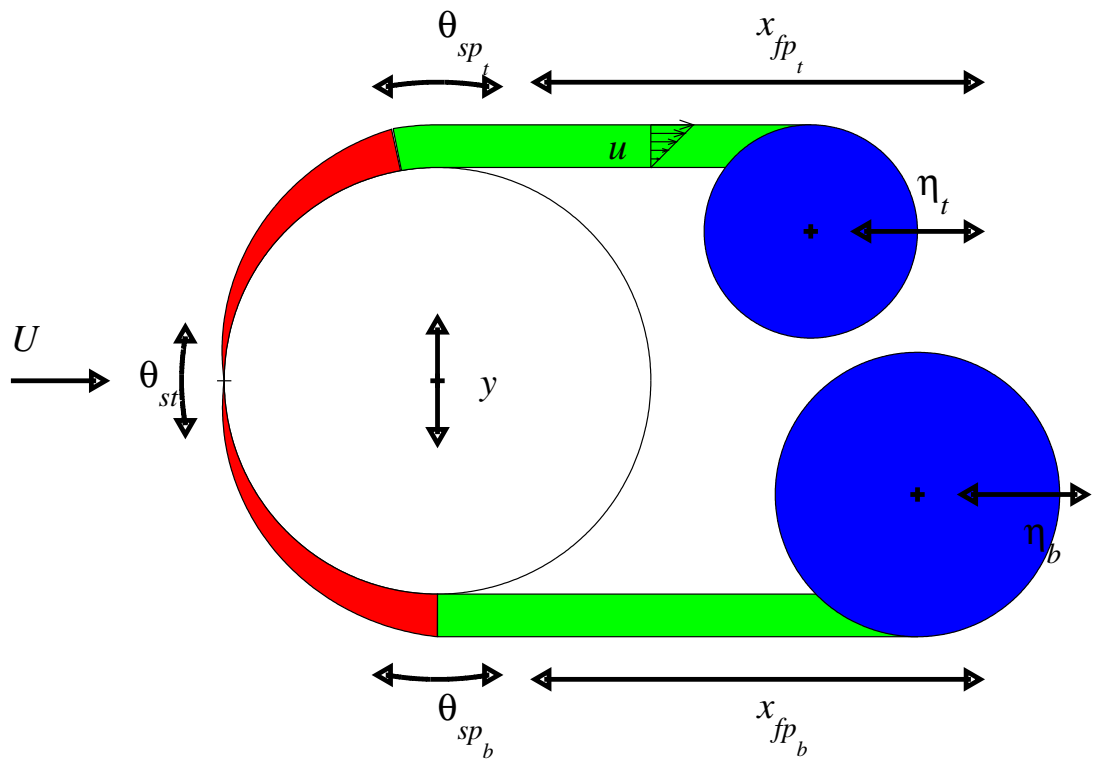


Figure 2.1: Schematic of important parameters from the geometry of the body and attached flow with first order approximations.

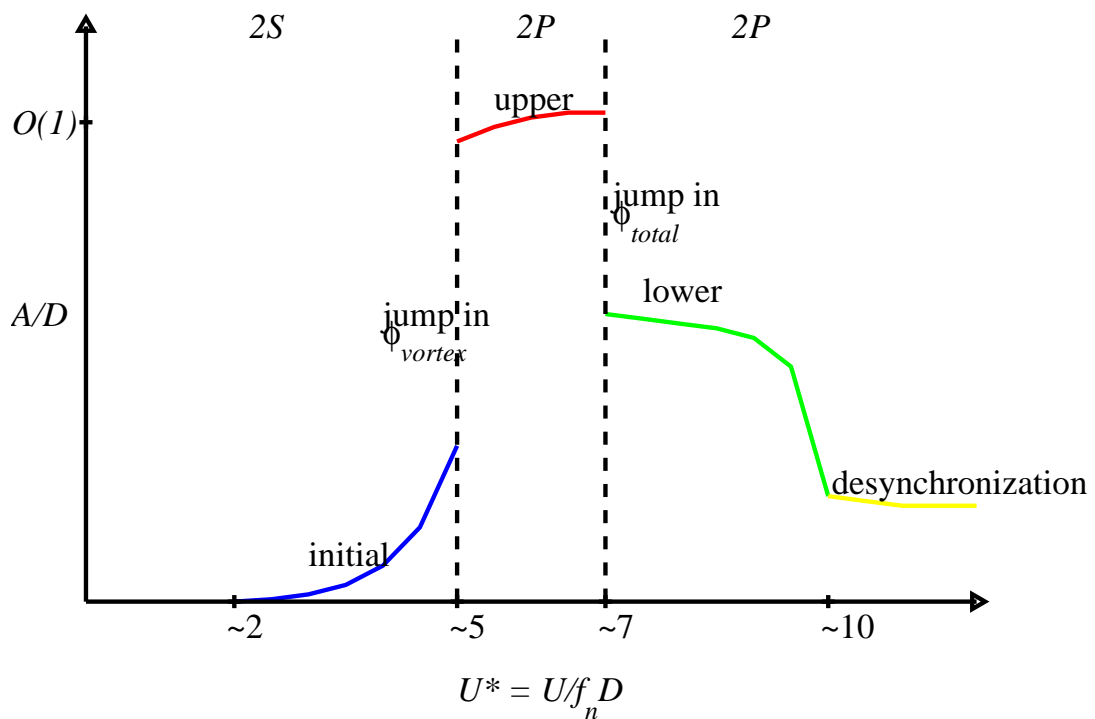


Figure 2.2: A generalized plot of the range of synchronization with the typical initial, upper, and lower branches, where a hysteresis typically occurs between the initial and upper branches and the upper and lower branches (Williamson and Govardhan 2004).

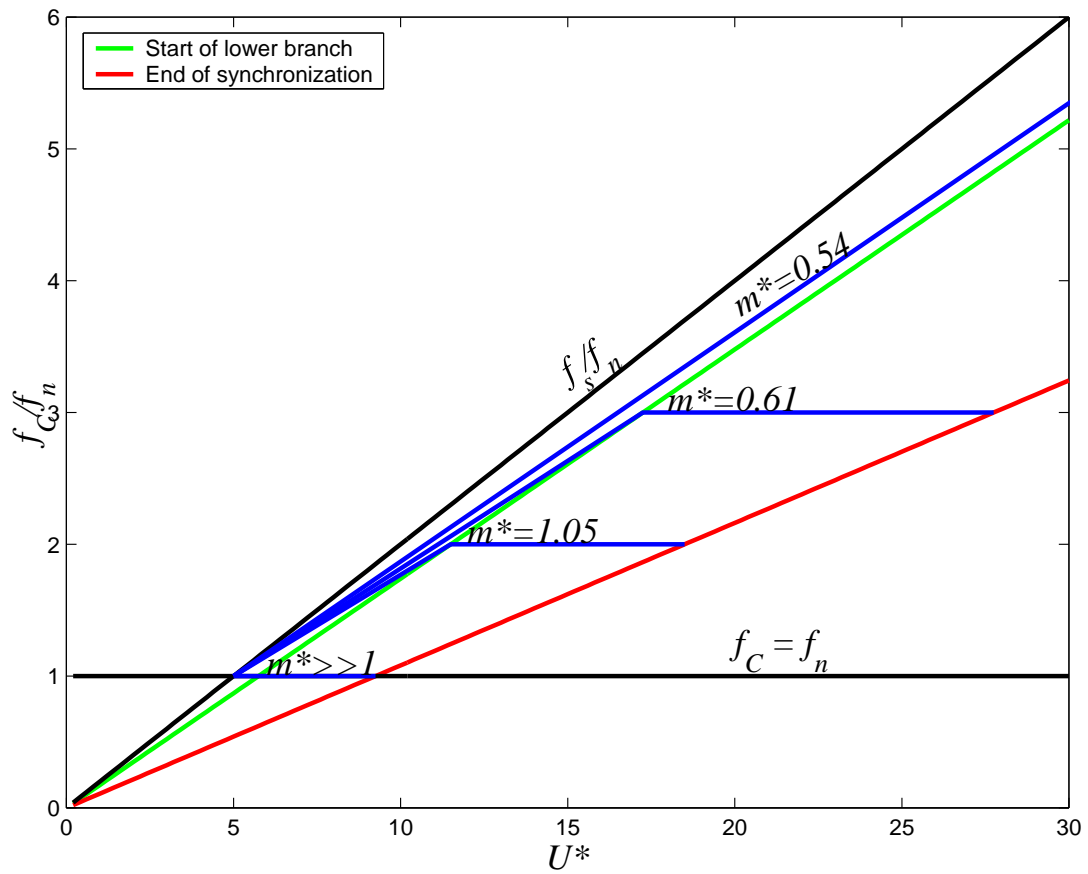


Figure 2.3: The effect of the mass ratio on the frequency of response for the cylinder during lock-in from experiments (Govardhan and Williamson 2000).



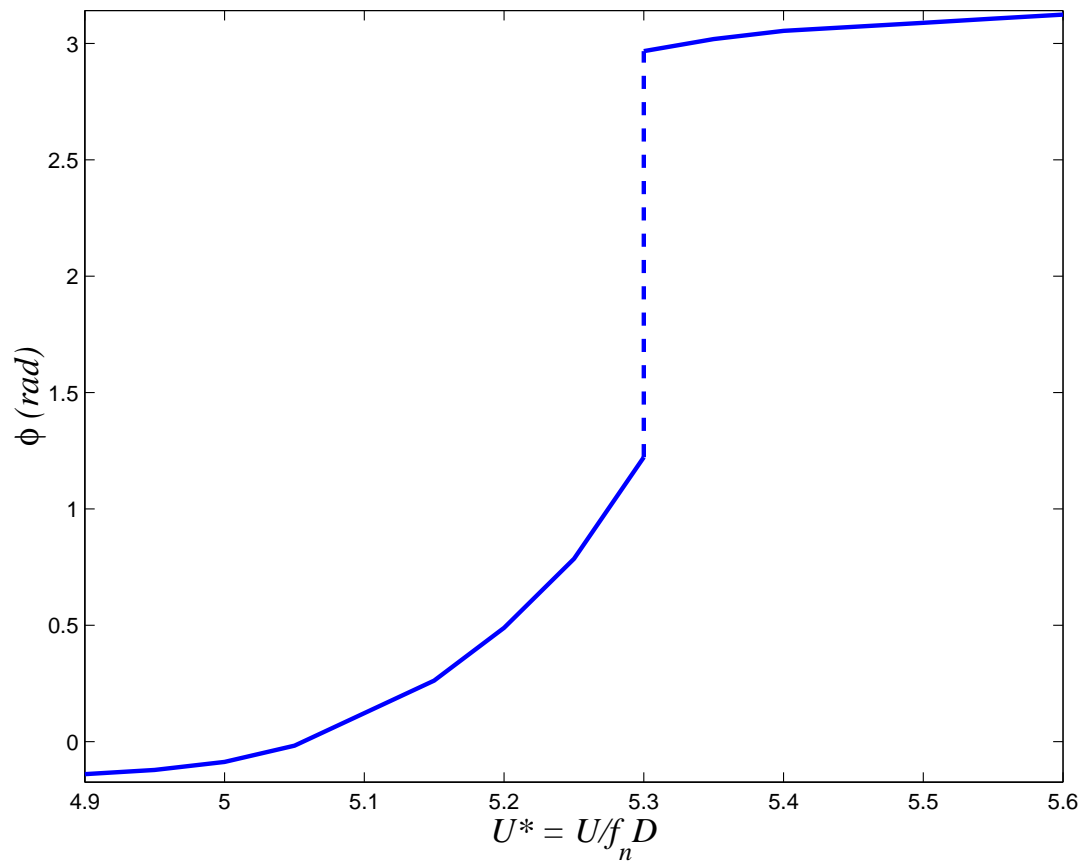


Figure 2.4: A schematic of the approximate nature of the phase shift between fluid forcing and cylinder displacement at lock-in (Sumer and Fredsøe 1997).

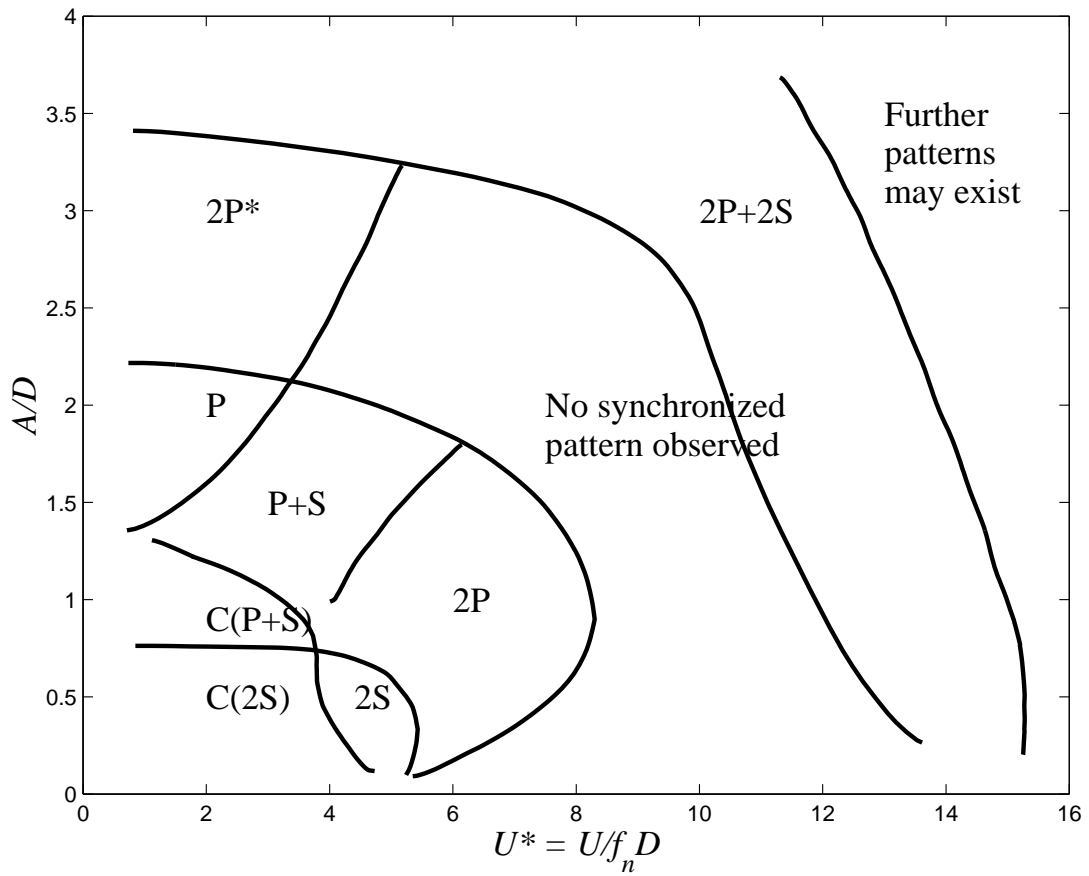


Figure 2.5: The regimes of the vortex patterns for a forced oscillating cylinder with non-dimensional velocity and amplitude for the axes (Williamson and Roshko 1988).

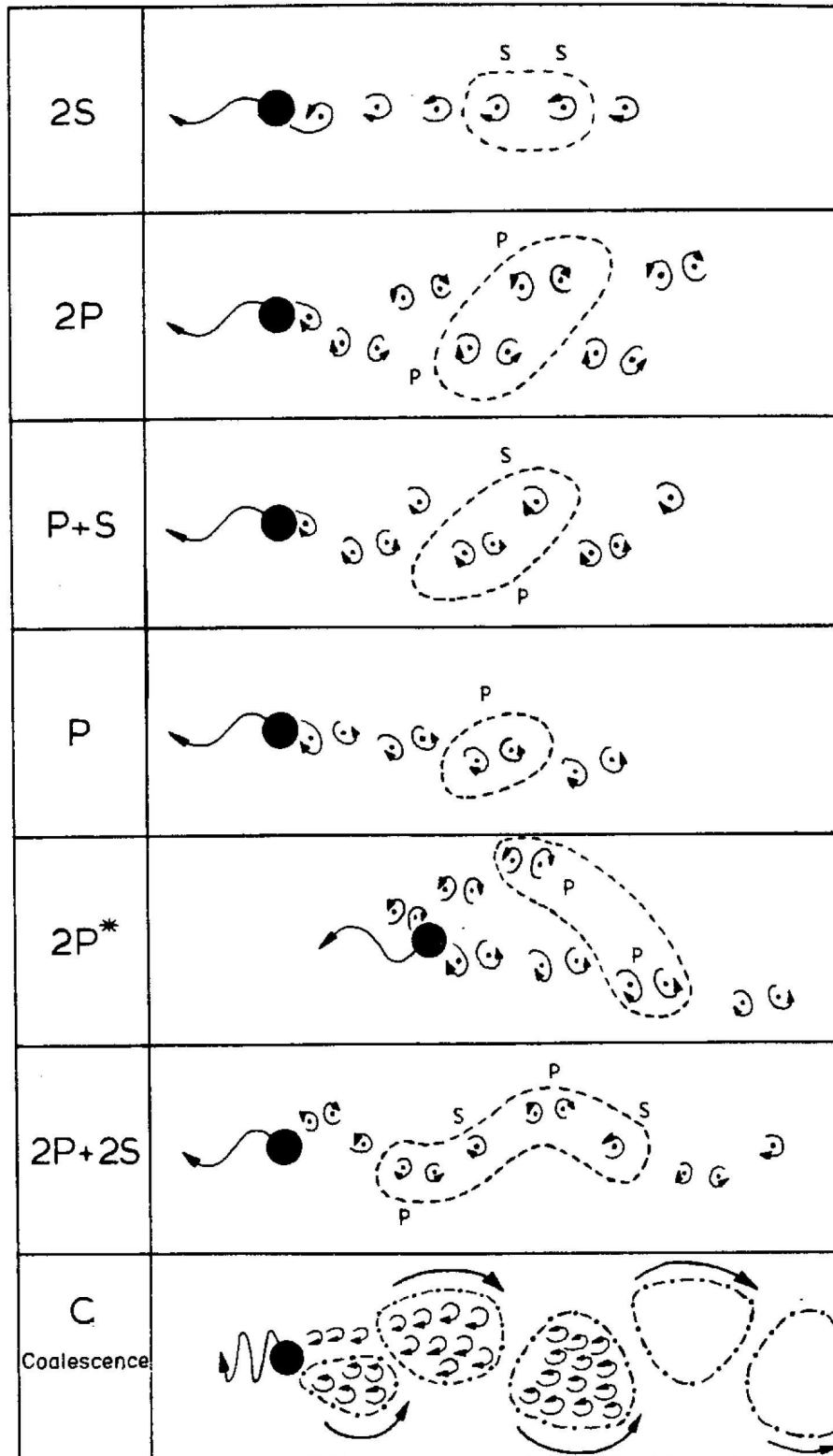


Figure 2.6: The vortex patterns identified using a forced oscillating cylinder (Williamson and Roshko 1988).

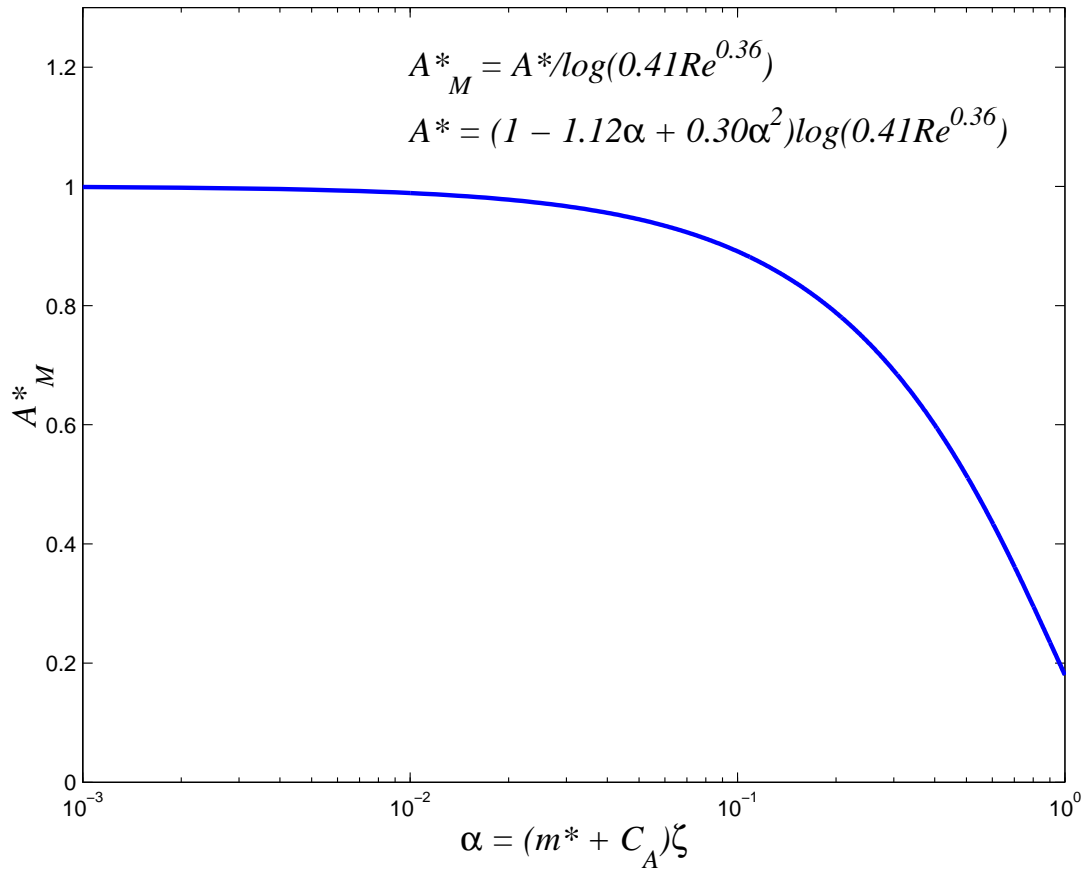


Figure 2.7: The modified Griffin plot, with Skop-Griffin parameter plotted against a non-dimensional amplitude (Govardhan and Williamson 2006).

## CHAPTER 3

### Development of a Mathematical Model of VIV

*The model to be developed and used in this dissertation will be a nonlinear, single degree-of-freedom equation developed from generalized energy equations using Hamilton's principle.* To begin, we will define the degree-of-freedom. The obvious degree-of-freedom is the motion of the cylinder perpendicular to the free-stream. This degree-of-freedom will be denoted using the variable  $y$ , and is a function of time ( $y(t)$ ). The cylinder is only allowed one degree-of-freedom, as this is practical for the VIVACE system. Often times, two degrees of freedom are present, where inline motion is also affecting the cylinder, although not of the same order of magnitude. However, in VIVACE, the second degree-of-freedom is restricted.

Once the variables have been declared, and their behavior based on the above section's physical features, the Lagrangian equation and Hamilton's principle will be applied. Hamilton's principle is necessary because it allows for the presence of non-conservative forces. Just based on the mass-spring-dashpot example, we already know that there are non-conservative forces due to damping. Obviously, the viscosity in the fluid also leads to a dissipation of energy when looking within a non-infinite fluid mass. Therefore, Hamilton's principle is the appropriate choice here.

### 3.1 Hamilton's Principle

William Rowen Hamilton developed the variational indicator for admissible motion of a dynamic system between specified configurations. By applying calculus of variations to the variational indicator, Lagrange's equations are recovered. Many references cover the variational indicator for Hamilton's Principle (Crandall, Karnopp, Kurtz, and Pridmore-Brown 1968, Harrison and Nettleton 1997, Jordan and Smith 1999, Langhaar 1989). The explanation that follows most closely resembles that outlined in Crandall, Karnopp, Kurtz, and Pridmore-Brown (1968).

The derivation of Hamilton's principle begins with deriving the force-momentum variational indicator, separating the potential energy from conservative forces,  $V(\xi_1, \dots, \xi_n)$  and generalized, nonconservative forces,  $\Xi_j$ . This gives the following relationship for  $n$  independent force-momentum relations.  $f_i$  is the forcing terms,  $\delta R_i$  is the variational distance of of the force terms, and the product is work energy.  $\delta V$  is the variational potential energy, and  $\delta \xi_j$  is the degree-of-freedom, which is  $y$  for the given model.

$$\sum_{i=1}^N f_i \cdot \delta R_i = -\delta V + \sum_{j=1}^n \Xi_j \delta \xi_j \quad (3.1)$$

Integration by parts leads to a relationship for the variation of the kinetic coenergy,  $T$ . Then, the entire expression is integrated over time, leading to the expression for the variational indicator, V.I.

$$\text{V.I.} = \int_{t_1}^{t_2} \left[ \delta (T - V) + \sum_{j=1}^n \Xi_j \delta \xi_j \right] dt \quad (3.2)$$

The above equation already references the Lagrangian,  $\mathcal{L} = T - V$ , where the Lagrangian is a function of the degrees of freedom and time.

$$V = V(\xi_1, \xi_2, \dots, \xi_n) \quad (3.3)$$

$$T = T(\dot{\xi}_1, \dot{\xi}_2, \dots, \dot{\xi}_n, \xi_1, \xi_2, \dots, \xi_n, t) \quad (3.4)$$

$$\mathcal{L} = T - V = \mathcal{L}(\dot{\xi}_1, \dot{\xi}_2, \dots, \dot{\xi}_n, \xi_1, \xi_2, \dots, \xi_n, t) \quad (3.5)$$

The variation of the Lagrangian is given as follows.

$$\delta\mathcal{L} = \sum_{j=1}^n \left( \frac{\partial\mathcal{L}}{\partial\dot{\xi}_j} \delta\dot{\xi}_j + \frac{\partial\mathcal{L}}{\partial\xi_j} \delta\xi_j \right) \quad (3.6)$$

The variational indicator, with application of commutativity for  $\dot{\delta}_j = d(\delta\xi_j)/dt$ , then becomes the following integral.

$$\text{V.I.} = \int_{t_1}^{t_2} \sum_{j=1}^n \left[ \frac{\partial\mathcal{L}}{\partial\dot{\xi}_j} \frac{d}{dt} \delta\xi_j + \frac{\partial\mathcal{L}}{\partial\xi_j} \delta\xi_j + \Xi_j \delta\xi_j \right] dt \quad (3.7)$$

Since this is variational calculus and all displacements in the model derivation are artificial,  $\delta\xi_j$  vanishes at  $t_1$  and  $t_2$ , leaving behind the Lagrange's equation with the addition of the nonconservative forces, where all geometrical variables have been expressed in terms of the generalized coordinates  $\xi_j$ .

$$\frac{\partial}{\partial t} \left( \frac{\partial\mathcal{L}}{\partial\dot{\xi}_j} \right) - \frac{\partial\mathcal{L}}{\partial\xi_j} = \Xi_j \quad (3.8)$$

In the model developed in this thesis, it is important to express everything in terms of energy before deriving Lagrange's equations from Hamilton's principle. This includes the nonconservative, or dissipative, forces. For this reason, we will back step to express these forces in terms of a variational work term. This only slightly changes the final Lagrange's equations.

$$\delta W_j = \Xi_j \delta\xi_j \quad (3.9)$$

$$\Xi_j = \frac{\delta W}{\delta\xi_j} \quad (3.10)$$

$$\frac{\partial}{\partial t} \left( \frac{\partial\mathcal{L}}{\partial\dot{\xi}_j} \right) - \frac{\partial\mathcal{L}}{\partial\xi_j} = \frac{\delta W}{\delta\xi_j} \quad (3.11)$$

This is the equation that will be used to take the derived energies to a system of force equations. Again, there is only going to be one generalized coordinate, the

single degree-of-freedom of the cylinder,  $y$ , so the above equation can be simplified to a single equation where  $j = 1$ .

$$\frac{\partial}{\partial t} \left( \frac{\partial \mathcal{L}}{\partial \dot{y}} \right) - \frac{\partial \mathcal{L}}{\partial y} = \frac{\delta W}{\delta y} \quad (3.12)$$

First, the kinetic coenergy,  $T$ , must be defined. This is the work required to increase a body's velocity from rest to some velocity  $v$ . It is a coenergy because of the definition of the Lagrangian. The attached fluid is considered as an addition to the cylinder, so there is kinetic coenergy for the cylinder and for the attached fluid, separately defined but part of the same system. Second, the potential energy,  $V$ , must be defined. The potential energy is the work done to transfer the body from one configuration to another. The obvious contributor to the potential energy is the body spring.

In general terms, the kinetic coenergy and the potential energy can include any combination of the body displacement, body velocity, wake parameter displacement, and wake parameter velocity. A general definition for a such a single degree-of-freedom system can be defined as follows.

$$T = \frac{1}{2} M(y, \dot{y}) \dot{y}^2 \quad (3.13)$$

$$V = \frac{1}{2} K(y, \dot{y}) y^2 \quad (3.14)$$

In the above equations,  $M$  represents the inertial coefficients, typically representing some sort of mass or added mass.  $K$  represents stiffness terms, such as spring coefficients. They can all be a function, linear or nonlinear, of  $(y, \dot{y})$  as stated above. Now the only, but most important step, in the development of our own model, is to determine how to properly represent all the energy in the system in order to derive the force system of equations. We want to incorporate the behavior of the stagnation



point, separation point, formation point, and von Kármán vortex shedding. We want to express all terms in terms of  $Re$ ,  $St$ ,  $m$ ,  $c$ , and  $k$ .

### 3.2 First-Order Approximations for Energy

Expressions for the energy are now derived. The entire fluid cannot be considered, as this would account for infinite energy. Therefore, the energy is found in the fluid that appears to affect the cylinder, and their energy can be expressed using the cylinder displacement  $y$  and velocity  $\dot{y}$ . As outlined in Chapter 2, certain parts of the fluid can be considered attached, and the energy within any attached fluid is derived with first-order approximations here.

The attached fluid can be divided into four parts: the boundary layer, the shear layer, the attached von Kármán vortex, and dissipated energy, each segment being present separately in the top layer and the bottom layer of the cylinder (see Figure 3.1). The top layer has one vorticity orientation (into the plane or clockwise), while the bottom layer has the opposite vorticity orientation (out of the plane or counterclockwise). The flow of energy is as follows. Energy from the free-stream is captured (advected) into the boundary layer ( $BL$ ) while the fluid is in contact with the body. This follows well from what is known about energy transfer and shear stress at a solid-fluid boundary. The energy in the boundary layer is then transported downstream into the shear layer ( $SL$ ). This will be represented by seaming the velocity profile at the end of the boundary layer with the velocity profile at the beginning of the shear layer. The energy continues downstream within the shear layer until the shear layer ends. At the end of the shear layer, the energy now splits, where a certain percentage,  $\alpha$ , feeds into the attached von Kármán vortex ( $KV$ ), allowing it to grow, and the rest,  $1 - \alpha$ , is lost downstream through dissipation. The shear layer energy output is seamed with the attached vortex growth through the mass flux. All

energies determined in the following sections represent energy impacting the system, where the system is the cylinder, top and bottom boundary layers, top and bottom shear layers, and top and bottom attached vortices. All energies effect the body in the system.

Later, the timing of the vortex shedding will be seamed with the timing of the minimum values of the formation point,  $x_{fp}$ , the separation point,  $\theta_{sp}$ , and the stagnation point,  $\theta_{st}$ , where the stagnation point is affected by both the top and the bottom. Then, as the vortex grows, each of these values also reach its maximum values.

### 3.3 Stationary Cylinder

#### 3.3.1 Boundary Layer Energy

In order to determine what parameters play a role in the total energy and how they affect the energy, a first order approximation can lead to great insight. For the kinetic co-energy in the boundary layer, *assuming that the velocity profile from the surface of the cylinder to free-stream is linear with the radius, and the boundary layer thickness is linearly increasing with the angle*, the below approximations can be made for the top boundary layer, denoted by the super-subscript  $t$  (see Figure 2.1). The bottom boundary layer ( $b$ ) has a similar expression where boundary layer thickness  $\delta$  becomes a function of  $\theta_{sp_b}$ , which is negative, rather than  $\theta_{sp_t}$ , which is positive. The same expression can be used both for the top and bottom boundary layer.

$$R < r < R + \delta, \quad 0 < \theta < 2\pi \quad (3.15)$$

$$u_r(r, \theta) = 0 \quad (3.16)$$

$$u_\theta(r, \theta) = \alpha r + \beta \quad (3.17)$$

$$u_\theta(R) = 0 \quad (3.18)$$

$$u_\theta(R + \delta) = U \quad (3.19)$$

$$u_\theta(r) = \frac{U}{\delta}(r - R) \quad (3.20)$$

$$u_{BLt} = \sqrt{u_r^2 + u_\theta^2} = \frac{U}{\delta_t}(r - R) \quad (3.21)$$

$$\delta_t(\theta) = \alpha\theta + \beta \quad (3.22)$$

$$\delta_t(\theta_{st}) = 0 \quad (3.23)$$

$$\delta_t(\theta_{sp_t}) = \Delta \quad (3.24)$$

$$\delta_t(\theta) = \frac{\Delta}{\theta_{sp_t} - \theta_{st}}(\theta - \theta_{st}) \quad (3.25)$$

$$u_{BLb}(r) = \frac{U}{\delta_b}(r - R) \quad (3.26)$$

$$\delta_b(\theta) = \frac{\Delta}{\theta_{sp_b} - \theta_{st}}(\theta - \theta_{st}) \quad (3.27)$$

The kinetic co-energy within one side of the boundary layer can then be found by integrating the velocity from the stagnation point to the separation point and from the cylinder surface to the boundary layer thickness. The equation to be solved for one side of the boundary layer is as follows.

$$T_{BLt} = \frac{1}{2} \int_{\theta_{st}}^{\theta_{sp}} \int_R^{R+\delta_t} \rho u_{BLt}^2(r, \theta) r dr d\theta \quad (3.28)$$

The above double integral can be carried out by hand. However, it is tedious, and the final integration was performed using the Maple software (Maplesoft 2007). The result of the boundary layer energy integral is as follows.

$$T_{BLt} = \frac{\rho U^2 \Delta}{24} (2R + \Delta) (\theta_{sp_t} - \theta_{st}) \quad (3.29)$$

As can be seen from the above equation, the kinetic co-energy in the boundary layer is dependent upon all geometric inputs, particularly  $\theta_{st}$  and  $\theta_{sp}$ . Therefore, any motion that the stagnation point and separation point may experience will definitely

have an effect on the energy in the boundary layer. When  $\theta_{st}$  and  $\theta_{sp}$  become functions of time for more advanced approximations,  $T_{BL}$  will directly carry this time dependence from the integrals.

### 3.3.2 Shear Layer Energy

Next, we will examine a crude approximation of the shear layer. *Assuming that the separation point  $\theta_{sp}$  is around  $\frac{\pi}{2}$* , the shear layer can be approximated as a thin rectangular region leaving the top of the cylinder into the wake (see Figure 2.1). The shear layer exists, as defined above, between the separation point and the formation point. Therefore, *assuming a linear velocity profile between the dead-fluid region behind the cylinder and the free-stream*, as given below, the shear layer kinetic co-energy for one side of the cylinder can be represented as follows. The formation point  $x_{fp}$  is measured from the vertical axis of the center of the cylinder.

$$0 < \zeta < x_{fp}, \quad 0 < \xi < \Delta \quad (3.30)$$

$$u_{SL_t}(\xi) = \alpha\xi + \beta \quad (3.31)$$

$$u_{SL_t}(0) = 0 \quad (3.32)$$

$$u_{SL_t}(\Delta) = U \quad (3.33)$$

$$u_{SL_t}(\xi) = \frac{U}{\Delta}\xi \quad (3.34)$$

$$T_{SL_t} = \frac{1}{2} \int_0^\Delta \int_0^{x_{fp}} \rho u_{SL_t}^2(\zeta, \xi) d\zeta d\xi \quad (3.35)$$

$$T_{SL_t} = \frac{1}{6} \rho U^2 \Delta x_{fp_t} \quad (3.36)$$

As can be seen from the above result, the shear layer has been greatly simplified, and is only dependent on the formation point,  $x_{fp}$ . If the separation point had not been taken to be the top of the cylinder, the separation point  $\theta_{sp_t}$  would also have played an equally important role in the kinetic co-energy approximation. Adding in

the effect of  $\theta_{sp_t}$  to the above expression for the shear layer energy results in two separate expressions for when the  $\theta_{sp_t}$  is less than  $\frac{\pi}{2}$  on the top (greater than  $\frac{-\pi}{2}$  on the bottom) and when the  $\theta_{sp_t}$  is greater than  $\frac{\pi}{2}$  on the top (less than  $\frac{-\pi}{2}$  on the bottom).

For the case of  $\theta_{sp_t}$  less than  $\frac{\pi}{2}$  on the top, the following result can be obtained.

$$u_{SL_{t1}}(r) = \frac{U}{\Delta} (r - R) \quad \theta_{sp_t} < \theta < \frac{\pi}{2} \quad (3.37)$$

$$u_{SL_{t2}}(\xi) = \frac{U}{\Delta} \xi \quad \theta > \frac{\pi}{2} \quad (3.38)$$

$$T_{SL_t} = \frac{1}{2} \int_R^{R+\Delta} \int_{\theta_{sp_t}}^{\frac{\pi}{2}} \rho u_{SL_{t1}}^2(r, \theta) r dr d\theta + \frac{1}{2} \int_0^\Delta \int_0^{x_{fp_t}} \rho u_{SL_{t2}}^2(\zeta, \xi) d\zeta d\xi \quad (3.39)$$

$$T_{SL_t} = \frac{\rho \Delta U^2}{6} \left[ \left( \frac{3}{4} \Delta + R \right) \left( \frac{\pi}{2} - \theta_{sp_t} \right) + x_{fp_t} \right] \quad (3.40)$$

For the case of  $\theta_{sp}$  greater than  $\frac{\pi}{2}$  on the top, the expression only has one velocity equation and therefore only one integral. However, a new assumption has to be made in order to have one integral. *It is assumed that the perpendicular line from the cylinder is relatively vertical so that the horizontal distance is negligible, or  $\Delta \sin(\theta_{sp} - \frac{\pi}{2}) \ll R \sin(\theta_{sp} - \frac{\pi}{2})$ . This is simplified to  $\Delta \ll R$ , meaning the boundary layer thickness is much smaller than the radius of the cylinder. This is assumed to be true for the type of flow of interest.*

$$u_{SL_t}(\xi) = \frac{U}{\Delta} \xi \quad (3.41)$$

$$T_{SL_t} = \frac{1}{2} \int_0^\Delta \int_{R \sin(\theta_{sp_t} - \frac{\pi}{2})}^{x_{fp_t}} \rho u_{SL_t}^2(\zeta, \xi) d\zeta d\xi \quad (3.42)$$

$$T_{SL_t} = \frac{\rho}{6} \Delta U^2 \left( x_{fp_t} - R \sin \left( \theta_{sp_t} - \frac{\pi}{2} \right) \right) \quad (3.43)$$

### 3.3.3 Attached von Kármán Vortex Energy

*The energy within the vortex is assumed to effect the system as long as the vortex is classified as attached.* This follows logically from the Kutta-Joukowski Theorem,

where the lift force results from the **attached** circulation, or the spinning of the cylinder. By extension, it is argued that any vorticity affects the cylinder as long as the vorticity can be considered attached to the cylinder. Therefore, a vortex attached to the feeding shear layer is still attached to the cylinder. It is at the instant it detaches and is carried downstream that the vortex is no longer attached. Traditionally, it has been thought that there is a precise moment at which a vortex sheds. However, after close examination of many experimental images of vortex shedding, it is obvious that an attachment trail can be traced even after a vortex is considered shed. For this reason, the moment of vortex shedding is not so clearly defined, and caution should be used in defining the shedding criterion. In fact, the shedding process may be more gradual than instantaneous in nature. This hypothesis will be further tested in more advanced models.

For the linear model of the attached vortex, *the Rankine vortex model is assumed to be the best approximation of the real vortex*. This is because the Rankine vortex is already a linear model of a real vortex. It is a much better approximation of a real vortex than the irrotational model because there is finite vorticity at the center of the vortex for the Rankine vortex while the irrotational model has infinite vorticity at the center, which is impossible in nature. See Figure 3.2.

The radius of the vortex must be defined for the Rankine model. If the energy of the Rankine vortex was integrated to an infinite radius, the vortex would have infinite energy. Therefore, it is important to define the radius to which the energy of the vortex is to be integrated for affecting the cylinder. The parameter  $\eta$  will be used to define the radius of the vortex, and only the energy within this radius will be considered (see Figure 2.1). This is acceptable since the Rankine vortex has a velocity outside of the radius that decays to a zero free-stream. However, here

the free-stream is not zero and the vortex velocity does not need to be allowed to decay. At present,  $\eta$  will be considered constant. In the final model, it will become a function of time and a function of the mass flux from the shear layer. The Rankine vortex velocity magnitude up to the radius  $\eta$  is now defined as follows.

$$0 < r < \eta, \quad 0 < \theta < 2\pi \quad (3.44)$$

$$u_\theta = \omega r \quad (3.45)$$

$$u_r = 0 \quad (3.46)$$

If the free-stream velocity is assumed to follow the outside circumference of the vortex, the rotational velocity can then easily be defined using the same free-stream velocity as the boundary and shear layers. The kinetic co-energy is then found in similar fashion as with the boundary layer and shear layer.

$$u_{KV_t} = \frac{U}{\eta_t} r \quad (3.47)$$

$$T_{KV_t} = \frac{1}{2} \int_0^{2\pi} \int_0^{\eta_t} \rho u_{KV_t}^2(r) r \, dr \, d\theta \quad (3.48)$$

$$T_{KV_t} = \frac{1}{2} \int_0^{2\pi} \int_0^{\eta_t} \rho \frac{U^2 r^3}{\eta_t^2} \, dr \, d\theta \quad (3.49)$$

$$T_{KV_t} = \frac{\pi}{4} \rho U^2 \eta_t^2 \quad (3.50)$$

The total attached fluid energy using first-order approximations then results by simply summing the kinetic co-energies of the boundary layer, shear layer, and attached vortex. This will be our starting point upon which to build the energy model to be placed into the Hamilton equation.

### 3.4 Cylinder with Single Degree-of-Freedom

#### 3.4.1 Body Energy

The only degree of freedom is that of the body motion. The motion of the body is linear and does not need to be simplified for a linear approximation. Therefore,

the following linear equations for the energy of the body are the same equations that will be used throughout. The body has two conservative energies: co-kinetic (from the motion) and potential (from the spring). They are defined as follows.

$$T_{body} = \frac{1}{2}m\dot{y}^2 \quad (3.51)$$

$$V_{body} = \frac{1}{2}ky^2 \quad (3.52)$$

In addition to these two conservative energies, there is also a known nonconservative energy acting on the body in the form of damping. This will be developed later in this chapter, as nonconservative energy must be treated differently than conservative energy in the development of Hamilton's principle. There is also an unknown nonconservative energy acting on the wake which prevents all energy flowing into the von Kármán vortex. A mathematical representation of this nonconservative energy will also be developed in this chapter.

With the body energy now defined, the total system energy is changed. It is not a simple matter of summing the body energy with the attached fluid energy. The motion of the body must now be taken into account and new linear approximations of the system must be defined. *It is assumed at this point that the entire attached fluid experiences the body motion  $y$  uniformly across the boundary layer, shear layer, and von Kármán vortex.* This is an obvious over-simplification of the affect the body motion has on the attached fluid. However, it is a reasonable approximation as the effect of the body motion will be experienced by the entire attached fluid, and is estimated to be of the first order in influence. Future work could attempt to allow for only part of the body motion to translate to the attached fluid, or for there to be a delay between the body motion and the fluid motion.



### 3.4.2 Boundary Layer Energy with Body Motion

$$R < r < R + \delta, \quad 0 < \theta < 2\pi \quad (3.53)$$

$$u_r(r, \theta) = \dot{y} \sin(\theta) \quad (3.54)$$

$$u_\theta(r, \theta) = \frac{U}{\delta_t}(r - R) + \dot{y} \cos(\theta) \quad (3.55)$$

$$u_{BL_t}(r, \theta) = \sqrt{u_r^2 + u_\theta^2} = \sqrt{\frac{U^2}{\delta_t^2}(r - R)^2 + \frac{2U}{\delta_t}(r - R)\dot{y}\cos(\theta) + \dot{y}^2} \quad (3.56)$$

From mathematical software Maple:

$$\begin{aligned} T_{BL_t} = & \frac{\rho\Delta U^2}{24} [(2R + \Delta)(\theta_{sp_t} - \theta_{st})] + \frac{\rho\Delta U \dot{y}}{3} \left[ \frac{-2\Delta(\sin(\theta_{sp_t}) - \sin(\theta_{st}))}{(\theta_{sp_t} - \theta_{st})^2} \right] \\ & + \frac{\rho\Delta U \dot{y}}{6} \left[ \frac{(4\Delta + 3R)\cos(\theta_{sp_t}) - 3R\sin(\theta_{st})}{(\theta_{sp_t} - \theta_{st})} \right] \\ & + \frac{\rho\Delta U \dot{y}}{6} [2\Delta\sin(\theta_{sp_t}) + 3R\cos(\theta_{sp_t})] + \frac{\rho\Delta \dot{y}^2}{12} [(\Delta + 3R)(\theta_{sp_t} - \theta_{st})] \end{aligned} \quad (3.57)$$

### 3.4.3 Shear Layer Energy with Body Motion

$$0 < \zeta < x_{fp}, \quad 0 < \xi < \Delta \quad (3.58)$$

$$\theta_{sp_t} = \frac{\pi}{2}$$

$$u(\zeta, \xi) = \frac{U}{\Delta}\xi \quad (3.59)$$

$$v(\zeta, \xi) = \dot{y} \quad (3.60)$$

$$u_{SL_t}(\zeta, \xi) = \sqrt{u^2 + v^2} = \sqrt{\frac{U^2}{\Delta^2}\xi^2 + \dot{y}^2} \quad (3.61)$$

From mathematical software Maple:

$$T_{SL_t} = \frac{1}{2}\rho\Delta x_{fp_t} \left( \frac{U^2}{3} + \dot{y}^2 \right) \quad (3.62)$$

$$\theta_{sp_t} < \frac{\pi}{2}$$

$$u_{SL_{t1}}(r, \theta) = \sqrt{\frac{U^2}{\Delta^2}(r - R)^2 + \frac{U}{\Delta}(r - R)\dot{y}\cos(\theta) + \dot{y}^2} \quad (3.63)$$

$$u_{SL_{t2}}(\xi) = \sqrt{\frac{U^2}{\Delta^2}\xi^2 + \dot{y}^2} \quad (3.64)$$

$$\begin{aligned} T_{SL_t} &= T_{SL_{t1}} + T_{SL_{t2}} \\ &= \frac{\rho\Delta}{24} \left[ (3U^2\Delta + 6\dot{y}^2\Delta + 4U^2R + 12R\dot{y}^2) \left( \frac{\pi}{2} - \theta_{sp_t} \right) \right] \\ &\quad + \frac{\rho\Delta}{12} \left[ (2U\dot{y}\Delta + 3U\dot{y}R) (1 - \sin(\theta_{sp_t})) + 6x_{fp_t} \left( \frac{U^2}{3} + \dot{y}^2 \right) \right] \end{aligned} \quad (3.65)$$

$$\theta_{sp_t} > \frac{\pi}{2}$$

$$u_{SL_t}(\xi) = \sqrt{\frac{U^2}{\Delta^2}\xi^2 + \dot{y}^2} \quad (3.66)$$

$$T_{SL_t} = \frac{\rho\Delta}{2} \left( \frac{U^2}{3} + \dot{y}^2 \right) \left( x_{fp_t} - R \sin \left( \theta_{sp_t} - \frac{\pi}{2} \right) \right) \quad (3.67)$$

#### 3.4.4 Attached von Kármán Vortex Energy with Body Motion

$$0 < r < \eta, \quad 0 < \theta < 2\pi \quad (3.68)$$

$$u_\theta = \frac{U}{\eta}r + \dot{y}\cos(\theta) \quad (3.69)$$

$$u_r = \dot{y}\sin(\theta) \quad (3.70)$$

The above equations are implemented for both the top and bottom vortex. The energy from the top vortex only is given as follows.

$$u_{KV_t} = \sqrt{\frac{U^2r^2}{\eta_t^2} + 2\frac{Ur}{\eta_t}\dot{y}\cos(\theta) + \dot{y}^2} \quad (3.71)$$

$$T_{KV_t} = \frac{\pi\rho\eta_t^2}{4} (U^2 + 2\dot{y}^2) \quad (3.72)$$

### 3.5 Nonconservative Work

The most obvious example of a nonconservative work is the mechanical damping that is always present in the mass-spring-dashpot example.

$$\delta W_{body} = -cy\delta y \quad (3.73)$$

In addition, there are losses in the fluid. The nonconservative work in the fluid will be the dissipation of flow from the shear layer that does not feed the vortex. Since there is a set flow out of the shear layer, analytically defined for the linear velocity profile, it is easy to represent the flow that goes into the vortex and the flow that is dissipated directly into the wake and assumed to no longer have an effect on the system.

$$Q_{SLout} = u_{out} \cdot A = \frac{\Delta U}{2} \quad (3.74)$$

$$Q_{SLout} = Q_{KVin} + Q_{dissipated} \quad (3.75)$$

$$Q_{KVin} = \alpha \frac{\Delta U}{2} \quad (3.76)$$

$$Q_{dissipate} = (1 - \alpha) \frac{\Delta U}{2} \quad (3.77)$$

From the dissipated flow  $Q_{dissipated}$ , an expression for the work of this nonconservative component must be derived.

$$\delta W_{dissipated} = -\rho Q_{dissipated} u_{avg} \delta y \quad (3.78)$$

$$u_{avg} = \frac{1}{\Delta} \int_0^{\Delta} \frac{U}{\Delta} \xi d\xi = \frac{U}{2} \quad (3.79)$$

$$\delta W_{dissipated} = -(1 - \alpha) \rho \frac{\Delta U^2}{4} \delta y \quad (3.80)$$

### 3.6 Derivation of the Force Equations

The total conservative energy of the system can now be expressed summing the updated first-order approximations for the fluid with the energy of the body. At

this time, it is important to remember that there is a top and bottom shear layer, boundary layer, and von Kármán vortex. *The boundary layer thickness  $\Delta$  will be considered the same on the top and bottom, while  $\theta_{sp}$ ,  $x_{fp}$ , and  $\eta$  will all have separate top and bottom values.* There is only one  $\theta_{st}$ . It is also important to understand the sign that will be placed in front of terms from the top of the cylinder and the terms from the bottom of the cylinder. In order to determine the appropriate sign, the Kutta-Joukowski theorem is revisited. It is known that for clockwise rotation, the lift is in the positive  $y$ -direction, while for counter-clockwise rotation, the lift is in the negative  $y$ -direction. Understanding the basic rotational direction caused by the shear stress leads to the conclusion that the terms on the top of the cylinder create positive lift, and the terms on the bottom create negative lift. For this reason, negative signs will be placed in front of the terms on the top (will become positive when moved to the other side of the equal sign later).

$$\mathcal{L} = T - V \tag{3.81}$$

$$= T_{body} - (T_{BLt} + T_{SLt} + T_{KVt}) + (T_{BLb} + T_{SLb} + T_{KVb}) - V_{body}$$

$$\frac{\partial}{\partial t} \left( \frac{\partial \mathcal{L}}{\partial \dot{y}} \right) - \frac{\partial \mathcal{L}}{\partial y} = \Xi \tag{3.82}$$

With so many terms within each energy equation, it will be useful here to do the derivation separately in order to simplify and double check the terms before combining them into one large equation. This is possible because the Lagrangian is a linear operator.

### 3.6.1 Body Force

$$\mathcal{L}_{body} = T_{body} - V_{body} = \frac{1}{2}m\dot{y}^2 - \frac{1}{2}ky^2 \tag{3.83}$$

$$\frac{\partial}{\partial t} \left( \frac{\partial \mathcal{L}_{body}}{\partial \dot{y}} \right) - \frac{\partial \mathcal{L}_{body}}{\partial y} = F_{body} = m\ddot{y} + ky \tag{3.84}$$

### 3.6.2 Boundary Layer Force

$$\begin{aligned}
\mathcal{L}_{BL_t} = T_{BL_t} = & \frac{\rho\Delta U^2}{24} [(2R + \Delta) (\theta_{sp_t} - \theta_{st})] \\
& + \frac{\rho\Delta U \dot{y}}{3} \left[ \frac{-2\Delta (\sin(\theta_{sp_t}) - \sin(\theta_{st}))}{(\theta_{sp_t} - \theta_{st})^2} \right] \\
& + \frac{\rho\Delta U \dot{y}}{6} \left[ \frac{(4\Delta + 3R) \cos(\theta_{sp_t}) - 3R \sin(\theta_{st})}{(\theta_{sp_t} - \theta_{st})} \right] \\
& + \frac{\rho\Delta U \dot{y}}{6} [2\Delta \sin(\theta_{sp_t}) + 3R \cos(\theta_{sp_t})] \\
& + \frac{\rho\Delta \dot{y}^2}{12} [(\Delta + 3R) (\theta_{sp_t} - \theta_{st})]
\end{aligned} \tag{3.85}$$

$$\begin{aligned}
F_{BL_t} = & \frac{\rho\Delta U}{3} \left[ \frac{-2\Delta (2\cos(\theta_{sp_t})\dot{\theta}_{sp_t} - \cos(\theta_{st})\dot{\theta}_{st})}{(\theta_{sp_t} - \theta_{st})^2} \right] \\
& + \frac{\rho\Delta U}{3} \left[ \frac{4\Delta (\sin(\theta_{sp_t}) - \sin(\theta_{st})) (\dot{\theta}_{sp_t} - \dot{\theta}_{st})}{(\theta_{sp_t} - \theta_{st})^3} \right] \\
& + \frac{\rho\Delta U}{6} \left[ \frac{-(4\Delta - 3R) \sin(\theta_{sp_t})\dot{\theta}_{sp_t} + 3R \sin(\theta_{sp_t})\dot{\theta}_{st}}{(\theta_{sp_t} - \theta_{st})} \right] \\
& + \frac{\rho\Delta U}{2} \left[ \frac{R (\cos(\theta_{sp_t}) + \cos(\theta_{st})) (\dot{\theta}_{sp_t} - \dot{\theta}_{st})}{(\theta_{sp_t} - \theta_{st})^2} \right] \\
& + \frac{\rho\Delta U}{6} [2\Delta \cos(\theta_{sp_t})\dot{\theta}_{sp_t} - 3R \sin(\theta_{sp_t})\dot{\theta}_{sp_t}] \\
& + \frac{\rho\Delta}{6} (\Delta + 3R) \left[ \dot{y} (\dot{\theta}_{sp_t} - \dot{\theta}_{st}) + \ddot{y} (\theta_{sp_t} - \theta_{st}) \right]
\end{aligned} \tag{3.86}$$

### 3.6.3 Shear Layer Force

$$\theta_{sp_t} < \frac{\pi}{2}$$

$$\begin{aligned}
\mathcal{L}_{SL_t} = T_{SL_t} = & \frac{\rho\Delta}{24} \left[ (3U^2\Delta + 6\dot{y}^2\Delta + 4U^2R + 12R\dot{y}^2) \left( \frac{\pi}{2} - \theta_{sp_t} \right) \right] \\
& + \frac{\rho\Delta}{12} \left[ (2U\dot{y}\Delta + 3U\dot{y}R) (1 - \sin(\theta_{sp_t})) + 6x_{fp_t} \left( \frac{U^2}{3} + \dot{y}^2 \right) \right]
\end{aligned} \tag{3.87}$$

$$\begin{aligned}
F_{SL_t} = & \frac{\rho\Delta}{12} \left[ (6\Delta + 12R) \ddot{y} \left( \frac{\pi}{2} - \theta_{sp_t} \right) - (2\Delta + 3R) U \cos(\theta_{sp_t}) \dot{\theta}_{sp_t} \right] \\
& - \frac{\rho\Delta}{2} \left[ (\Delta - 2R) \dot{y} \dot{\theta}_{sp_t} \right] + \rho\Delta x_{fp_t} \ddot{y} + \rho\Delta \dot{x}_{fp_t} \dot{y}
\end{aligned} \tag{3.88}$$

$$\theta_{sp_t} > \frac{\pi}{2}$$

$$\mathcal{L}_{SL_t} = T_{SL_t} = \frac{\rho\Delta}{2} \left( \frac{U^2}{3} + \dot{y}^2 \right) \left( x_{fp_t} - R \sin \left( \theta_{sp_t} - \frac{\pi}{2} \right) \right) \quad (3.89)$$

$$F_{SL_t} = \rho\Delta \left[ \ddot{y} \left( x_{fp_t} - R \sin \left( \theta_{sp_t} - \frac{\pi}{2} \right) \right) + \dot{y} \left( \dot{x}_{fp_t} - R\dot{\theta}_{sp_t} \cos \left( \theta_{sp_t} - \frac{\pi}{2} \right) \right) \right] \quad (3.90)$$

### 3.6.4 Attached von Kármán Vortex Force

$$\mathcal{L}_{KV_t} = T_{KV_t} = \frac{\pi\rho\eta_t^2}{4} (U^2 + 2\dot{y}^2) \quad (3.91)$$

$$F_{KV_t} = \pi\rho (2\dot{\eta}_t\dot{y} + \eta_t^2\ddot{y}) \quad (3.92)$$

### 3.6.5 Nonconservative Forces

$$\delta W_{body} = -c\dot{y}\delta y \quad (3.93)$$

$$\Xi_{body} = \frac{\delta W_{body}}{\delta y} = -c\dot{y} \quad (3.94)$$

$$\delta W_{dissipated} = -(1-\alpha)\rho \frac{\Delta U^2}{4} \delta y \quad (3.95)$$

$$\Xi_{dissipated} = \frac{\delta W_{dissipated}}{\delta y} = -(1-\alpha)\rho \frac{\Delta U^2}{4} \quad (3.96)$$

A preliminary application of the Hamiltonian gives some insight into the results of the first-order approximation. Although everything to this point has been declared as simply as possible, there are already many terms that result from the derivatives. This is due to the fact that many parameters are a function of either  $t$  or  $\dot{y}$ , which both serve as the base for derivatives. All of the assumptions taken to arrive at this model to this point are summarized in Table 3.1.

### 3.7 Full Force Equation

There are several ways to look at the entire equation. First, the typical mass-spring-dashpot equation can be equated to the forcing terms as follows.

$$m\ddot{y} + c\dot{y} + ky = \Xi_{diss_t} + \Xi_{diss_b} + F_{BL_t} + F_{SL_t} + F_{KV_t} - F_{BL_b} - F_{SL_b} - F_{KV_b} \quad (3.97)$$

$$|\theta_{sp}| < \frac{\pi}{2}$$

$$\begin{aligned}
m\ddot{y} + c\dot{y} + ky &= -(1 - \alpha)\rho \frac{\Delta U^2}{2} + \frac{\rho \Delta^2 U}{3} \left[ \frac{-2 \left( 2\cos(\theta_{sp_t})\dot{\theta}_{sp_t} - \cos(\theta_{st})\dot{\theta}_{st} \right)}{(\theta_{sp_t} - \theta_{st})^2} \right] \\
&+ \frac{\rho \Delta^2 U}{3} \left[ \frac{4 \left( \sin(\theta_{sp_t}) - \sin(\theta_{st}) \right) \left( \dot{\theta}_{sp_t} - \dot{\theta}_{st} \right)}{(\theta_{sp_t} - \theta_{st})^3} \right] \\
&+ \frac{\rho \Delta U}{6} \left[ \frac{-(4\Delta - 3R) \sin(\theta_{sp_t})\dot{\theta}_{sp_t} + 3R \sin(\theta_{sp_t})\dot{\theta}_{st}}{(\theta_{sp_t} - \theta_{st})} \right] \\
&+ \frac{\rho \Delta U}{6} \left[ 2\Delta \cos(\theta_{sp_t})\dot{\theta}_{sp_t} - 3R \sin(\theta_{sp_t})\dot{\theta}_{sp_t} \right] \\
&+ \frac{\rho \Delta U}{2} \left[ \frac{R \left( \cos(\theta_{sp_t}) + \cos(\theta_{st}) \right) \left( \dot{\theta}_{sp_t} - \dot{\theta}_{st} \right)}{(\theta_{sp_t} - \theta_{st})^2} \right] \\
&+ \frac{\rho \Delta}{6} (\Delta + 3R) \left[ \dot{y} \left( \dot{\theta}_{sp_t} - \dot{\theta}_{st} \right) + \ddot{y} (\theta_{sp_t} - \theta_{st}) \right] \\
&+ \frac{\rho \Delta}{12} \left[ (6\Delta + 12R) \ddot{y} \left( \frac{\pi}{2} - \theta_{sp_t} \right) - (2\Delta + 3R) U \cos(\theta_{sp_t}) \dot{\theta}_{sp_t} \right] \\
&- \frac{\rho \Delta}{2} \left[ (\Delta - 2R) \dot{y} \dot{\theta}_{sp_t} \right] + \rho \Delta \left[ x_{fp_t} \ddot{y} + \dot{x}_{fp_t} \dot{y} \right] + \pi \rho \left[ 2\dot{\eta}_t \dot{y} + \eta_t^2 \ddot{y} \right] \\
&- \frac{\rho \Delta^2 U}{3} \left[ \frac{2 \left( 2\cos(\theta_{sp_b})\dot{\theta}_{sp_b} - \cos(\theta_{st})\dot{\theta}_{st} \right)}{(\theta_{st} - \theta_{sp_b})^2} \right] \\
&- \frac{\rho \Delta^2 U}{3} \left[ \frac{-4 \left( \sin(\theta_{sp_b}) - \sin(\theta_{st}) \right) \left( \dot{\theta}_{st} - \dot{\theta}_{sp_b} \right)}{(\theta_{st} - \theta_{sp_b})^3} \right] \\
&- \frac{\rho \Delta U}{6} \left[ \frac{-(4\Delta - 3R) \sin(\theta_{sp_b})\dot{\theta}_{sp_b} + 3R \sin(\theta_{sp_b})\dot{\theta}_{st}}{(\theta_{st} - \theta_{sp_b})} \right] \\
&+ \frac{\rho \Delta U}{6} \left[ 2\Delta \cos(\theta_{sp_b})\dot{\theta}_{sp_b} + 3R \sin(\theta_{sp_b})\dot{\theta}_{sp_b} \right] \\
&- \frac{\rho \Delta U}{2} \left[ \frac{R \left( \cos(\theta_{sp_b}) + \cos(\theta_{st}) \right) \left( \dot{\theta}_{st} - \dot{\theta}_{sp_b} \right)}{(\theta_{st} - \theta_{sp_b})^2} \right] \\
&- \frac{\rho \Delta}{6} (\Delta + 3R) \left[ \dot{y} \left( \dot{\theta}_{st} - \dot{\theta}_{sp_b} \right) + \ddot{y} (\theta_{st} - \theta_{sp_b}) \right] \\
&- \frac{\rho \Delta}{12} \left[ (6\Delta + 12R) \ddot{y} \left( \frac{\pi}{2} + \theta_{sp_b} \right) + (2\Delta + 3R) U \cos(\theta_{sp_b}) \dot{\theta}_{sp_b} \right] \\
&- \frac{\rho \Delta}{2} \left[ (\Delta - 2R) \dot{y} \dot{\theta}_{sp_b} \right] - \rho \Delta \left[ x_{fp_b} \ddot{y} + \dot{x}_{fp_b} \dot{y} \right] - \pi \rho \left[ 2\dot{\eta}_b \dot{y} + \eta_b^2 \ddot{y} \right]
\end{aligned}$$

(3.98)



$$|\theta_{sp}| > \frac{\pi}{2}$$

$$\begin{aligned}
m\ddot{y} + c\dot{y} + ky &= -(1 - \alpha)\rho \frac{\Delta U^2}{2} + \frac{\rho \Delta^2 U}{3} \left[ \frac{-2 \left( 2\cos(\theta_{sp_t})\dot{\theta}_{sp_t} - \cos(\theta_{st})\dot{\theta}_{st} \right)}{(\theta_{sp_t} - \theta_{st})^2} \right] \\
&+ \frac{\rho \Delta^2 U}{3} \left[ \frac{4 \left( \sin(\theta_{sp_t}) - \sin(\theta_{st}) \right) \left( \dot{\theta}_{sp_t} - \dot{\theta}_{st} \right)}{(\theta_{sp_t} - \theta_{st})^3} \right] \\
&+ \frac{\rho \Delta U}{6} \left[ \frac{-(4\Delta - 3R) \sin(\theta_{sp_t})\dot{\theta}_{sp_t} + 3R \sin(\theta_{sp_t})\dot{\theta}_{st}}{(\theta_{sp_t} - \theta_{st})} \right] \\
&+ \frac{\rho \Delta U}{6} \left[ 2\Delta \cos(\theta_{sp_t})\dot{\theta}_{sp_t} - 3R \sin(\theta_{sp_t})\dot{\theta}_{sp_t} \right] \\
&+ \frac{\rho \Delta U}{2} \left[ \frac{R \left( \cos(\theta_{sp_t}) + \cos(\theta_{st}) \right) \left( \dot{\theta}_{sp_t} - \dot{\theta}_{st} \right)}{(\theta_{sp_t} - \theta_{st})^2} \right] \\
&+ \frac{\rho \Delta}{6} (\Delta + 3R) \left[ \dot{y} \left( \dot{\theta}_{sp_t} - \dot{\theta}_{st} \right) + \ddot{y} (\theta_{sp_t} - \theta_{st}) \right] \\
&+ \rho \Delta \left[ \ddot{y} \left( x_{fp_t} - R \sin \left( \theta_{sp_t} - \frac{\pi}{2} \right) \right) + \dot{y} \left( \dot{x}_{fp_t} - R\dot{\theta}_{sp_t} \cos \left( \theta_{sp_t} - \frac{\pi}{2} \right) \right) \right] \\
&+ \pi \rho \left( 2\dot{\eta}_t \dot{y} + \eta_t^2 \ddot{y} \right) \\
&- \frac{\rho \Delta^2 U}{3} \left[ \frac{2 \left( 2\cos(\theta_{sp_b})\dot{\theta}_{sp_b} - \cos(\theta_{st})\dot{\theta}_{st} \right)}{(\theta_{st} - \theta_{sp_b})^2} \right] \\
&- \frac{\rho \Delta^2 U}{3} \left[ \frac{-4 \left( \sin(\theta_{sp_b}) - \sin(\theta_{st}) \right) \left( \dot{\theta}_{st} - \dot{\theta}_{sp_b} \right)}{(\theta_{st} - \theta_{sp_b})^3} \right] \\
&- \frac{\rho \Delta U}{6} \left[ \frac{-(4\Delta - 3R) \sin(\theta_{sp_b})\dot{\theta}_{sp_b} + 3R \sin(\theta_{sp_b})\dot{\theta}_{st}}{(\theta_{st} - \theta_{sp_b})} \right] \\
&+ \frac{\rho \Delta U}{6} \left[ 2\Delta \cos(\theta_{sp_b})\dot{\theta}_{sp_b} + 3R \sin(\theta_{sp_b})\dot{\theta}_{sp_b} \right] \\
&- \frac{\rho \Delta U}{2} \left[ \frac{R \left( \cos(\theta_{sp_b}) + \cos(\theta_{st}) \right) \left( \dot{\theta}_{st} - \dot{\theta}_{sp_b} \right)}{(\theta_{st} - \theta_{sp_b})^2} \right] \\
&- \frac{\rho \Delta}{6} (\Delta + 3R) \left[ \dot{y} \left( \dot{\theta}_{st} - \dot{\theta}_{sp_b} \right) + \ddot{y} (\theta_{st} - \theta_{sp_b}) \right] \\
&- \rho \Delta \left[ \ddot{y} \left( x_{fp_b} - R \sin \left( -\theta_{sp_b} - \frac{\pi}{2} \right) \right) + \dot{y} \left( \dot{x}_{fp_b} + R\dot{\theta}_{sp_b} \cos \left( -\theta_{sp_b} - \frac{\pi}{2} \right) \right) \right] \\
&- \pi \rho \left( 2\dot{\eta}_b \dot{y} + \eta_b^2 \ddot{y} \right)
\end{aligned}$$

(3.99)

However, it is obvious that many terms can be rearranged into added mass  $m_a$  and added fluid damping  $c_a$  terms, leaving terms without a dependence on  $y$  on the right hand side.

$$(m + m_a)\ddot{y} + (c + c_a)\dot{y} + ky = F \quad (3.100)$$

$$|\theta_{sp}| < \frac{\pi}{2}$$

$$m\ddot{y} + c\dot{y} + ky$$

$$\begin{aligned}
& + \rho \left[ \Delta \left( \theta_{st} \left( \frac{\Delta}{3} + R \right) + (\theta_{sp_t} + \theta_{sp_b}) \left( \frac{\Delta}{3} + \frac{R}{2} \right) + (x_{fp_b} - x_{fp_t}) \right) + \pi (\eta_b^2 - \eta_t^2) \right] \ddot{y} \\
& + \rho \left[ \Delta \left( \dot{\theta}_{st} \left( \frac{\Delta}{3} + R \right) + (\dot{\theta}_{sp_t} + \dot{\theta}_{sp_b}) \left( \frac{\Delta}{3} + \frac{R}{2} \right) + (\dot{x}_{fp_b} - \dot{x}_{fp_t}) \right) + 2\pi (\dot{\eta}_b - \dot{\eta}_t) \right] \dot{y} \\
& = -(1 - \alpha)\rho \frac{\Delta U^2}{2} + \frac{\rho \Delta^2 U}{3} \left[ \frac{-2 \left( 2\cos(\theta_{sp_t})\dot{\theta}_{sp_t} - \cos(\theta_{st})\dot{\theta}_{st} \right)}{(\theta_{sp_t} - \theta_{st})^2} \right] \\
& + \frac{\rho \Delta^2 U}{3} \left[ \frac{4(\sin(\theta_{sp_t}) - \sin(\theta_{st}))(\dot{\theta}_{sp_t} - \dot{\theta}_{st})}{(\theta_{sp_t} - \theta_{st})^3} \right] \\
& + \frac{\rho \Delta U}{6} \left[ \frac{-(4\Delta - 3R)\sin(\theta_{sp_t})\dot{\theta}_{sp_t} + 3R\sin(\theta_{sp_t})\dot{\theta}_{st}}{(\theta_{sp_t} - \theta_{st})} \right] \\
& + \frac{\rho \Delta U}{6} \left[ 2\Delta\cos(\theta_{sp_t})\dot{\theta}_{sp_t} - 3R\sin(\theta_{sp_t})\dot{\theta}_{sp_t} \right] \\
& + \frac{\rho \Delta U}{2} \left[ \frac{R(\cos(\theta_{sp_t}) + \cos(\theta_{st}))(\dot{\theta}_{sp_t} - \dot{\theta}_{st})}{(\theta_{sp_t} - \theta_{st})^2} \right] - \frac{\rho \Delta}{12} (2\Delta + 3R)U\cos(\theta_{sp_t})\dot{\theta}_{sp_t} \\
& - \frac{\rho \Delta^2 U}{3} \left[ \frac{-2 \left( 2\cos(\theta_{sp_b})\dot{\theta}_{sp_b} - \cos(\theta_{st})\dot{\theta}_{st} \right)}{(\theta_{st} - \theta_{sp_b})^2} \right] \\
& + \frac{\rho \Delta^2 U}{3} \left[ \frac{4(\sin(\theta_{sp_b}) - \sin(\theta_{st}))(\dot{\theta}_{st} - \dot{\theta}_{sp_b})}{(\theta_{st} - \theta_{sp_b})^3} \right] \\
& - \frac{\rho \Delta U}{6} \left[ \frac{-(4\Delta - 3R)\sin(\theta_{sp_b})\dot{\theta}_{sp_b} + 3R\sin(\theta_{sp_b})\dot{\theta}_{st}}{(\theta_{st} - \theta_{sp_b})} \right] \\
& + \frac{\rho \Delta U}{6} \left[ 2\Delta\cos(\theta_{sp_b})\dot{\theta}_{sp_b} + 3R\sin(\theta_{sp_b})\dot{\theta}_{sp_b} \right] \\
& - \frac{\rho \Delta U}{2} \left[ \frac{R(\cos(\theta_{sp_b}) + \cos(\theta_{st}))(\dot{\theta}_{st} - \dot{\theta}_{sp_b})}{(\theta_{st} - \theta_{sp_b})^2} \right] - \frac{\rho \Delta}{12} (2\Delta + 3R)U\cos(\theta_{sp_b})\dot{\theta}_{sp_b}
\end{aligned} \tag{3.101}$$

$$|\theta_{sp}| > \frac{\pi}{2}$$

$$m\ddot{y} + c\dot{y} + ky$$

$$\begin{aligned}
& + \rho \left[ \Delta \left( \theta_{st} \left( \frac{\Delta}{3} + R \right) + (\theta_{sp_t} + \theta_{sp_b}) \left( \frac{\Delta}{3} + \frac{R}{2} \right) + (x_{fp_b} - x_{fp_t}) \right) + \pi (\eta_b^2 - \eta_t^2) \right] \ddot{y} \\
& + \rho \left[ \Delta \left( \dot{\theta}_{st} \left( \frac{\Delta}{3} + R \right) + (\dot{\theta}_{sp_t} + \dot{\theta}_{sp_b}) \left( \frac{\Delta}{3} + \frac{R}{2} \right) + (\dot{x}_{fp_b} - \dot{x}_{fp_t}) \right) + 2\pi (\dot{\eta}_b - \dot{\eta}_t) \right] \dot{y} \\
& = -(1 - \alpha)\rho \frac{\Delta U^2}{2} + \frac{\rho \Delta^2 U}{3} \left[ \frac{-2 \left( 2\cos(\theta_{sp_t})\dot{\theta}_{sp_t} - \cos(\theta_{st})\dot{\theta}_{st} \right)}{(\theta_{sp_t} - \theta_{st})^2} \right] \\
& + \frac{\rho \Delta^2 U}{3} \left[ \frac{4(\sin(\theta_{sp_t}) - \sin(\theta_{st}))(\dot{\theta}_{sp_t} - \dot{\theta}_{st})}{(\theta_{sp_t} - \theta_{st})^3} \right] \\
& + \frac{\rho \Delta U}{6} \left[ \frac{-(4\Delta - 3R)\sin(\theta_{sp_t})\dot{\theta}_{sp_t} + 3R\sin(\theta_{sp_t})\dot{\theta}_{st}}{(\theta_{sp_t} - \theta_{st})} \right] \\
& + \frac{\rho \Delta U}{6} \left[ 2\Delta\cos(\theta_{sp_t})\dot{\theta}_{sp_t} - 3R\sin(\theta_{sp_t})\dot{\theta}_{sp_t} \right] \\
& + \frac{\rho \Delta U}{2} \left[ \frac{R(\cos(\theta_{sp_t}) + \cos(\theta_{st}))(\dot{\theta}_{sp_t} - \dot{\theta}_{st})}{(\theta_{sp_t} - \theta_{st})^2} \right] \\
& - \frac{\rho \Delta^2 U}{3} \left[ \frac{-2 \left( 2\cos(\theta_{sp_b})\dot{\theta}_{sp_b} - \cos(\theta_{st})\dot{\theta}_{st} \right)}{(\theta_{st} - \theta_{sp_b})^2} \right] \\
& + \frac{\rho \Delta^2 U}{3} \left[ \frac{4(\sin(\theta_{sp_b}) - \sin(\theta_{st}))(\dot{\theta}_{st} - \dot{\theta}_{sp_b})}{(\theta_{st} - \theta_{sp_b})^3} \right] \\
& - \frac{\rho \Delta U}{6} \left[ \frac{-(4\Delta - 3R)\sin(\theta_{sp_b})\dot{\theta}_{sp_b} + 3R\sin(\theta_{sp_b})\dot{\theta}_{st}}{(\theta_{st} - \theta_{sp_b})} \right] \\
& + \frac{\rho \Delta U}{6} \left[ 2\Delta\cos(\theta_{sp_b})\dot{\theta}_{sp_b} + 3R\sin(\theta_{sp_b})\dot{\theta}_{sp_b} \right] \\
& - \frac{\rho \Delta U}{2} \left[ \frac{R(\cos(\theta_{sp_b}) + \cos(\theta_{st}))(\dot{\theta}_{st} - \dot{\theta}_{sp_b})}{(\theta_{st} - \theta_{sp_b})^2} \right]
\end{aligned}$$

(3.102)

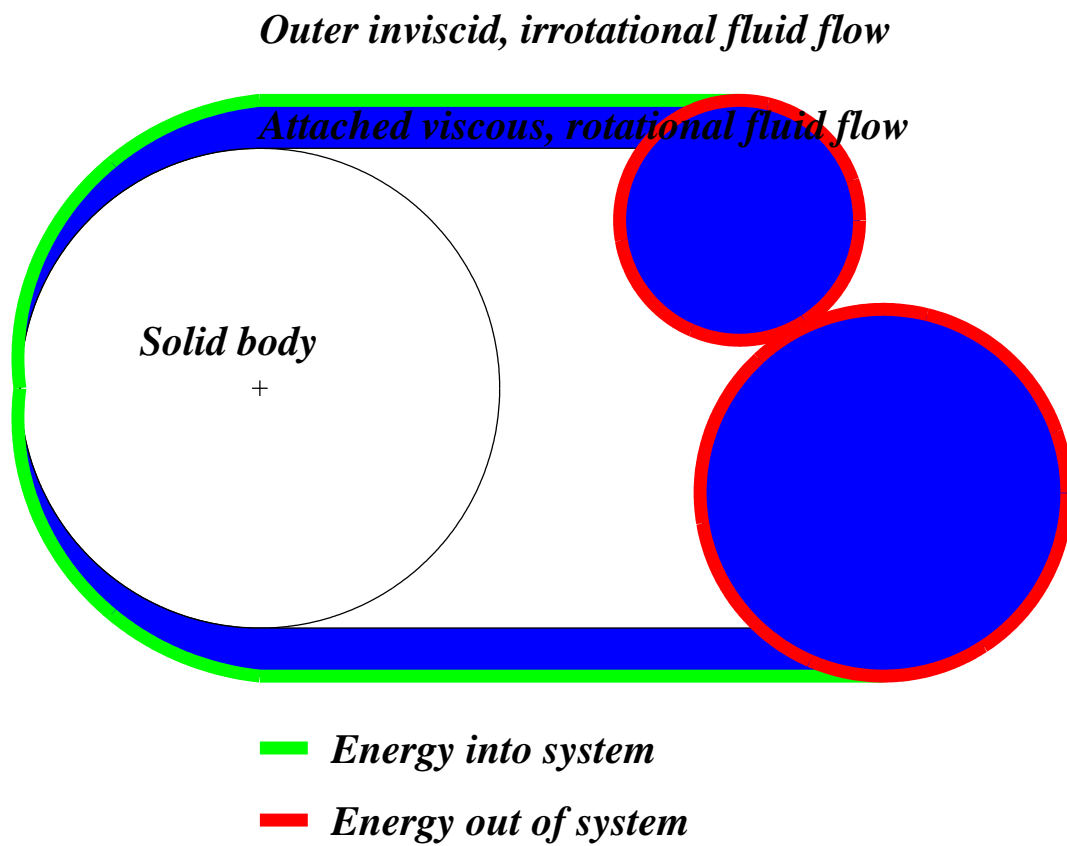


Figure 3.1: Schematic of body and attached fluid region, showing area of energy into and out of the system, including dissipation into the wake at the end of the shear layer.

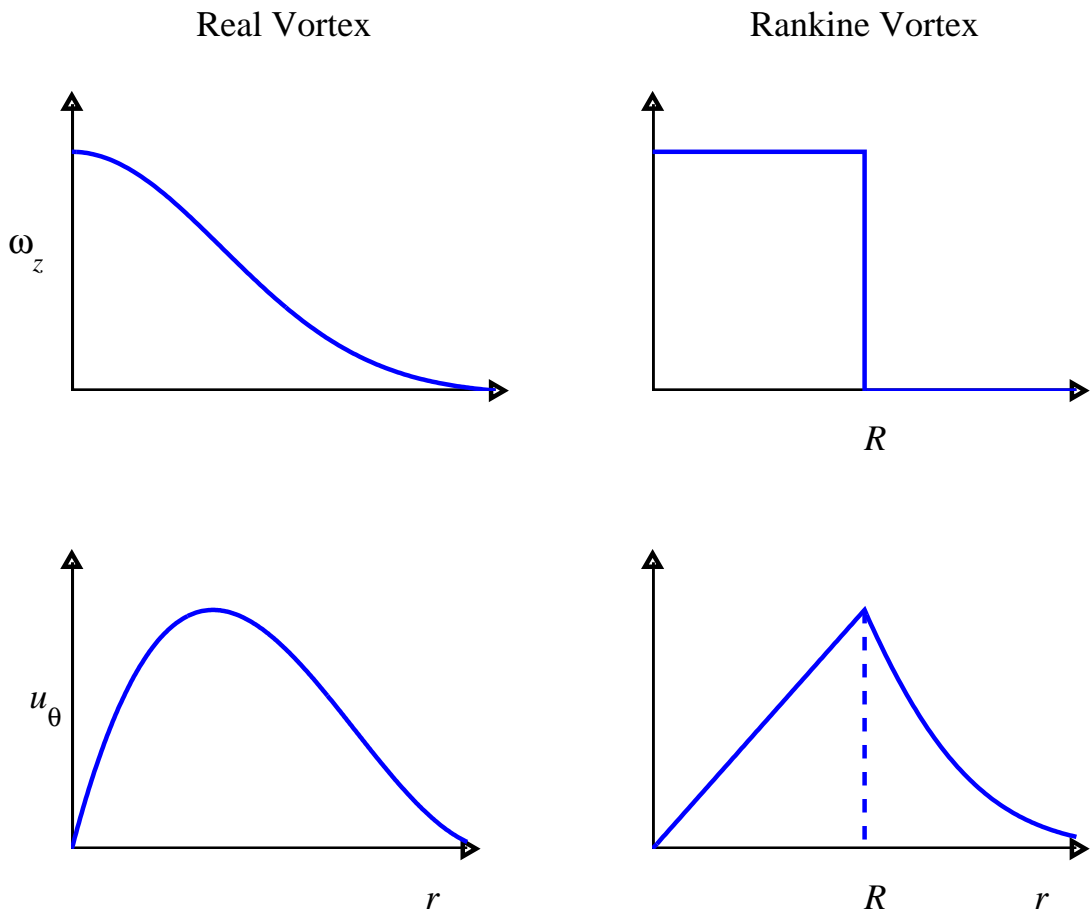


Figure 3.2: Rankine approximation compared to the nature of a real vortex.

Table 3.1: Assumptions used in the development of the first-order approximations for inputs into the derived energy model.

| <i>Assumptions for First-Order Approximations</i> |   |
|---|---|
| 1.  | the fluid-structure interaction of VIV can be effectively modeled in two-dimensions for VIVACE  |
| 2.  | the model is a nonlinear, single degree-of-freedom equation developed from generalized energy equations using Hamilton's principle      |
| 3.  | the velocity profile from the surface of the cylinder to free-stream is linear with the radius  |
| 4.  | the boundary layer thickness is linearly increasing with the angle  |
| 5.  | a linear velocity profile between the dead-fluid region behind the cylinder and the free-stream   |
| 6.  | the boundary layer thickness is much smaller than the radius of the cylinder  |
| 7.  | the energy within the vortex effects the system as long as the vortex is classified as attached   |
| 8.  | the Rankine vortex model is the best approximation of the real vortex   |
| 9.  | the entire attached fluid experiences the body motion $\dot{y}$ uniformly across the shear layer, boundary layer, and von Kármán vortex |
| 10.   | the boundary layer thickness $\Delta$ will be considered the same on the top and bottom   |
| 11.   | $\theta_{sp}$ , $x_{fp}$ , and $\eta$ will all have separate top and bottom values  |
| 12.   | $m$ , $k$ , $c$ , $\rho$ , $U$ , $\Delta$ , $R$ , and $\alpha$ are constant in time   |
| 13.   | $y$ , $\theta_{st}$ , $\theta_{sp}$ , $x_{fp}$ , and $\eta$ are functions of time   |

## CHAPTER 4

### Testing and Verifying Mathematical Model with Linear Approximations

In order to examine the results produced from the mathematical model derived in the previous model, several plots are created. These include a plot of the maximum amplitude of oscillation of the cylinder divided by the diameter of the cylinder ( $A/D$ ) versus the velocity reduced by the natural frequency and the diameter of the cylinder ( $U^* = U/f_n D$ ), a plot of the phase difference between the maximum positive lift and the maximum positive displacement ( $\phi$ ) versus the reduced velocity, and the frequency of response with maximum energy (in some cases, there may be multiple frequencies present in an energy spectrum, but only the one with maximum energy will be taken in this case) normalized by the natural frequency of the cylinder ( $f_r/f_n$ ) versus the reduced velocity. In the  $A/D$  plot, the range of synchronization can be observed. In the  $\phi$  plot, a phase shift of  $180^\circ$  is expected at the point of resonance ( $f_n = f_s$ ). In the frequency plot, it is expected that the maximum frequency response will lock-in to the natural frequency around  $f_n = f_s$ , and remain locked-in for higher  $U^*$  until a certain point at which it locks out. Later, a plot of the vortex shedding mode can be created, where the number of vortices shed from each side during one full cycle of cylinder motion can be counted. Empty plots with the above described



axes are shown in Figure 4.1.

$$F = f \sin(\omega t)y = A \sin(\omega t + \phi) \quad (4.1)$$

#### 4.1 Numerical Simulation

Numerical simulations are needed to discover how the system model responds to periodic inputs. The Runge-Kutta Method of Order Four (RK4) is used to numerically integrate this second-order derivative. The development of this method is outlined here for those who are not familiar with it. The derivation and discussion are taken from Mathews and Fink (2004), but many numerical method texts outline this method. The Runge-Kutta Method was selected because it is derived from the Taylor method with the same order of accuracy, but in Runge-Kutta there is no need to compute higher derivatives. The result is an accurate and stable program. The fourth-order method is most popular because increased accuracy beyond the order four would increase the computational effort beyond worth for the case of most simulations.

To derive RK4, the Taylor series is taken to order four.

$$y_{k+1} = y_k + h \frac{dy}{dt_k} + \frac{h^2}{2} \frac{d^2y}{dt_k^2} + \frac{h^3}{6} \frac{d^3y}{dt_k^3} + \frac{h^4}{24} \frac{d^4y}{dt_k^4} + O(h^{N+1}) \quad (4.2)$$

$$\frac{d^{(j)}y}{dt^{(j)}} = f^{(j-1)}(t, y(t)) \quad (4.3)$$

It is then re-written in the desired form.

$$y_{k+1} = y_k + w_1k_1 + w_2k_2 + w_3k_3 + w_4k_4 \quad (4.4)$$

$$k_1 = hf(t_k, y_k)$$

$$k_2 = hf(t_k + a_1h, y_k + b_1k_1) \quad (4.5)$$

$$k_3 = hf(t_k + a_2h, y_k + b_2k_1 + b_3k_2)$$

$$k_4 = hf(t_k + a_3h, y_k + b_4k_1 + b_5k_2 + b_6 + k_3)$$

The terms in the above equations are then matched to the terms in the Taylor series expansion, resulting in eleven equations for thirteen unknowns. It is then convenient to assign values to two coefficients to solve the equations. The result is RK4.

$$y_{k+1} = y_k + \frac{1}{2} (f_1 + 2f_2 + 2f_3 + f_4) \quad (4.6)$$

$$\begin{aligned} f_1 &= f(t_k, y_k) \\ f_2 &= f\left(t_k + \frac{h}{2}, y_k + \frac{h}{2}f_1\right) \\ f_3 &= f\left(t_k + \frac{h}{2}, y_k + \frac{h}{2}f_2\right) \\ f_4 &= f(t_k + h, y_k + hf_3) \end{aligned} \quad (4.7)$$

In the case of the derived model, it is a second-order differential equation to be solved for  $y$ . Therefore, the model must be split into two equations where the highest derivative of each equation is only first order. This is easily accomplished by denoting the variables  $y$  and  $\dot{y}$  as two separate variables as follows.

$$\begin{aligned} x_1(t) &= y(t) \\ x_2(t) &= \dot{y} = \dot{x}_1 \end{aligned} \quad (4.8)$$

$$\dot{x}_2 = \ddot{y} = \ddot{x}_1$$

Replacing all of the  $y$ ,  $\dot{y}$ , and  $\ddot{y}$  variables with  $x_1$  and  $x_2$  and adding in the equation  $x_2(t) = \dot{x}_1$  results in two first-order differential equations that can then be solved numerically using RK4. The MATLAB program was then taken directly from Mathews and Fink (2004), “Program 9.9 (Runge-Kutta Method of Order  $N = 4$  for Systems),” pages 533 to 534.

## 4.2 Sinusoidal Input

Several parameters must be defined as inputs for the system. As a first step, a sinusoidal input is used as the simplest periodic input. Although lacking physical

meaning, it is a stepping stone to investigating the output.

$$\begin{aligned}
\eta_t &= \eta_o + \delta\eta \sin(2\pi f_s t + \phi_{\eta_t}) \\
\eta_b &= \eta_o + \delta\eta \sin(2\pi f_s t + \phi_{\eta_b}) \\
x_{fp_t} &= x_{fp_o} + \delta x \sin(2\pi f_s t + \phi_{fp_t}) \\
x_{fp_b} &= x_{fp_o} + \delta x \sin(2\pi f_s t + \phi_{fp_b}) \\
\theta_{sp_t} &= \theta_{sp_{t_o}} + \delta\theta_{sp} \sin(2\pi f_s t + \phi_{sp_t}) \\
\theta_{sp_b} &= \theta_{sp_{b_o}} + \delta\theta_{sp} \sin(2\pi f_s t + \phi_{sp_b}) \\
\theta_{st} &= \delta\theta_{st} \sin(2\pi f_s t + \phi_{st})
\end{aligned} \tag{4.9}$$

$$\begin{aligned}
\eta_o &= R/2 & \delta\eta &= R/2 & \phi_{\eta_t} &= 0 & \phi_{\eta_b} &= \pi \\
x_{fp_o} &= 2R & \delta x &= R & \phi_{fp_t} &= 0 & \phi_{fp_b} &= \pi \\
\theta_{sp_{t_o}} &= 4\pi/9 & \delta\theta_{sp} &= \pi/18 & \phi_{sp_t} &= 0 & \theta_{sp_{b_o}} &= -4\pi/9 \\
\phi_{sp_b} &= 0 & \delta\theta_{st} &= \pi/18 & \phi_{st} &= 0
\end{aligned} \tag{4.10}$$

Below are the physical inputs used for the sinusoidal input simulation. Although the below values are dimensional, they are converted to non-dimensional form for most computations, and can easily be entered non-dimensionally if desired. It is merely the fact that this research group has performed numerous simulations, and therefore reasonable dimensional inputs could easily be entered, where reasonable refers to the appropriate order of magnitude. Also, recall that everything in this body of work is in two dimensions. For this reason, certain values may be per unit length.

$$\begin{aligned}
0.01 \leq U \leq 2m/s & \quad m = 10kg/m & \quad k = 100N/m^2 \\
\rho = 1000kg/m^3 & \quad D = 0.1m & \quad \Delta = D/100m \\
c = 5Ns/m^2 & \quad \nu = 1e - 6m^2/s
\end{aligned} \tag{4.11}$$

The inputs are represented in a plot given Figure 4.2. The resulting range of

synchronization, phase between forcing and displacement, and frequency of response with maximum energy are then shown for the wide range of flow velocities in Figures 4.6 and 4.11. Already, indications of a range of synchronization with an upper and lower branch are shown. In addition, lock-in for a certain range of values is also shown, with lock-out at higher reduced velocities. The break in the amplitude of response plot is due to the fact that the amplitudes in the region are much larger than the rest of the range and not physically representative of the nature of the problem. However, with further refinement of the model, it is seen that this inconsistency is eliminated in the next section.

### 4.3 Flow-Based Input

It is apparent that this model is very promising even with a sinusoidal input. However, none of the above inputs actually mimics the physical inputs a cylinder with vortex shedding would experience. Vortex shedding is considered under the category of relaxation oscillations, where there is slow build up followed by a sudden discharge. The input, or the stagnation point, separation points, formation points, and vortex radius, will not behave like a sine wave. In fact, based on the relationship of the velocity flow into the vortex and the size of the vortex, it is found that instead of behaving sinusoidally with time, the response should be proportional to the square root of time, reaching a certain critical maximum for the vortex size or energy, and then dropping back to zero (either instantaneously or over several time-steps). This then turns the vortex radius  $\eta$  into a function of the incoming velocity profile, and no longer a user defined input.

$$Q_{SL_{out}} = \int_0^{\Delta} u_{SL_{out}} d\xi \quad (4.12)$$

$$u_{SL_{out}} = \frac{U}{\Delta} \xi \quad (4.13)$$

$$Q_{SL_{out}} = \frac{U\Delta}{2} \quad (4.14)$$

The velocity exiting the shear layer is in fact only a function of the free-stream velocity  $U$  as the entire system is moving with velocity  $\dot{y}$ , and therefore no fluid ever exits the system from the cylinder motion. When defining the dissipated work for the system, the amount of fluid entering the vortex was limited by the user input constant  $\alpha$ , making the input into the vortex equal to  $\alpha Q_{SL_{out}}$  rather than the entire flow.

$$Q_{KV_{in}} = \alpha Q_{SL_{out}} = \alpha \frac{U\Delta}{2} \quad (4.15)$$

The mass flux for constant density is equal to the flow times density. From this relationship, we can define how large the attached von Kármán vortex is, and define the radius  $\eta$  from the flow in. Recall that everything is defined in two-dimensions, so the mass and flow are per unit length.

$$\dot{m}_{KV} = \rho Q_{KV_{in}} = \alpha \rho \frac{U\Delta}{2} \quad (4.16)$$

$$m_{KV} = \int_0^t \dot{m}_{KV} dt = \alpha \rho \frac{U\Delta}{2} t \quad (4.17)$$

$$m_{KV} = \pi \rho \eta^2 = \alpha \rho \frac{U\Delta}{2} t \quad (4.18)$$

$$\eta = \sqrt{\alpha \frac{U\Delta}{2\pi} t} \quad (4.19)$$

This statement will be true until a certain time  $T_s$ , at which time the vortex will shed, possibly gradually, and then  $\eta$  will go back to zero and repeat the growth as if from  $t = 0$ . When the vortex sheds, the formation point, separation point, and stagnation point will also be effected and *will be assumed to move to their minimum values relative to the side (top or bottom) from which the vortex has shed as  $\eta$  goes to zero*. The resulting correlation between the vortex size, formation point, separation

point, and stagnation point will lead to a time dependence proportional to the square root of time,  $\propto \sqrt{t}$ , for each of these inputs.

$$\begin{aligned}
\eta_t &= \sqrt{\alpha \frac{U\Delta}{2\pi} t_t} & \eta_b &= \sqrt{\alpha \frac{U\Delta}{2\pi} t_b} \\
x_{fp_t} &= x_{fp_o} + \sqrt{\frac{\delta x^2}{T_s} t_t} & x_{fp_b} &= x_{fp_o} + \sqrt{\frac{\delta x^2}{T_s} t_b} \\
\theta_{sp_t} &= \theta_{sp_{t_o}} + \sqrt{\frac{\delta \theta^2}{T_s} t_t} & \theta_{sp_b} &= \theta_{sp_{b_o}} - \sqrt{\frac{\delta \theta^2}{T_s} t_b} \\
\theta_{st} &= \sqrt{\frac{\delta \theta^2}{T_s} t_t} - \sqrt{\frac{\delta \theta^2}{T_s} t_b}
\end{aligned} \tag{4.20}$$

As stated above, the time input into the parameter goes from  $t = 0$  to  $t = T_s$  and back to  $t = 0$ . In the future, the time at which the vortex is shed can become a physically based computation. For now, however,  $T_s$  will be input as  $1/f_s$ , which is calculated from the Strouhal number  $St = 0.21$ . Also, the time input will be shifted by half a period for the bottom parameters versus the top parameters.

$$\begin{aligned}
t_t &= t - \text{floor} \left( \frac{t}{T_s} \right) T_s \\
t_b &= (t + T_s/2) - \text{floor} \left( \frac{(t+T_s/2)}{T_s} \right) T_s
\end{aligned} \tag{4.21}$$

In the above equations, *floor* “rounds the elements...to the nearest integers towards minus infinity” and is a built in function of the computational software (MathWorks 2006).

Figures 4.16 to 4.21 show the responses to the inputs shown in 4.12 with the following values.

$$\begin{aligned}
x_{fp_o} &= 0 & \delta x &= 2R \\
\theta_{sp_{t_o}} &= 4\pi/9 & \delta \theta &= \pi/18 & \theta_{sp_{b_o}} &= -4\pi/9
\end{aligned} \tag{4.22}$$

$$\begin{aligned}
0.01 &\leq U \leq 2m/s & m &= 10kg/m & k &= 100N/m^2 \\
\rho &= 1000kg/m^3 & D &= 0.1m & \Delta &= D/100m \\
c &= 5Ns/m^2 & \nu &= 1e-6m^2/s & \alpha &= 0.25
\end{aligned} \tag{4.23}$$

Already, there is an increased complexity visible in Figures 4.16 to 4.18 over Figures 4.6 to 4.8, especially in the maximum frequency of response. However, lock-in and a range of synchronization are still present, and as long as there is lock-in, the forced vortex shedding frequency is already allowing for distinct vortex shedding modes to appear, i.e., if the cylinder is responding at  $f_n$ , and the shedding frequency is  $f_s = 2f_n$ , then the resulting vortex shedding mode would be two vortices per side per cycle, named 2P.

An interesting and promising feature is the fact that although the input signal is a periodic square-root of time signal, the response of the cylinder motion appears more like a sinusoidal response. This indicates that the nonlinearity of the model promises to allow for the body to respond in the nature found in experimental results.

#### 4.4 Vortex Shedding Criteria

##### 4.4.1 Critical Energy

Up to this point, the vortex shedding has been forced at the Strouhal period,  $T_s$ . However, once the cylinder is moving, it no longer follows the Strouhal trend. The vortices must be allowed to shed without forcing, and the model must react accordingly. Therefore, any sort of forced periodic input is no longer useful. The Strouhal period will not be used as a time input. Instead, a physical input will be used. Based on what is known from experimental results and basic physical intuition, two shedding criteria will be used: the influence of cylinder velocity  $\dot{y}$  and the influence of the free-stream velocity  $U$  on the energy of the attached vortices.

First, knowing at what point a vortex will have shed without the motion of the cylinder, a critical kinetic co-energy for the vortex at the moment that shedding begins can be found. Preliminary estimates can be found using the linear velocity

profile of the feeding shear layer. Critical energy will be denoted by  $T_{crit}$ .

$$T_{KV} = \frac{\pi\rho\eta^2U^2}{4} \quad (4.24)$$

For the case of the stationary cylinder, it is known that the vortex sheds at time  $T_s$ , and the growth of the vortex was given above. A critical vortex radius  $\eta_{crit}$  can then be given, and a critical energy can then be found.

$$\eta_{crit} = \sqrt{\alpha \frac{U\Delta}{2\pi} T_s} \quad (4.25)$$

$$T_{crit} = \frac{\pi}{4} \rho U^2 \eta_{crit}^2 \quad (4.26)$$

$$T_{crit} = \frac{\alpha}{8} \rho \Delta T_s U^3 \quad (4.27)$$

With the entire system moving with the cylinder velocity  $\dot{y}$ , the energy is a good choice of shedding criteria. The non-dimensional critical energy,  $T_{crit}/(\rho D^2 U^2)$ , becomes only a function of the Strouhal number. If the Strouhal number is given as a function of the Reynolds number, then follows the critical energy as a function of Reynolds number. This is a satisfying relationship, since it is known that  $Re$  defines much of the VIV problem. The result of using this  $T_{crit}$  as the shedding criteria is shown in Figures 4.26 to 4.33. The most promising change in the results here is the fact that there is no longer a gap around a reduced velocity of  $U^* = 10$  due to the amplitude of oscillation heading towards infinity. These amplitudes, as a result of critical shedding rather than forced shedding, have come down and are almost in line with the other portions of the range of synchronization.

No matter what velocity profile is used, the critical values always have the same proportionality.

$$\eta_{crit} \propto \sqrt{\alpha U \Delta T_s} \quad (4.28)$$

$$T_{crit} \propto \alpha \rho U^3 \Delta T_s \quad (4.29)$$



The energy of the vortex for the case of the moving cylinder for comparison against the shedding criteria is given as follows. When  $T_{KV} \geq T_{crit}$ , as given in Equation 5.27, the vortex sheds.

$$T_{KV} = \frac{\pi}{4} \rho \eta^2 \left( \underbrace{U^2}_{\text{vorticity}} + \underbrace{2\dot{y}^2}_{\text{cylinder motion}} \right) \quad (4.30)$$

The current approximations force the wake to move with the same velocity as the cylinder. As a first approximation, this is appropriate. However, from experimental visualizations, it is known that the wake becomes exposed as its motion lags behind that of the cylinder. As a result, vortices may also be shed prior to reaching the critical energy due to the presence of the free-stream encountering the attached vortices. The effect can also be approximated by an increase in energy due to the position of the cylinder in its trajectory. The effective attached vortex energy can be calculated from a weighted sum of that already found from the vortex moving with the cylinder superimposed with a component that results from the vortex moving with the free-stream velocity. This is the next step of the analysis.

## 4.5 Analysis of Results

### 4.5.1 Qualitative Discussion

It is easily recognizable that there are several key VIV components already present even without a complete model. A range of synchronization is easily recognizable, beginning just before the natural frequency and decaying in amplitude slowly above the natural frequency. The range of synchronization response shows characteristics of an upper branch and lower branch. It is hypothesized that further refinement of the model will lead to more definable VIV features in the range of synchronization.

In addition to the synchronization, lock-in of the response frequency is obvious. In addition, there is a visible over-reach at the beginning of lock-in, a characteristic of

water and not air. This influences the idea that the model does account for influence of the fluid, most likely the density of water since that is the most prolific term. In addition, when the mass is varied, particularly at very low mass ratios, there are obvious differences in the frequency of response of the cylinder at lock-in. This is illustrated best by comparing Figure 4.33 with the experimentally-derived results of Govardhan and Williamson (2000) shown in Figure 2.3. It becomes obvious that the mathematical model incorporates this recently described feature of VIV, where not only is the frequency at lock-in dependent on the mass ratio for very low mass ratios  $m^* < 1$ , but the slope approaching the frequency at lock-in also is varied based on the mass ratio. These two features are showed in both the mathematical model developed here and the experimental results of Govardhan and Williamson (2000)

With more refinement of the model, it is hypothesized that in addition to the range of synchronization and lock-in, there is a further possibility of capturing distinct vortex shedding modes. If this is possible, the model would establish itself as the obvious best choice for VIV above all other models. At that point, quantitative results would become most important, for all the major qualitative points would be apparent.

#### **4.5.2 Quantitative Discussion**

Although the model can be assessed as a success when examining the qualitative response, the quantitative response is lacking in several aspects. Moving through the progression of the inputs from the sinusoidal to the square root of time to the unforced shedding, the development of the upper and lower branches in the amplitude of response can be seen. However, the magnitude of this amplitude with respect to the diameter of the cylinder is several orders of magnitude off. The magnitude of  $A/D$  is expected to be on the order of 1, or  $10^0$ . However, all cases maintained

maximum amplitudes of response normalized by the diameter on the order of  $10^{-4}$ , four order of magnitude lower than what is expected, except for certain over-excited responses often tending towards infinity around reduced velocity  $U^* = 10$ . This is a surprising result considering how well the qualitative features of the  $A/D$  were met. It is believed that the energy is underestimated. However, it is not greatly underestimated. Tests have been performed where the forcing terms were artificially multiplied by a constant. It was observed that this artificial amplification in the forcing lead to a nonlinear increase in the amplitude of response. For instance, multiplying all forcing terms by 2 resulted in the amplitudes being multiplied by over 3. Multiplying the forcing terms by 3 amplified the amplitudes by over 22 from the case of no artificial amplification, with some points becoming over-excited and heading towards infinity. Finally, multiplying the forcing by 4 sent a sizable portion of the points towards infinity, making it difficult to assess the magnitude of the amplification of the amplitudes. Therefore, it is hypothesized that a small, physically based increase in the energy of the system can result in larger amplitudes, and achieving quantitative success with this model is possible.

For the phase shift between the forcing and the displacement, however, the quantitative results came out exactly as measured in experiments once the vortex shedding was unforced. This was not true for the cases of the sinusoidal and square-root of time inputs, but once the vortex was allowed to shed at a critical energy, the phase shift plot aligns perfectly with experimental results. This is very encouraging for several reasons. First, it shows that the model has great potential to capture a variety of VIV characteristics, already qualitatively demonstrating a range of synchronization followed by desynchronization, and now quantitatively capturing the phase shift at the region of lock-in. Second, with the development of a critical energy for vortex

shedding, this specific feature was captured. This suggests that the vortex shedding criteria is reasonable. In addition to leading to an appropriate phase shift plot, the vortex shedding criteria also proved to eliminate the over-excited amplitudes of response around a reduced velocity of 10, and in fact bring this region down to something similar to what has been defined in VIV as the lower branch.

Lock-in is a quantitative feature. Therefore, the fact that it can be observed in the plots already suggests quantitative success. For several cases, lock-in does not occur until reduced velocities higher than 5, where 5 is the value around which lock-in is expected to occur. However, it is obvious that damping and higher reduced mass ratios both have an effect on increasing reduced velocity at the point of lock-in. It is important at this point to revisit how the response frequency is determined. A peak from the Fast-Fourier Transform (FFT) energy spectrum is selected from a line plot for the frequency of response. For the cases in which the response frequency is around a certain value rather than directly at a certain value, this can be misleading. A better understanding of this can be found by studying the energy spectrum outputs that are shown in Figures 4.4, 4.14, and 4.24 for the cases of sinusoidal, square-root of time, and critical energy shedding, respectively. It is proposed that a bar graph may be better at determining the frequency of response rather than a line graph, therefore encapsulating the cases in which the response is around but not exactly at one point. This will be examined further in future work. It is hypothesized that this modification can lead to lock-out in cases in which lock-out is not currently observed.

Many modifications can therefore be made in order to better model the phenomenon of VIV as well as to better analyze the output. The next chapter will examine some of these modifications, many incorporating the Reynolds number dependence of characteristics and variables, and determine which show improvement

over the current unforced shedding model with linear velocity inputs. At this point, the standard or base-line for comparison is this model, and all improvements will be taken one at a time to determine if they are beneficial to the model or not.

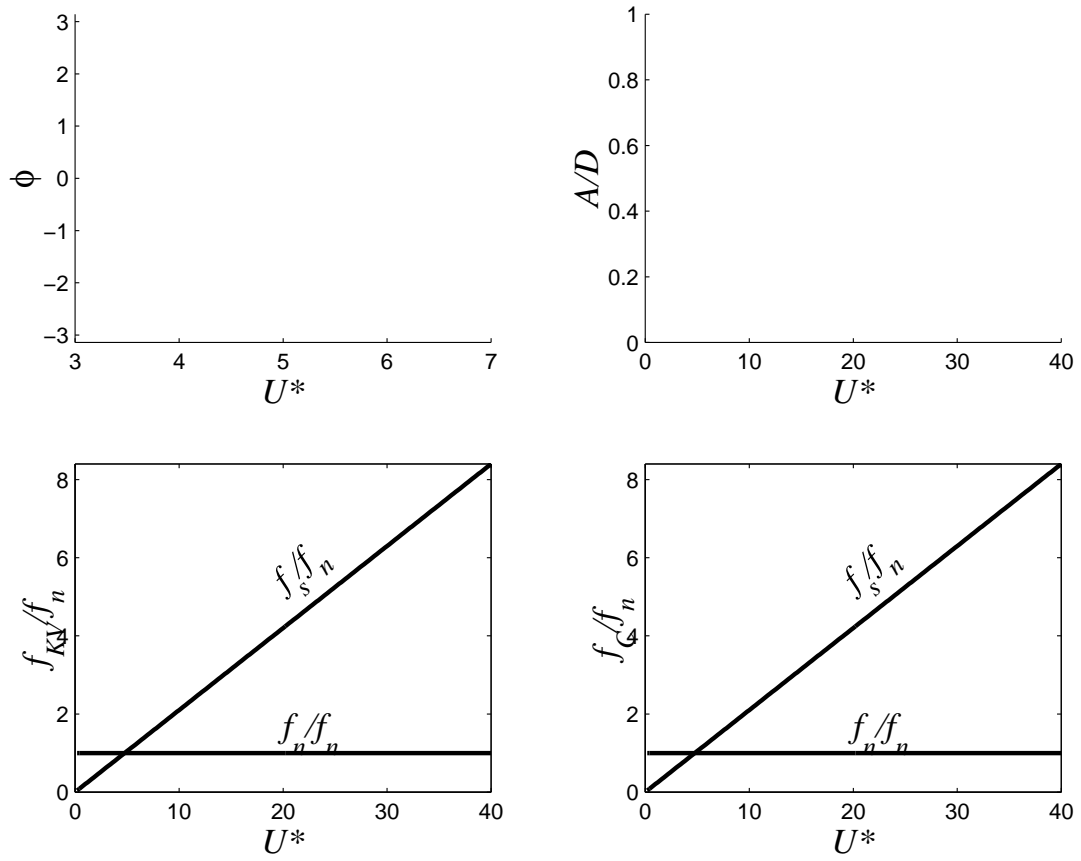


Figure 4.1: The axes for the plots that are used for examining numerical results of the developed model.

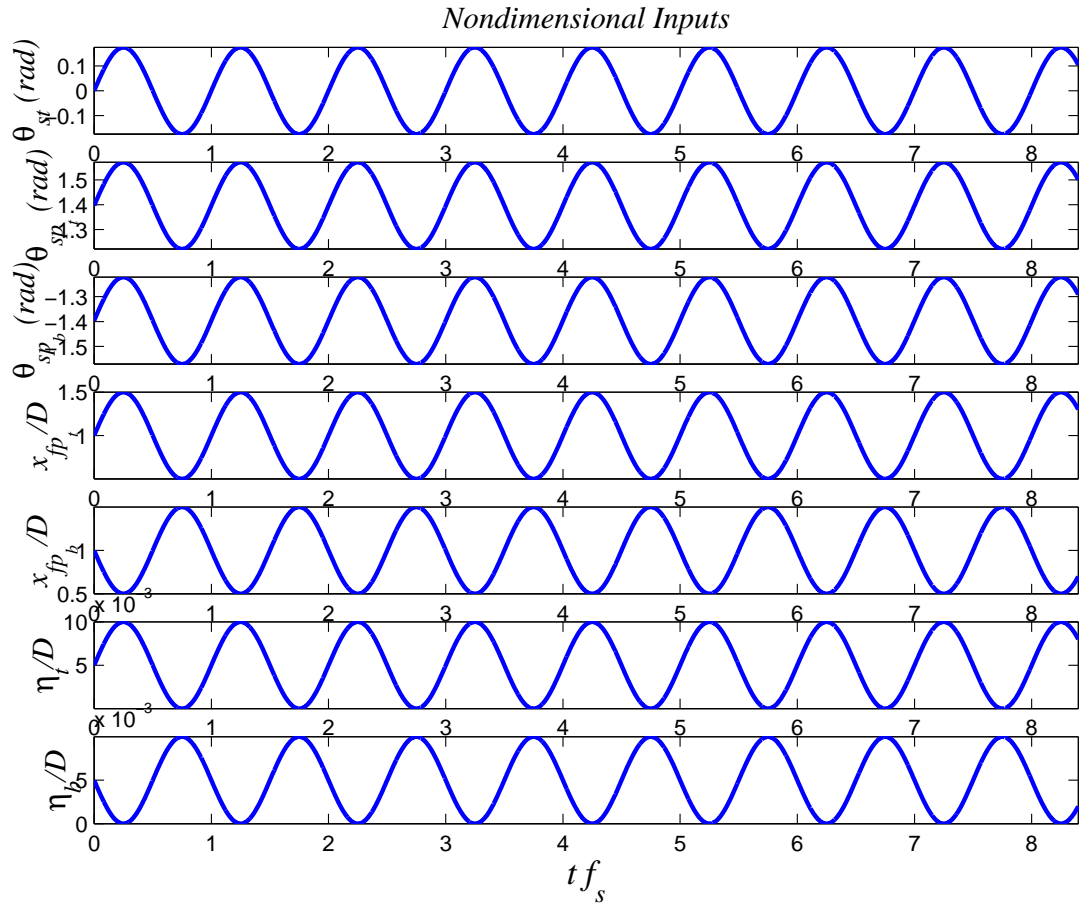


Figure 4.2: Sinusoidal time inputs for the stagnation point, top and bottom separation points, top and bottom formation points, and top and bottom attached vortex radii, where  $m^* = 1$ ,  $\zeta = 1$ ,  $f_n = 1$   $D = 0.1m$ , and  $2 \times 10^3 < Re < 4 \times 10^5$ .

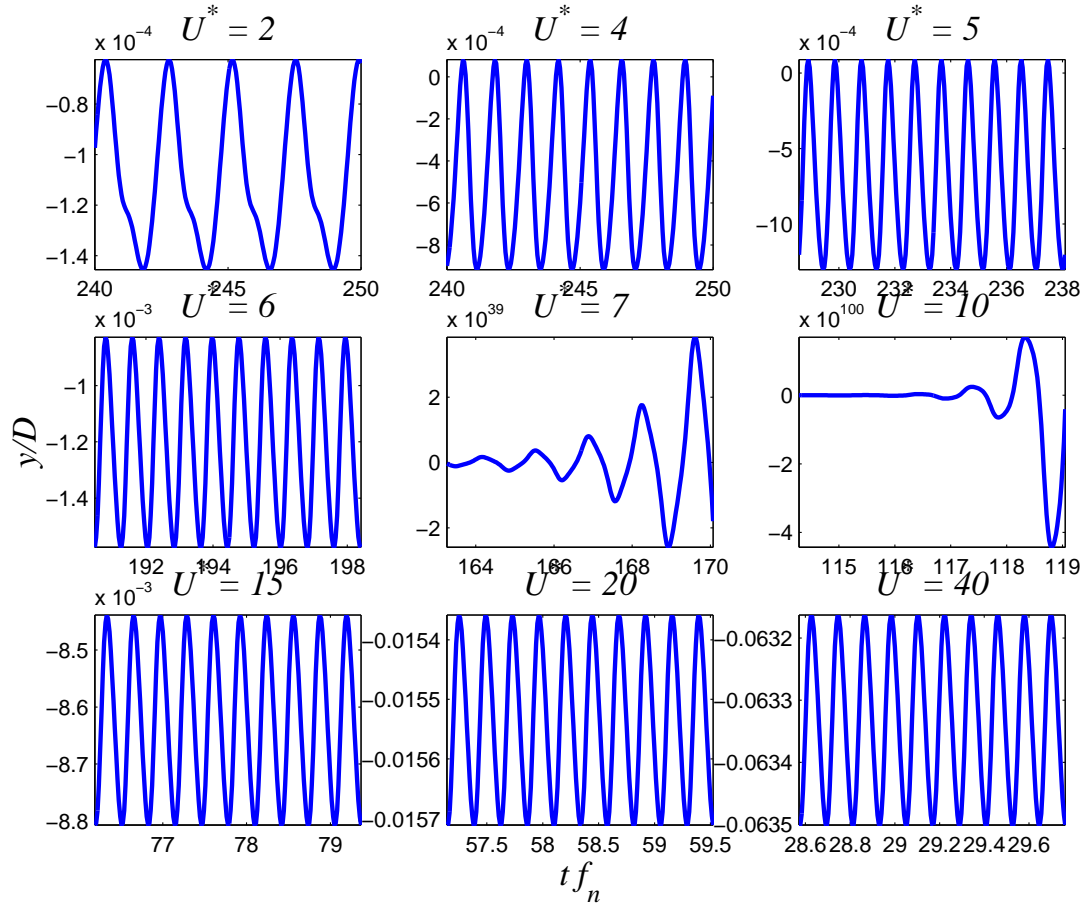


Figure 4.3: Cylinder displacement output from a sinusoidal time input for various reduced velocities, where  $m^* = 1$ ,  $\zeta = 1$ ,  $f_n = 1$ ,  $D = 0.1m$ , and  $2 \times 10^3 < Re < 4 \times 10^5$ .



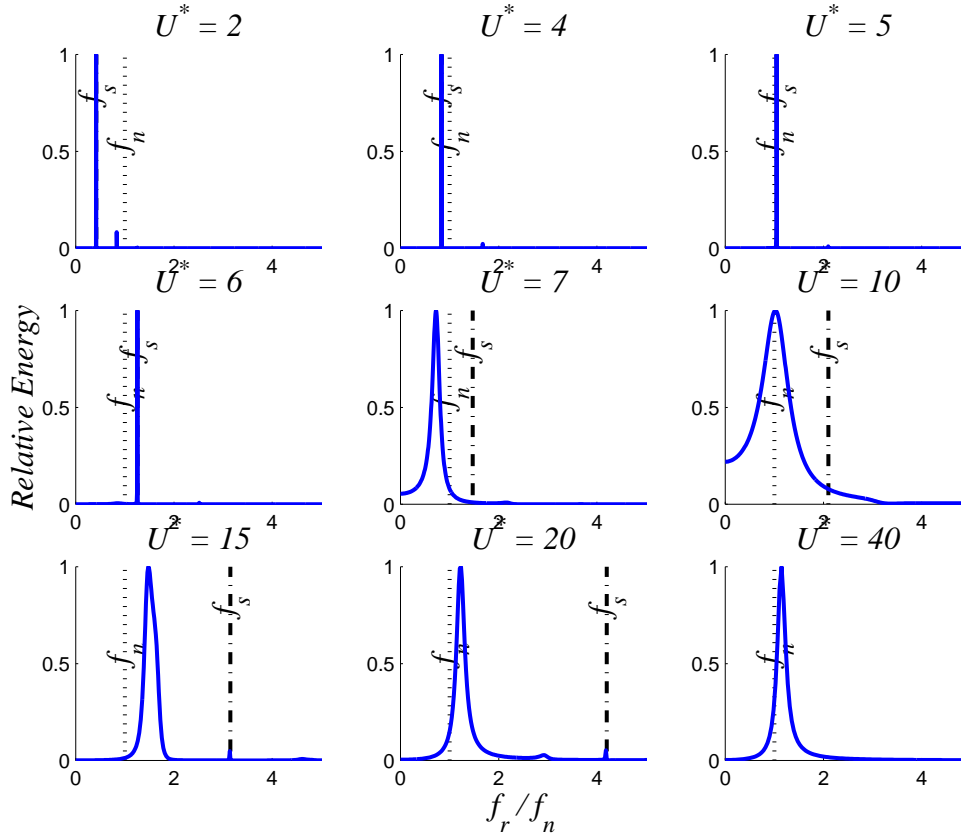


Figure 4.4: Cylinder displacement frequency energy spectrum from a sinusoidal time input for various reduced velocities, where  $m^* = 1$ ,  $\zeta = 1$ ,  $f_n = 1$ ,  $D = 0.1m$ , and  $2 \times 10^3 < Re < 4 \times 10^5$ .

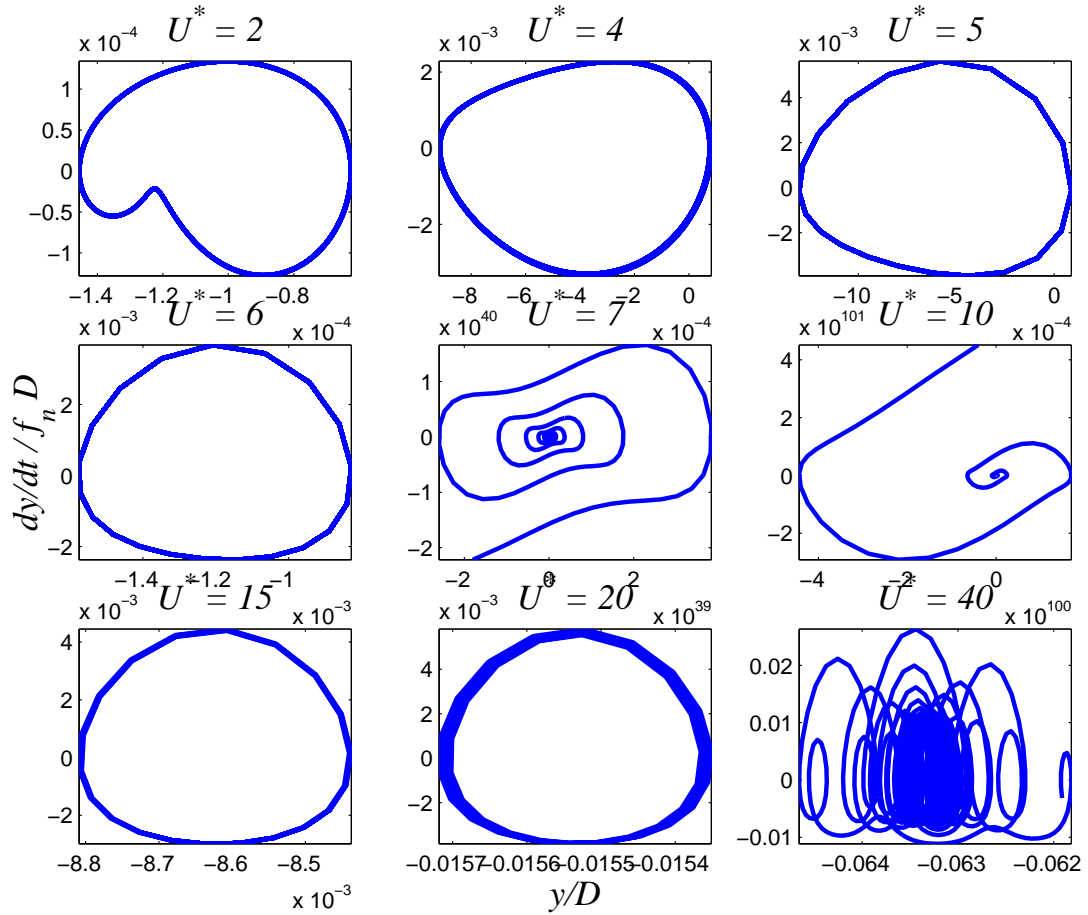


Figure 4.5: Cylinder displacement versus velocity phase plots from a sinusoidal time input for various reduced velocities, where  $m^* = 1$ ,  $\zeta = 1$ ,  $f_n = 1$ ,  $D = 0.1m$ , and  $2 \times 10^3 < Re < 4 \times 10^5$ .

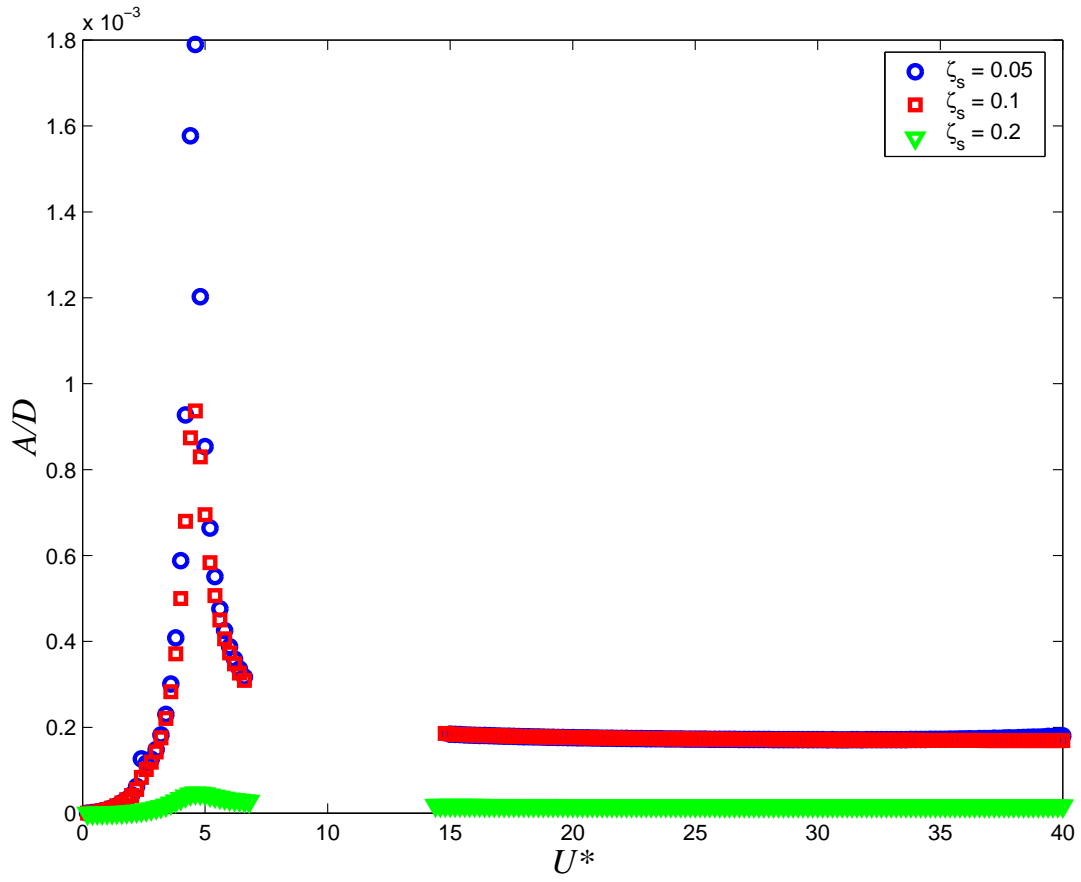


Figure 4.6: Cylinder amplitude response from a sinusoidal time input with varying damping coefficients for various reduced velocities, where  $m^* = 1$ ,  $f_n = 1$ ,  $D = 0.1m$ , and  $2 \times 10^3 < Re < 4 \times 10^5$ .

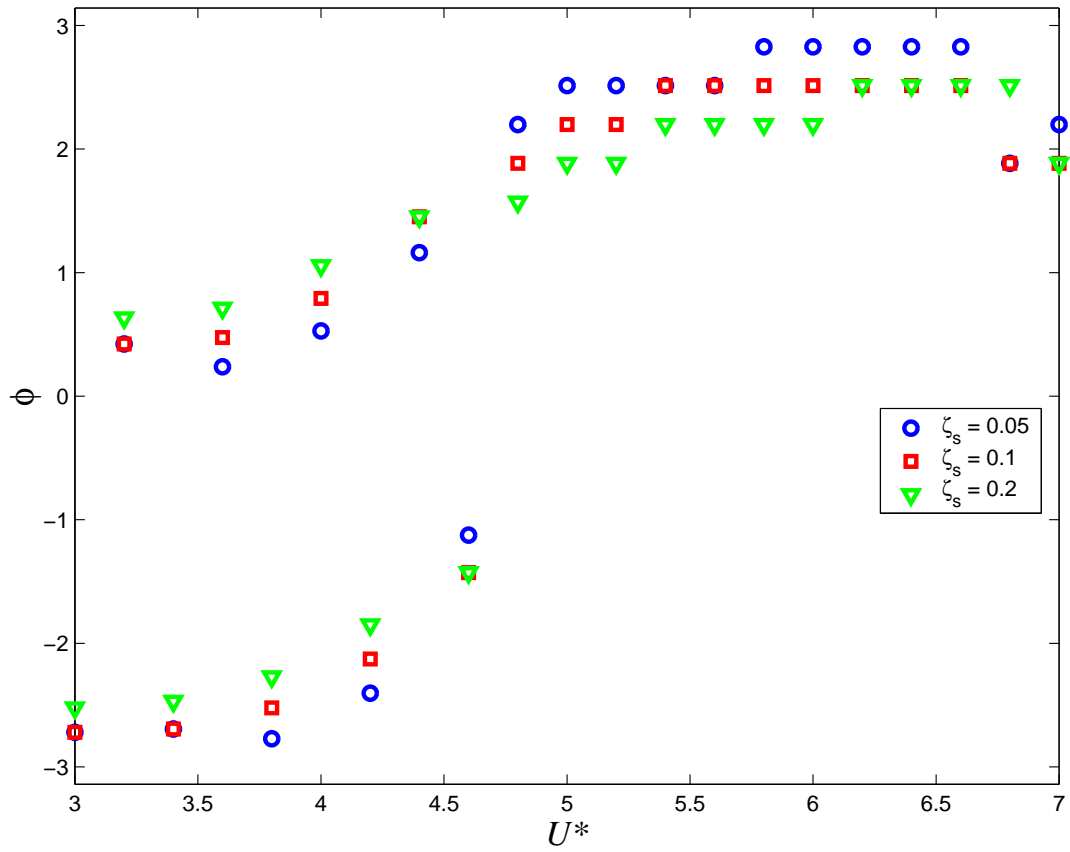


Figure 4.7: Cylinder phase-shift response from a sinusoidal time input with varying damping coefficients for various reduced velocities, where  $m^* = 1$ ,  $f_n = 1$ ,  $D = 0.1m$ , and  $2 \times 10^3 < Re < 4 \times 10^5$ .

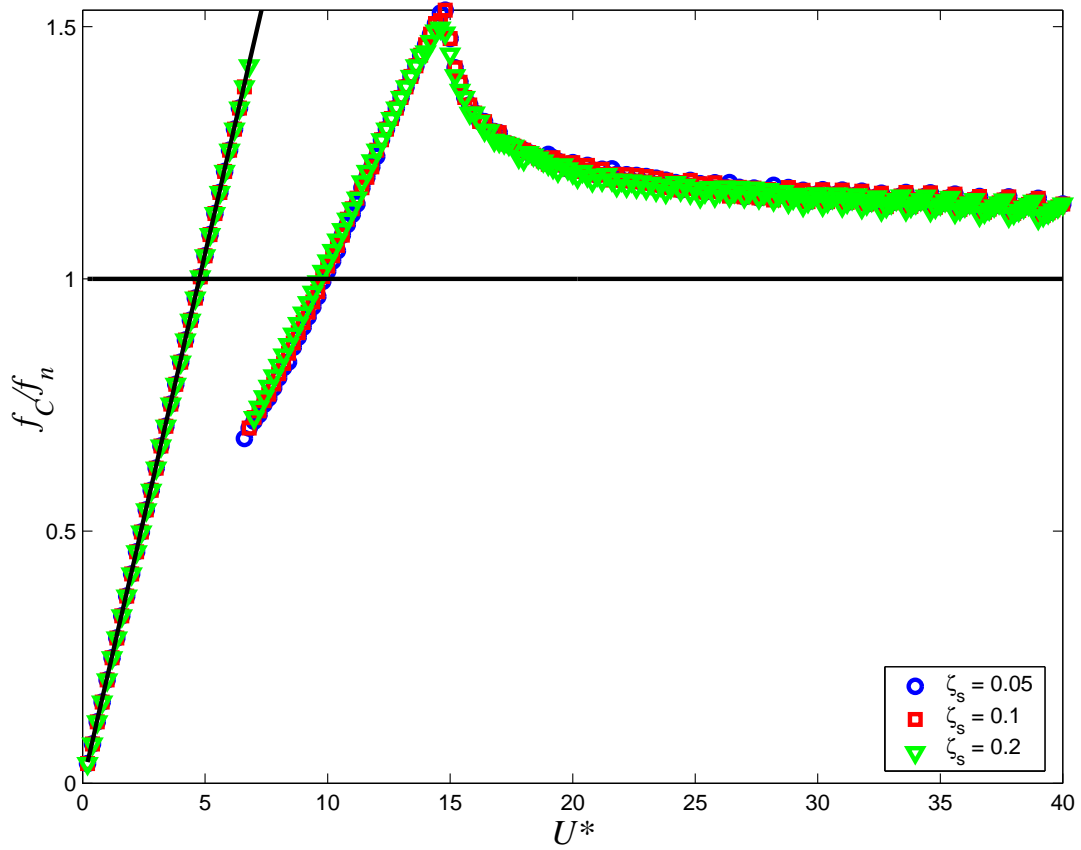


Figure 4.8: Cylinder peak-frequency response from a sinusoidal time input with varying damping coefficients for various reduced velocities, where  $m^* = 1$ ,  $f_n = 0.5679$  and  $D = 0.1m$ .

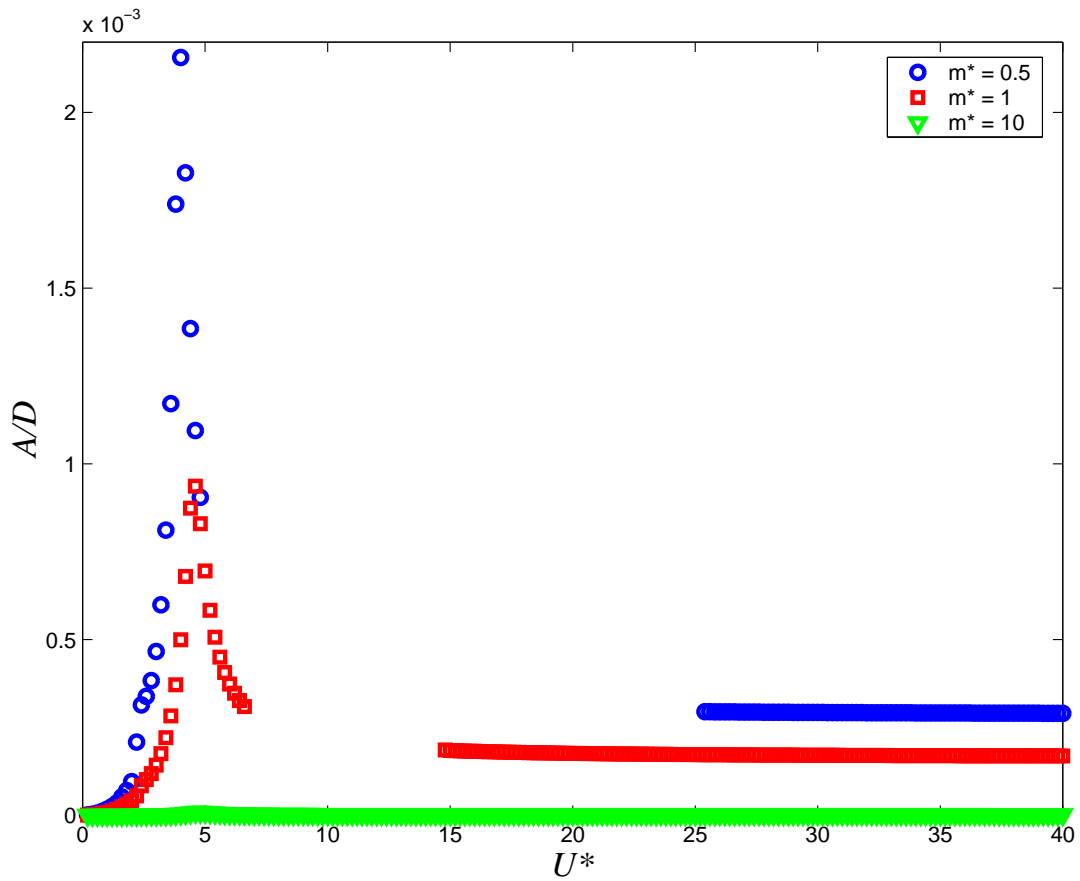


Figure 4.9: Cylinder amplitude response from a sinusoidal time input with varying damping coefficients for various reduced velocities.

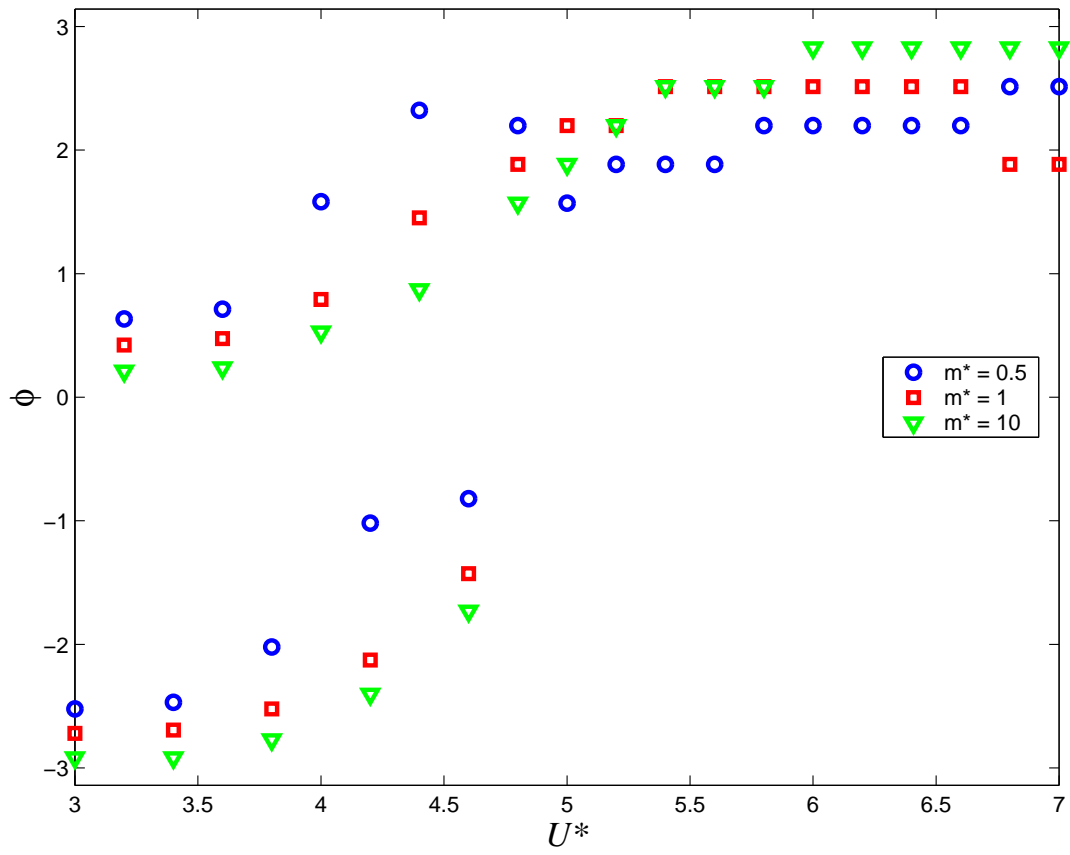


Figure 4.10: Cylinder phase-shift response from a sinusoidal time input with varying damping coefficients for various reduced velocities.

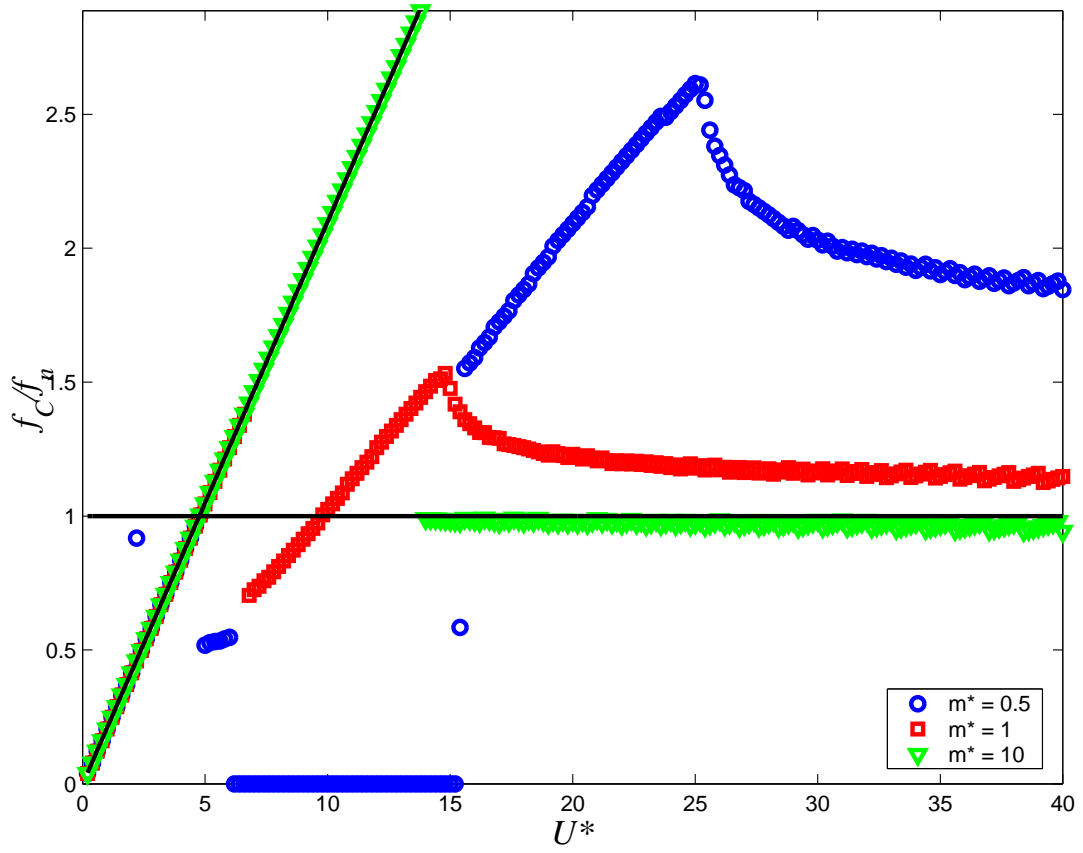


Figure 4.11: Cylinder peak-frequency response from a sinusoidal time input with varying damping coefficients for various reduced velocities.



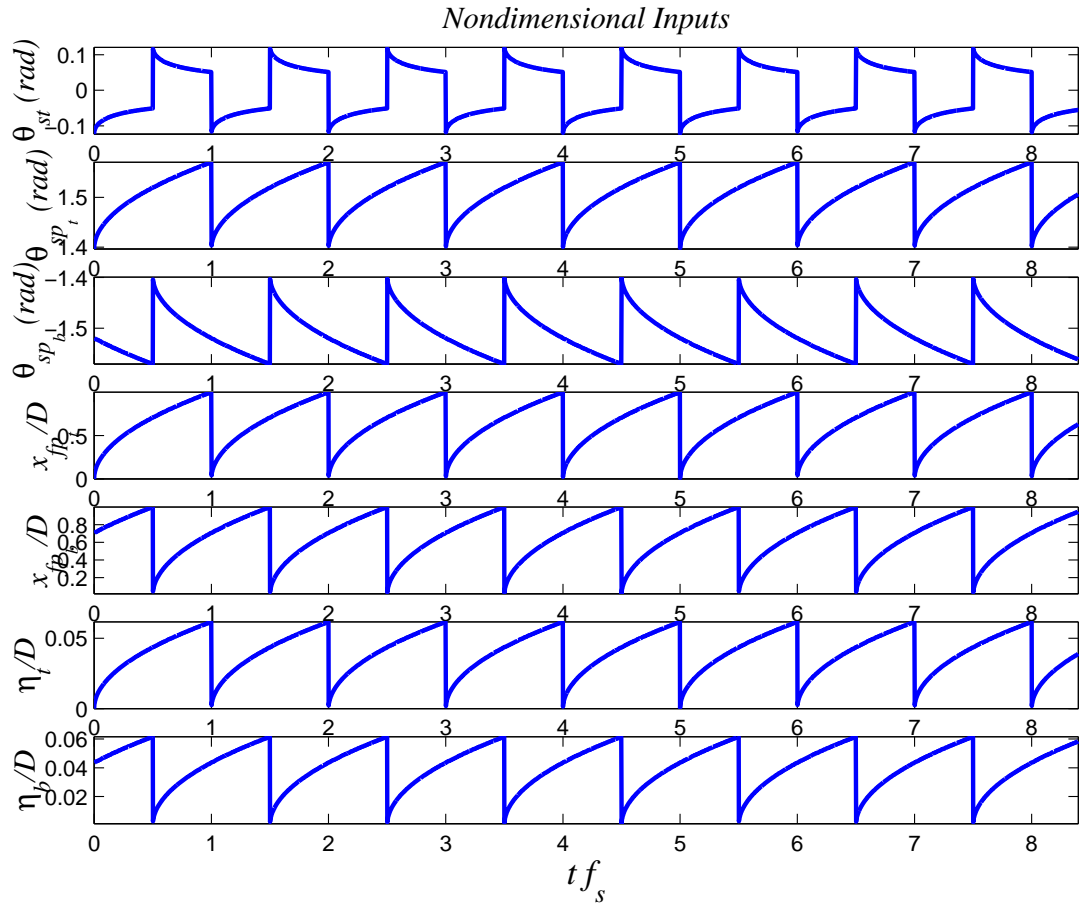


Figure 4.12: Square-root of time inputs for the stagnation point, top and bottom separation points, top and bottom formation points, and top and bottom attached vortex radii, where  $m^* = 1$ ,  $\zeta = 1$ ,  $f_n = 1$ ,  $D = 0.1m$ , and  $2 \times 10^3 < Re < 4 \times 10^5$ .

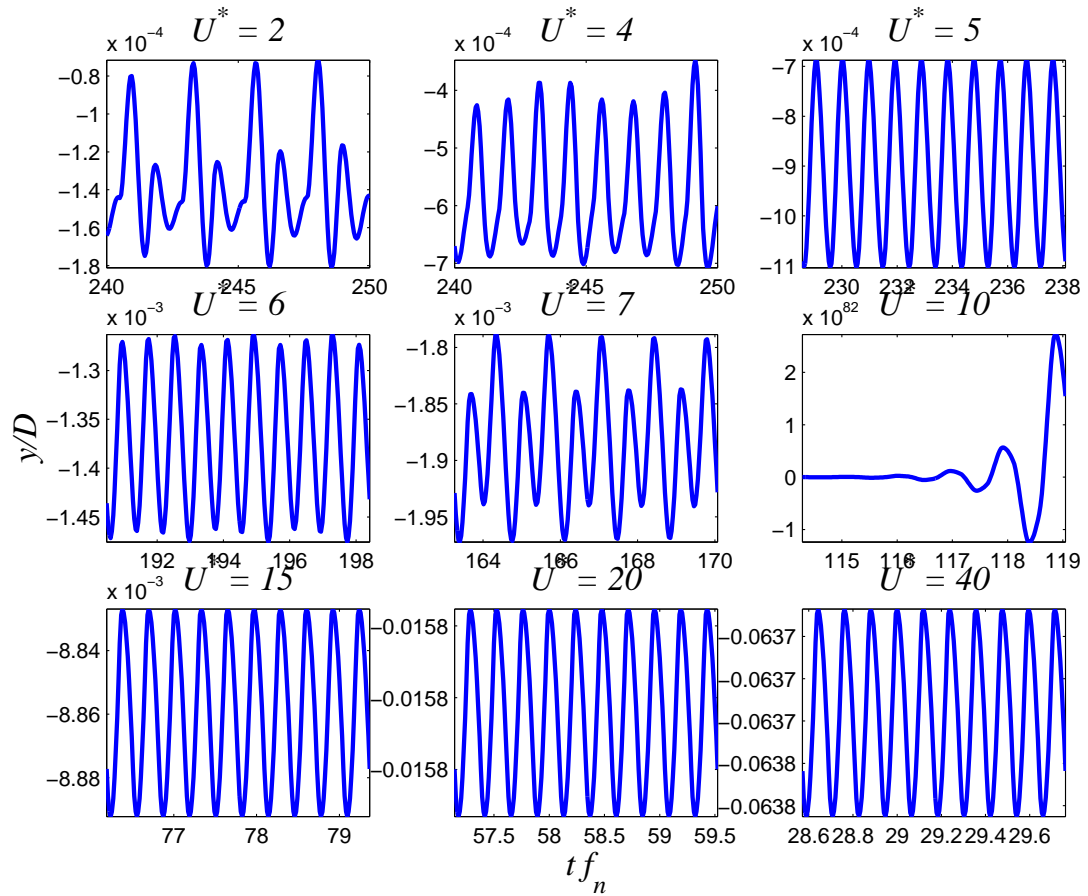


Figure 4.13: Cylinder displacement output from a square-root of time input for various reduced velocities, where  $m^* = 1$ ,  $\zeta = 1$ ,  $f_n = 1$ ,  $D = 0.1m$ , and  $2 \times 10^3 < Re < 4 \times 10^5$ .

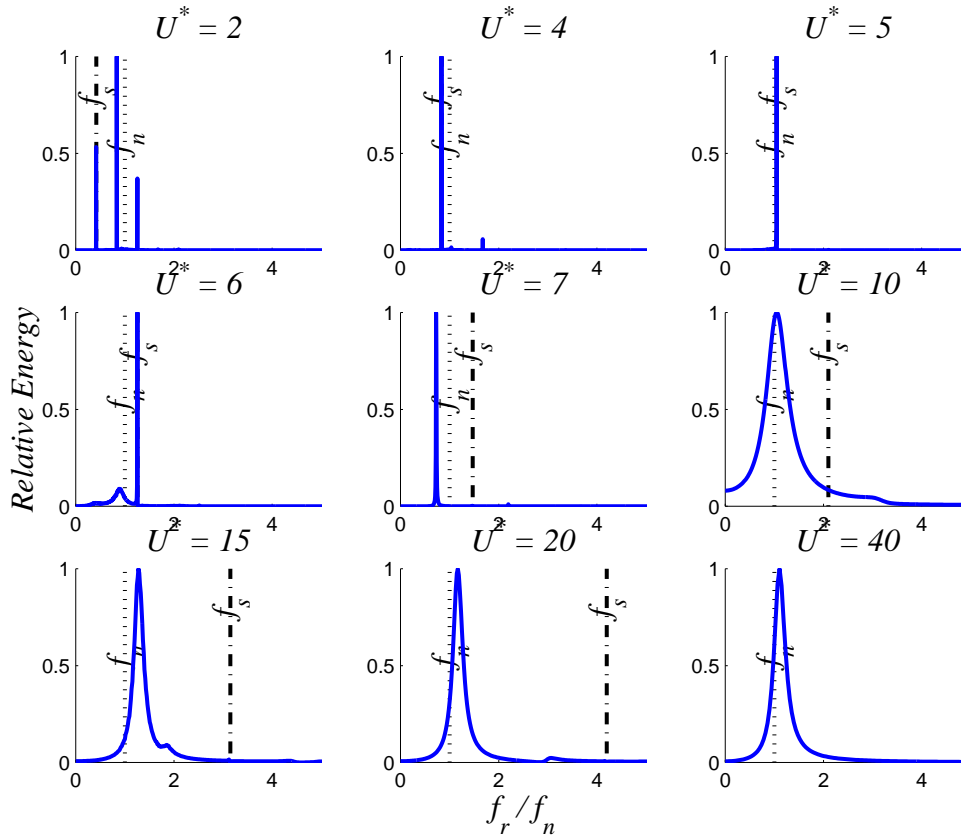


Figure 4.14: Cylinder-displacement frequency-energy spectrum from a square-root of time input for various reduced velocities, where  $m^* = 1$ ,  $\zeta = 1$ ,  $f_n = 1$ ,  $D = 0.1m$ , and  $2 \times 10^3 < Re < 4 \times 10^5$ .

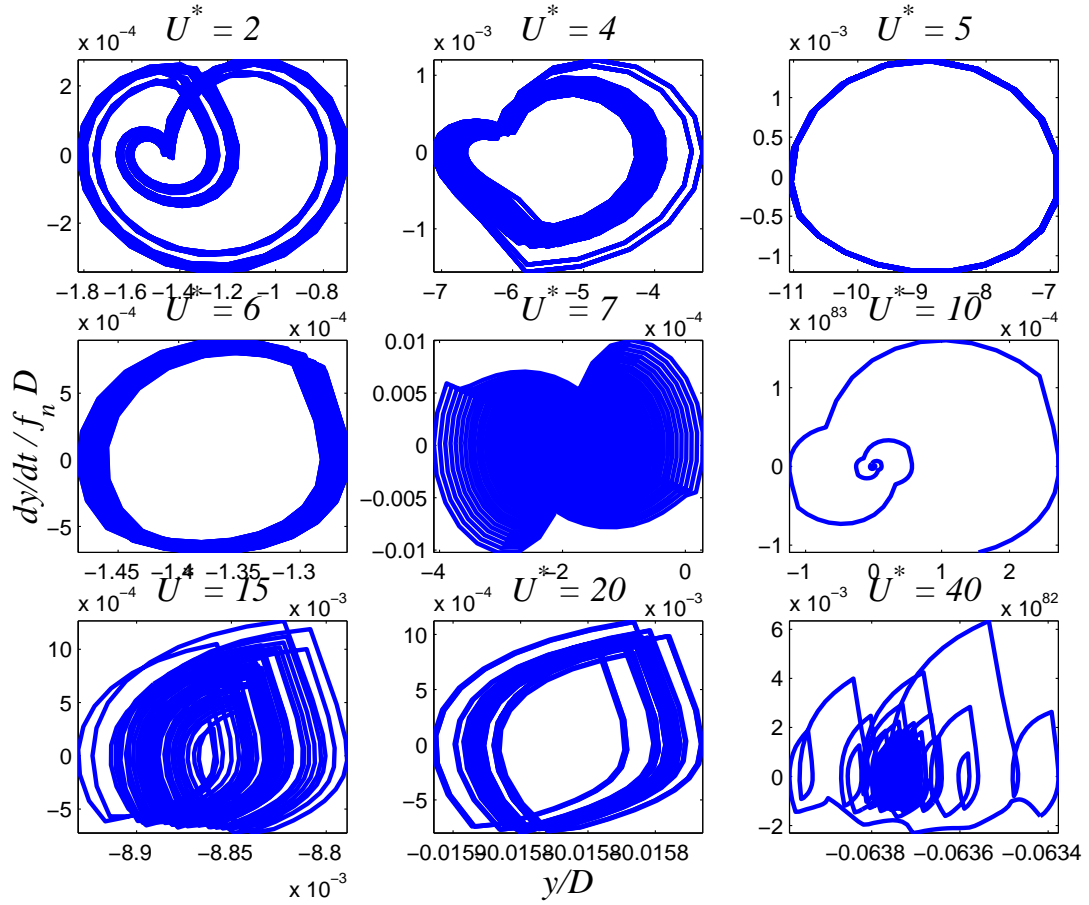


Figure 4.15: Cylinder displacement versus velocity phase plots from a square-root of time input for various reduced velocities, where  $m^* = 1$ ,  $\zeta = 1$ ,  $f_n = 1$ ,  $D = 0.1m$ , and  $2 \times 10^3 < Re < 4 \times 10^5$ .

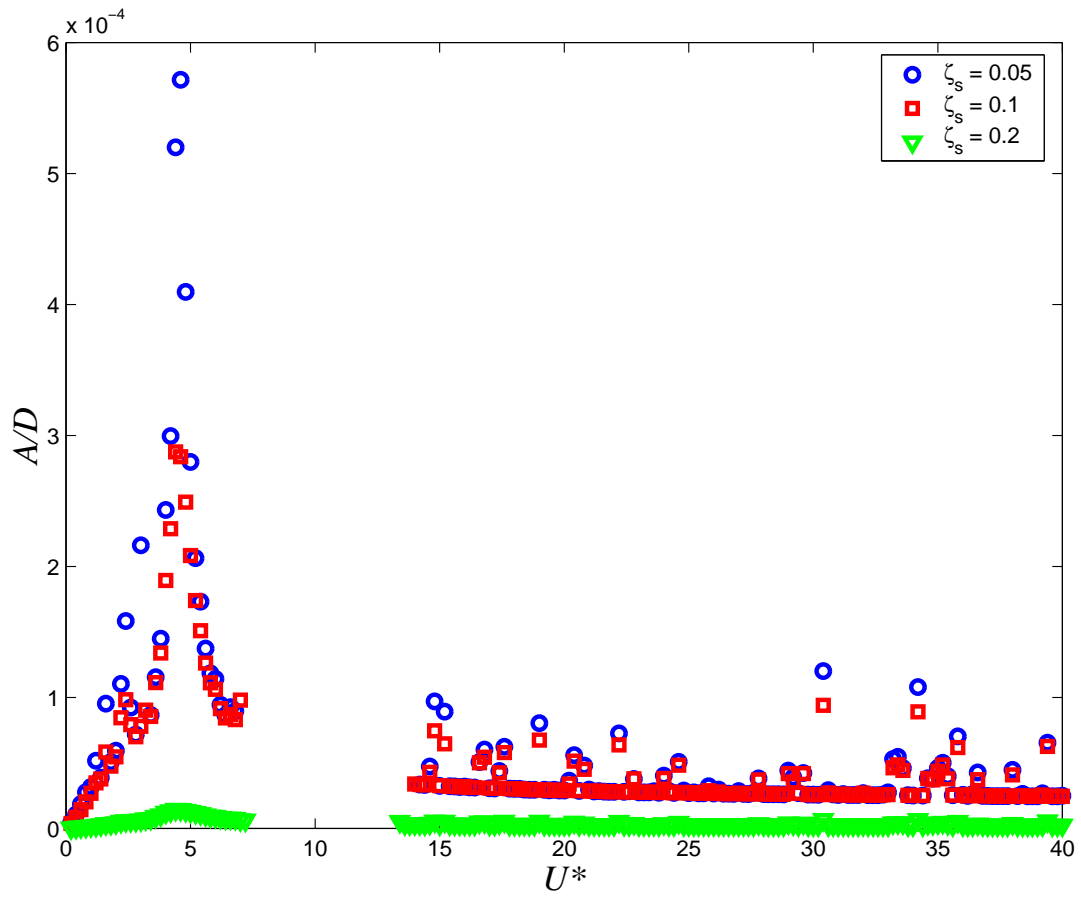


Figure 4.16: Cylinder amplitude response from a square-root of time input with varying damping coefficients for various reduced velocities, where  $m^* = 1$ ,  $f_n = 1$ ,  $D = 0.1m$ , and  $2 \times 10^3 < Re < 4 \times 10^5$ .

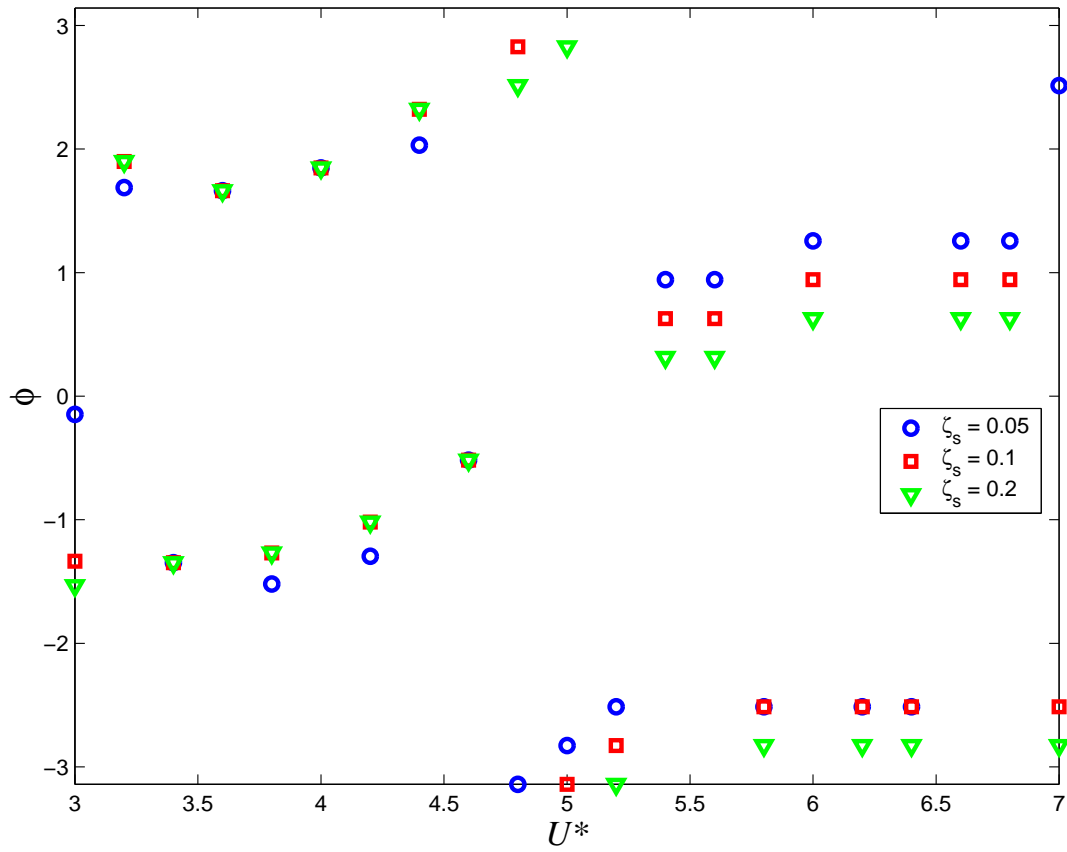


Figure 4.17: Cylinder phase-shift response from a square-root of time input with varying damping coefficients for various reduced velocities, where  $m^* = 1$ ,  $f_n = 1$ ,  $D = 0.1m$ , and  $2 \times 10^3 < Re < 4 \times 10^5$ .

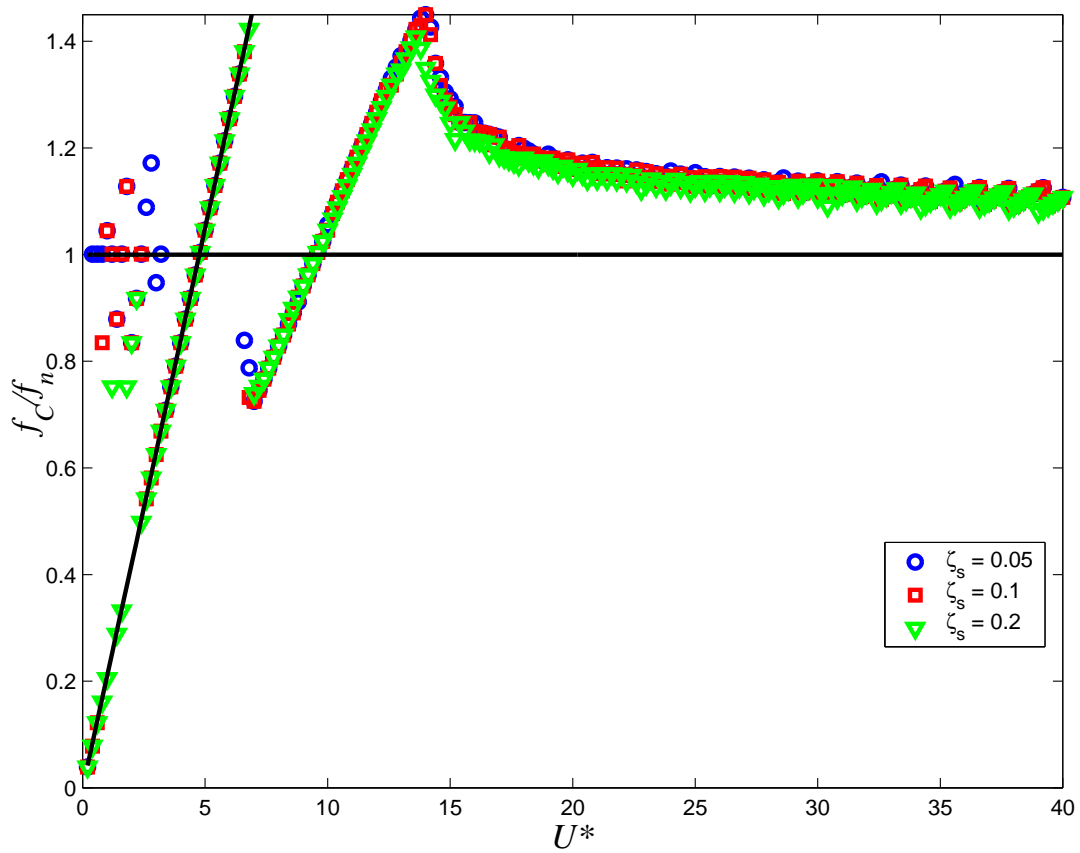


Figure 4.18: Cylinder peak-frequency response from a square-root of time input with varying damping coefficients for various reduced velocities, where  $m^* = 1$ ,  $f_n = 1$ ,  $D = 0.1m$ , and  $2 \times 10^3 < Re < 4 \times 10^5$ .

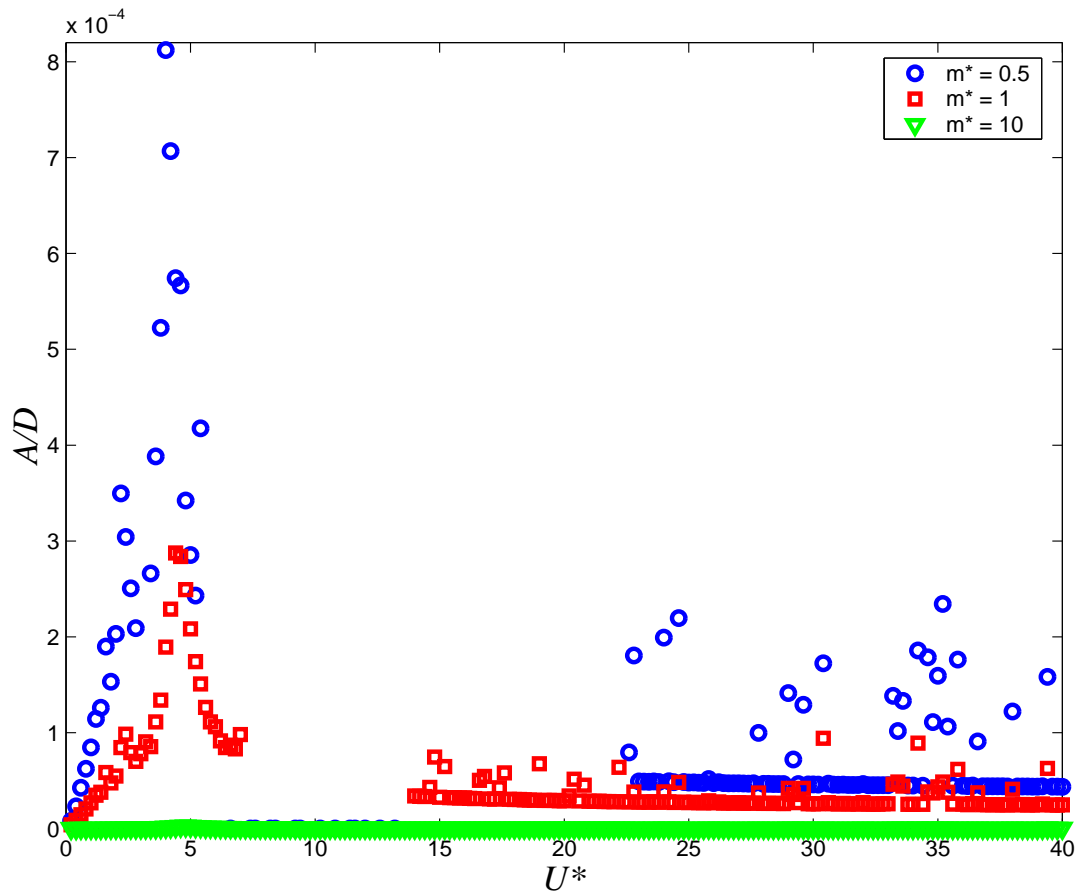


Figure 4.19: Cylinder amplitude response from a square-root of time input with varying damping coefficients for various reduced velocities.



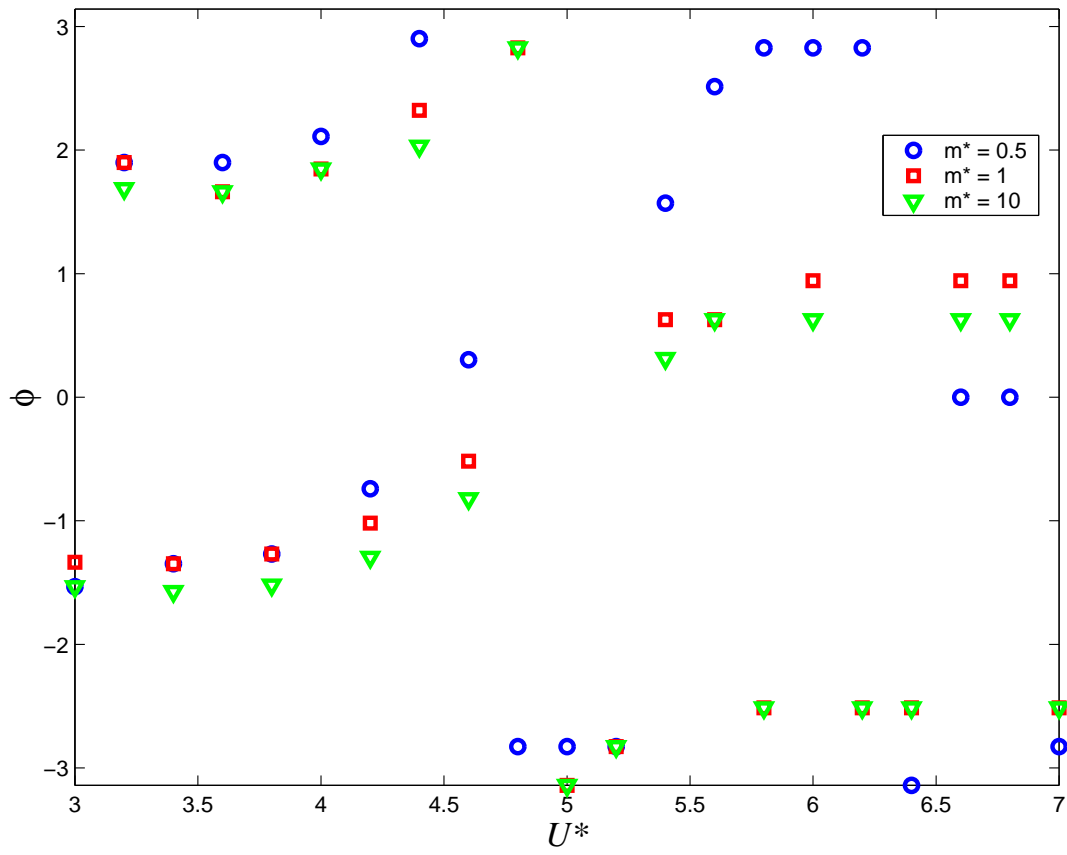


Figure 4.20: Cylinder phase-shift response from a square-root of time input with varying damping coefficients for various reduced velocities.

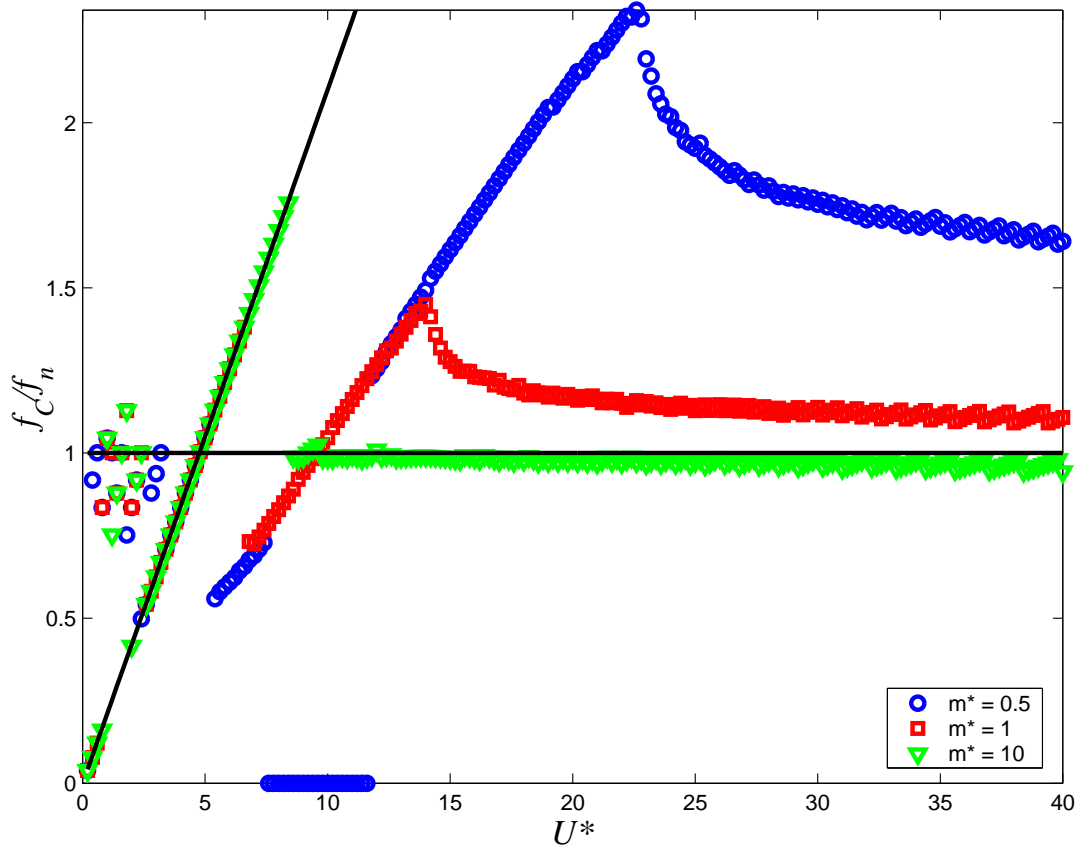


Figure 4.21: Cylinder peak-frequency response from a square-root of time input with varying damping coefficients for various reduced velocities.

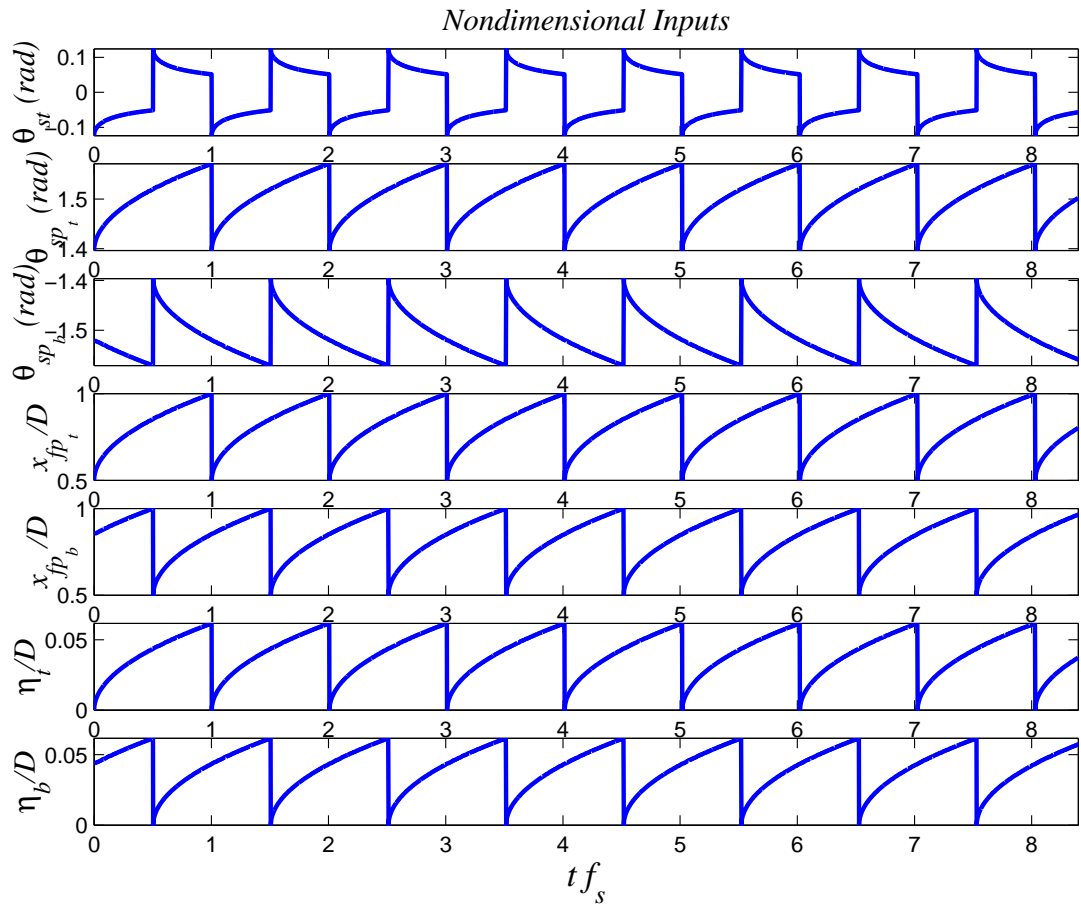


Figure 4.22: Square-root of time with critical energy shedding inputs for the stagnation point, top and bottom separation points, top and bottom formation points, and top and bottom attached vortex radii, where  $m^* = 1$ ,  $\zeta = 1$ ,  $f_n = 1$ ,  $D = 0.1m$ , and  $2 \times 10^3 < Re < 4 \times 10^5$ .

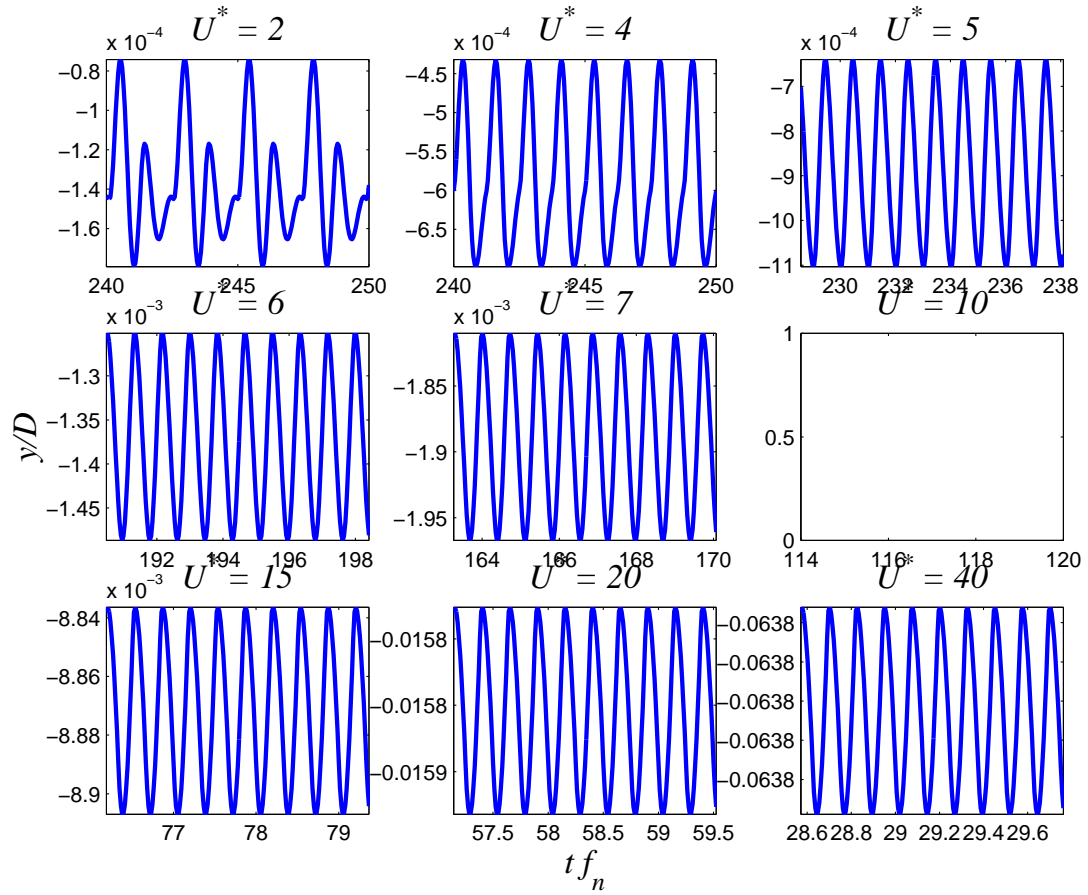


Figure 4.23: Cylinder displacement output from a square-root of time with critical energy shedding input for various reduced velocities, where  $m^* = 1$ ,  $\zeta = 1$ ,  $f_n = 1$ ,  $D = 0.1m$ , and  $2 \times 10^3 < Re < 4 \times 10^5$ .

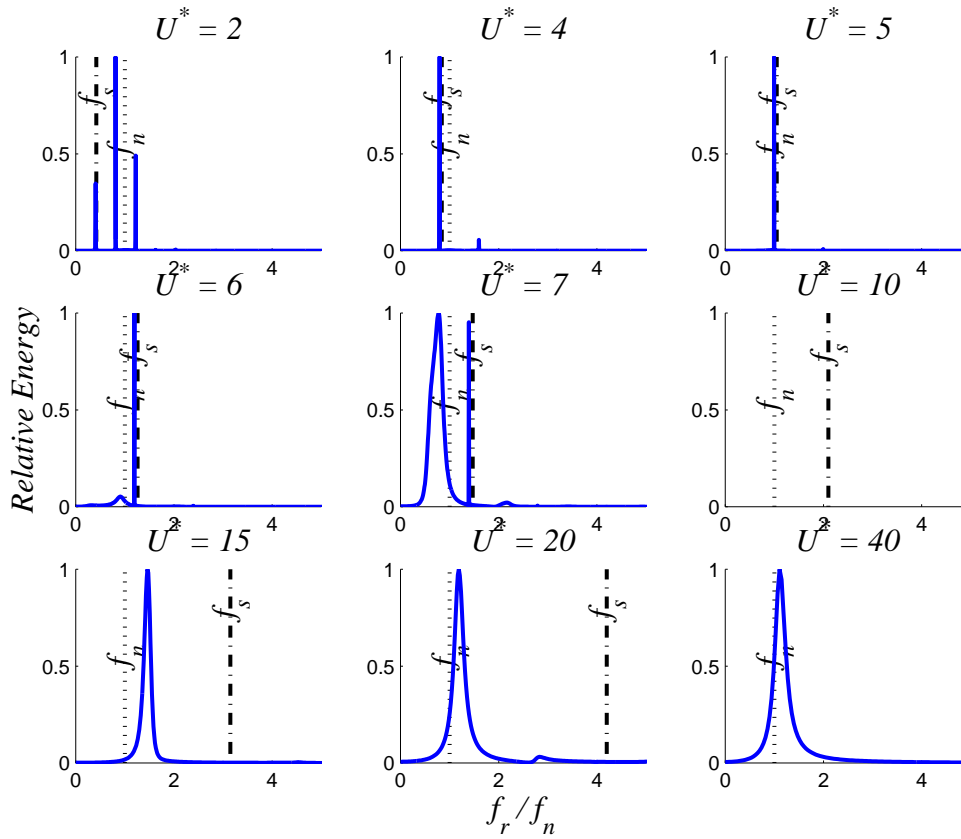


Figure 4.24: Cylinder-displacement frequency-energy spectrum from a square-root of time with critical energy shedding input for various reduced velocities, where  $m^* = 1$ ,  $\zeta = 1$ ,  $f_n = 1$ ,  $D = 0.1m$ , and  $2 \times 10^3 < Re < 4 \times 10^5$ .

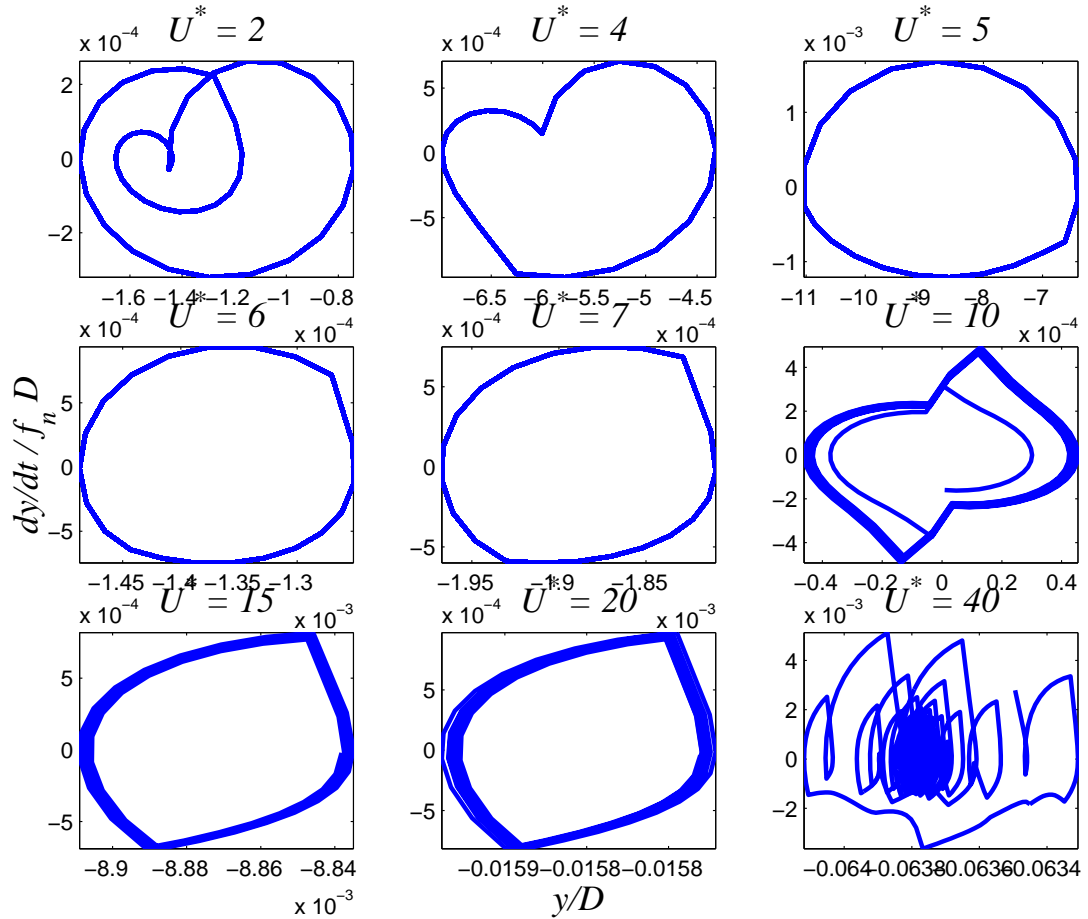


Figure 4.25: Cylinder displacement versus velocity phase plots from a square-root of time with critical energy shedding input for various reduced velocities, where  $m^* = 1$ ,  $\zeta = 1$ ,  $f_n = 0$ ,  $D = 0.1m$ , and  $2 \times 10^3 < Re < 4 \times 10^5$ .

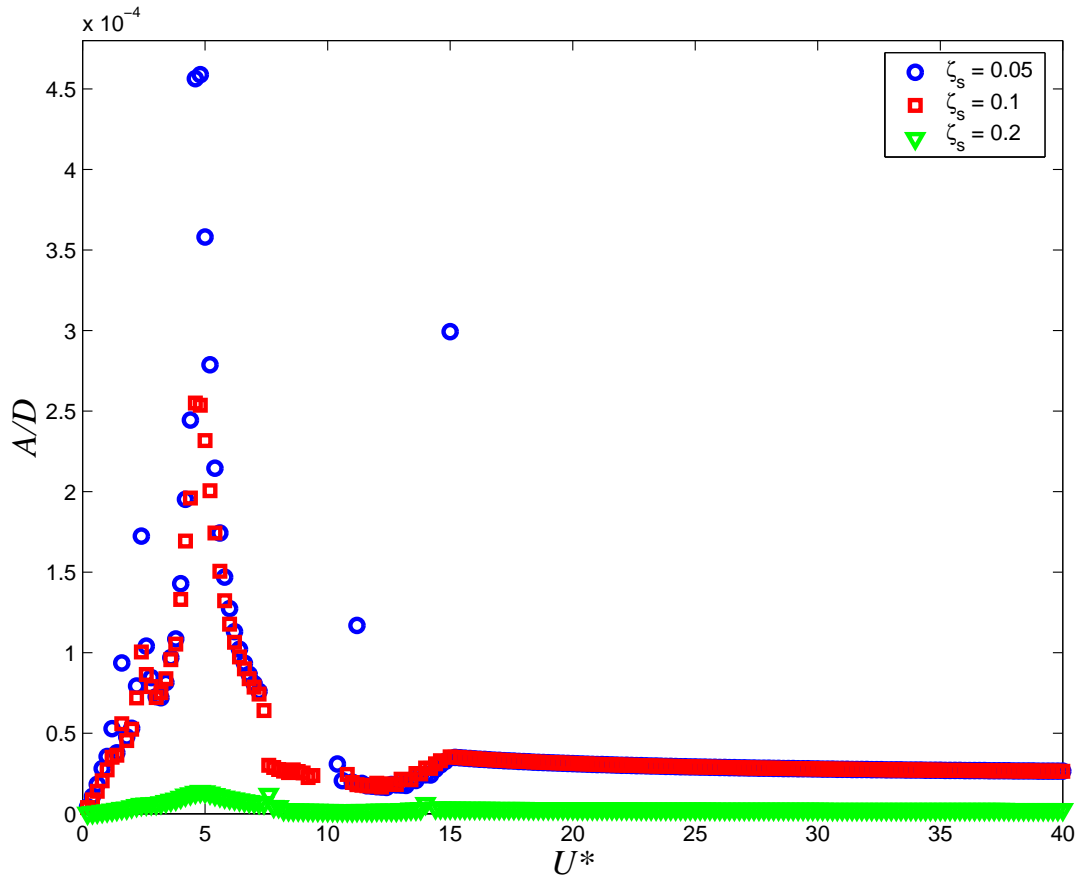


Figure 4.26: Cylinder amplitude response from a square-root of time with critical energy shedding input with varying damping coefficients for various reduced velocities, where  $m^* = 1$ ,  $f_n = 1$ ,  $D = 0.1m$ , and  $2 \times 10^3 < Re < 4 \times 10^5$ .

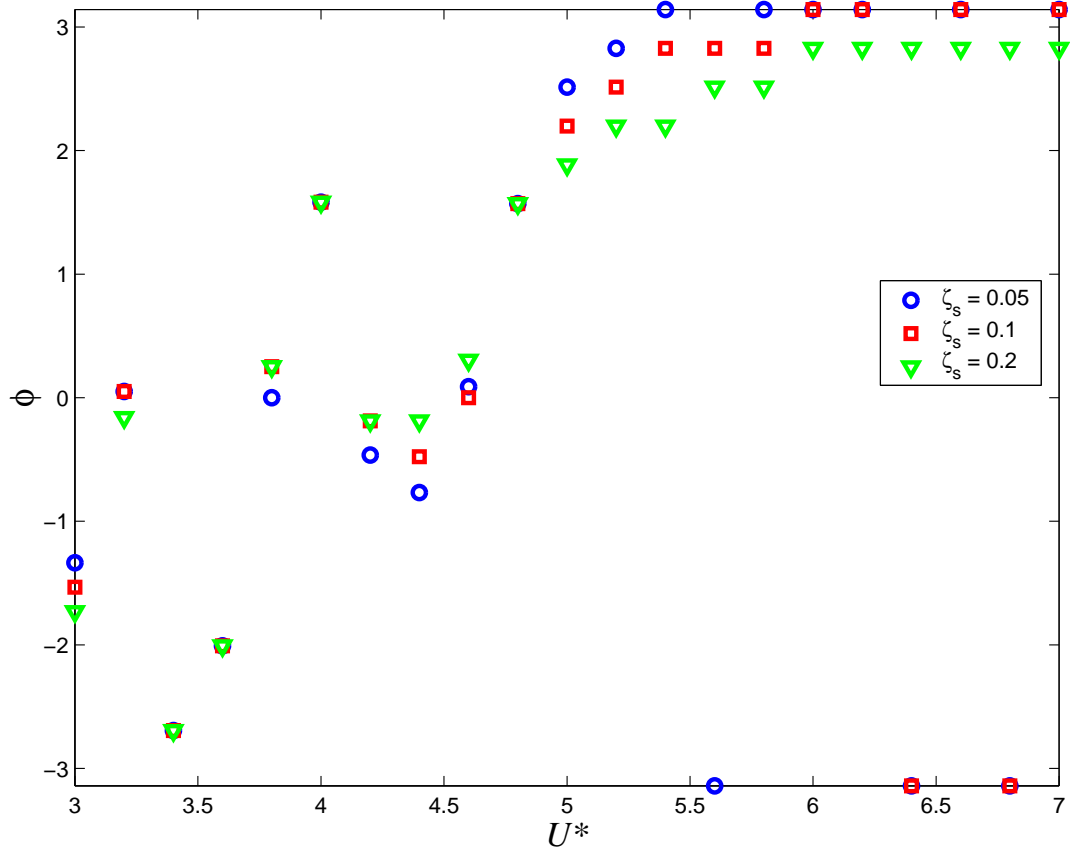


Figure 4.27: Cylinder phase-shift response from a square-root of time with critical energy shedding input with varying damping coefficients for various reduced velocities, where  $m^* = 1$ ,  $f_n = 1$ ,  $D = 0.1m$ , and  $2 \times 10^3 < Re < 4 \times 10^5$ .



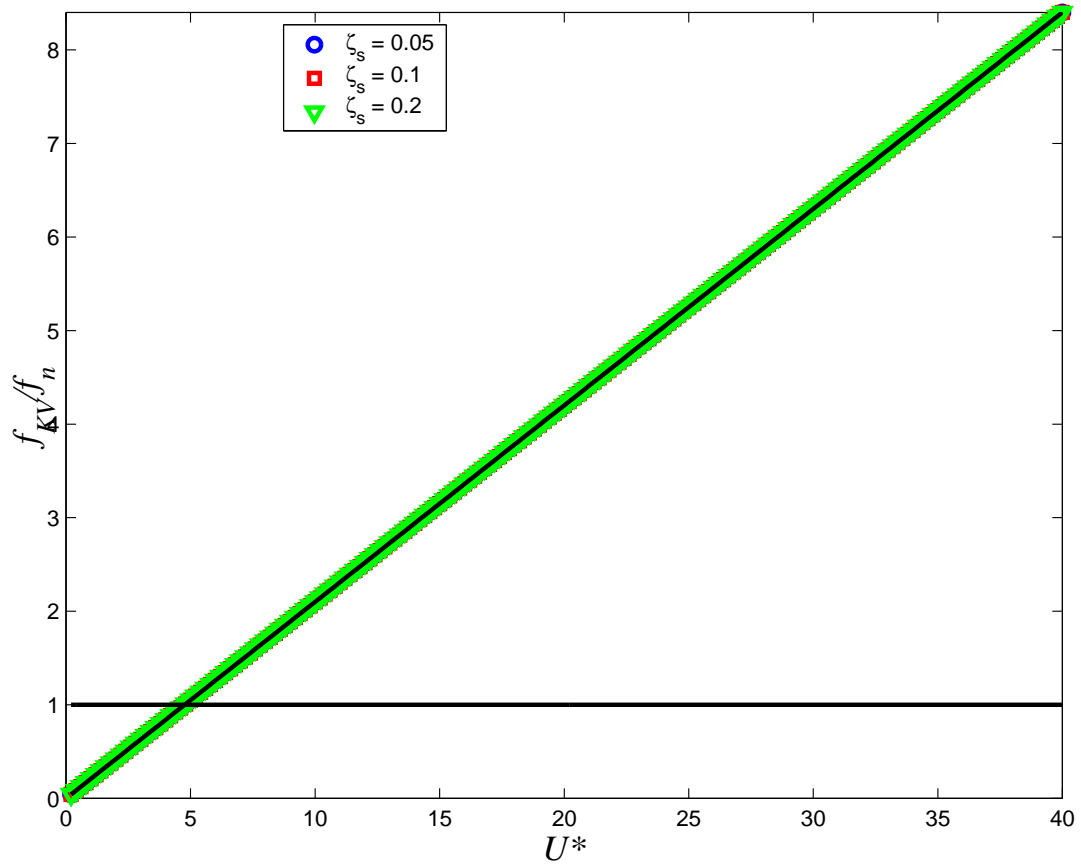


Figure 4.28: Vortex-shedding peak-frequency response from a square-root of time with critical energy shedding input with varying damping coefficients for various reduced velocities, where  $m^* = 1$ ,  $f_n = 1$ ,  $D = 0.1m$ , and  $2 \times 10^3 < Re < 4 \times 10^5$ .

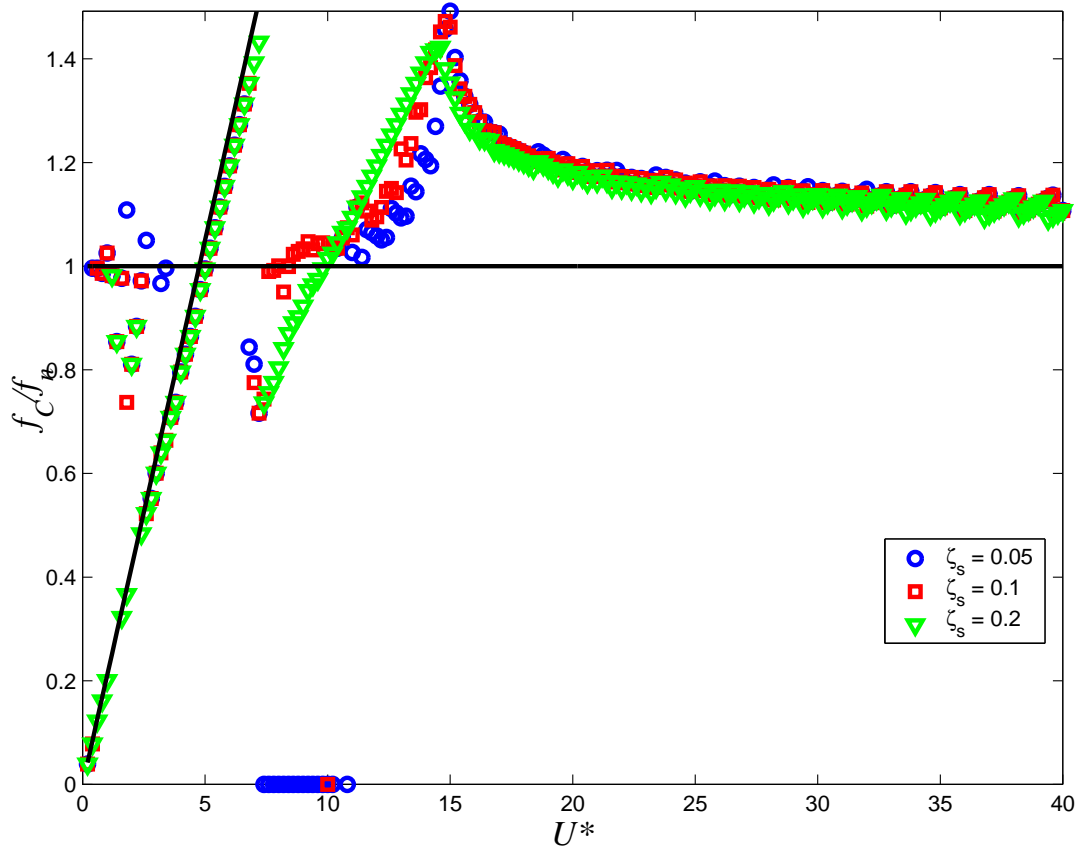


Figure 4.29: Cylinder peak-frequency response from a square-root of time with critical energy shedding input with varying damping coefficients for various reduced velocities, where  $m^* = 1$ ,  $f_n = 1$ ,  $D = 0.1m$ , and  $2 \times 10^3 < Re < 4 \times 10^5$ .

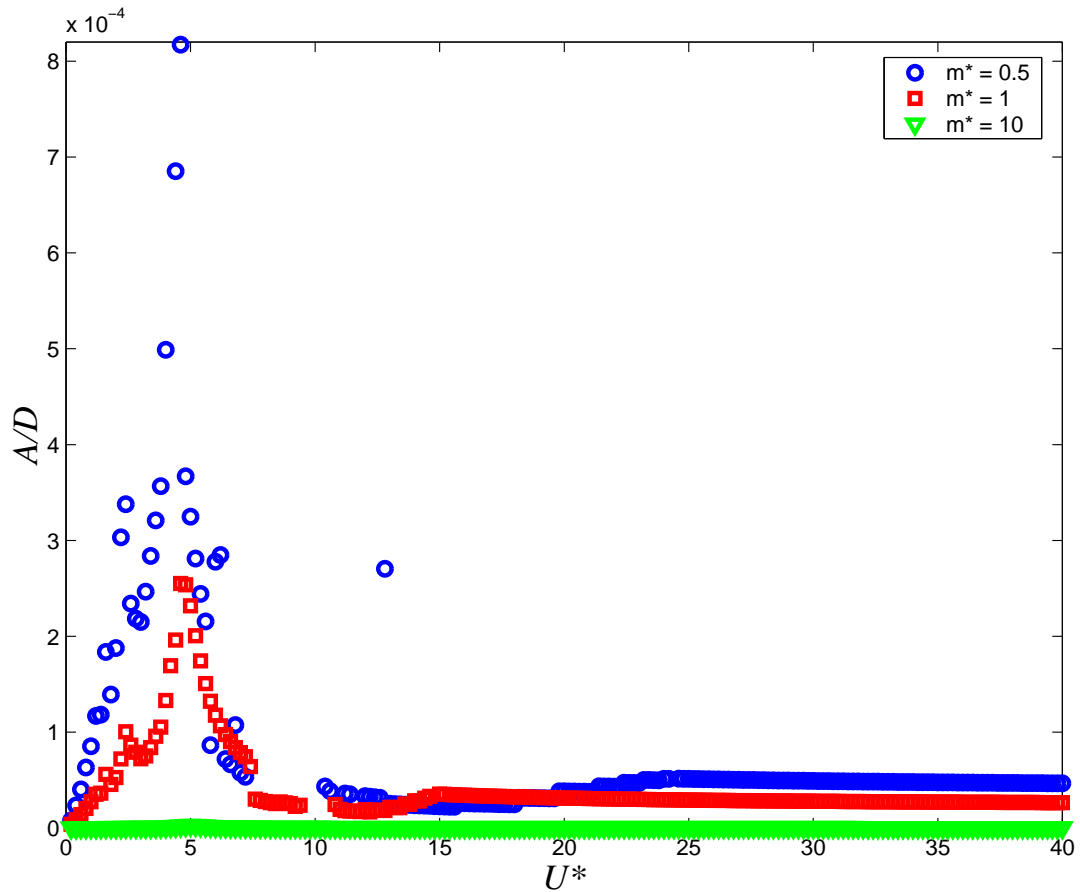


Figure 4.30: Cylinder amplitude response from a square-root of time with critical energy shedding input with varying damping coefficients for various reduced velocities.

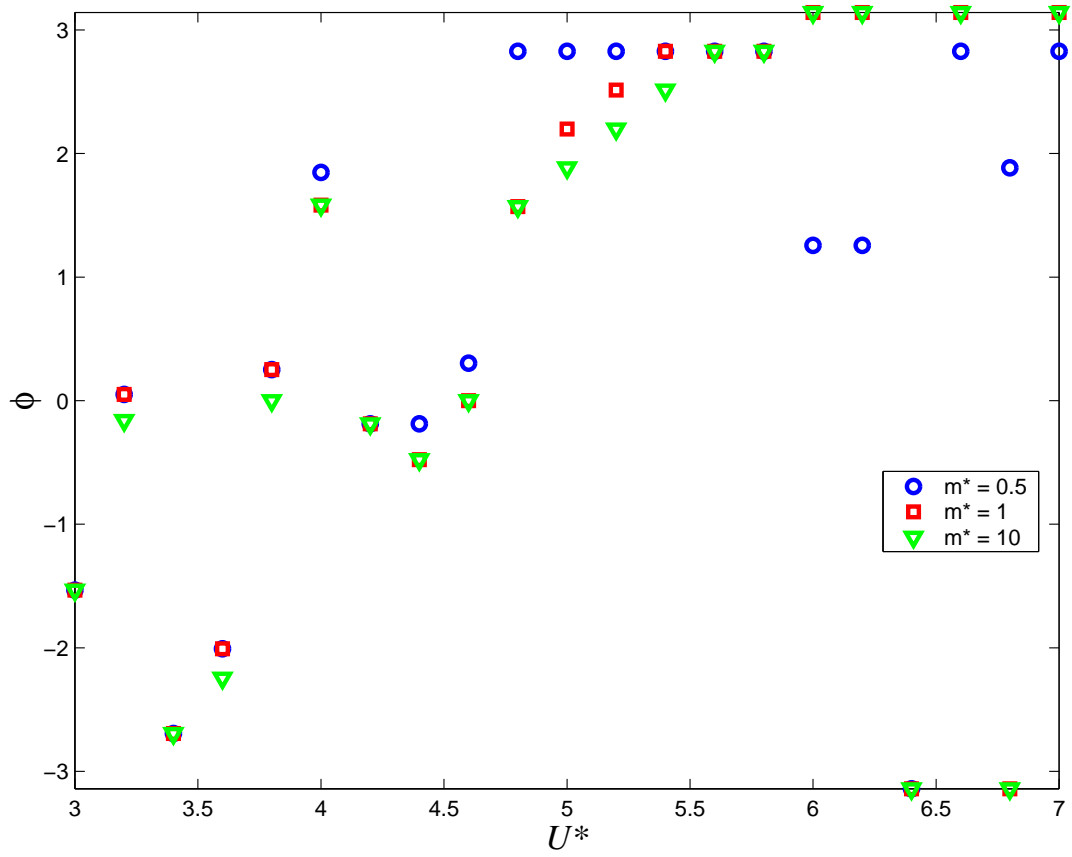


Figure 4.31: Cylinder phase-shift response from a square-root of time with critical energy shedding input with varying damping coefficients for various reduced velocities.

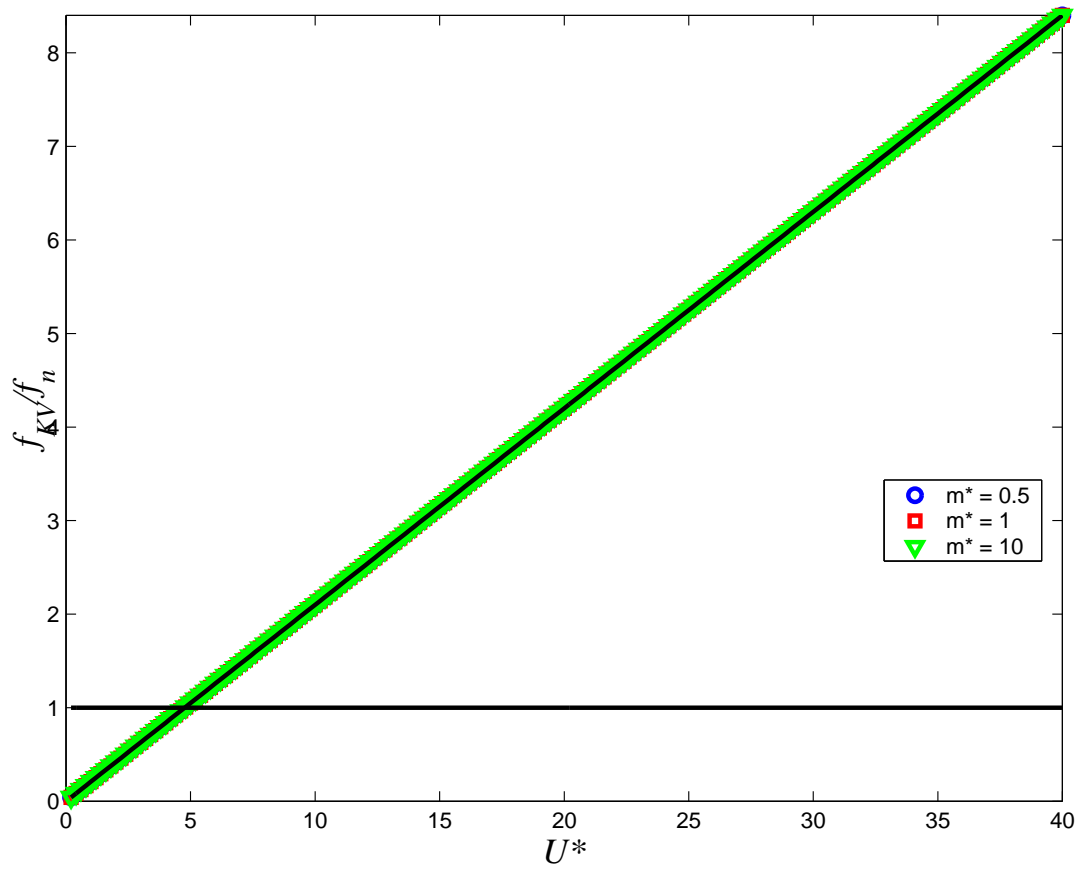


Figure 4.32: Vortex-shedding peak-frequency response from a square-root of time with critical energy shedding input with varying damping coefficients for various reduced velocities.

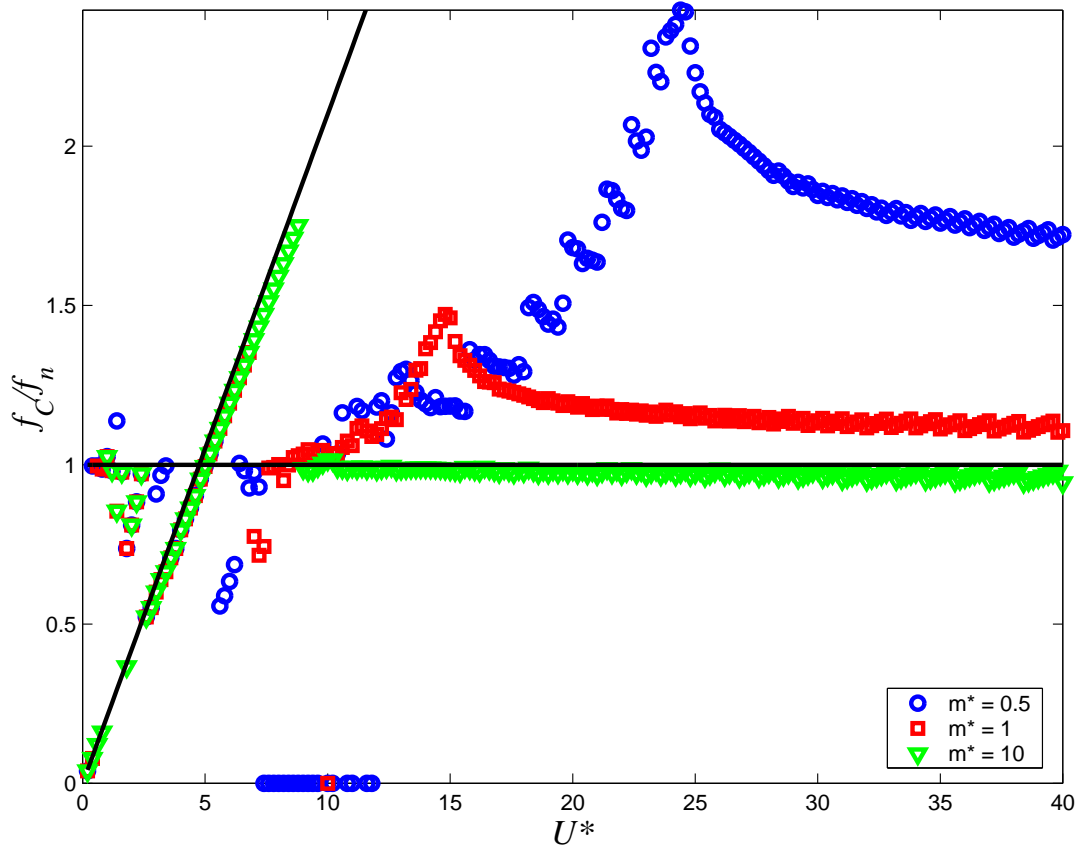


Figure 4.33: Cylinder peak-frequency response from a square-root of time with critical energy shedding input with varying damping coefficients for various reduced velocities.

## CHAPTER 5

### Mathematical Model Improvements

In the chapter, improvements to the math model are tested. Looking back at the inputs used for the mathematical model in Chapter 4, rough order of magnitude estimates for the zero and fluctuations of all inputs for the boundary layer and shear layer were used. As a first approximation, this should indicate the proper characteristics of the problem. However, when trying to improve upon the model and capture the real physics behind the problem, order of magnitude estimates may not capture all the characteristics of the problem. As was obvious in the result analysis of Chapter 4, the energy fluctuations appear to be greatly underestimated, resulting in an underestimate of the body response by 4 orders of magnitude. The non-dimensional amplitude response is expected to be on the order of  $A/D \approx 1$ , however, the results from the previous section showed  $A/D \approx 1 \times 10^{-4}$ . In this chapter, we try to rectify this gross underestimate without losing the correct phase shift between the displacement and the forcing, as well as lock-in and all the success achieved by this model so far. In addition to attempting to increase the amplitude of response by improving upon the physics of the model, an attempt is made to show lock-out outside of the range of synchronization, where as results to this point show lock-in with no lock-out phenomenon.

## 5.1 Reynolds Number Based Inputs

Many of the inputs that were set to constants, such as the separation point zero position, the boundary layer thickness, and the formation point zero position, are in fact proven functions of Reynolds number. For the several of these inputs, the information has been found through extensive experimentation of stationary circular cylinders. The boundary layer thickness combines experimental data with a theoretically based formulation. Each input that can be improved upon using data sets over Reynolds number will be done so here. Linear interpolation will be used for points at which no data is available. Curve smoothing, rather than curve-fitting, will be applied as has been done in the past due to the discontinuous characteristics of many flow-field properties.

### 5.1.1 Strouhal Number

In Chapter 2, the Strouhal number was defined as an important characteristic of the VIV phenomenon. The Strouhal number was in fact one of the first characteristics defined for the problem, long before the von Kármán vortex street was defined. There are extensive data sets available, from  $Re = 49$  all the way up to  $Re = 7.1 \times 10^6$ . Several curves have been fit to certain Reynolds number regimes as defined by Zdravkovich (1997), and outlined in Table 1.1. Williamson and Brown (1998) defined the curves for the entire laminar regime as well as for the TrW2 to TrSL1 regimes. Previously, it had been suggested that, for certain discrete portions of the  $St - Re$  regime, a curve could be fit to an equation as a function of one over  $Re$ . However, Williamson and Brown (1998) showed that a much better fit came from one over the square-root of  $Re$ , and a theoretically-based argument for such a relationship is outlined in the paper. Therefore, for certain low  $Re$ , equations rather than data



sets are used at this point in the model.

$$St = A + \frac{B}{\sqrt{Re}} + \frac{C}{Re} + \dots \quad (5.1)$$

Figure 5.1 shows the entire range of the  $St - Re$  regime with curves predating the work of Williamson and Brown (1998) for  $Re < 1200$ , but the general representation of the  $St - Re$  regime is captured and for this reason included in this chapter. The equations that will be used for  $Re < 1200$  are as follows.

$$\begin{aligned} St &= 0.2665 - \frac{1.018}{\sqrt{Re}} & 49 < Re < 178 \\ St &= 0.2175 - \frac{6.66}{Re} & 178 < Re < 260 \\ St &= 0.2234 - \frac{0.3490}{\sqrt{Re}} & 260 < Re < 1200 \end{aligned} \quad (5.2)$$

The second equation above comes from the curve-fitting work of Ponta and Aref (2004). For  $Re > 1200$ , the data collected by Schewe (1983) is used to interpolate the Strouhal number. The above equations cover the Laminar regime, the TrW1, and the TrW2 to TrSL1, respectively. From  $Re = 1200$  to  $Re = 23000$ , linear interpolation is used. Above  $Re = 23000$ , a fairly complete data set showing the effect of subcritical and supercritical transition were obtained by Schewe (1983). These data points were obtained by the author via private communication with Schewe.

### 5.1.2 Separation Point

Finding the actual separation point on a cylinder is a complicated process stemming from the Navier-Stokes equations. Several attempts have been made over the last two-hundred years to approximate the separation point on a cylinder. Some of the results are within less than two percent of the experimental separation point for a stationary cylinder (White 1991). Since the validation of each of these many theories comes from experimental data, experimental data will be used as the input of the separation point in the model developed here (Achenbach 1968; Achenbach 1971). It will be interpolated from 5.6.

Throughout the laminar flow and subcritical flow regime, the mean separation point remains fairly constant. Entering the transition regime, the mean separation point greatly increases, effectively reducing the thickness of the wake. Then, once transition to turbulence is complete, the separation point is again approximately constant, and not as large an angle as during transition. This widens the wake once again.

The data points were obtained by approximating the points in Achenbach (1968). The smoothed curve was also obtained by approximating the curves from Achenbach (1971). A plot of these data sets used as the input for the mathematical model is shown in 5.6.

In addition to the mean position of the separation point, the motion or excursion of the separation point is also an input parameter that can be taken from experimentation. Sarpkaya (1992) states that “in steady flow, the position of the separation point is nearly stationary, except for small excursions about  $\pm 3$  degrees” on a circular cylinder. It is also important to point out that in the case of oscillatory flow, the excursion of the separation point can be as much as 120 degrees (Sarpkaya 2001). Since it can be considered that the cylinder is experiencing oscillatory flow when undergoing oscillations due to VIV, larger excursions of the separation point may be possible. A more advanced model could allow for the separation point to move according to the motion of the cylinder. However, at this point, the separation point motions remains an input parameter and will be taken for now to move  $\pm 3$  degrees around the mean separation point.

### **5.1.3 Formation Point**

The first coining of the idea of the formation point comes from Gerrard (1966), and this defining point of the geometry of a cylinder in VIV has remained a critical

feature since. Norberg (1987a) did work to show the relationship of the formation length, or formation point as referred to in this dissertation due to the fact that it is measured from the center of the cylinder and not the separation point, to the Reynolds number. The resulting experimental data show a smooth curve, starting around three diameters at laminar flow, and peaking again just under 3 diameters around  $Re = 10^3$  before decaying once again and seemingly leveling off around  $Re = 10^5$ . The smoothed curve was obtained from Norberg via private communication and is shown in Figure 5.11.

Although the data set for the smoothed curve begins at the lowest possible Reynolds numbers for flow around a cylinder experiencing vortex shedding, the data set concludes within the transition regime. At  $Re = 2 \times 10^5$ , the flow is entering transition of the boundary layer flow after completing transition in the shear layer. This transition of the boundary layer has proven very important in the Strouhal number as well as the separation point, where both change greatly at the beginning and the end of this supercritical regime. It is proposed here, however, that for the formation point, data up to  $Re = 2 \times 10^5$  is sufficient since this point appears to only be affected by the shear layer itself. Therefore, since transition in the shear layer has been completed by  $Re = 2 \times 10^5$ , the formation point will no longer greatly change. This can be argued from the fact that for both the Strouhal number and separation point from the previous two sections showed no noticeable transition in their values over the transition of the shear layer ( $350 < Re < 2 \times 10^5$ ). However, this range is precisely the area over which the formation point has its largest fluctuations after beginning vortex shedding. It is assumed that *the formation length slowly decays as the Reynolds number goes to infinity above  $Re = 2 \times 10^5$ .*

The effect of using this smoothed curve to determine the formation length of each

simulation based on  $Re$  is tested and shown in Figures 5.12 to 5.15.

#### 5.1.4 Boundary Layer Thickness

The Boundary layer thickness is known to be a function of Reynolds number  $Re$ . Therefore, the linear approximation for the boundary layer thickness is an oversimplification of boundary layer, and a better approximation should be used. In Schlichting (1968), a relationship is developed between the frictional and inertial forces in order to determine the thickness of the boundary layer. The following relationship is then given.

$$\delta \propto \sqrt{\frac{\nu l}{U}} \quad (5.3)$$

It is assumed that *the length  $l$  can be replaced by the arc length  $R\theta$  for the case of a circular cylinder*. In addition, Schlichting (1968) uses the Blasius coefficient of 5 for the case of a flat plate. *Assuming that the boundary layer is much smaller than the radius of the cylinder, the flat plate boundary layer is a close approximation of the cylinder boundary layer*.

$$\delta = 5\sqrt{\frac{\nu R\theta}{U}} \quad (5.4)$$

At this point, it is not desired to change the entire boundary layer profile. The linear profile will be maintained for now, but the Blasius-type profile will be implemented and assessed for value later in the chapter. For now, the end boundary layer thickness parameter  $\Delta$  will be found using the above equation, and compared against the constant value of  $\Delta$  used up to this point.

$$\Delta = 5\sqrt{\frac{\nu R\theta_{sp0}}{U}} \quad (5.5)$$

The resulting effect of allowing the boundary-layer maximum thickness  $\Delta$  is an increase in the amplitude of response at synchronization, shown in Figure 5.16. In fact, implementing the above Reynolds-number based input for  $\Delta$  nearly doubles the

amplitude of response. This is a promising result since the amplitude of response is quantitatively the furthest from the observed phenomenon. An increase of any kind is very promising. Implementing Blasius-type functions throughout the attached fluid becomes of great interest at this point.

Finally, since the inclusion of the Reynolds-number based Strouhal number, separation point, formation point, and maximum boundary-layer thickness had a positive or negligible effect, they are all combined for future input into the final mathematical model. In this sense, any subtle differences due to the Reynolds number input have the possibility of being captured with the model. The result of all four inputs is shown in Figures 5.20 to 5.23.

## 5.2 Blasius-Type Functions

Up to this point, the geometry and velocity profiles have been selected to be the simplest known functions to satisfy the most important conditions, such as no-slip and no-penetration. However, the linear geometry and velocity profiles can be easily improved upon by considering the Blasius-type functions, represented by the equation below. This will allow for the energy to become more physically meaningful.

$$\eta_{Blasius} = y\sqrt{\frac{U}{\nu x}} \quad (5.6)$$

Although Blasius first developed the similarity variable for a flat plate, it is applicable to a wide variety of flows. The assumption that *the boundary layer thickness is much smaller than the radius of the cylinder* allows this similarity variable to be used in the geometry of the boundary layer. Blasius-type solutions have also been found for mixing layers, which is the category under which the shear layer falls. Finally, although the velocity profiles for the Blasius-type functions may not be explicitly found, there is a long list of profiles that can be used since they allow for flow

separation to be represented. Assessing the value added to the model by incorporating Blasius-type functions into the boundary layer, shear layer, and velocity profile follow.

### 5.2.1 Boundary Layer Geometry

Using the stagnation point  $\theta_{st}$  as the zero point, and knowing that  $\theta_t > 0$  and  $\theta_b < 0$ , the following equations will be used to improve the energy approximation in the boundary layer.

$$\delta_t = 5\sqrt{\frac{\nu R(\theta - \theta_{st})}{U}} \quad (5.7)$$

$$\delta_t = 5\sqrt{\frac{\nu R(\theta_{st} - \theta)}{U}} \quad (5.8)$$

It is important to note that the boundary layer thickness is no longer a function of the separation point, nor is there a specified maximum thickness. This change reflects the real physics of the boundary layer problem. However, it also greatly complicates the problem, since the boundary layer thickness at separation was used as the thickness of the shear layer. A modification to defining the thickness must be found, since constant variation will not fit with the simplified nature of the model.

In order to avoid such complications, the assumption that *the variation in the length of the boundary layer is minimal* is put into place. This leads to the reasonable estimate that boundary layer thickness at the point of separation is constant, and therefore constant throughout the shear layer as well. This single assumption leads to a major simplification of implementing the square-root relationship for the thickness of the boundary layer.

$$\Delta = 5\sqrt{\frac{\nu R\theta_{sp0}}{U}} \quad (5.9)$$

$$\delta = \Delta\sqrt{\frac{\theta - \theta_{st}}{\theta_{sp} - \theta_{st}}} \quad (5.10)$$

Inputting the above equation into the energy equations from Chapter 2 will only change the boundary layer terms. Therefore, the modified energy equations for the boundary layer are the only terms outlined below. There is a further complication due to the integration with the square-root relationship of the boundary layer thickness. The result is Fresnel integrals. However, the Fresnel integrals are well defined, and the author was able to implement a table into the numerical simulations in order to evaluate these expression.

The result of implementing these equations into the numerical simulator give the results shown in Figures 5.24 to 5.27. As with allowing  $\Delta$  to become a function of  $Re$ , there is again a promising increase in the amplitude of response of the cylinder while not destroying the qualitative successes already noted in the outline of the amplitude of response as well as the phase shift and the frequency of response of the cylinder.

It is also important to compare the effect of the square-root geometry of the boundary layer to the linear geometry previously used for the same  $\Delta$ . The computation time for the square-root geometry was over twice that for the linear geometry. Such an increase in computation time should only be allowed if the result is a significant improvement. This is much the same as selecting a numerical method. A higher-order method may improve the numerical results, but at a cost on the computation time. At some point it is found that, for a particular problem, the increased accuracy is not worth the increased computation time. This is the same idea presented here. Is the increased computation time of the square-root geometry worth the increased accuracy of the same terminal boundary layer thickness with linear geometry?

Figures 5.28 to 5.31 show the comparison between the square-root and linear geometries with the same terminal maximum boundary-layer thickness. They are

fairly similar with almost the same amplitudes. The linear geometry seems to respond stronger at  $U^* \approx 2.5$ , which at first glance is not very desirable, but increased responses have been observed in several experimental ranges of synchronization. In the end, it is determined that for this first attempt at a rigorously-derived VIV mathematical model, the linear geometry will suffice to determine the validity of the model.

### 5.2.2 Shear Layer Geometry

Up to this point, the shear layer has maintained a constant thickness. It is, however, a free-shear layer between the free-stream fluid outside the wake, and the unattached dead fluid. The dead fluid is so named because the velocity is zero between the two shear layers. The fact that it is unattached is emphasized because it has been traditionally found that the dead fluid does not effect the body. As a result of the two different streams in viscous fluid, the shear layer expands with distance based on a Blasius-type similarity variable. The expansion is both on the top and the bottom of the of the shear layer, with an approximate similarity variable for this case being around 7 (see White (1991), Figure 4-17). This results in the following relationship.

$$\eta = \delta_{SL} \sqrt{\frac{U}{2x\nu}} \approx 7 \quad (5.11)$$

$$\delta_{SL} \approx 10 \sqrt{\frac{\nu x}{U}} \quad (5.12)$$

Since it was already determined above that the a linear growth is nearly as effective of a model as a square-root growth in the case of the boundary layer, the same will be applied for the shear layer. The force equations with the square-root growth was found for the square-root growth and was observed to have the same asymptotical Fresnel integrals, therefore it is proposed that assuming the same for the linear versus square root growth is substantial.



The resulting modification of the shear layer is added to the results already found for the Blasius-based boundary layer thickness. At the instant of separation, the fluid is considered tripped. In this way, *at any point after separation the fluid is assumed to have an increased expansion despite any portion that may still be traveling over the cylinder*. Since the flow is considered tripped after separation and large increases in the thickness are expected, this assumption is not so a large departure from the physics of the problem. In addition, describing a flow after it has separated has not yet been done analytically, so only general properties of the flow can be modeled. This results in the following relationships for the distance to be used as the input for the shear layer maximum thickness. Due to having to follow the curvature of the body, separate expressions are used for the case of the separation point before versus after 90 degrees.

$$\begin{aligned}\theta_{sp} &< \frac{\pi}{2} \\ d &= R\left(\frac{\pi}{2} - \theta_{sp}\right) + x_{fp} \\ \Delta_{SL} &= 10\sqrt{\frac{\nu d}{U}}\end{aligned}\tag{5.13}$$

$$\begin{aligned}\delta_{SL} &= \frac{\Delta_{SL} - \Delta_{BL}}{d} R(\theta - \theta_{sp}) + \Delta_{BL} & \theta < \frac{\pi}{2} \\ \delta_{SL} &= \frac{\Delta_{SL} - \Delta_{BL}}{d} \left[ R\left(\frac{\pi}{2} - \theta_{sp}\right) + \zeta \right] + \Delta_{BL} & 0 < \zeta < x_{fp}\end{aligned}\tag{5.14}$$

$$\begin{aligned}\theta_{sp} &> \frac{\pi}{2} \\ d &= x_{fp} - R \sin\left(\theta_{sp} - \frac{\pi}{2}\right) \\ \Delta_{SL} &= 10\sqrt{\frac{\nu d}{U}}\end{aligned}\tag{5.15}$$

$$\delta_{SL} = \frac{\Delta_{SL} - \Delta_{BL}}{d} \left[ \zeta - R \sin\left(\theta_{sp} - \frac{\pi}{2}\right) \right] + \Delta_{BL} \quad R \sin\left(\theta_{sp} - \frac{\pi}{2}\right) < \zeta < x_{fp}\tag{5.16}$$

The same velocity profile is still used, where it is equal to zero at the bottom of the shear layer, and linearly increases to the freestream velocity at the shear layer thickness.

The energy and force equations that result from the above equation, particularly for the case of separation less than 90 degrees, have an overwhelming number of terms. The increase in the number of operations when input into the numerical integrator is so much that it again becomes not worth the increased computation power. A minor simplification to the shear layer can greatly reduce the number of terms. If the starting point of the shear layer is always assumed to be at the y-axis of the cylinder center, where  $x = 0$ , the only parameters that depend on time are the formation point and the cylinder displacement. The resulting force equation should give a good indication of the improvement in including a linearly growing shear layer as opposed to a uniformly-thick shear layer. This is the core purpose of the derivation of a new VIV model, and any observations that come from this simplified shear layer model should provide significant insight into the applicability of the model and the sensitivity to such things as the shear layer thickness variation.

$$T_{SL} = \frac{1}{12}\rho x_{fp} (U^2 + 3\dot{y}^2) (\Delta_{SL} - \Delta_{BL}) \quad (5.17)$$

$$F_{SL} = \frac{1}{2}\rho \dot{x}_{fp} \dot{y} (\Delta_{SL} - \Delta_{BL}) + \frac{1}{2}\rho x_{fp} \ddot{y} (\Delta_{SL} - \Delta_{BL}) \quad (5.18)$$

The results are shown in Figures 5.32 through 5.35. It can be seen that there is a substantial improvement once again in the amplitude of oscillation, increasing the amplitude ratio up to  $4 \times 10^{-3}$ , the highest amplitudes yet seen for the test case of  $m^* = 1$ ,  $\zeta = 0.1$  and  $f_n = 1$ . This is nearly a full order of magnitude improvement over the constant shear layer thickness. This is promising, showing the ease with which the amplitude may be increased with the addition of more physical representations of the energy. It also shows, however, how delicate the balance between the energy input and the vortex shedding criteria is. This is exemplified by the increased number of points found on the zero horizontal axis for the frequency

plots and by the loss of the phase shift at lock-in (Figure 5.33). Although the amplitudes were significantly increased, the other characteristics that coincided well with the phenomenon have been disturbed by the addition of energy. The highly nonlinear nature of the model is the supposed culprit for this alteration, and it is of the utmost importance to maintain the balance between energy and vortex shedding.

### 5.3 Velocity Profiles

In the previous chapters, a model was developed using assumptions for first-order velocity profiles in the fluid to derive the system energy. However, the actual velocity profiles are likely to be better approximated by higher-order profiles. The differences between the results obtained in the previous chapter will now be compared to results for higher-order profiles. The linear velocity profile implemented previously underestimates the energy within the system. Although the actual velocity profile cannot be solved since it comes from the Navier-Stokes equations, a more reasonable approximation can be used. In textbooks, either a sinusoidal or cubic velocity profile are common. *It is assumed that a cubic velocity profile is best suited for the boundary layer.* The velocity profile is again matched at the interface of the boundary layer and the shear layer. The interface profile is held constant throughout the shear layer, and is used to determine the flow out of the shear layer to feed the attached vortex. *A fuller velocity profile can be assumed to model a more turbulent boundary and shear layer.*

White (1994) uses several velocity profiles to model the fuller velocity profile of a boundary layer. Two of these are listed below. Each is implemented into the energy equations, and the resulting force equations are numerically integrated. Both the boundary layer and the shear layer equations change, but the attached vortex

equation remains the same, with only the flow into the vortex changing as a result.

$$u = U \sin\left(\frac{\pi y}{2\delta}\right) \quad (5.19)$$

Additionally, from White (1994) there is the cubed relationship for a flat plate as given below.

$$u = \frac{U}{2} \left( 3\frac{y}{\delta} - \left(\frac{y}{\delta}\right)^3 \right) \quad (5.20)$$

For the boundary layer, equations 5.19 and 5.20 use the substitution  $y = r - R$ . As they appear here, they model the shear layer.

It has often times been found experimentally that the actual velocity profile may have a maximum higher than the free-stream velocity. When considering the effects of viscosity and separation on the flow, this makes sense. Often, the maximum is around 1.2 times greater than the free-stream. It may be of interest to incorporate such a profile here.

The full force equations were derived using the above velocity profiles. However, neither provided noticeable differences in the response plots. Therefore, it is asserted that the linear velocity profile is the most appropriate due to the simplicity of working with it and the closeness in approximation of viscous flow over a curved surface.

## 5.4 Parametric Variation

### 5.4.1 Energy Dissipation

In the model that has been developed in Chapter 3, there is only one undefined parameter that can be examined within this section and that is the energy dissipation variable  $\alpha$ . Originally, it was argued that the dissipated energy from the shear layer to the attached vortex is approximately around 50% of the energy (Bearman 1984). Examining the results thus far in this dissertation shows that there is a need for increased energy within the system as defined. Therefore, it can be argued that not

all of the energy has been accounted for thus far. Following this argument, it can be said that the dissipation factor,  $\alpha$  can arguably be removed, or even used as an amplification factor instead of dissipation. Therefore, this section will examine the result of, first, placing the dissipation at the shear layer to attached vortex boundary to zero by letting  $\alpha = 1$ , and then to allow the parameter  $\alpha$  to act as an amplification factor by allowing it to be greater than one.

In the case of  $\alpha > 1$ , the dissipation force term in the full equations must be eliminated in order to avoid a physically meaningless parameter;  $\alpha$  in this case only represents an artificial amplification and should not factor into non-conservative work terms previously derived.

The results are shown in Figures 5.36 to 5.39. The most interesting output is the fact there there is now an observable point of lock-out, where the cylinder is no longer responding near its natural frequency, in the area at the end of the range of synchronization. This had not been previously observed with this math model. The concept of lock-out is one observed experimentally and is documented in Sumer and Fredsøe (1997). However, the concept of the cylinder always responding around its natural frequency and never locking out has also been observed (Raghavan 2007). Therefore, it is interesting to note that not only has lock-out now been observed, but a desynchronization range has also been observed with the cylinder still responding at its natural frequency.

With it's capability of capturing lock-out, as well as a slightly increased amplitude response, it is determined that  $\alpha = 1$  is the best choice for the model at this point in time.

## 5.5 Other Examined Factors

During the process of developing an improved math model, other ideas for improving the model were tested, even when not entirely physically meaningful or verifiable. However, in order to demonstrate the extent to which ideas for improvement were tested, several of the concepts are outlined here.

- One idea was to see if the dead-fluid region behind the cylinder and between the shear layers may in fact have a beneficial affect on the model. It has been traditionally argued that the dead-fluid region is not attached to the body, and therefore should not be part of the system as defined here. However, the concept was tested anyway. It was found that, since the dead fluid only acts in terms of the motion of the cylinder (i.e., it is trapped between the shear layers and forced to oscillate with the system in the  $y$ -direction), the result was purely an added mass term. As expected, this only reduced the maximum amplitudes, while leaving the other results (phase shift, frequency response) almost the same.
- As mentioned in the previous chapter, artificial amplification of the forcing terms was also performed in order to determine how sensitive the model is to increases in energy (or forcing). The result there was highly nonlinear, where a small amplification of the forcing terms resulted in a relatively large amplification of the cylinder displacement. This is a strong indication that not all energy has been captured into the model, while maintaining its physically-meaningful aspects. The artificial amplification was performed in two ways. First, all forcing terms were multiplied by the amplification factor. Then, only forcing terms from each portion of the system were multiplied. For instance, only the boundary layer terms were amplified, followed by only the shear layer terms and only the attached vortex terms. This lead to the conclusion that the attached

vortex had the largest effect on the model, followed by the boundary layer and then the shear layer.

- The concept that the attached vortex may have a larger effect on the model than any other leads into the next idea is tested. With so many terms representing each part of the system, it was of interest to see if any one part could properly model the phenomenon of VIV. For instance, since the attached vortex seems to affect the largest change on the system, what if it was the only term present, thus eliminating the need to model the boundary layer and the shear layer. Thus, each portion was modeled with the cylinder degree of freedom, and it was found that no single part captured the phenomenological features seen when all three are combined. Therefore, it is emphasized here that VIV is the result of not just the boundary layer, and not just the attached vortices, nor just the shear layer, but a combination of the three. This was a good test for better understanding the phenomenon of VIV and what factors play a role.
- Following from the test of different velocity profiles, the idea of using the constant free-stream velocity across the boundary layer and shear layer thickness was also tested. The results showed the necessity of having a varying velocity profile, where many of the observed VIV features were absent in the constant velocity profile. The equations, though, did appear more simply, but there is no advantage in this if VIV is not captured.

## 5.6 Final Force Equations

After examining the effects of the changes that have been considered, the final force equations are now presented. These force equations represent what is believed to be the best possible representation of VIV at this point in time. Due to the

complexity of the phenomenology, there are perhaps many more improvements that can be made that will provide better responses. However, the current list exhausts those believed to be most important and have the most effect.

The final force equation begins with what was written at the end of Chapter 3, with the following additions. The Strouhal number, separation point, formation point, and boundary layer final thickness all come from the Reynolds-based inputs outlined in this chapter. The shear layer thickness is held constant at this point. Although it seemed very promising to include a growth of the shear layer as outlined above, there were more negative aspects than positive with the current method of implementation. It is suggested that this be a point of further study, whereas simple equations can be developed for use in the model without disturbing the delicate balance of the nonlinear model. In addition to all of this, the dissipation parameter  $\alpha$  is set equal to one rather than one-half, with the argument that there is no need to dissipate energy when not all the energy has yet been accounted for.

$$m\ddot{y} + c\dot{y} + ky = \Xi_{diss_t} + \Xi_{diss_b} + F_{BL_t} + F_{SL_t} + F_{KV_t} - F_{BL_b} - F_{SL_b} - F_{KV_b} \quad (5.21)$$



$$|\theta_{sp}| < \frac{\pi}{2}$$

$$\begin{aligned}
m\ddot{y} + c\dot{y} + ky &= -(1 - \alpha)\rho \frac{\Delta U^2}{2} + \frac{\rho \Delta^2 U}{3} \left[ \frac{-2 \left( 2\cos(\theta_{sp_t})\dot{\theta}_{sp_t} - \cos(\theta_{st})\dot{\theta}_{st} \right)}{(\theta_{sp_t} - \theta_{st})^2} \right] \\
&+ \frac{\rho \Delta^2 U}{3} \left[ \frac{4 \left( \sin(\theta_{sp_t}) - \sin(\theta_{st}) \right) \left( \dot{\theta}_{sp_t} - \dot{\theta}_{st} \right)}{(\theta_{sp_t} - \theta_{st})^3} \right] \\
&+ \frac{\rho \Delta U}{6} \left[ \frac{-(4\Delta - 3R) \sin(\theta_{sp_t})\dot{\theta}_{sp_t} + 3R \sin(\theta_{sp_t})\dot{\theta}_{st}}{(\theta_{sp_t} - \theta_{st})} \right] \\
&+ \frac{\rho \Delta U}{6} \left[ 2\Delta \cos(\theta_{sp_t})\dot{\theta}_{sp_t} - 3R \sin(\theta_{sp_t})\dot{\theta}_{sp_t} \right] \\
&+ \frac{\rho \Delta U}{2} \left[ \frac{R \left( \cos(\theta_{sp_t}) + \cos(\theta_{st}) \right) \left( \dot{\theta}_{sp_t} - \dot{\theta}_{st} \right)}{(\theta_{sp_t} - \theta_{st})^2} \right] \\
&+ \frac{\rho \Delta}{6} (\Delta + 3R) \left[ \dot{y} \left( \dot{\theta}_{sp_t} - \dot{\theta}_{st} \right) + \ddot{y} (\theta_{sp_t} - \theta_{st}) \right] \\
&+ \frac{\rho \Delta}{12} \left[ (6\Delta + 12R) \ddot{y} \left( \frac{\pi}{2} - \theta_{sp_t} \right) - (2\Delta + 3R) U \cos(\theta_{sp_t}) \dot{\theta}_{sp_t} \right] \\
&- \frac{\rho \Delta}{2} \left[ (\Delta - 2R) \dot{y} \dot{\theta}_{sp_t} \right] + \rho \Delta \left[ x_{fp_t} \ddot{y} + \dot{x}_{fp_t} \dot{y} \right] + \pi \rho \left[ 2\dot{\eta}_t \dot{y} + \eta_t^2 \ddot{y} \right] \\
&- \frac{\rho \Delta^2 U}{3} \left[ \frac{2 \left( 2\cos(\theta_{sp_b})\dot{\theta}_{sp_b} - \cos(\theta_{st})\dot{\theta}_{st} \right)}{(\theta_{st} - \theta_{sp_b})^2} \right] \\
&- \frac{\rho \Delta^2 U}{3} \left[ \frac{-4 \left( \sin(\theta_{sp_b}) - \sin(\theta_{st}) \right) \left( \dot{\theta}_{st} - \dot{\theta}_{sp_b} \right)}{(\theta_{st} - \theta_{sp_b})^3} \right] \\
&- \frac{\rho \Delta U}{6} \left[ \frac{-(4\Delta - 3R) \sin(\theta_{sp_b})\dot{\theta}_{sp_b} + 3R \sin(\theta_{sp_b})\dot{\theta}_{st}}{(\theta_{st} - \theta_{sp_b})} \right] \\
&+ \frac{\rho \Delta U}{6} \left[ 2\Delta \cos(\theta_{sp_b})\dot{\theta}_{sp_b} + 3R \sin(\theta_{sp_b})\dot{\theta}_{sp_b} \right] \\
&- \frac{\rho \Delta U}{2} \left[ \frac{R \left( \cos(\theta_{sp_b}) + \cos(\theta_{st}) \right) \left( \dot{\theta}_{st} - \dot{\theta}_{sp_b} \right)}{(\theta_{st} - \theta_{sp_b})^2} \right] \\
&- \frac{\rho \Delta}{6} (\Delta + 3R) \left[ \dot{y} \left( \dot{\theta}_{st} - \dot{\theta}_{sp_b} \right) + \ddot{y} (\theta_{st} - \theta_{sp_b}) \right] \\
&- \frac{\rho \Delta}{12} \left[ (6\Delta + 12R) \ddot{y} \left( \frac{\pi}{2} + \theta_{sp_b} \right) + (2\Delta + 3R) U \cos(\theta_{sp_b}) \dot{\theta}_{sp_b} \right] \\
&- \frac{\rho \Delta}{2} \left[ (\Delta - 2R) \dot{y} \dot{\theta}_{sp_b} \right] - \rho \Delta \left[ x_{fp_b} \ddot{y} + \dot{x}_{fp_b} \dot{y} \right] - \pi \rho \left[ 2\dot{\eta}_b \dot{y} + \eta_b^2 \ddot{y} \right]
\end{aligned}$$

(5.22)

$$|\theta_{sp}| > \frac{\pi}{2}$$

$$\begin{aligned}
m\ddot{y} + c\dot{y} + ky = & -(1 - \alpha)\rho \frac{\Delta U^2}{2} + \frac{\rho \Delta^2 U}{3} \left[ \frac{-2 \left( 2\cos(\theta_{sp_t})\dot{\theta}_{sp_t} - \cos(\theta_{st})\dot{\theta}_{st} \right)}{(\theta_{sp_t} - \theta_{st})^2} \right] \\
& + \frac{\rho \Delta^2 U}{3} \left[ \frac{4 \left( \sin(\theta_{sp_t}) - \sin(\theta_{st}) \right) \left( \dot{\theta}_{sp_t} - \dot{\theta}_{st} \right)}{(\theta_{sp_t} - \theta_{st})^3} \right] \\
& + \frac{\rho \Delta U}{6} \left[ \frac{-(4\Delta - 3R) \sin(\theta_{sp_t})\dot{\theta}_{sp_t} + 3R \sin(\theta_{sp_t})\dot{\theta}_{st}}{(\theta_{sp_t} - \theta_{st})} \right] \\
& + \frac{\rho \Delta U}{6} \left[ 2\Delta \cos(\theta_{sp_t})\dot{\theta}_{sp_t} - 3R \sin(\theta_{sp_t})\dot{\theta}_{sp_t} \right] \\
& + \frac{\rho \Delta U}{2} \left[ \frac{R \left( \cos(\theta_{sp_t}) + \cos(\theta_{st}) \right) \left( \dot{\theta}_{sp_t} - \dot{\theta}_{st} \right)}{(\theta_{sp_t} - \theta_{st})^2} \right] \\
& + \frac{\rho \Delta}{6} (\Delta + 3R) \left[ \dot{y} \left( \dot{\theta}_{sp_t} - \dot{\theta}_{st} \right) + \ddot{y} (\theta_{sp_t} - \theta_{st}) \right] \\
& + \rho \Delta \left[ \ddot{y} \left( x_{fp_t} - R \sin \left( \theta_{sp_t} - \frac{\pi}{2} \right) \right) + \dot{y} \left( \dot{x}_{fp_t} - R\dot{\theta}_{sp_t} \cos \left( \theta_{sp_t} - \frac{\pi}{2} \right) \right) \right] \\
& + \pi \rho \left( 2\dot{\eta}_t \dot{y} + \eta_t^2 \ddot{y} \right) \\
& - \frac{\rho \Delta^2 U}{3} \left[ \frac{2 \left( 2\cos(\theta_{sp_b})\dot{\theta}_{sp_b} - \cos(\theta_{st})\dot{\theta}_{st} \right)}{(\theta_{st} - \theta_{sp_b})^2} \right] \\
& - \frac{\rho \Delta^2 U}{3} \left[ \frac{-4 \left( \sin(\theta_{sp_b}) - \sin(\theta_{st}) \right) \left( \dot{\theta}_{st} - \dot{\theta}_{sp_b} \right)}{(\theta_{st} - \theta_{sp_b})^3} \right] \\
& - \frac{\rho \Delta U}{6} \left[ \frac{-(4\Delta - 3R) \sin(\theta_{sp_b})\dot{\theta}_{sp_b} + 3R \sin(\theta_{sp_b})\dot{\theta}_{st}}{(\theta_{st} - \theta_{sp_b})} \right] \\
& + \frac{\rho \Delta U}{6} \left[ 2\Delta \cos(\theta_{sp_b})\dot{\theta}_{sp_b} + 3R \sin(\theta_{sp_b})\dot{\theta}_{sp_b} \right] \\
& - \frac{\rho \Delta U}{2} \left[ \frac{R \left( \cos(\theta_{sp_b}) + \cos(\theta_{st}) \right) \left( \dot{\theta}_{st} - \dot{\theta}_{sp_b} \right)}{(\theta_{st} - \theta_{sp_b})^2} \right] \\
& - \frac{\rho \Delta}{6} (\Delta + 3R) \left[ \dot{y} \left( \dot{\theta}_{st} - \dot{\theta}_{sp_b} \right) + \ddot{y} (\theta_{st} - \theta_{sp_b}) \right] \\
& - \rho \Delta \left[ \ddot{y} \left( x_{fp_b} - R \sin \left( -\theta_{sp_b} - \frac{\pi}{2} \right) \right) + \dot{y} \left( \dot{x}_{fp_b} + R\dot{\theta}_{sp_b} \cos \left( -\theta_{sp_b} - \frac{\pi}{2} \right) \right) \right] \\
& - \pi \rho \left( 2\dot{\eta}_b \dot{y} + \eta_b^2 \ddot{y} \right)
\end{aligned}$$

(5.23)

The above forcing equation is evaluated with the following inputs and conditions.

$$\begin{aligned}
\eta_t &= \sqrt{\alpha \frac{U \Delta_{SL}}{2\pi} t_t} & \eta_b &= \sqrt{\alpha \frac{U \Delta_{SL}}{2\pi} t_b} \\
x_{fp_t} &= x_{fp_o} + \sqrt{\frac{\delta x^2}{T_s} t_t} & x_{fp_b} &= x_{fp_o} + \sqrt{\frac{\delta x^2}{T_s} t_b} \\
\theta_{sp_t} &= \theta_{sp_{t_o}} + \sqrt{\frac{\delta \theta^2}{T_s} t_t} & \theta_{sp_b} &= \theta_{sp_{b_o}} - \sqrt{\frac{\delta \theta^2}{T_s} t_b} \\
\theta_{st} &= \sqrt{\frac{\delta \theta^2}{T_s} t_t} - \sqrt{\frac{\delta \theta^2}{T_s} t_b}
\end{aligned} \tag{5.24}$$

$$\begin{aligned}
x_{fp_o} &= f(Re) & \delta x &= R \\
\theta_{sp_{t_o}} &= f(Re) & \delta \theta &= \pi/18 \\
\theta_{sp_{b_o}} &= f(Re) \\
T_s &= f(Re) & \alpha &= 1
\end{aligned} \tag{5.25}$$

$$t_t(i+1) = \begin{cases} t_t(i) + \Delta t & T_{KV} < T_{crit} \\ 0 & T_{KV} \geq T_{crit} \end{cases} \tag{5.26}$$

$$t_b(i+1) = \begin{cases} t_b(i) + \Delta t & T_{KV} < T_{crit} \\ 0 & T_{KV} \geq T_{crit} \end{cases}$$

$$T_{crit} = \frac{\alpha}{8} \rho \Delta T_s U^3 \tag{5.27}$$

The quantitative and qualitative analysis of the above math model is performed in the final chapter of the dissertation.

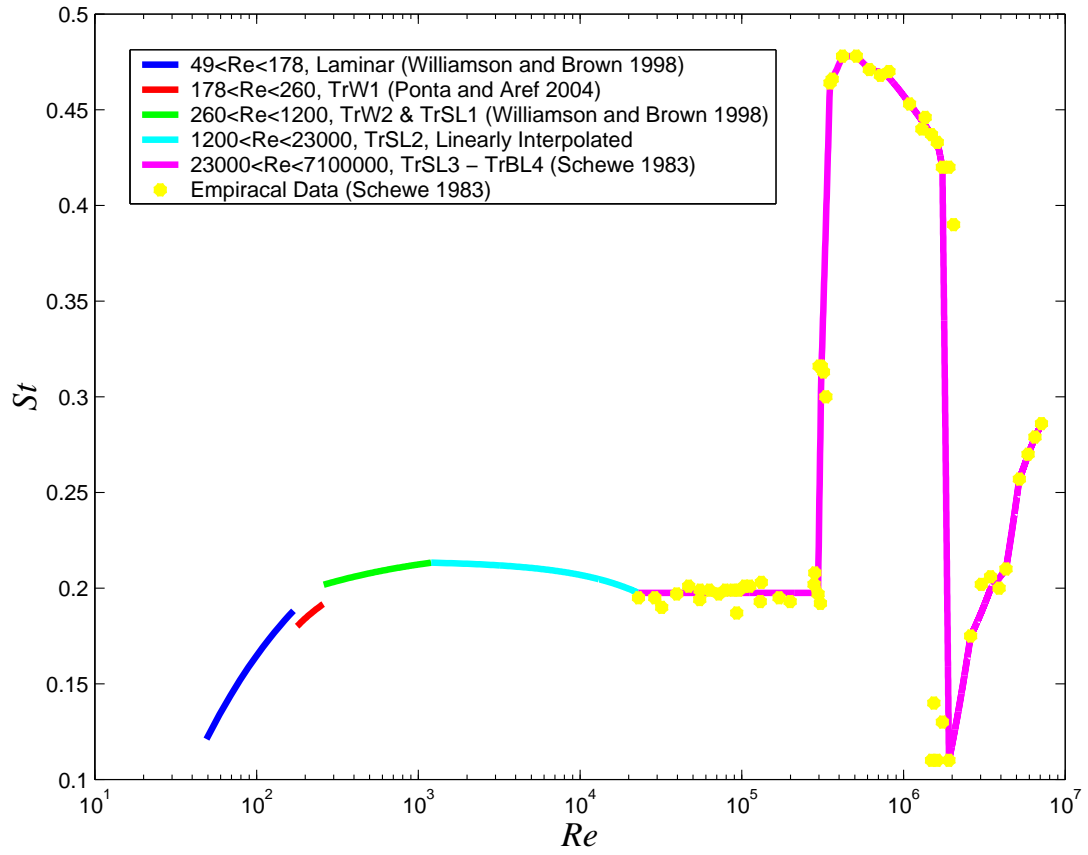


Figure 5.1: The non-dimensional Strouhal number over Reynolds number for a stationary cylinder (Sumer and Fredsøe 1997). Other experiments have not agreed with the smooth jump shown during Boundary Layer Transition.

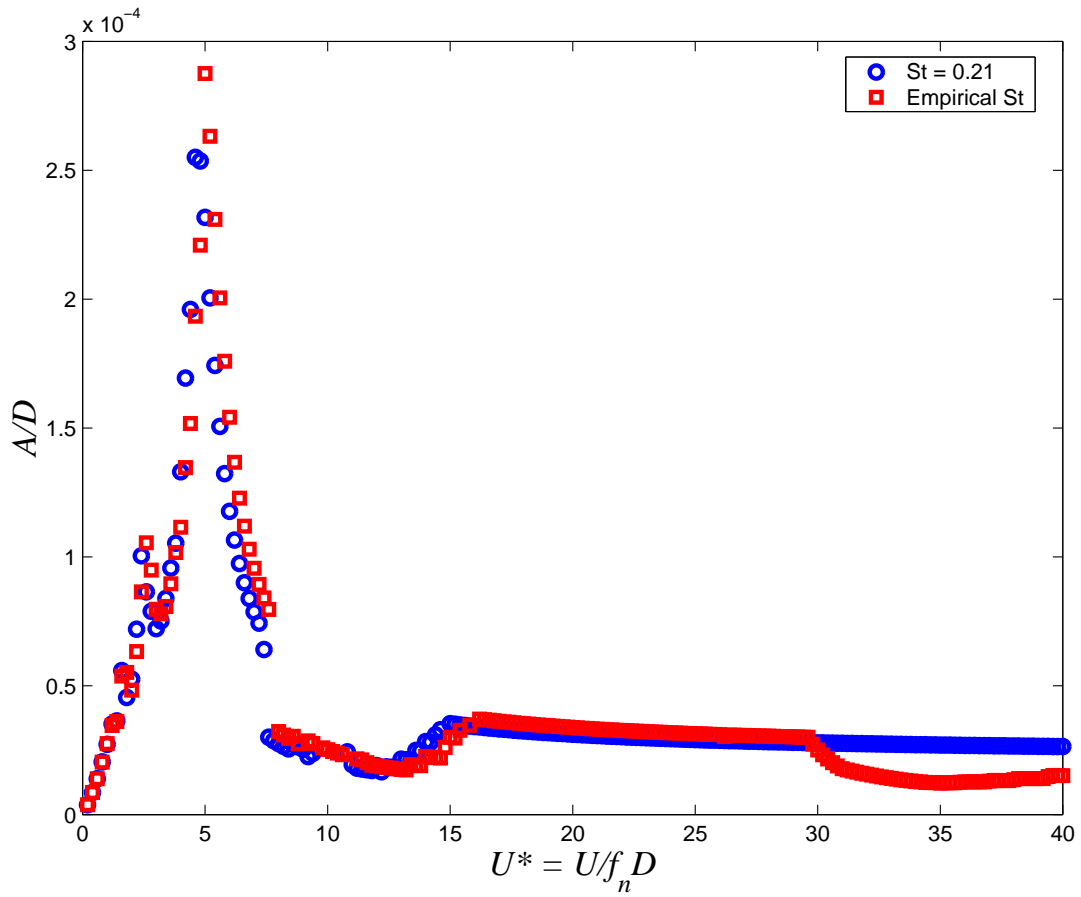


Figure 5.2: Comparison of the amplitude response for the implementation of a Reynolds-number-based Strouhal number to a constant Strouhal number.

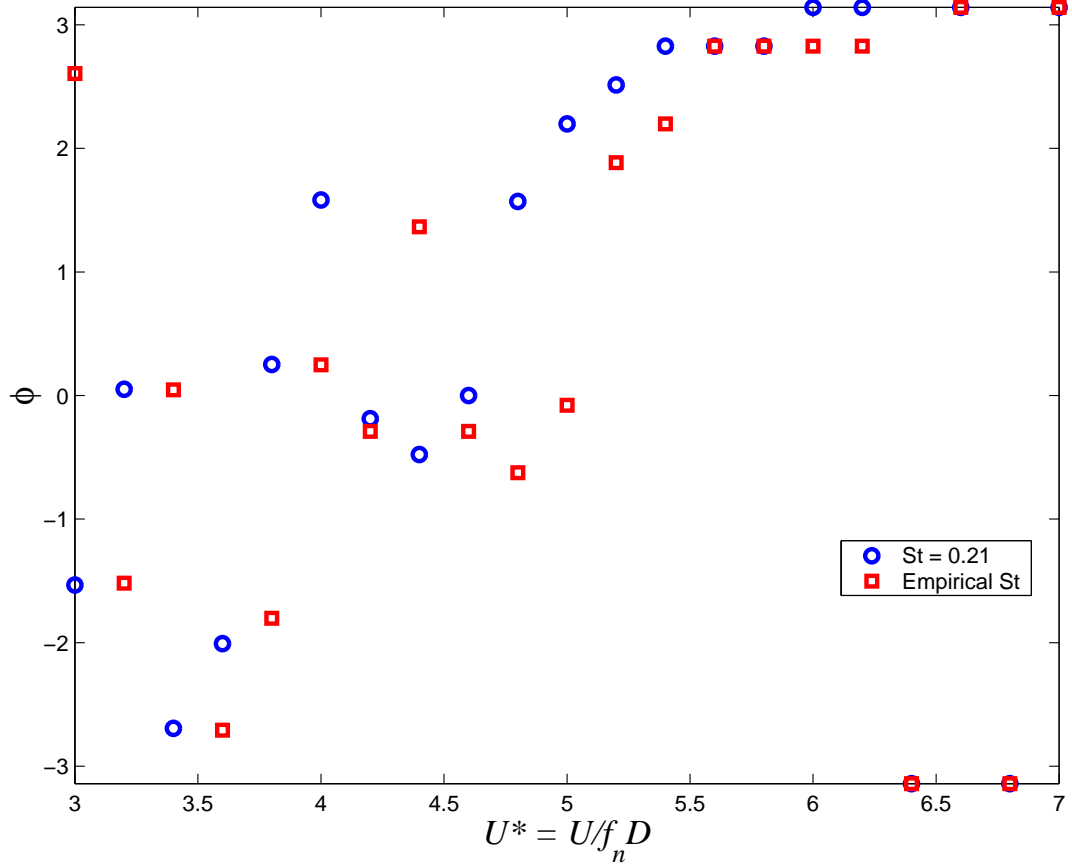


Figure 5.3: Comparison of the phase-shift response for the implementation a Reynolds-number-based Strouhal number to a constant Strouhal number.

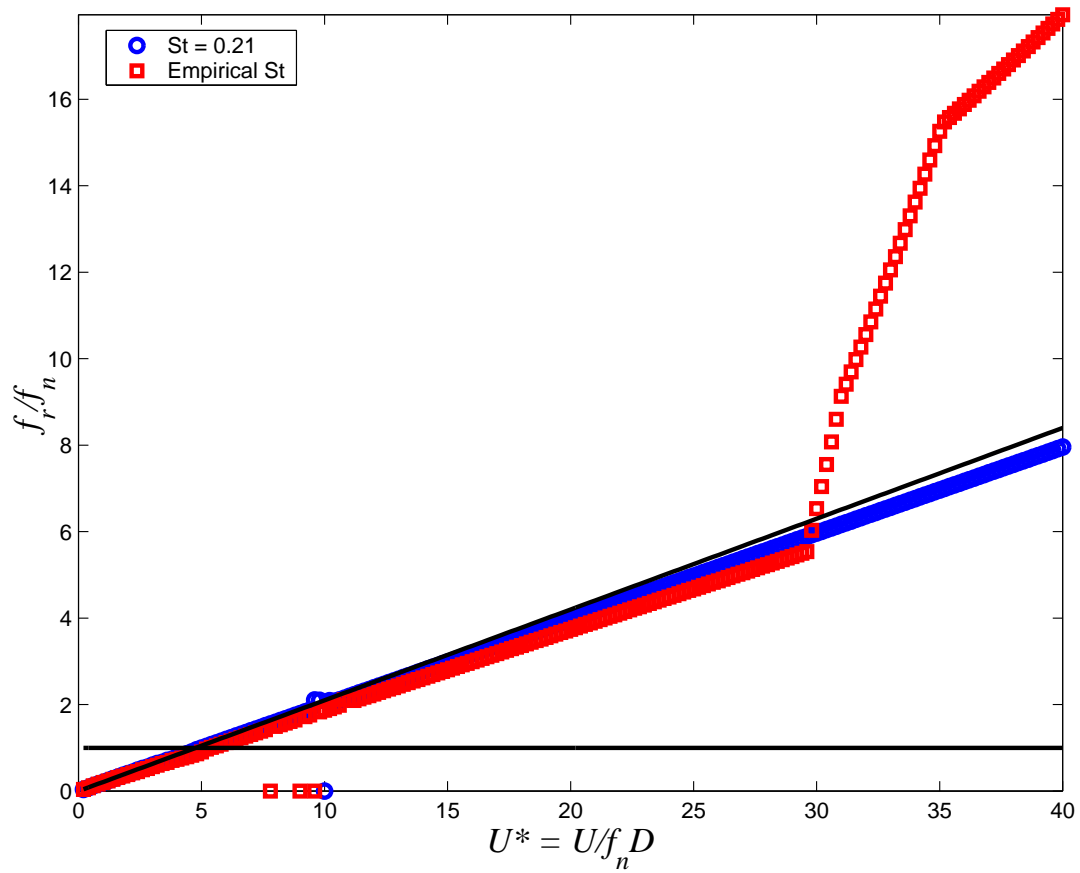


Figure 5.4: Comparison of the vortex-shedding frequency response for the implementation of a Reynolds-number-based Strouhal number to a constant Strouhal number.

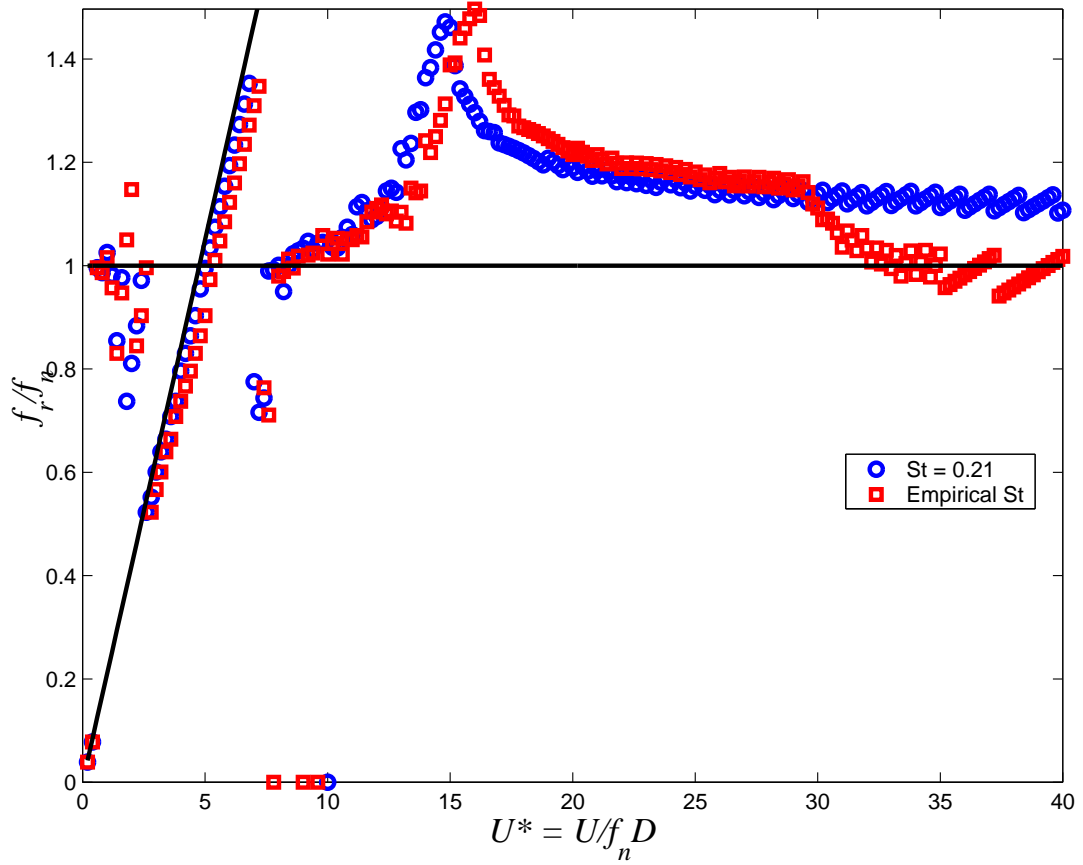


Figure 5.5: Comparison of the cylinder frequency response for the implementation of a Reynolds-number-based Strouhal number to a constant Strouhal number.



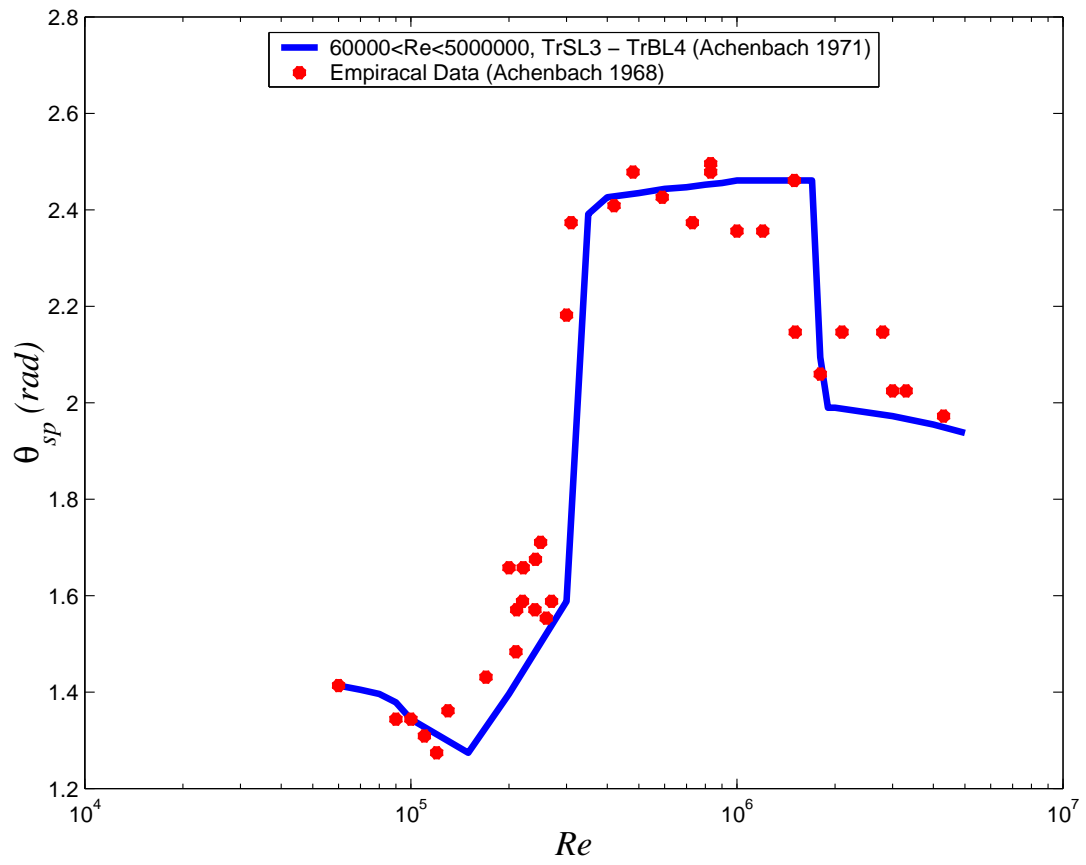


Figure 5.6: The position of the separation point over Reynolds number for a stationary cylinder with points originally from Achenbach (1968) (Sumer and Fredsøe 1997).

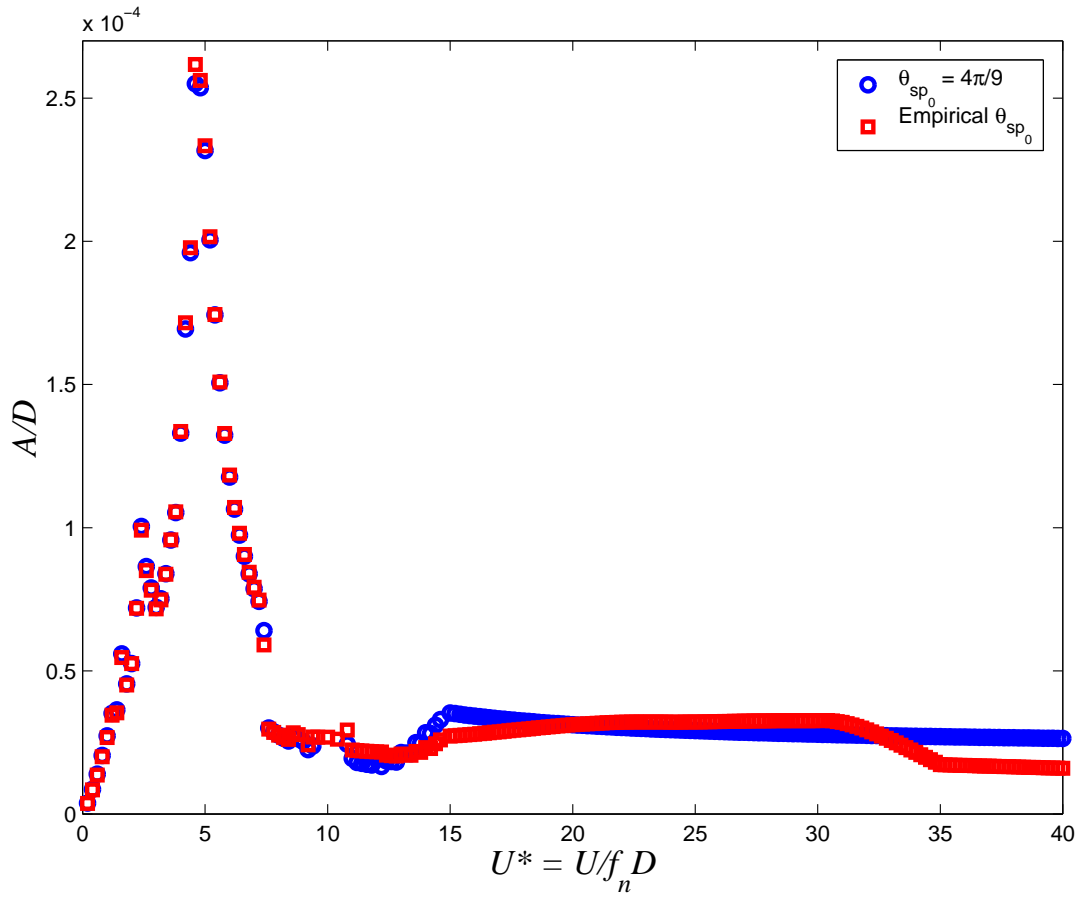


Figure 5.7: Comparison of the amplitude response for the implementation of a Reynolds-number-based separation point to a constant separation point.

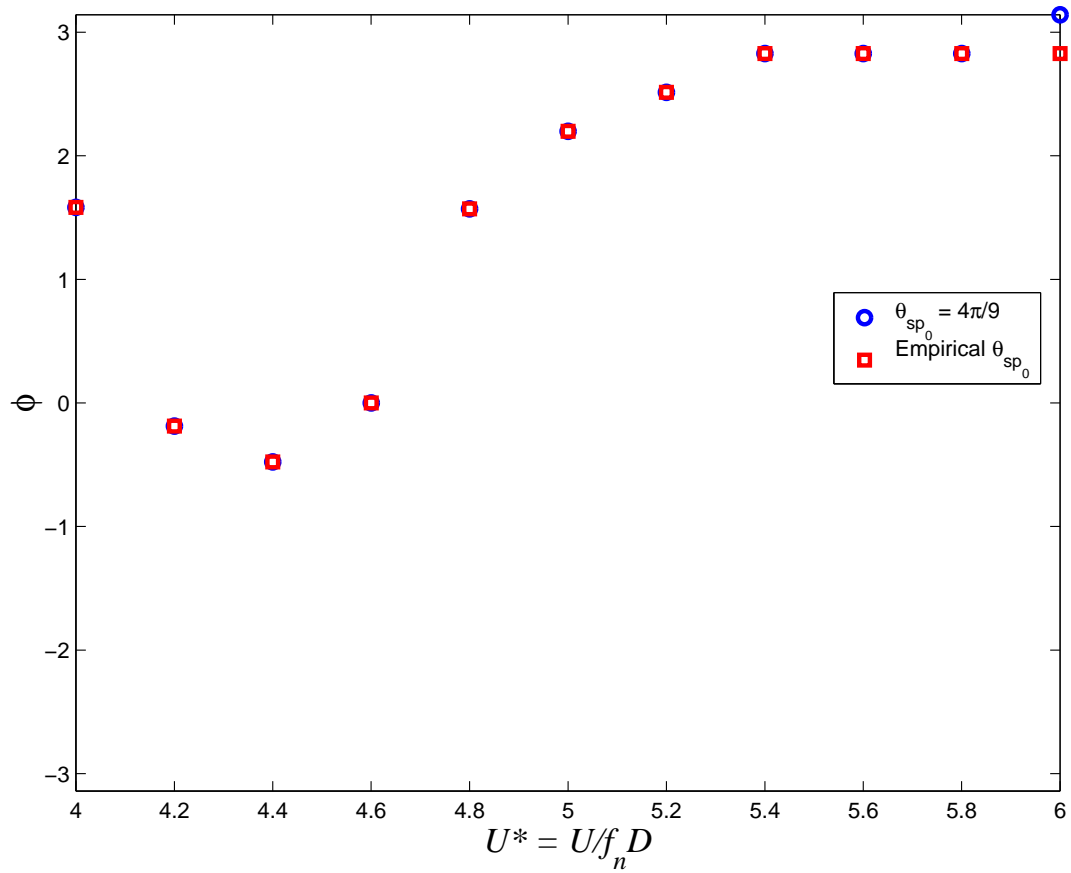


Figure 5.8: Comparison of the phase-shift response for the implementation of a Reynolds-number-based separation point to a constant separation point.

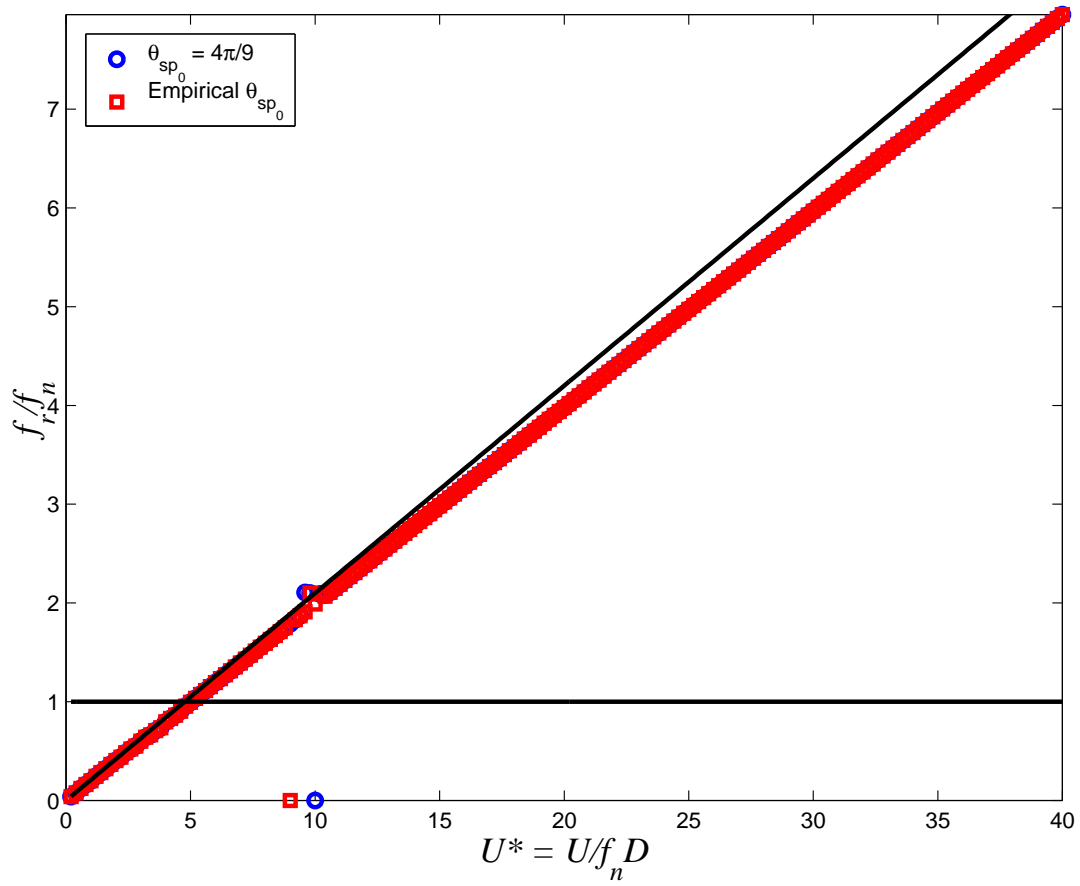


Figure 5.9: Comparison of the vortex-shedding frequency response for the implementation of a Reynolds-number-based separation point to a constant separation point.

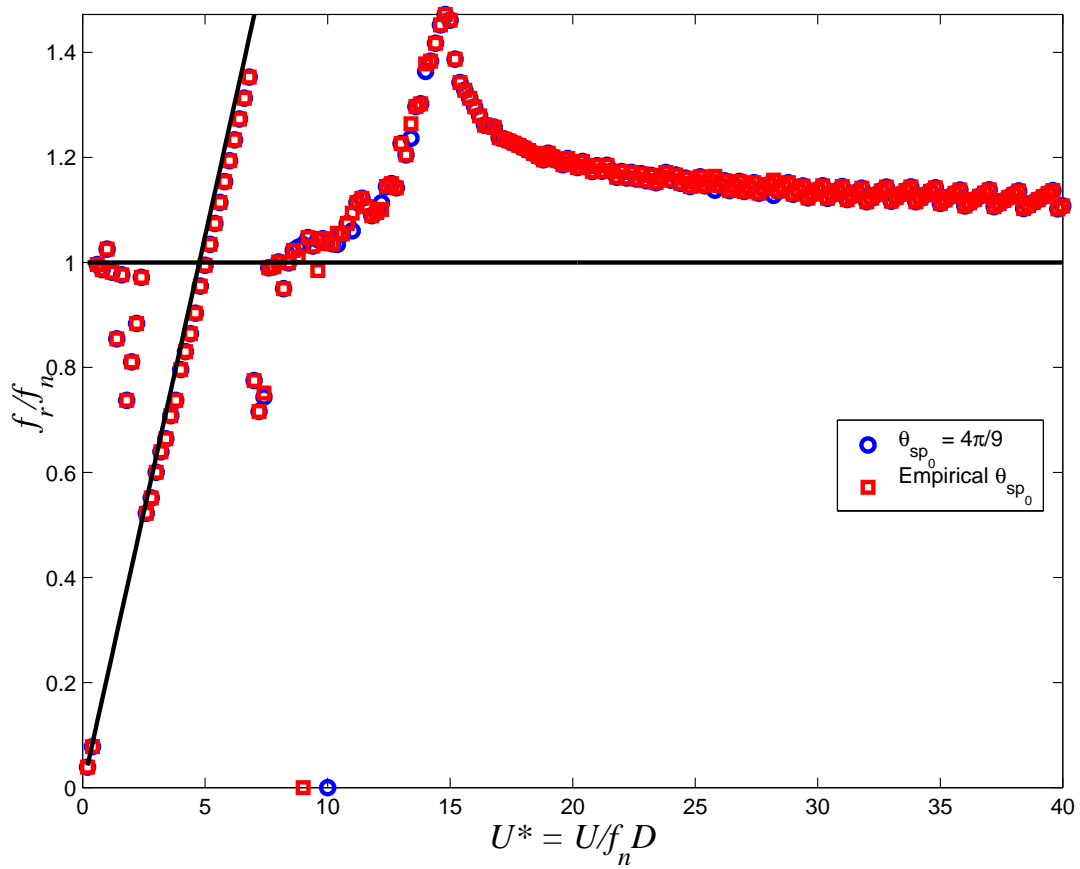


Figure 5.10: Comparison of the cylinder frequency response for the implementation of a Reynolds-number-based separation point to a constant separation point.

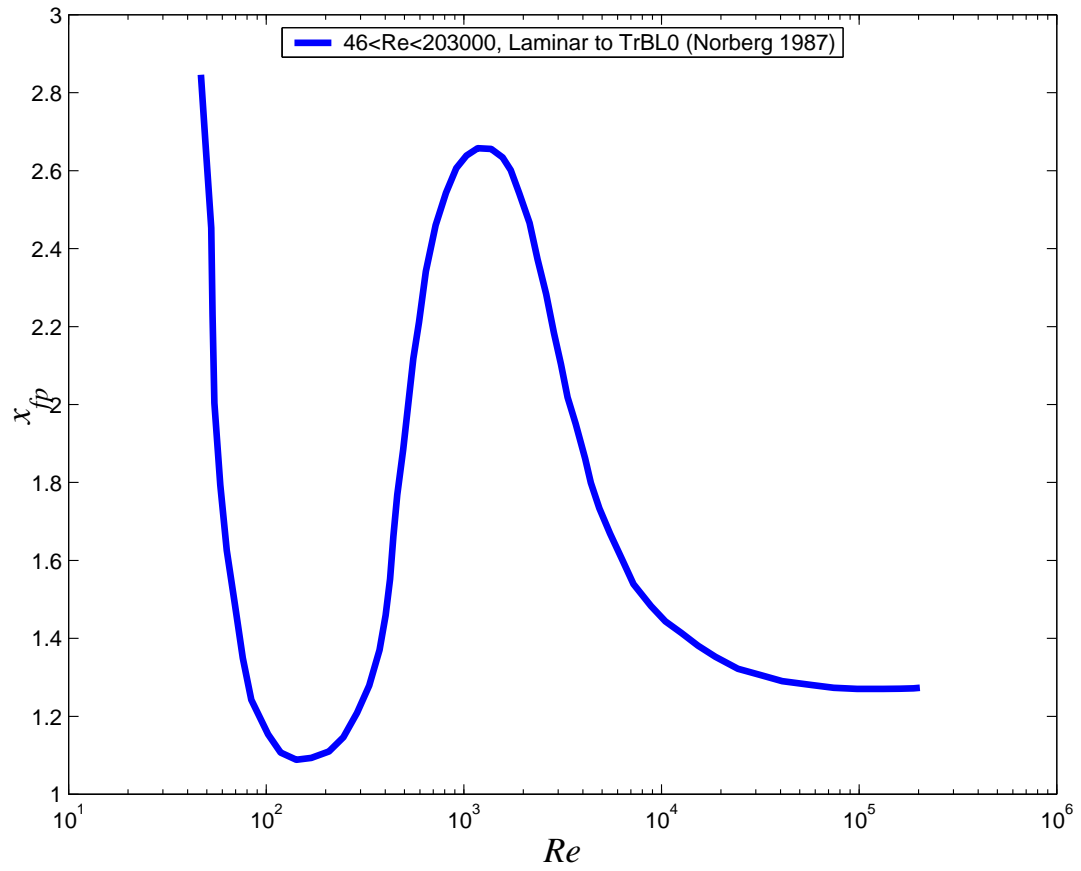


Figure 5.11: The formation length (formation point) from center of a stationary cylinder over Reynolds number (Norberg 1987b).

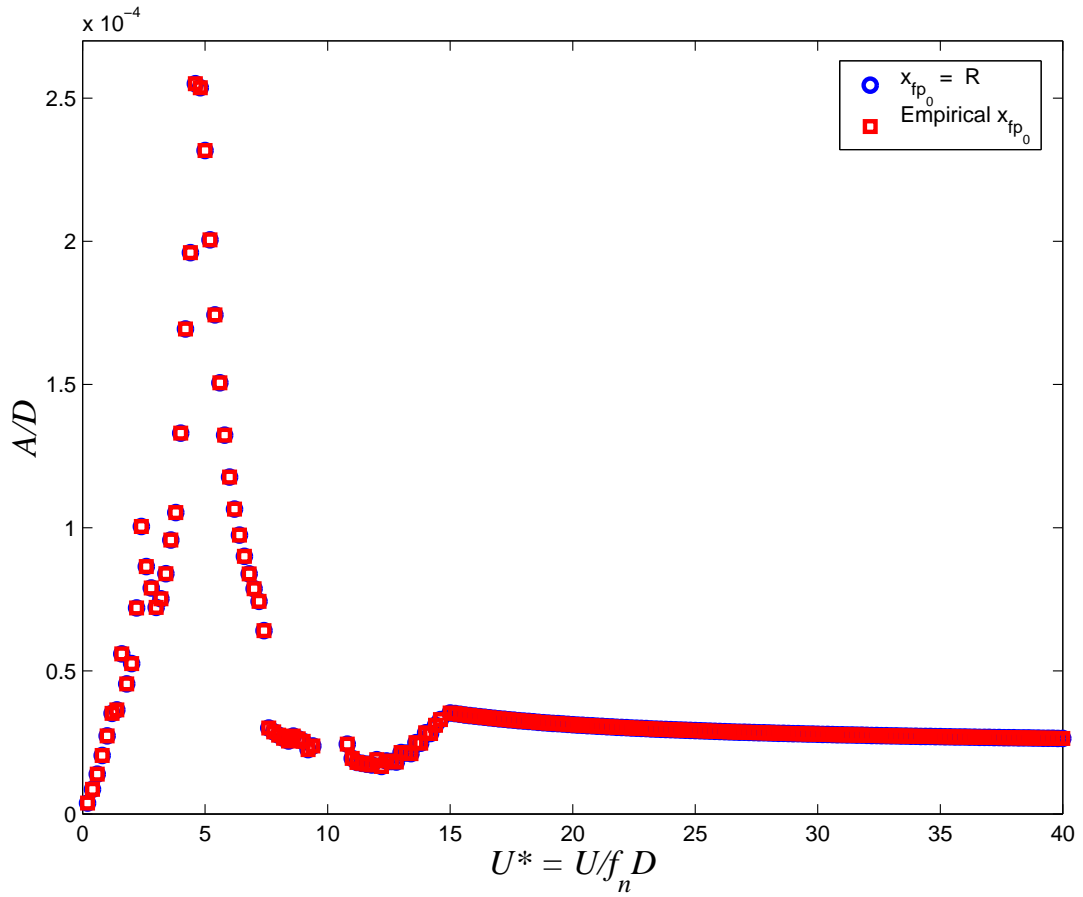


Figure 5.12: Comparison of the amplitude response for the implementation of a Reynolds-number-based formation point to a constant formation point.

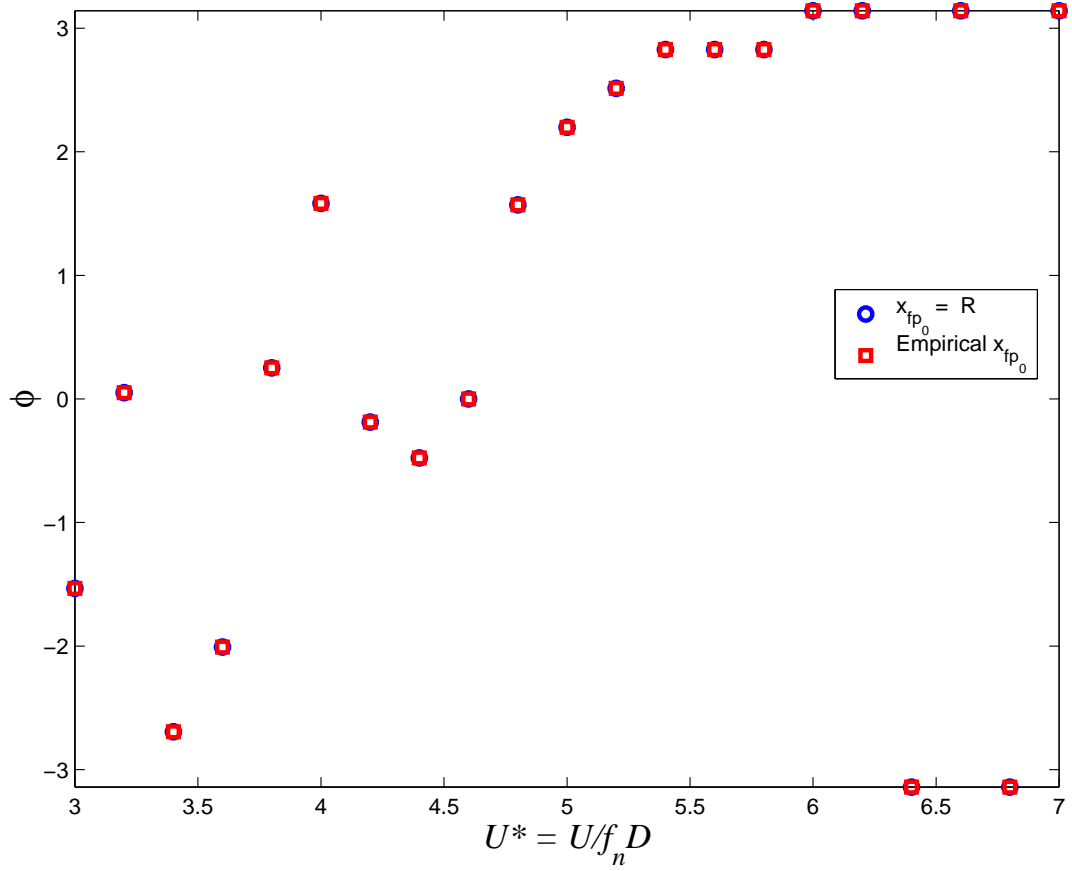


Figure 5.13: Comparison of the phase-shift response for the implementation of a Reynolds-number-based formation point to a constant formation point.



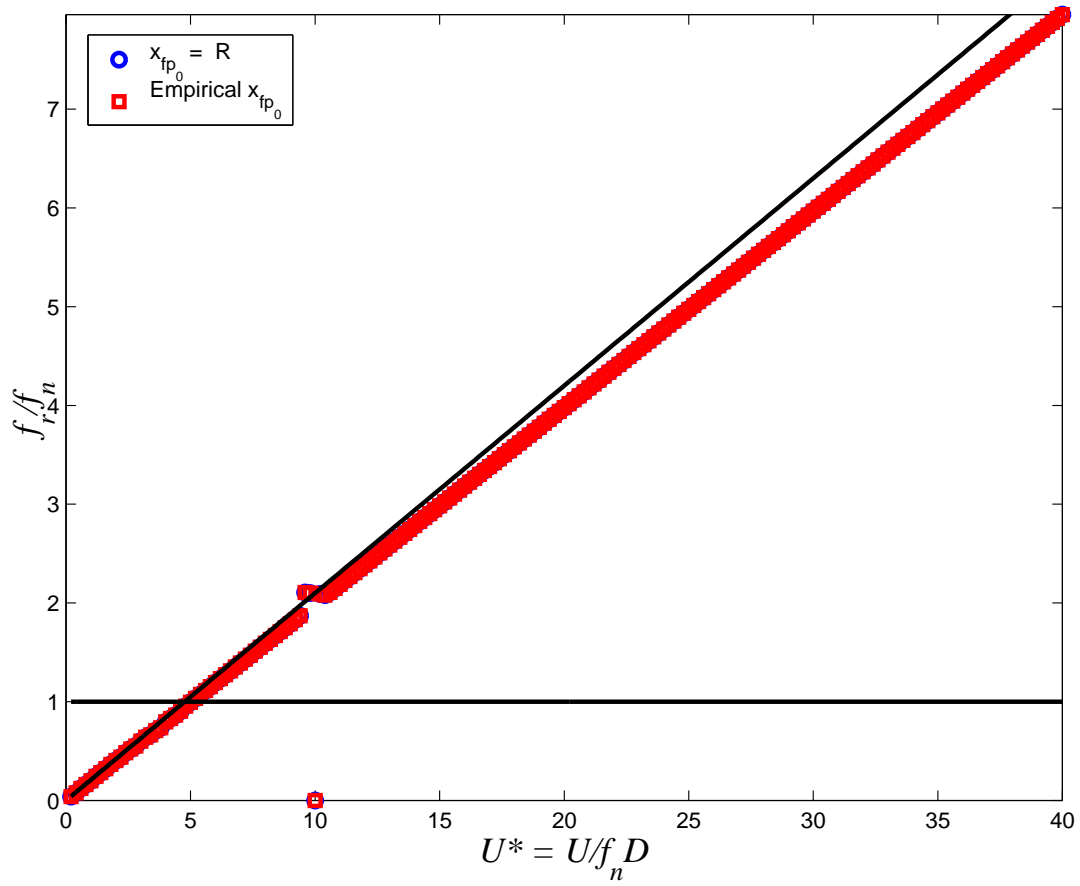


Figure 5.14: Comparison of the vortex-shedding frequency response for the implementation of a Reynolds-number-based formation point to a constant formation point.

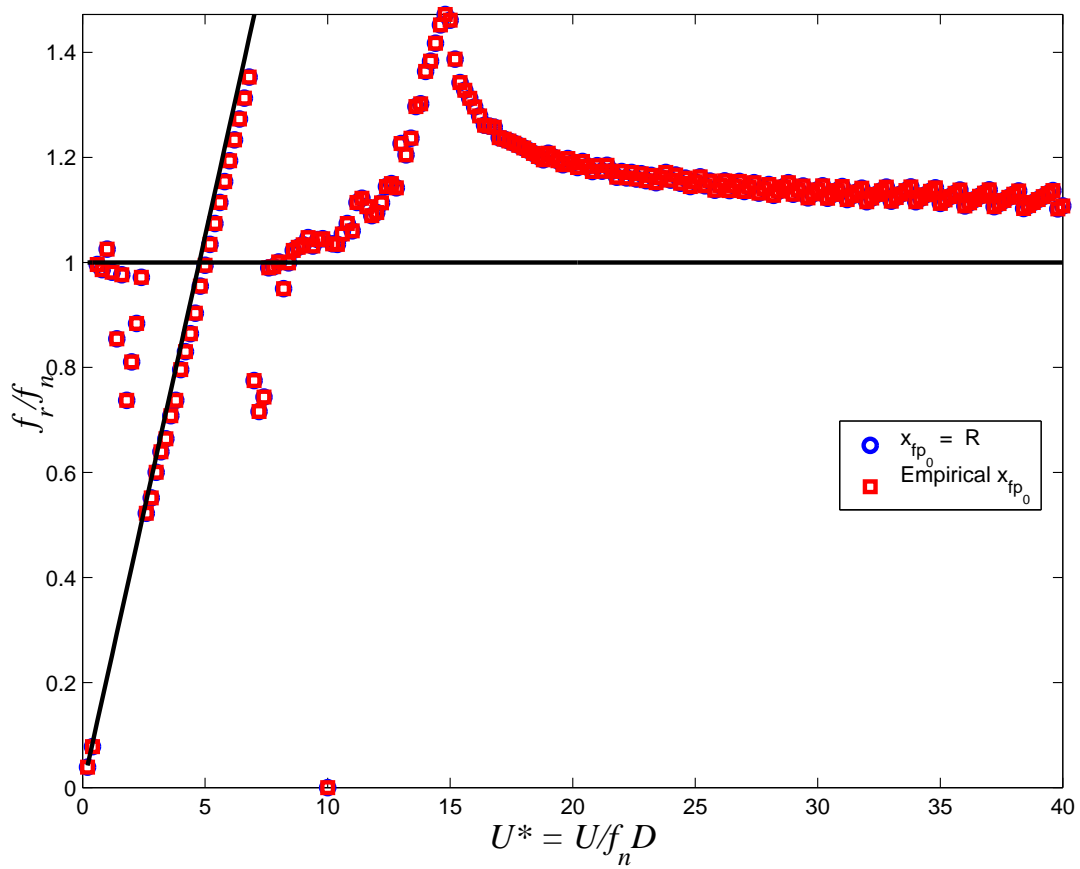


Figure 5.15: Comparison of the cylinder frequency response for the implementation of a Reynolds-number-based formation point to a constant formation point.

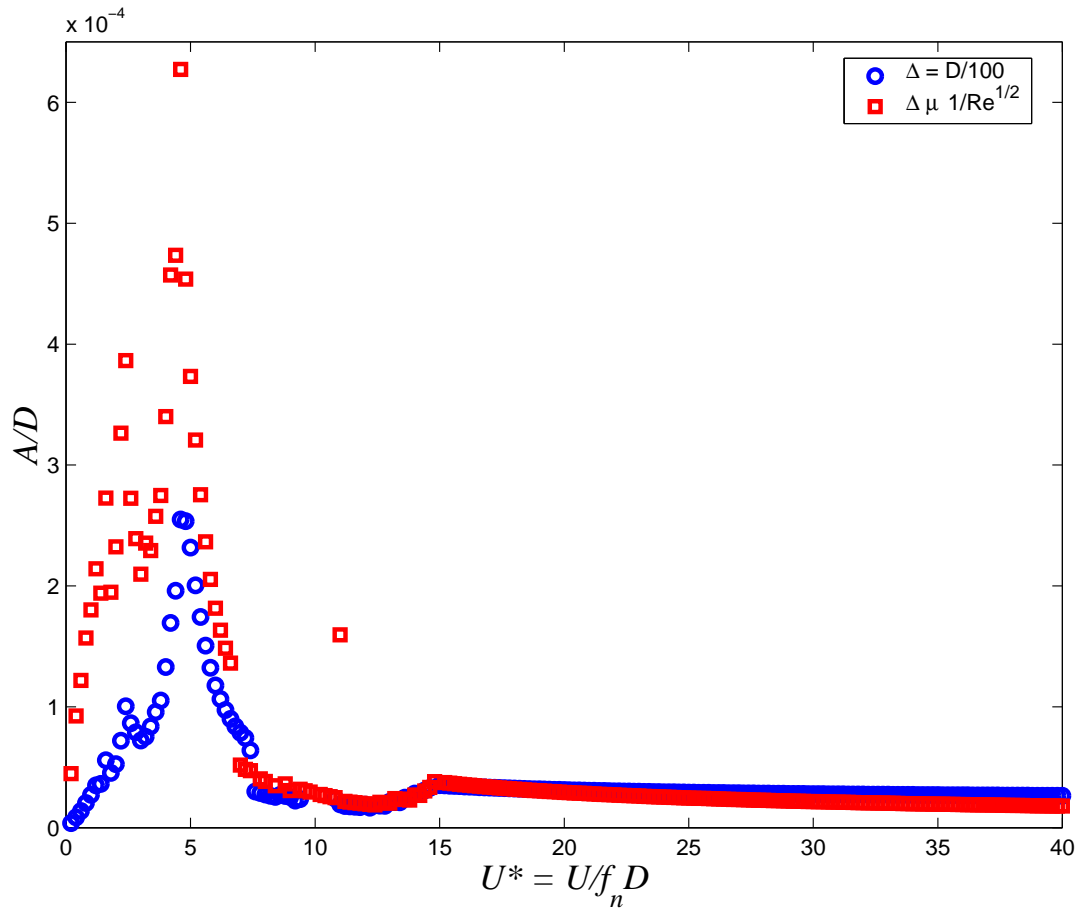


Figure 5.16: Comparison of the amplitude response for the implementation of a Reynolds-number-based maximum boundary-layer thickness to a constant maximum boundary-layer thickness.

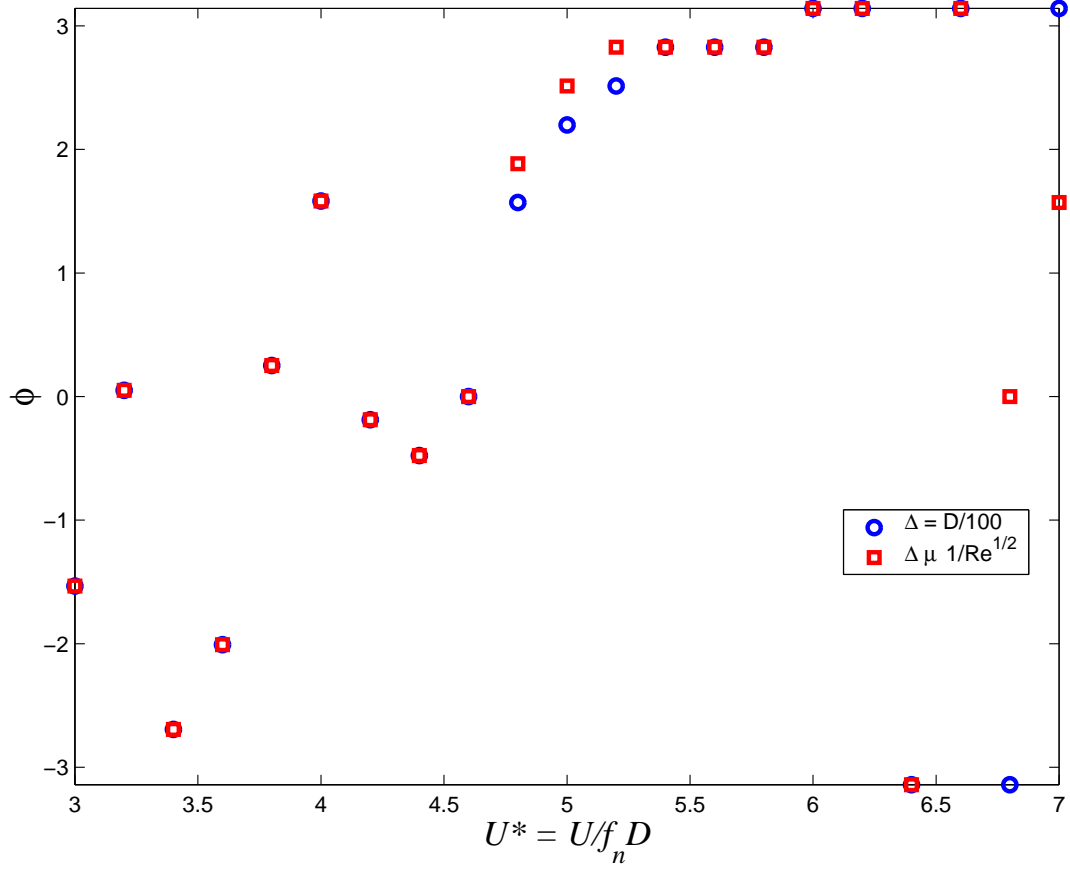


Figure 5.17: Comparison of the phase-shift response for the implementation of a Reynolds-number-based maximum boundary-layer thickness to a constant maximum boundary-layer thickness.

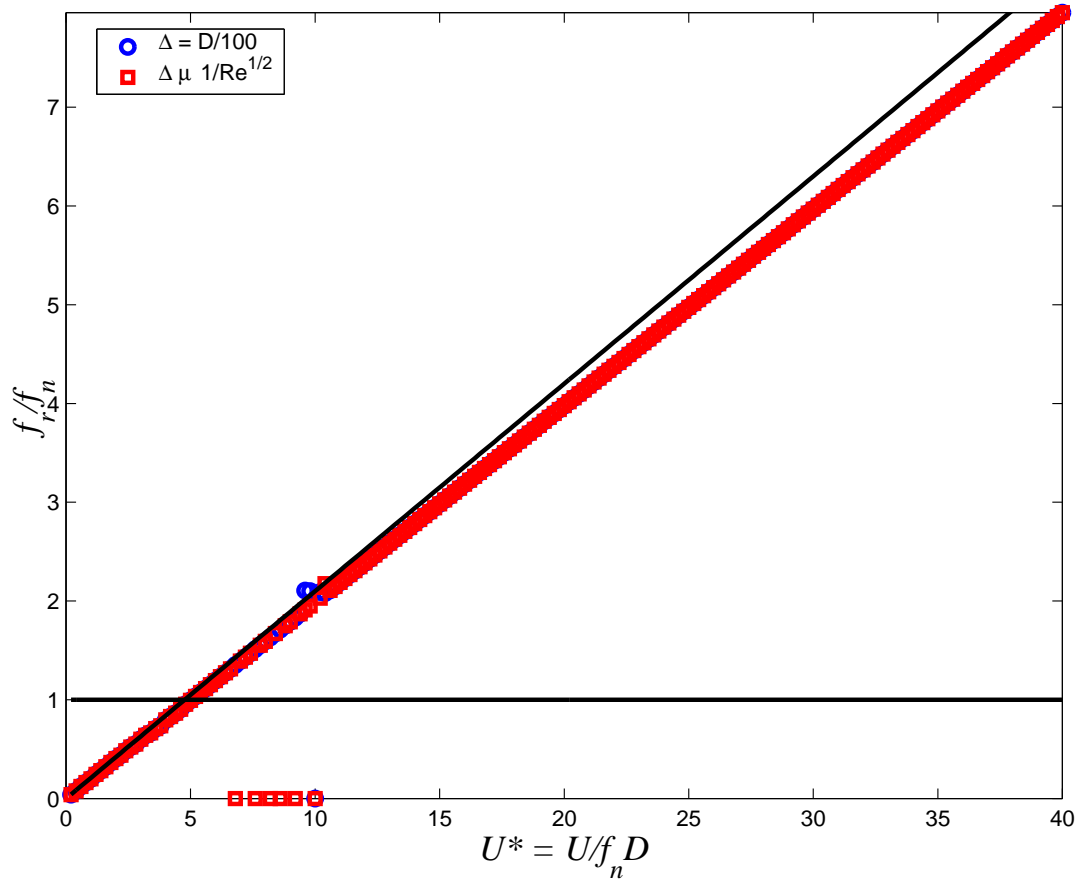


Figure 5.18: Comparison of the vortex-shedding frequency response for the implementation of a Reynolds-number-based maximum boundary-layer thickness to a constant maximum boundary-layer thickness.

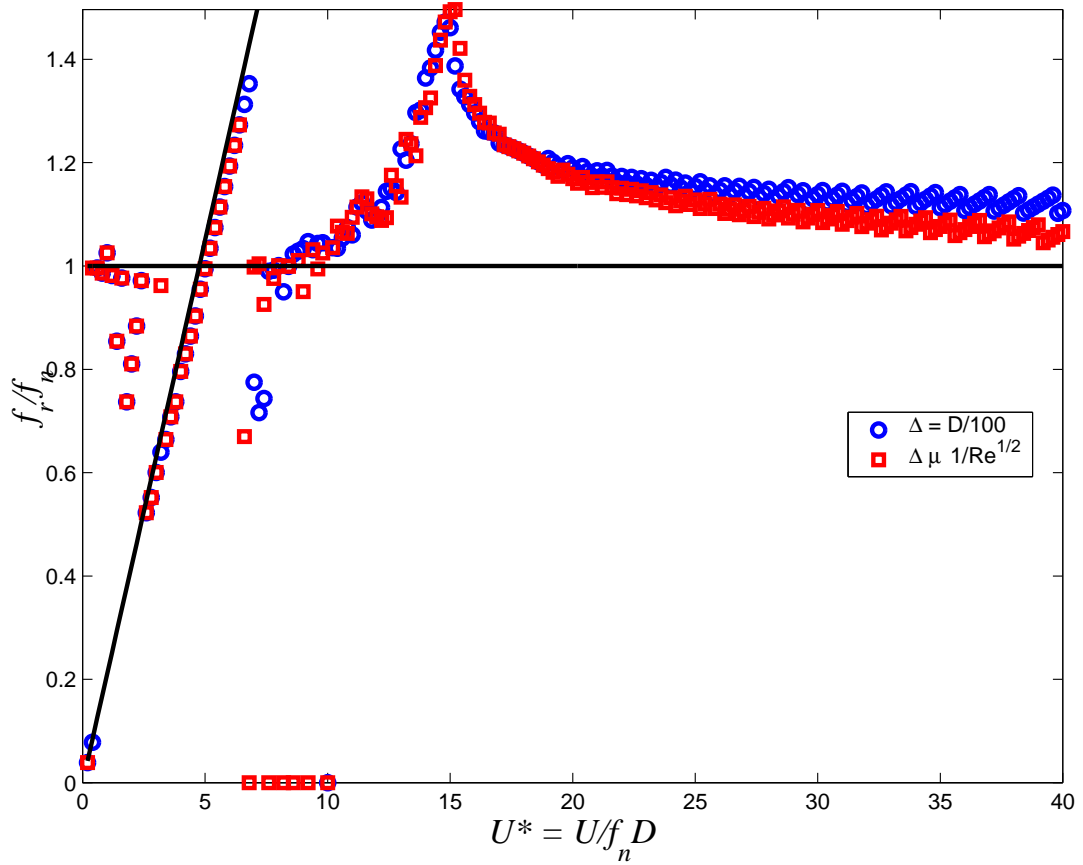


Figure 5.19: Comparison of the cylinder frequency response for the implementation of a Reynolds-number-based maximum boundary-layer thickness to a constant maximum boundary-layer thickness.

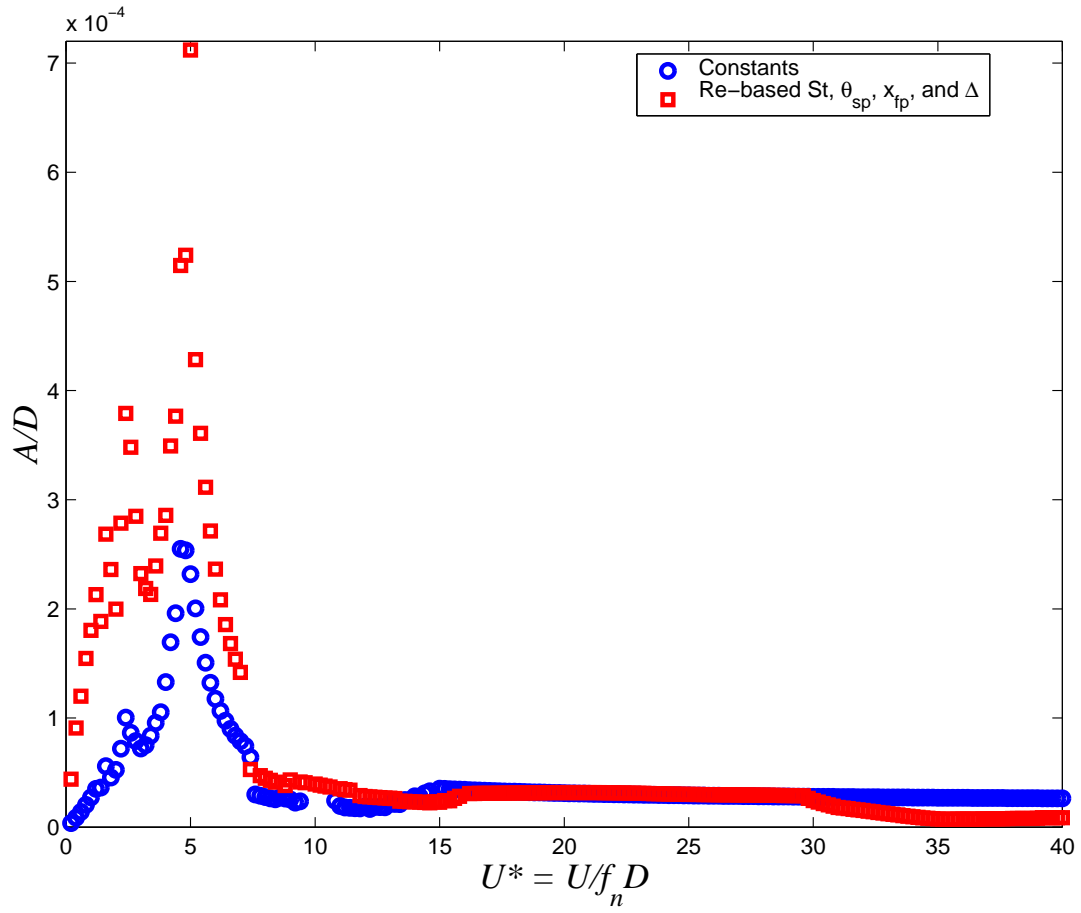


Figure 5.20: Comparison of the amplitude response for the implementation of a Reynolds-number-based Strouhal number, separation point, formation point, and maximum boundary-layer thickness to constant inputs.

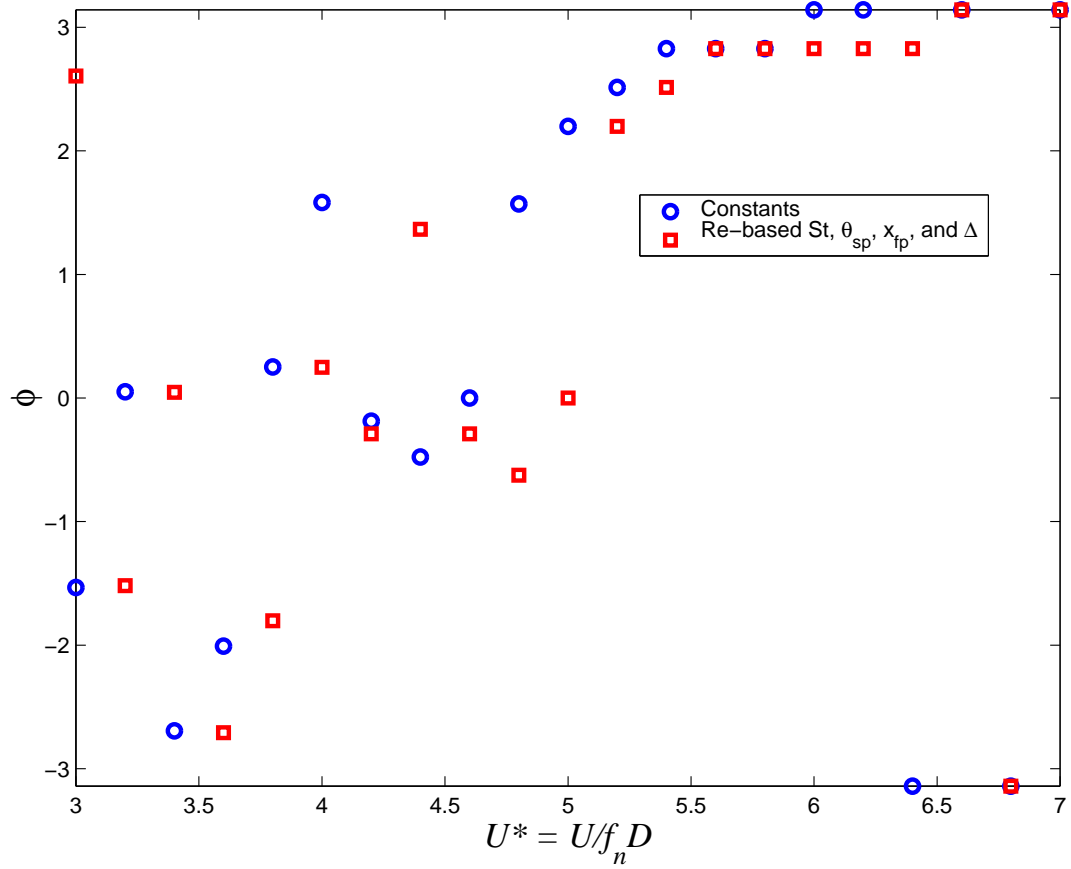


Figure 5.21: Comparison of the phase-shift response for the implementation of a Reynolds-number-based Strouhal number, separation point, formation point, and maximum boundary-layer thickness to constant inputs.



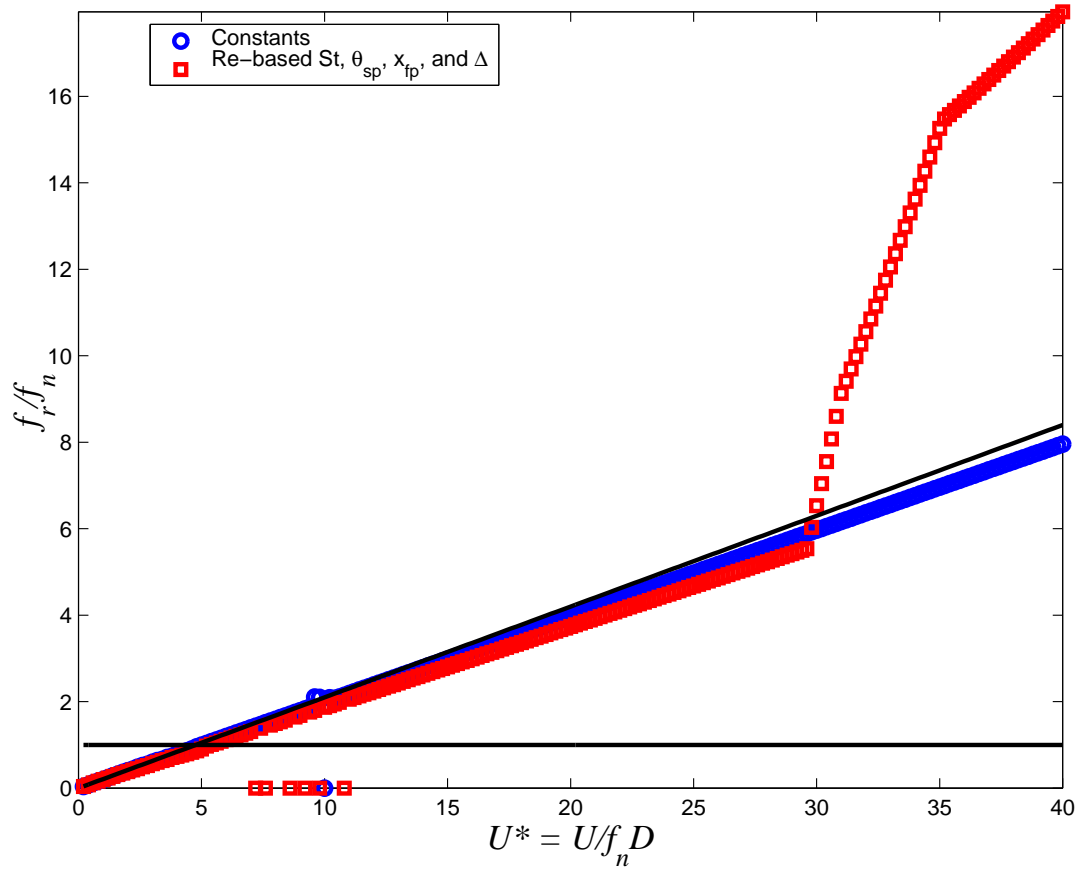


Figure 5.22: Comparison of the vortex-shedding frequency response for the implementation of a Reynolds-number-based Strouhal number, separation point, formation point, and maximum boundary-layer thickness to constant inputs.

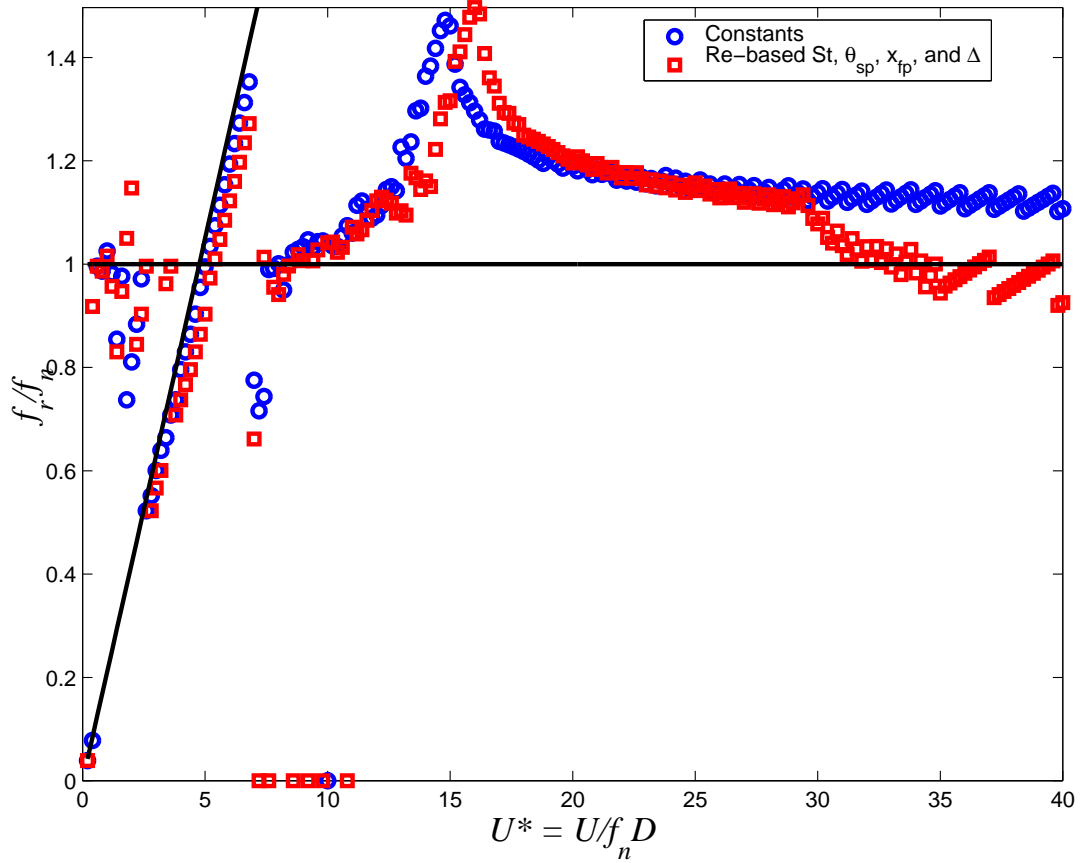


Figure 5.23: Comparison of the cylinder frequency response for the implementation of a Reynolds-number-based Strouhal number, separation point, formation point, and maximum boundary-layer thickness to constant inputs.

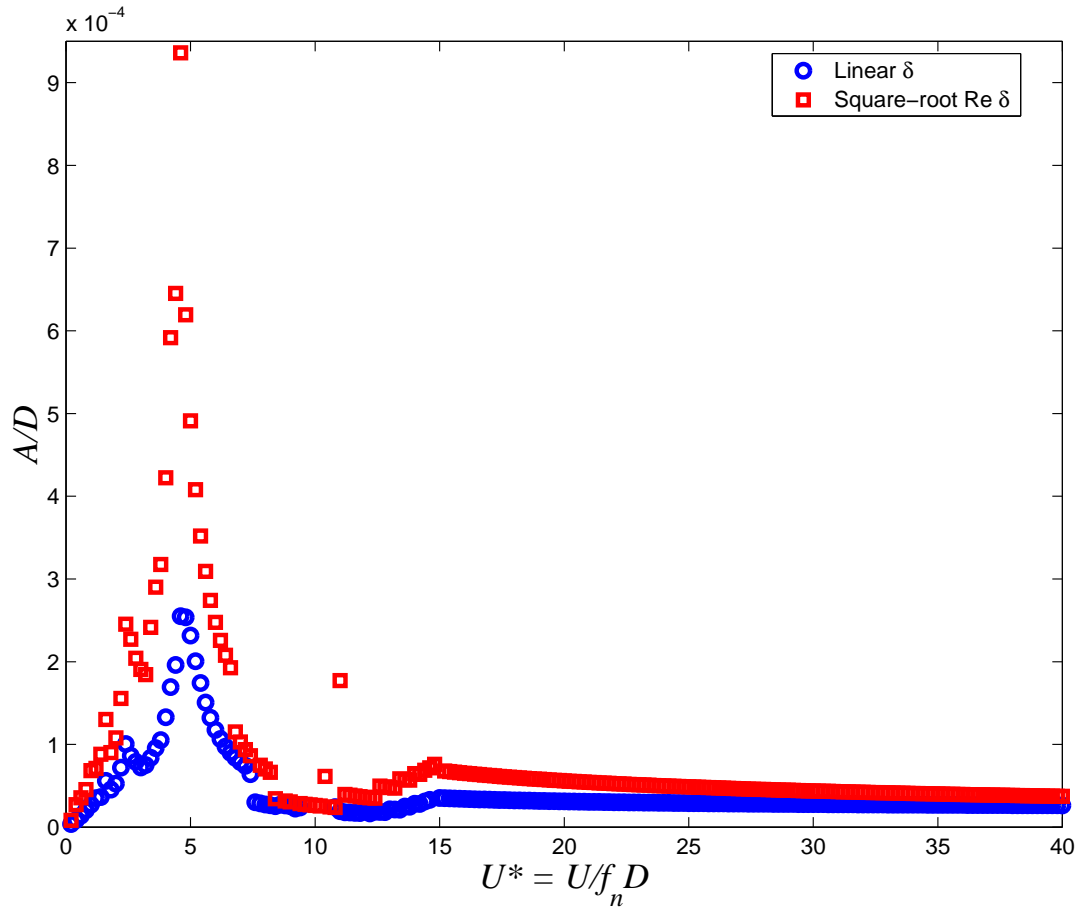


Figure 5.24: Comparison of the amplitude response for the implementation of a Reynolds-number-based boundary-layer growth (square-root of arc-length) to a linear boundary-layer growth.

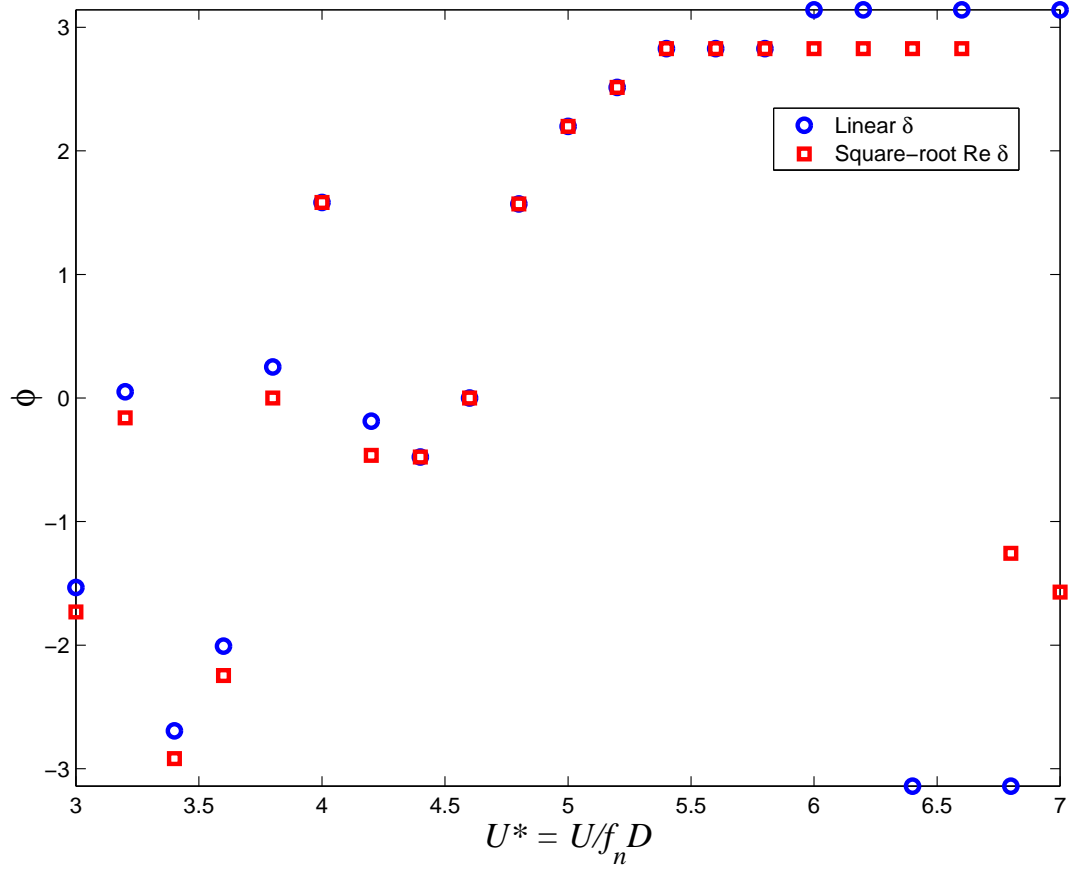


Figure 5.25: Comparison of the phase-shift response for the implementation of a Reynolds-number-based boundary-layer growth (square-root of arc-length) to a linear boundary-layer growth.

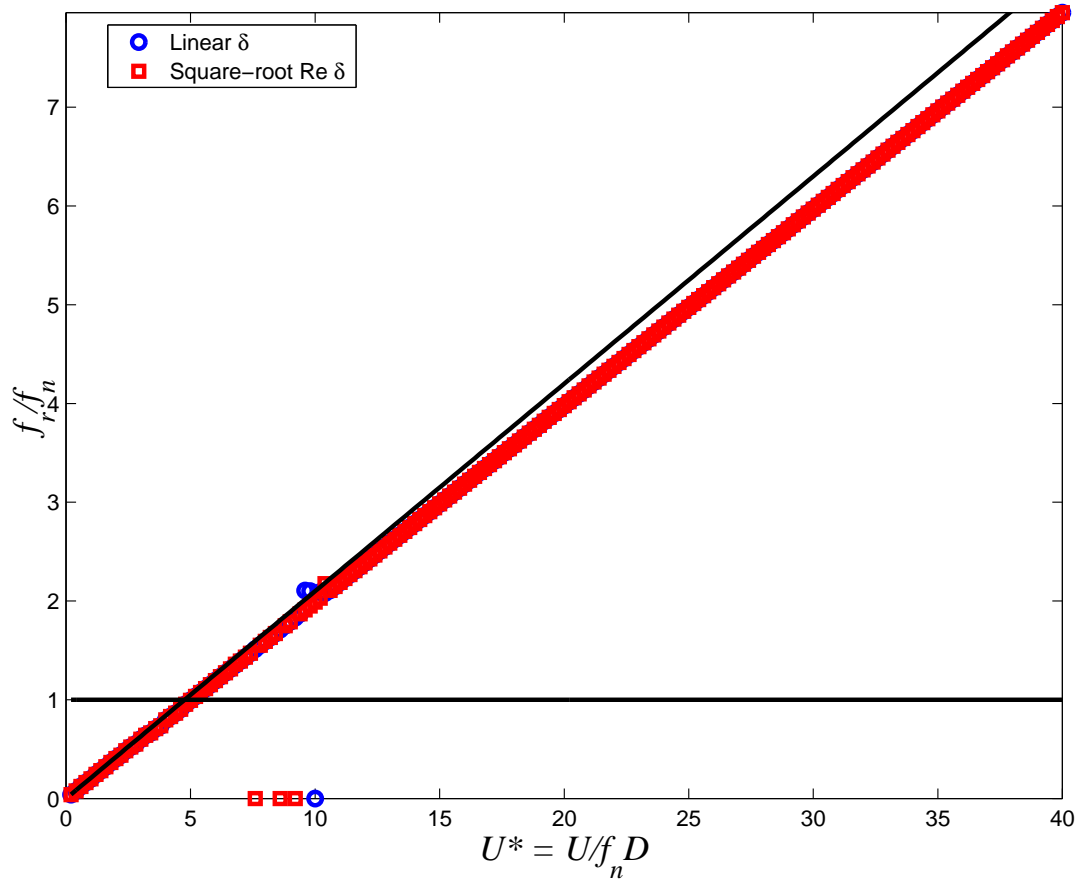


Figure 5.26: Comparison of the vortex-shedding frequency response for the implementation of a Reynolds-number-based boundary-layer growth (square-root of arc-length) to a linear boundary-layer growth.

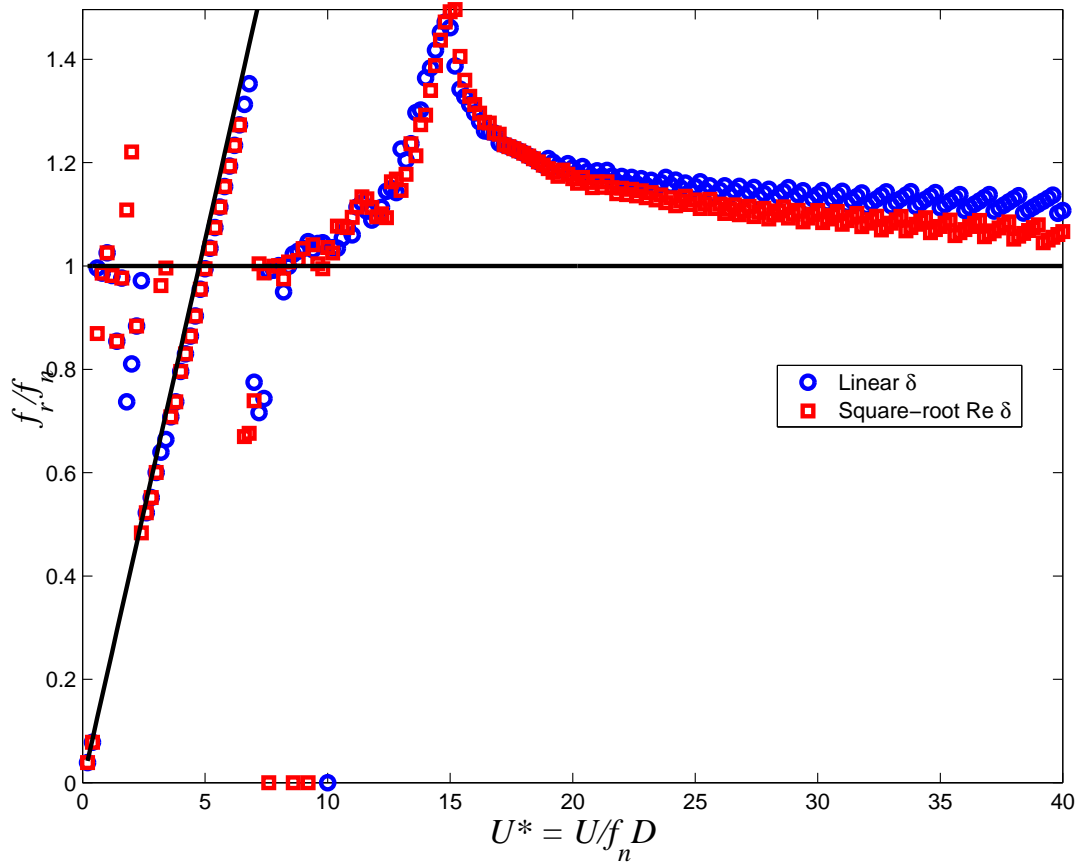


Figure 5.27: Comparison of the cylinder frequency response for the implementation of a Reynolds-number-based boundary-layer growth (square-root of arc-length) to a linear boundary-layer growth.

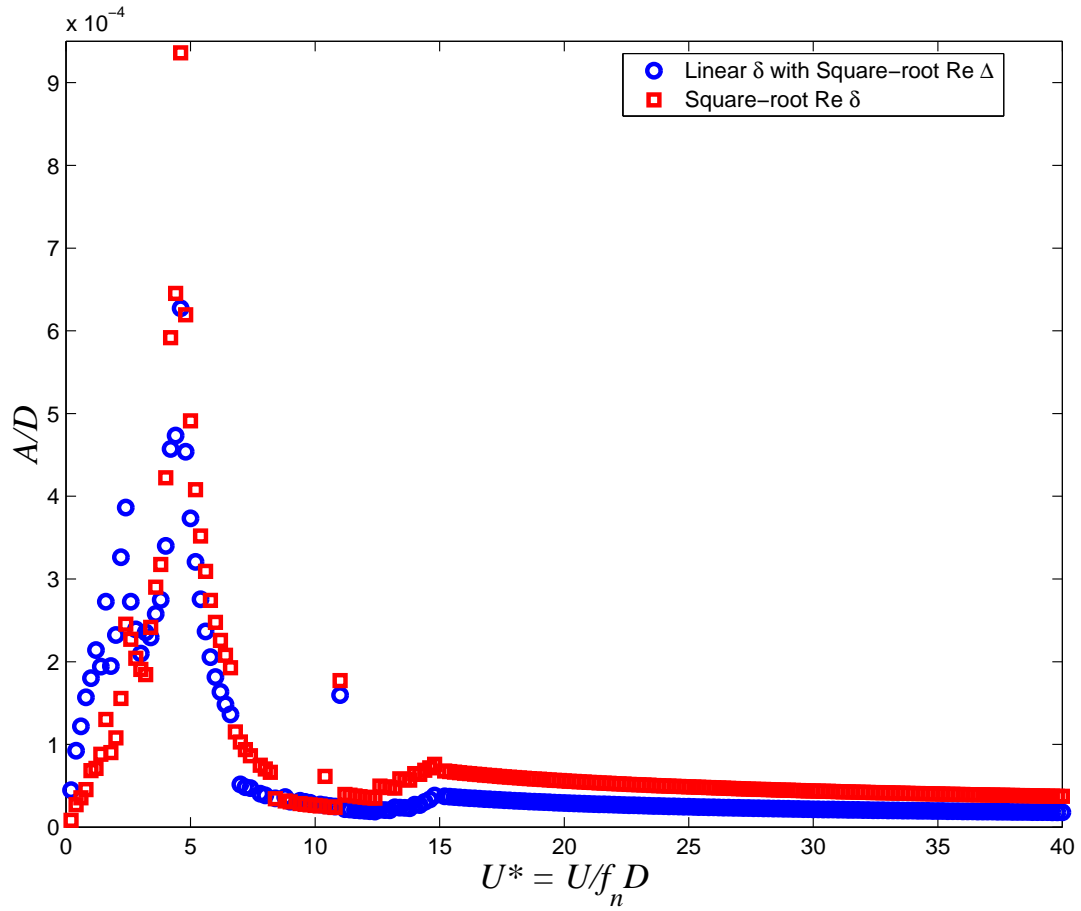


Figure 5.28: Comparison of the amplitude response for the implementation of a Reynolds-number-based boundary-layer growth (square-root of arc-length) to a linear boundary-layer growth with the same maximum boundary layer thickness.

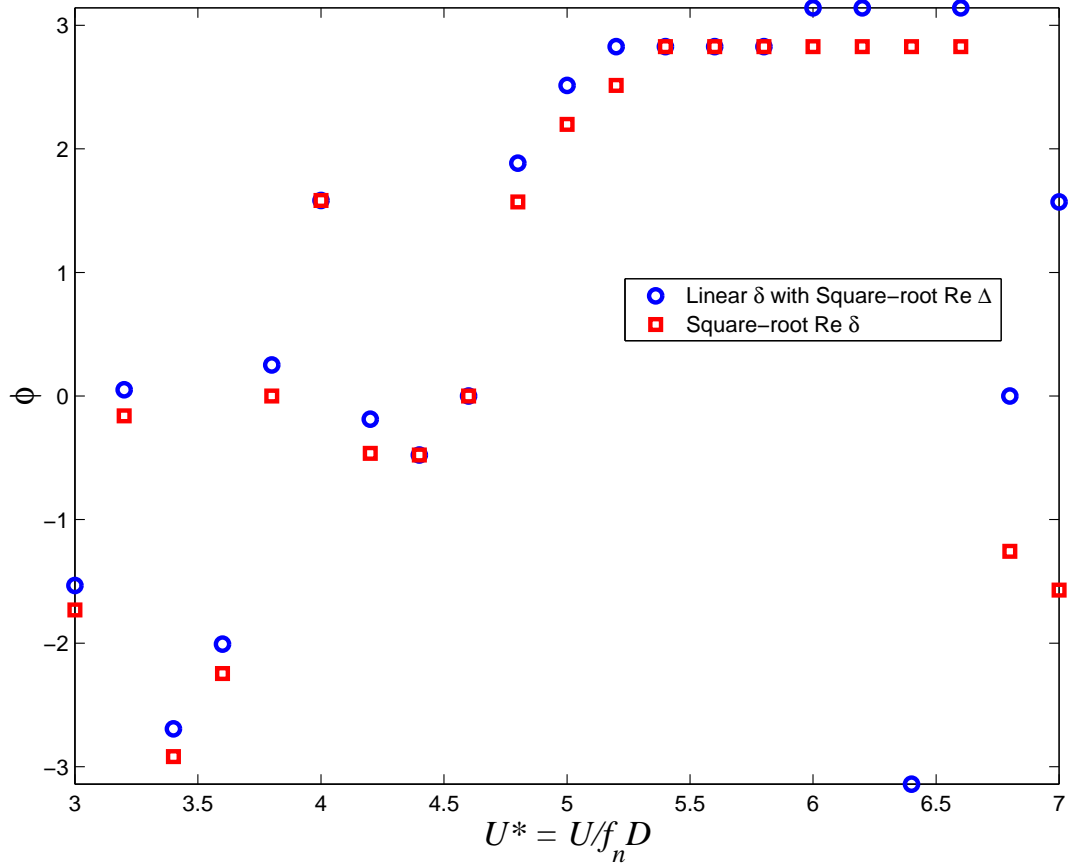


Figure 5.29: Comparison of the phase-shift response for the implementation of a Reynolds-number-based boundary-layer growth (square-root of arc-length) to a linear boundary-layer growth with the same maximum boundary layer thickness.



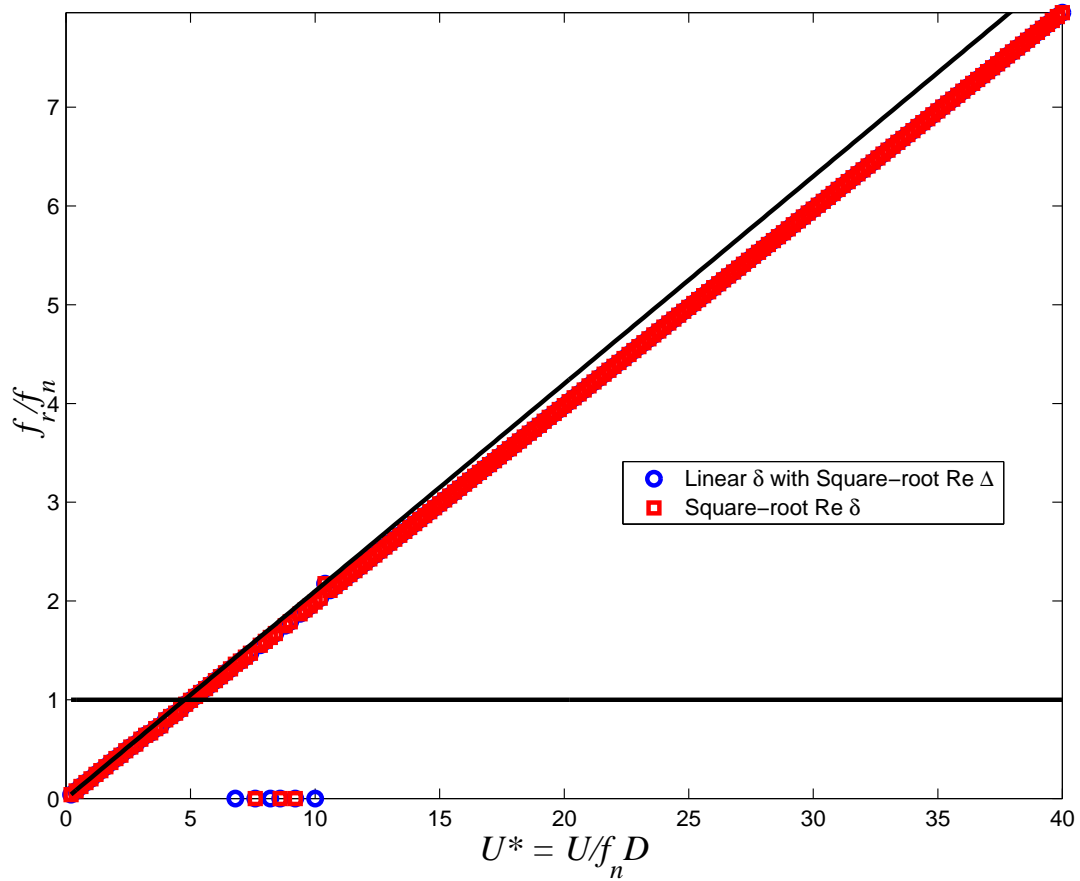


Figure 5.30: Comparison of the vortex-shedding frequency response for the implementation of a Reynolds-number-based boundary-layer growth (square-root of arc-length) to a linear boundary-layer growth with the same maximum boundary layer thickness.

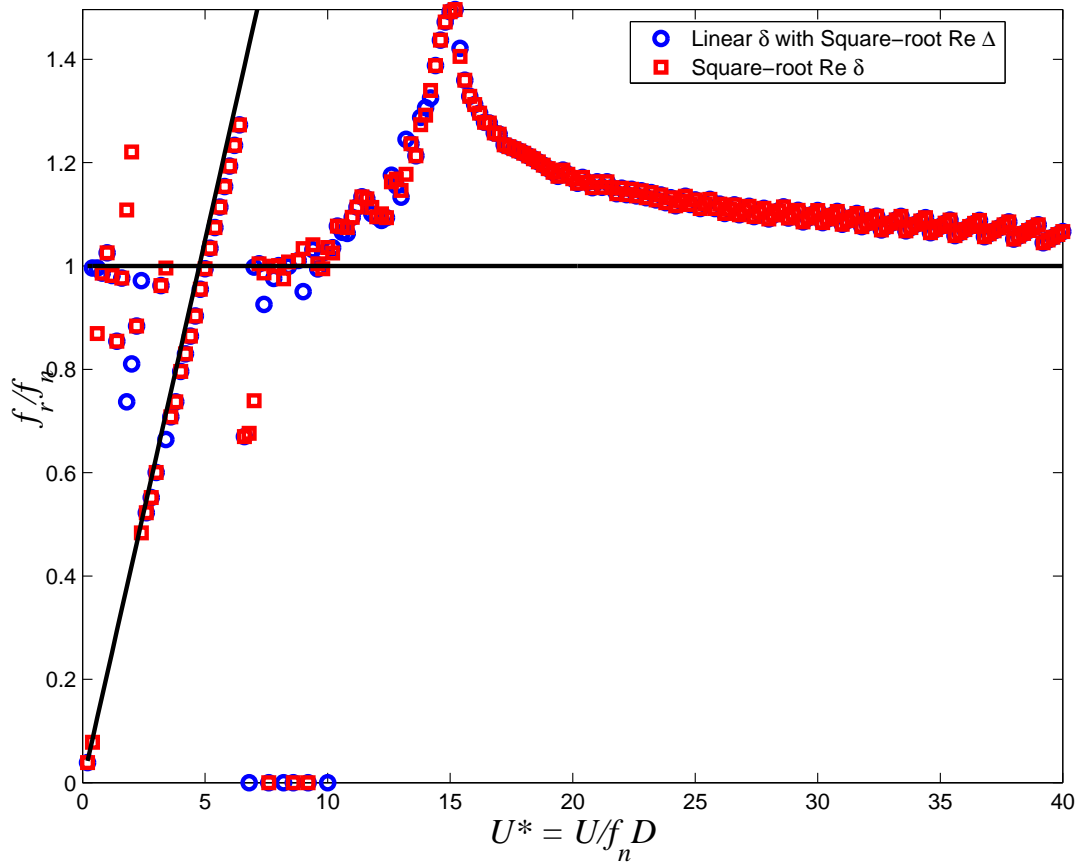


Figure 5.31: Comparison of the cylinder frequency response for the implementation of a Reynolds-number-based boundary-layer growth (square-root of arc-length) to a linear boundary-layer growth with the same maximum boundary layer thickness.

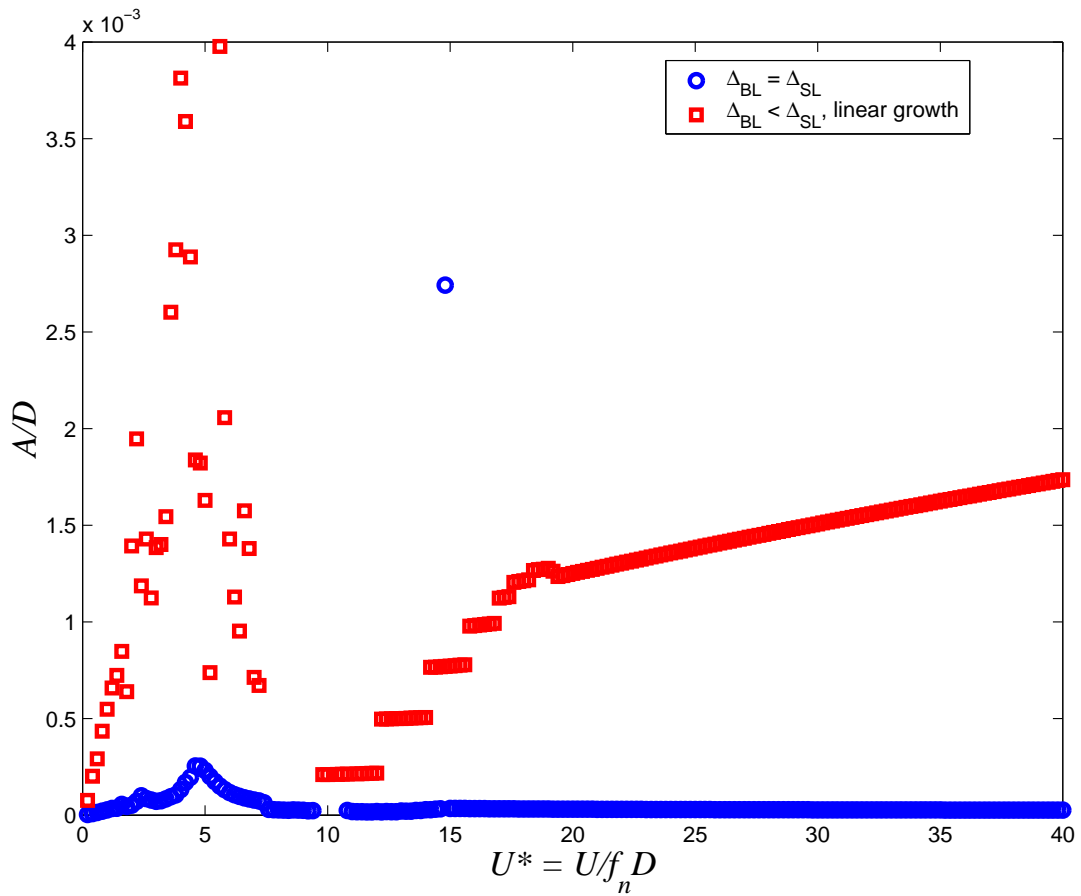


Figure 5.32: Comparison of the amplitude response for the implementation of a linear shear-layer growth with Reynolds number based maximum shear layer thickness with a constant shear layer thickness both with Reynolds number based maximum boundary layer thickness. The gap around reduced velocity 10 is the result of the response amplitude going to infinity.

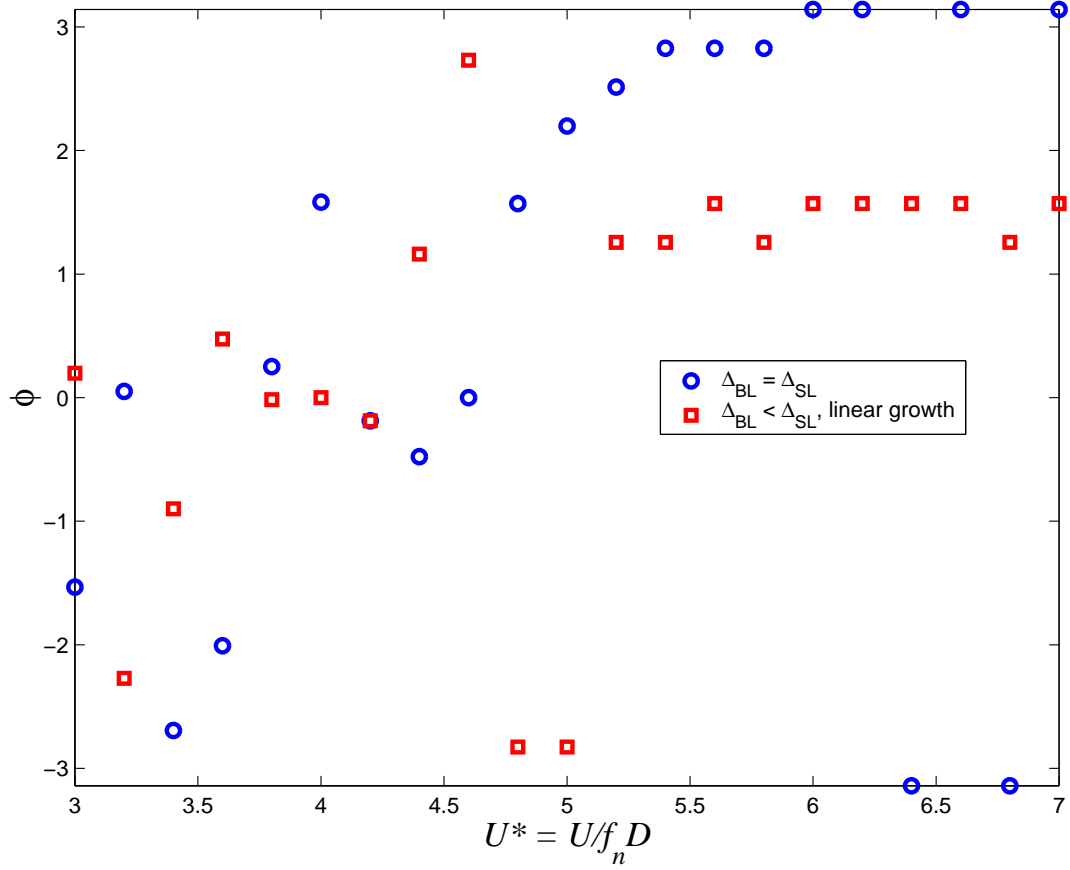


Figure 5.33: Comparison of the phase-shift response for the implementation of a linear shear-layer growth with Reynolds number based maximum shear layer thickness with a constant shear layer thickness both with Reynolds number based maximum boundary layer thickness.

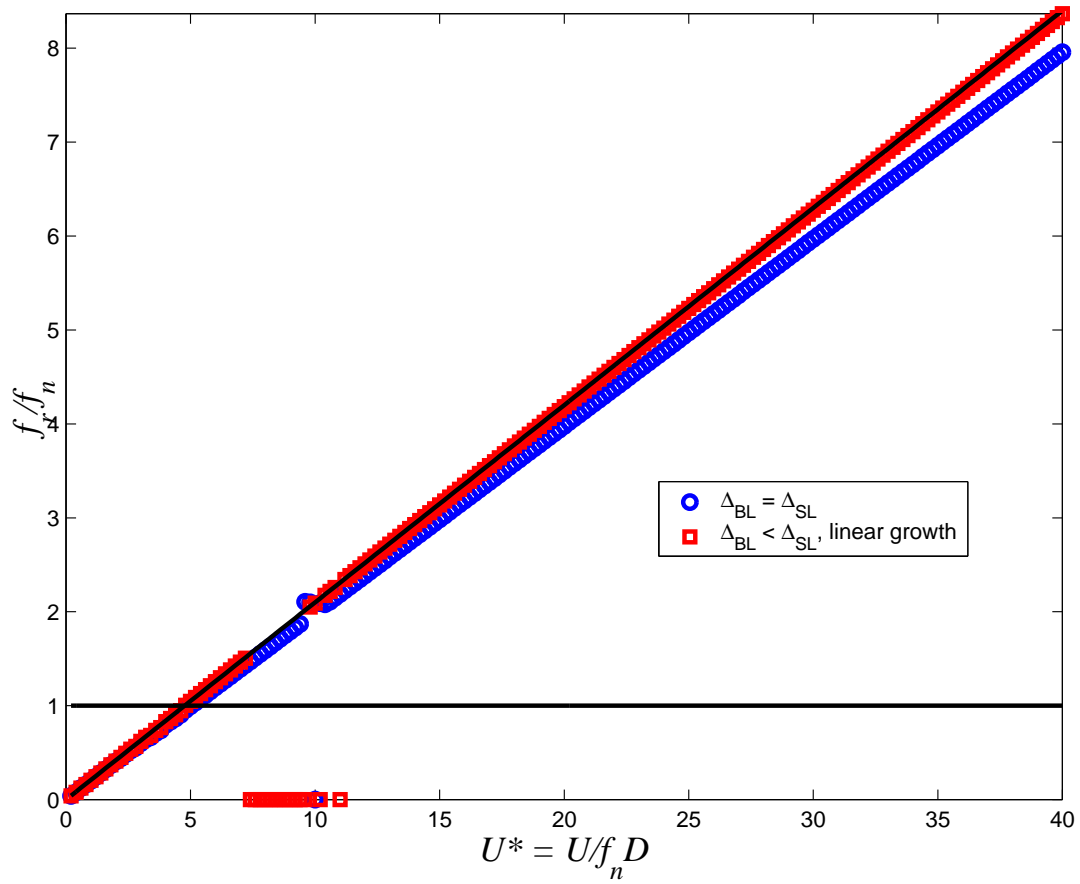


Figure 5.34: Comparison of the vortex-shedding frequency response for the implementation of a linear shear-layer growth with Reynolds number based maximum shear layer thickness with a constant shear layer thickness both with Reynolds number based maximum boundary layer thickness.

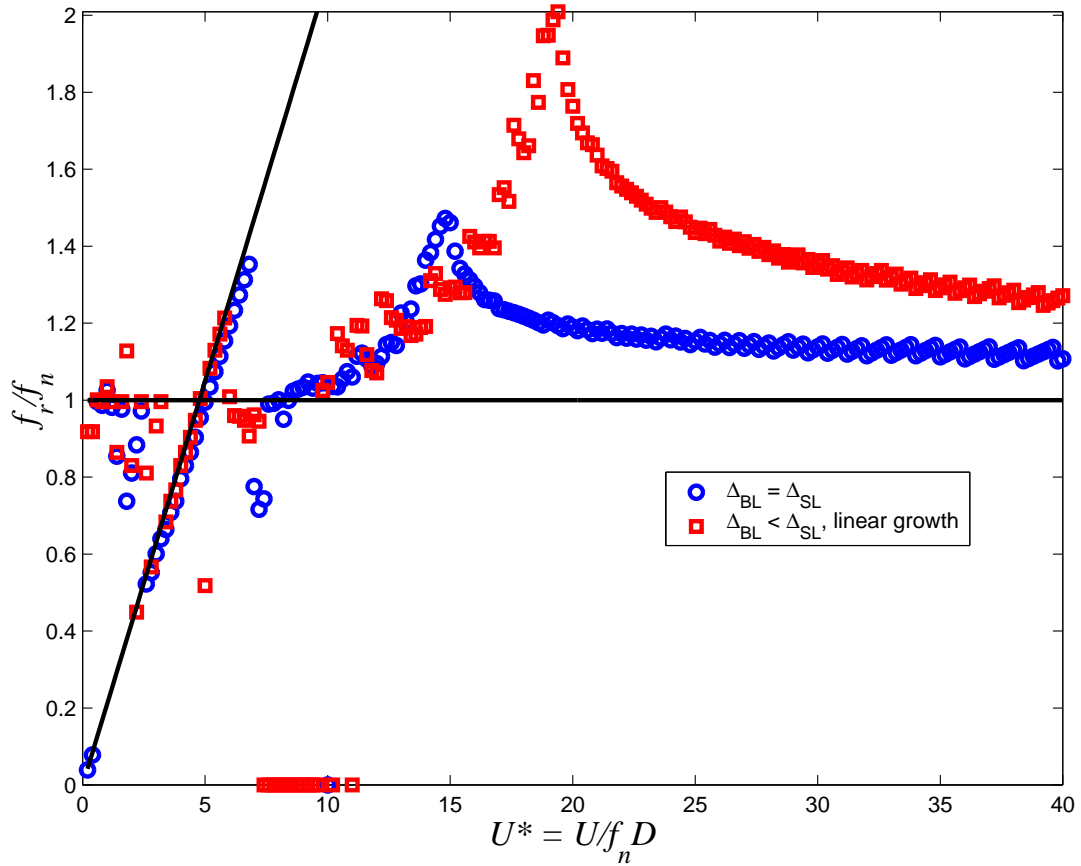


Figure 5.35: Comparison of the cylinder frequency response for the implementation of a linear shear-layer growth with Reynolds number based maximum shear layer thickness with a constant shear layer thickness both with Reynolds number based maximum boundary layer thickness. The frequency response points of zero correspond to infinite amplitude response, an inaccuracy of the model.

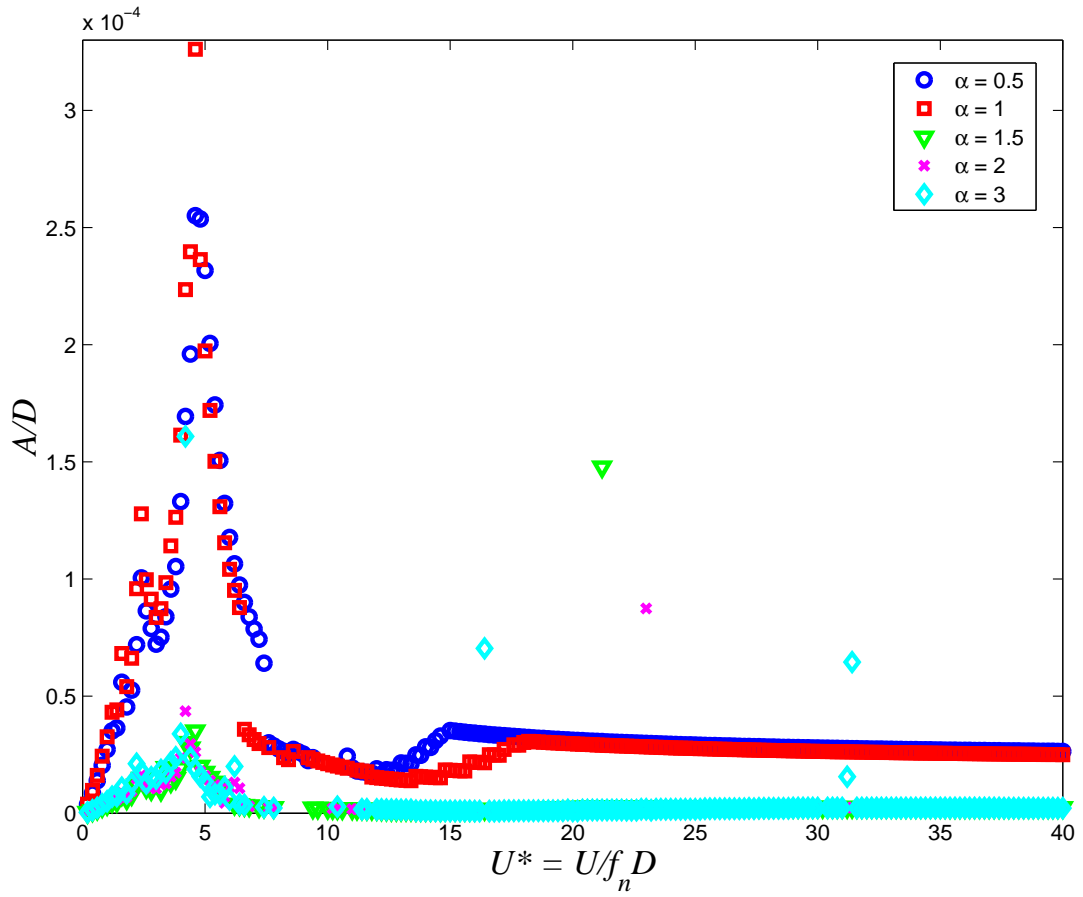


Figure 5.36: Comparison of the amplitude response for various values of the dissipation/amplification parameter  $\alpha$ .

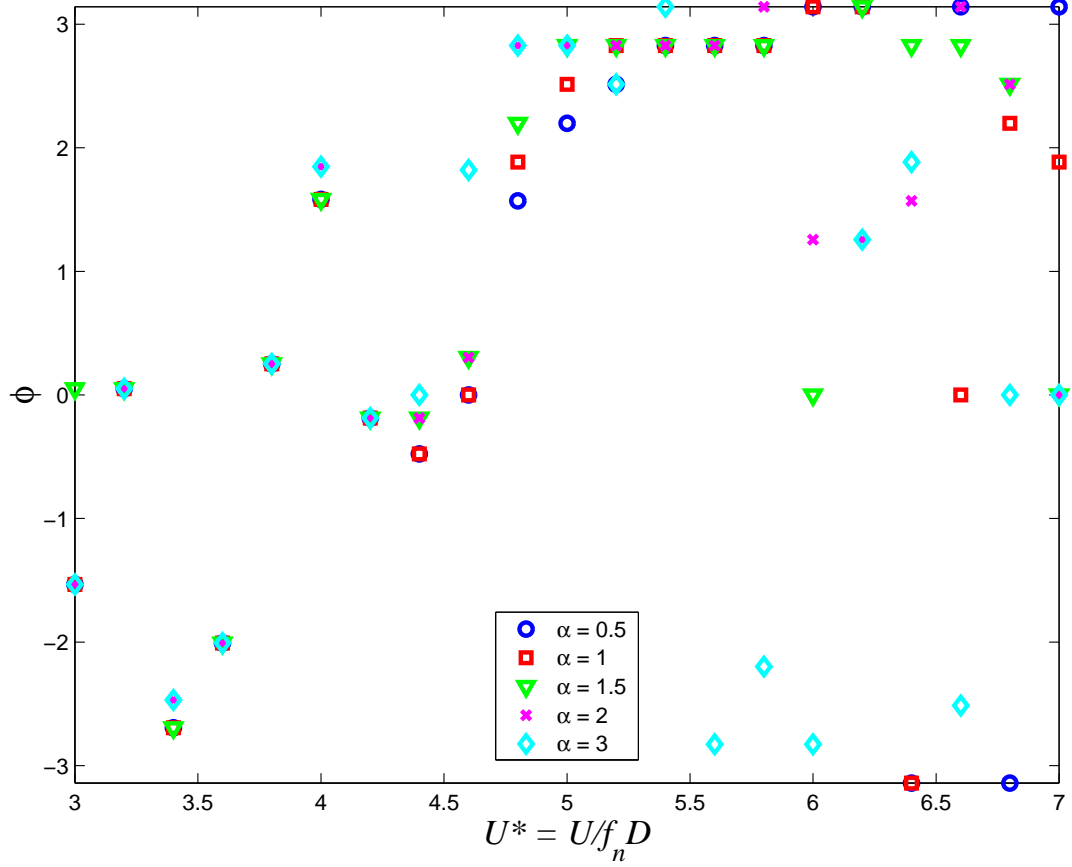


Figure 5.37: Comparison of the phase-shift response for various values of the dissipation parameter  $\alpha$ , with testing for energy entrainment in place of dissipation.



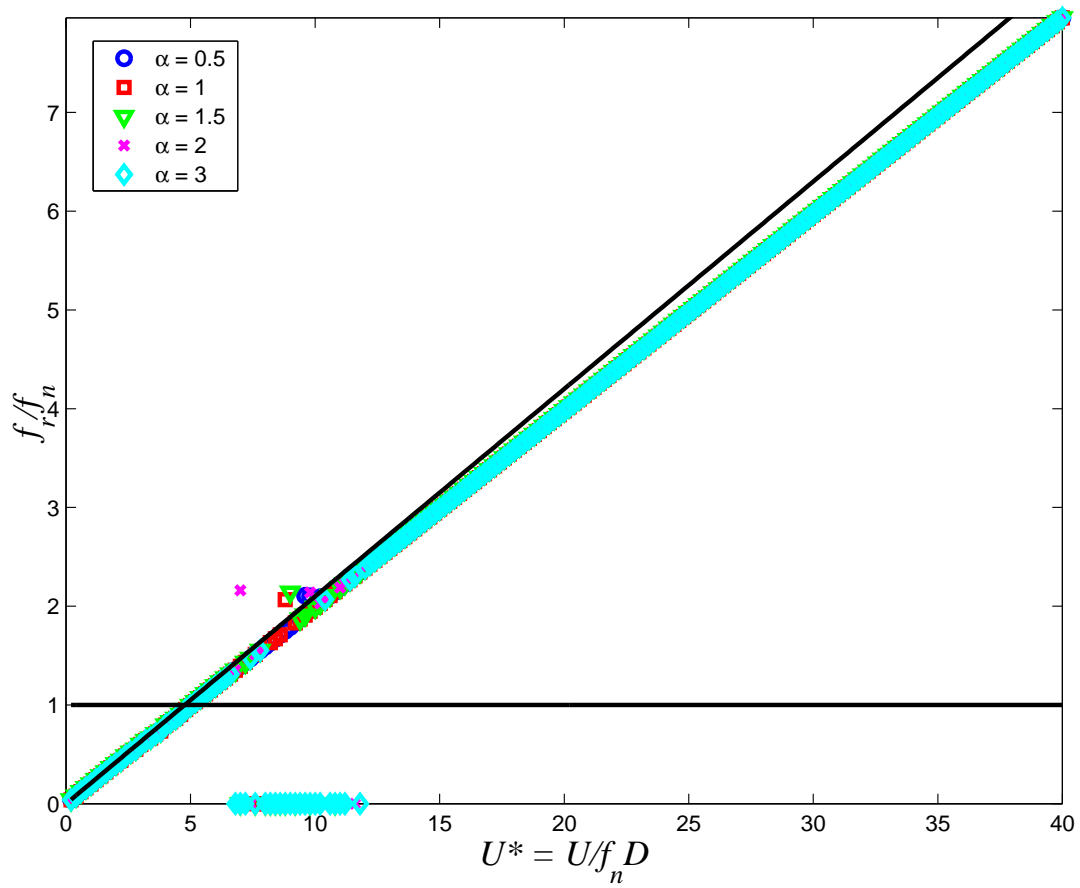


Figure 5.38: Comparison of the vortex-shedding frequency response for various values of the dissipation/amplification parameter  $\alpha$ .

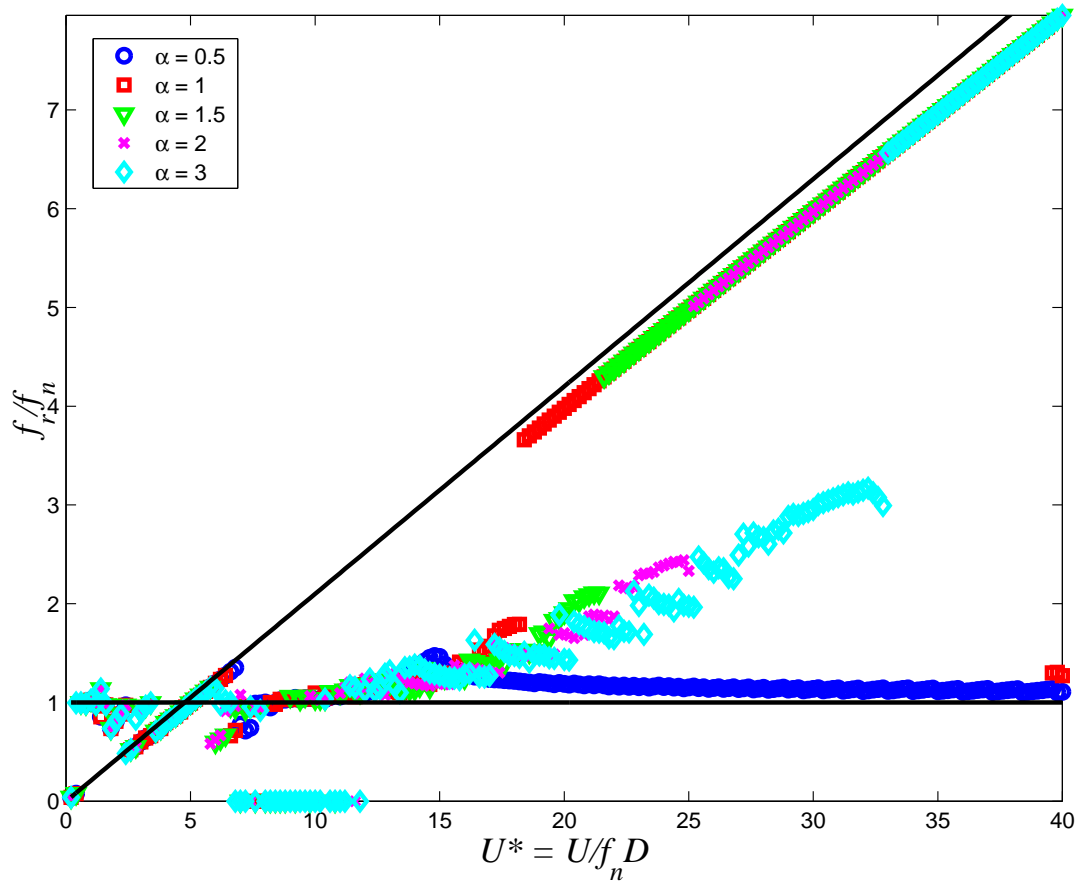


Figure 5.39: Comparison of the cylinder frequency response for various values of the dissipation/amplification parameter  $\alpha$ .

Table 5.1: Final math model inputs and outputs.

| <i>Inputs</i>       |                      | <i>Outputs</i> |
|---------------------|----------------------|----------------|
| <i>User-defined</i> | <i>Model-defined</i> |                |
| $U^*$               | $St$                 | $y(t)$         |
| $m^*$               | $\theta_{st}$        | $\phi$         |
| $\zeta$             | $\theta_{sp_{t,b}}$  | $f_{KV}$       |
| $f_n$               | $x_{fp_{t,b}}$       | $f_C$          |
| $Re$                | $\eta_{t,b}$         |                |
| $D$                 | $T_{crit}$           |                |
| $\rho$              |                      |                |

## CHAPTER 6

### Comparison to Experimental Results and Extant Models

#### 6.1 Comparison to Experimental Results

There is a seemingly limitless number of experimental data sets available for vortex-induced vibrations. Three test cases with four data sets have been selected for comparison here. A benchmark data set used in most any comprehensive discussion of VIV comes from Feng (1968). This case was one of the first complete data sets on the phenomenon of VIV and is often used for comparison against new experimental, analytical, and computational results. It is only natural, therefore, to compare the present model to those results. Govardhan and Williamson (2000) performed experiments for the same conditions and found slight variations in the results. The present model is compared in the same plot to both of these data sets. Both data sets were obtained by private communication with Williamson.

A third data set also obtained by private communication with Williamson also was published in Govardhan and Williamson (2000). This case differs from that used to compare against Feng (1968) since the mass ratio is referred to as “high” in Feng (1968), while for this second data set from Govardhan and Williamson (2000) represents a “low” mass ratio. Finally, a fourth data set was obtained by picking points off of the plots presented in Anagnostopoulos and Bearman (1992), where the Reynolds number range is much lower, and the mass ratio is moderate. The defining

parameters of each case is given in Table 6.1. The  $Re$  regime definitions are taken from Zdravkovich (1997) and were outlined in Chapter 1.

The mathematical model was run for each of the cases as defined in Table 6.1, and the results are shown in Figures 6.1 to 6.10. The equations used come from the final force equations presented in Chapter 5. The data for the cases taken from Feng (1968) and Govardhan and Williamson (2000) were obtained via private communication with Williamson. The data for the case from Anagnostopoulos and Bearman (1992) was visually pulled from the plots by the author, allowing for greater error in the values.

It can be seen that overall, the math model is not yet up to standard for comparison to experimental results. However, there is a great deal of success in the model. In the case of the high mass-ratio experiments of Feng (1968) and Govardhan and Williamson (2000), shown in Figures 6.1 to 6.4, the amplitudes are not on the same order of magnitude, and the phase-shift is altered due to the inputs. However, lock-in is still visible within an acceptable range for the simulation, and the vortex-shedding frequency extrapolated from the experimental results of Feng (1968) seem to align with what was found by the model.

In the case of the low mass ratio of Govardhan and Williamson (2000) and the low damping ratio of Anagnostopoulos and Bearman (1992), the results of the model are non-existent during lock-in for the first case and entirely for the second case because the amplitudes went to infinity throughout the test range. It has been noted that with low damping ratios, the model does tend to infinity, despite the vortex shedding criterion built in. This is a point worth further examination.

## 6.2 Comparison to Extant Models

### 6.2.1 Linear Single Degree-of-Freedom Equation

Although the single degree-of-freedom linear model, where the forcing term is defined with an amplitude and sinusoidal signal, has been proposed as a legitimate model of VIV, there is no need to compare the current model to it because it would result in the same results as those from experiments. This is due to the fact that the lift coefficients come directly from experiments, and the amplitudes are therefore a direct result of this input.

### 6.2.2 van der Pol Oscillator

As outlined in Chapter 1, there are several types of models that have been developed over the years. Many had two degrees of freedom, with some type of wake parameter. Sometimes that parameter represented lift while other times it represented the attached fluid in some way. However, one thing is in common with **most** published VIV models: they attempted modeling VIV using a van der Pol Oscillator. This includes the models derived from the similar Landau equation as well as the model proposed by Blevins (1974) and even the model derived using Hamilton's Principle in Billah (1989). Since they all have characteristics taken from the van der Pol Oscillator, one of the more recent models will be selected for comparison. It is argued that any previous models would have been equally or less successful at modeling VIV in order for the more recent model to be published. The model selected come from Facchinetti, de Langre, and Biolley (2004), and couples the van der Pol Oscillator with the acceleration of the cylinder. The values of the parameters used in the reference are also given below.  $C_a$  is the added mass coefficient,  $St$  is the Strouhal number,  $\gamma$  is the stall parameter,  $C_{L_0}$  is the reference lift coefficient for a fixed cylinder,  $\epsilon$  is the van der Pol coefficient, and  $A$  is also defined from the

van der Pol system in combination with  $\epsilon$ . For the selection of the values of these parameters, it is recommended to review Facchinetti, de Langre, and Biolley (2004) as this is a large part of the article.

$$\begin{aligned} (m + \frac{1}{4}\pi C_a \rho D^2) \ddot{y} + (c + \gamma \rho f_s D^2) \dot{y} + ky &= \frac{1}{4}\rho U^2 D C_{L_0} q \\ \ddot{q} + \epsilon f_s (q^2 - 1) \dot{q} + f_s^2 q &= \frac{A}{D} \ddot{y} \end{aligned} \quad (6.1)$$

$$\begin{aligned} C_a &= 1 & St &= 0.2 & \gamma &= 0.8 \\ C_{L_0} &= 0.3 & \epsilon &= 0.3 & A &= 12 \end{aligned} \quad (6.2)$$

For the results comparing the current model to the model in Facchinetti, de Langre, and Biolley (2004), see Figures 6.11 to 6.14. Facchinetti, de Langre, and Biolley (2004) tested coupling the wake variable to the cylinder displacement in three ways: through cylinder displacement, through cylinder velocity, and through cylinder acceleration. It was concluded in the article that the best coupling comes from acceleration, because of the wider range of synchronization that is observed with the displacement versus reduced velocity. Although this amplitude of response is on the same order of magnitude as experimental results, the Facchinetti, de Langre, and Biolley (2004) model underestimates the amplitudes throughout the range of synchronization. This underestimation of the amplitudes of response is a fairly common occurrence in most all mathematical models used for VIV.

With what has been observed in the rigorous derivation of the present model, it can be stated that the coupling between the fluid and the cylinder is most likely a result of both the cylinder velocity and acceleration, as each term in the attached fluid resulted in a cylinder velocity and acceleration term. It is suggested that, although there is no physical justification for using the van der Pol oscillator, future advocates of the model may find it useful to couple the equations using both the velocity and acceleration. There is perhaps some physics in this argument based on

the derivation of the model derived in this dissertation.

In addition, non-zero initial conditions are necessary for the van der Pol oscillator coupled equations. In the model derived here, however, zero initial conditions result in the same response as non-zero initial conditions. This is due in part to the fact that the current model has only one degree of freedom in the system, the cylinder vertical motion. In addition, the implementation of the assumed character of the wake replaces the need for initial conditions, as the vortices are started  $180^\circ$  out of phase with each other in terms of the Strouhal period. However, this is very beneficial because it shows the self-excitation of the system in terms of forcing the cylinder to respond.

Although the current math model fails to match the relative success of the van der Pol oscillator in terms of the amplitude of oscillation, the current model far exceeds the results of the van der Pol oscillator for the other three features of phase-shift, vortex-shedding frequency and cylinder frequency. The van der Pol oscillator has never captured the phase-shift at lock-in. Also, the vortex-shedding frequency, or in this case the lifting frequency, are also not captured in addition to the failure of the van der Pol oscillator to capture frequency lock-in of the cylinder itself. This indicates the lack of physics from forcing a van der Pol curve to fit VIV data. Yes, most designs are done around the maximum amplitude response that can be forced by the van der Pol coefficients, but to what degree can those values be trusted if the phenomenon has not been captured.

### **6.3 Comparison to Baselines**

In Chapter 2, certain features were shown in order to define the phenomenon of VIV. These features were referred to in the quantitative and qualitative analysis presented at the end of Chapter 4 for the development of the linear model. At this

point, it is of interest to not just compare the model quantities and qualities, but to actually overlay the results of the model with the actual figures from Chapter 2. This helps further gage the success of this model.

In Chapter 2, the character of the phase-shift at lock-in was shown in a plot, giving both a quantitative and qualitative baseline. In addition, the basic characteristics of the range of synchronization were given with the initial, upper and lower branches followed by desynchronization. Already, it has been asserted that the math model shows characteristics of these branches, and it will be further outlined here. The vortex-shedding patterns have been hinted at, and can be analyzed given the frequency of vortex shedding versus the frequency of the cylinder motion for this model. In addition, experimental results have shown higher frequencies at lock-in for mass ratios below one, a characteristic already observed with this model but further outlined here. Finally, the modified Griffin plot was brought up as an experimental result of VIV, although the validity of such a comparison is still controversial. All of these are shown in plots below for some manner of comparison in Figures 6.15 to 6.20.

In comparison to the baselines, there are several features that appear in the math model. The phase shift (Figure 6.15), for mass ratios of 10 and 1.05, is appropriate in nature, although the phase shift for the lower mass ratios is not properly captured. In general, the capturing of the phase shift has been the most robustly present feature. For the range of synchronization (Figure 6.17), there are definitely signs of the initial, upper, and lower branches being present in all of the models, and the desynchronization can be attached to the range of reduced velocities where the response steadily tapers off. The initial branch in all cases, however, seems to start at a reduced velocity of zero rather than around 2. There is a jump in the amplitude



response around  $U^* = 2.5$ , which corresponds to the first sub-harmonic of the natural frequency. From there, the upper branch sometimes begins before  $U^* = 5$ , although for  $m^* = 10$ , it does appear around  $U^* = 5$ . Afterwards, there are heightened responses that could be associated with the lower branch. However, particularly in the cases of the lower mass ratios of 0.54 and 0.61, there is a large gap around  $U^* = 10$ , corresponding to the first super-harmonic of the natural frequency. This is where the model has seen the most problems with the amplitude of response, and often times the amplitudes head to infinity around the first super-harmonic. It is believed that with a better modeling of the vortex shedding criterion, this would no longer be observed, since a vortex would shed before enough energy would be captured in the system to force such high amplitude motions. In other words, an infinite amplitude indicates that the model has accumulated infinite energy in order to respond as such. VIV is a self-limiting phenomenon, and allowing the vortex to shed **before** the amplitude response goes to infinity will avoid the divergence.

The vortex-shedding mode analysis is very encouraging (Figure 6.18). The plot results from multiplying the vortex shedding frequency by two, so as to represent the vortex from the top and the vortex from the bottom, and then divided by the corresponding cylinder frequency response. The results show that, within the considered range of synchronization, there is a possibility for both the traditional  $2S$  mode, as well the  $2P$  which has been extensively documented. Additionally, as the plot extends to higher velocities, it can be seen that for the case where the cylinder frequency locks in to the natural frequency, the number of vortices shed continues to increase. The encouraging part of this is the fact that the math model can indeed capture various vortex shedding modes, unlike other models where the the body must be forced at the frequency at which it is expected to respond. The latter is how

the linear-forcing model is operated. The ability to capture various vortex shedding modes within a math model is very encouraging.

$$\frac{Vortices}{Cycle} = \frac{2 * f_{KV}}{f_C} \quad (6.3)$$

The next comparison shows some promise, where low-mass-ratio cylinders have experimentally been observed to lock in to higher frequencies than the natural frequency. This characteristic was slightly better captured by the model presented in Chapter 4. However, even with the addition of the Reynolds based parameters, the concept is still visible. The frequency at which the lower mass ratios lock in is not as close to unity as other test cases. For further evidence of the frequency response for various mass ratios, it is recommended to review the results in Chapter 4.

Finally, an attempt is made to compare the math model to the modified Griffin plot in Figure 6.20 (Govardhan and Williamson 2006). However, since it has already been observed that the amplitudes are not on the order of magnitude of one as expected for VIV, it is obvious that this attempt is not a success.

Table 6.1: Selected experimental data sets for comparison against developed mathematical model.

| <i>Publication</i>                 | $f_n$ | $\zeta$ | $m^*$ | $m^*\zeta$ | <i>Fluid</i> | <i>Re Regime</i> |
|------------------------------------|-------|---------|-------|------------|--------------|------------------|
| Feng (1968)                        |       |         | 320   | 0.250      | water        | TrSL1            |
| Govardhan and Williamson (2000)    |       | 0.00151 | 8.63  |            | water        | TrSL2            |
| Anagnostopoulos and Bearman (1992) | 7.016 | 0.0012  | 17.78 |            | water        | L2               |

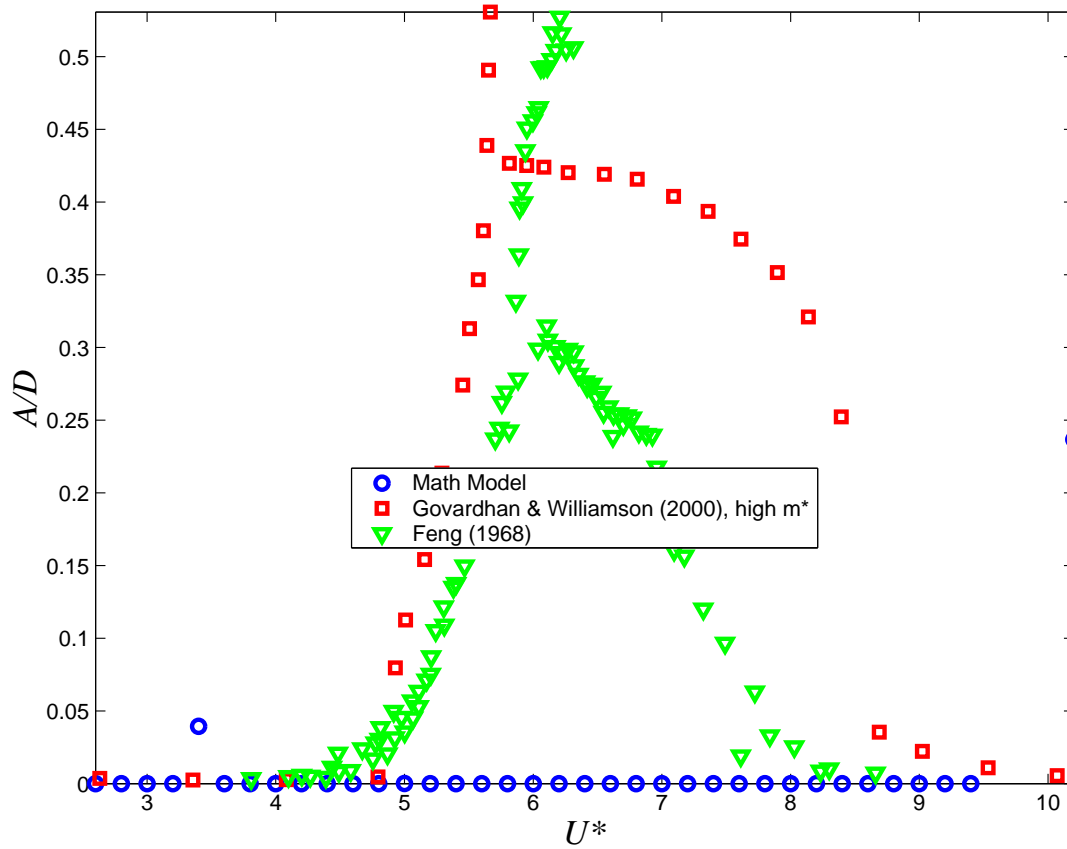


Figure 6.1: Comparison of the amplitude response of the developed math model to the high mass ratio experimental data sets from Feng (1968) and Govardhan and Williamson (2000), data received via private communication from Williamson.

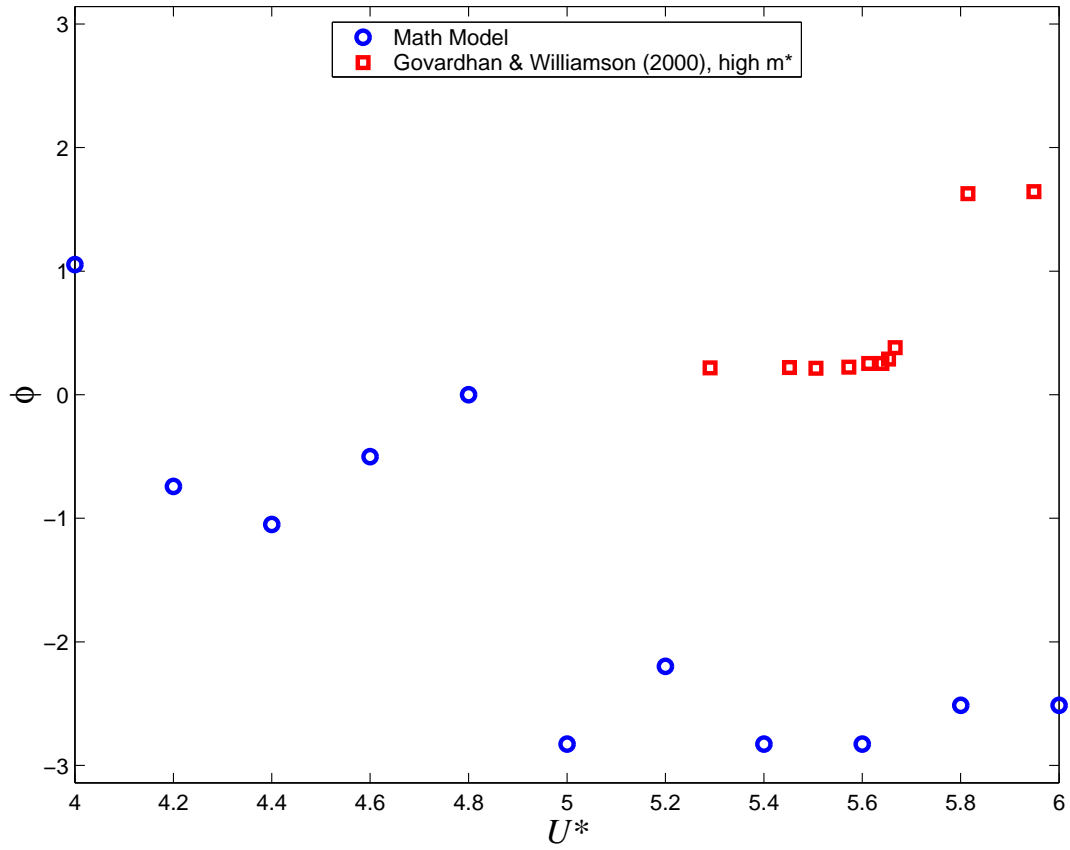


Figure 6.2: Comparison of the phase-shift response of the developed math model to the high mass ratio experimental data sets from Feng (1968) and Govardhan and Williamson (2000), data received via private communication from Williamson.

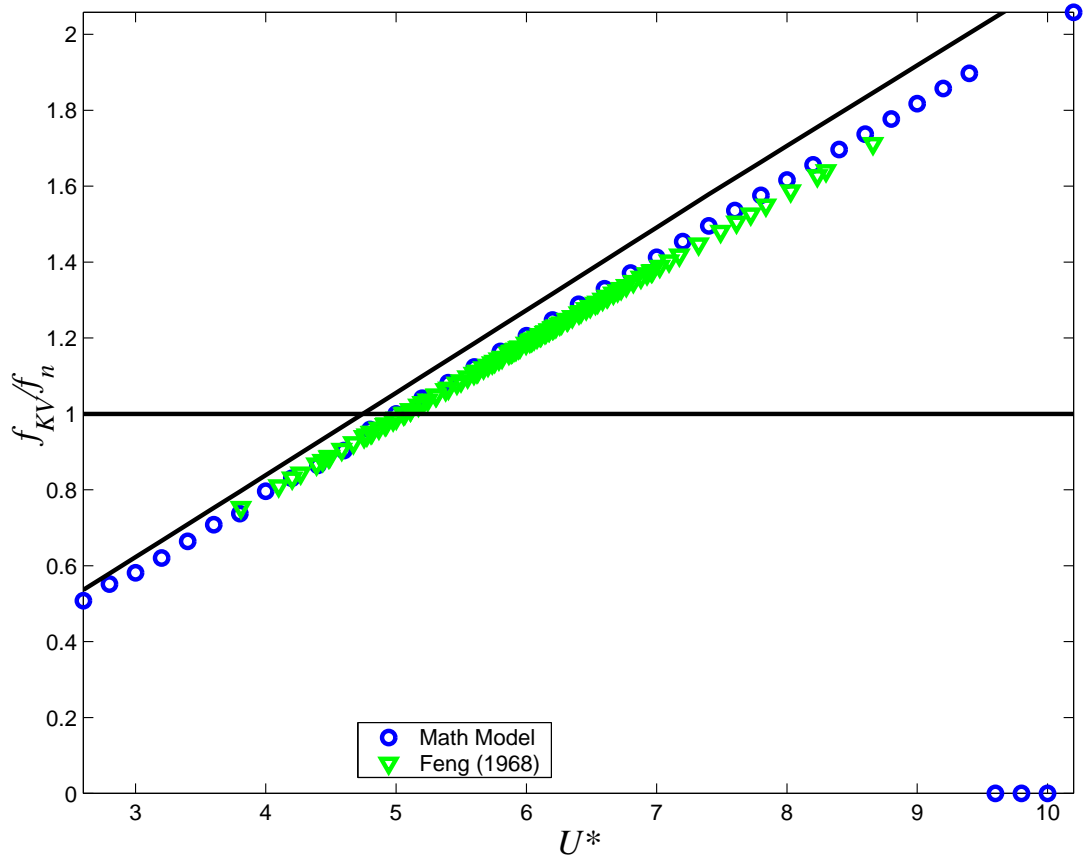


Figure 6.3: Comparison of the vortex-shedding frequency response of the developed math model to the high mass ratio experimental data sets from Feng (1968) and Govardhan and Williamson (2000), data received via private communication from Williamson.

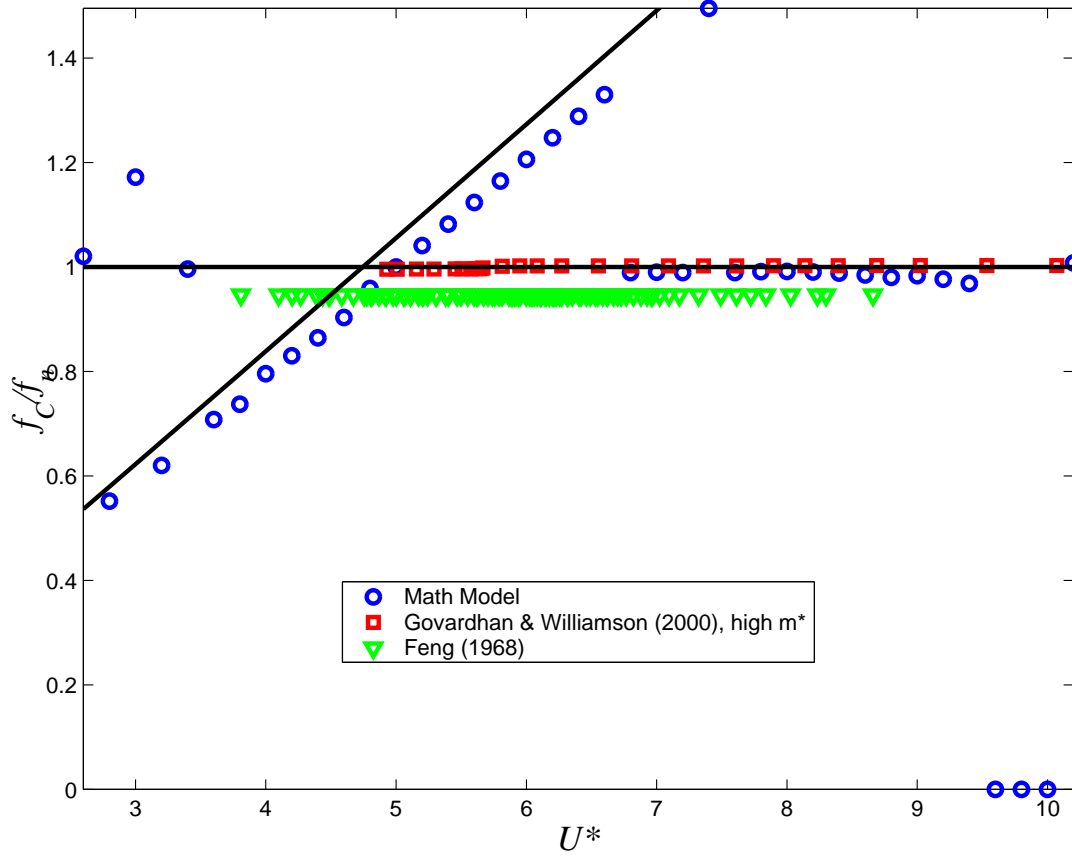


Figure 6.4: Comparison of the cylinder frequency response of the developed math model to the high mass ratio experimental data sets from Feng (1968) and Govardhan and Williamson (2000), data received via private communication from Williamson.

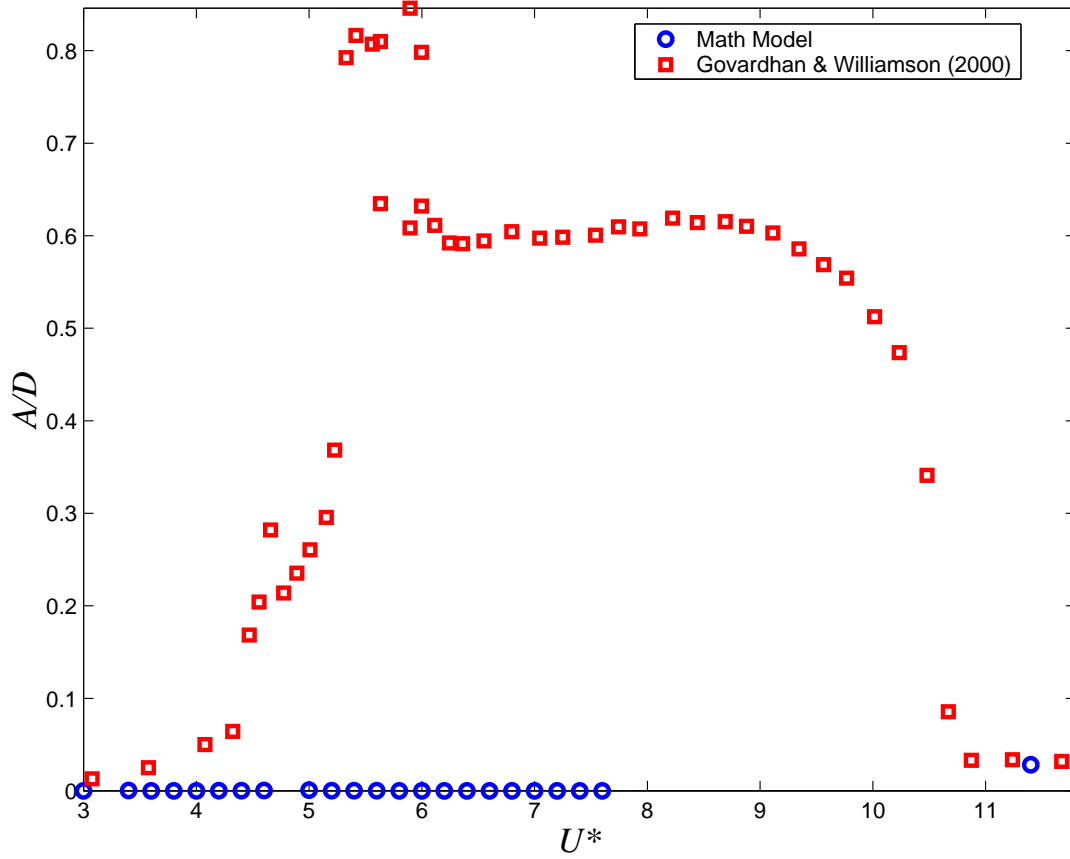


Figure 6.5: Comparison of the amplitude response of the developed math model to the low mass ratio experimental data set from Govardhan and Williamson (2000), data received via private communication from Williamson.



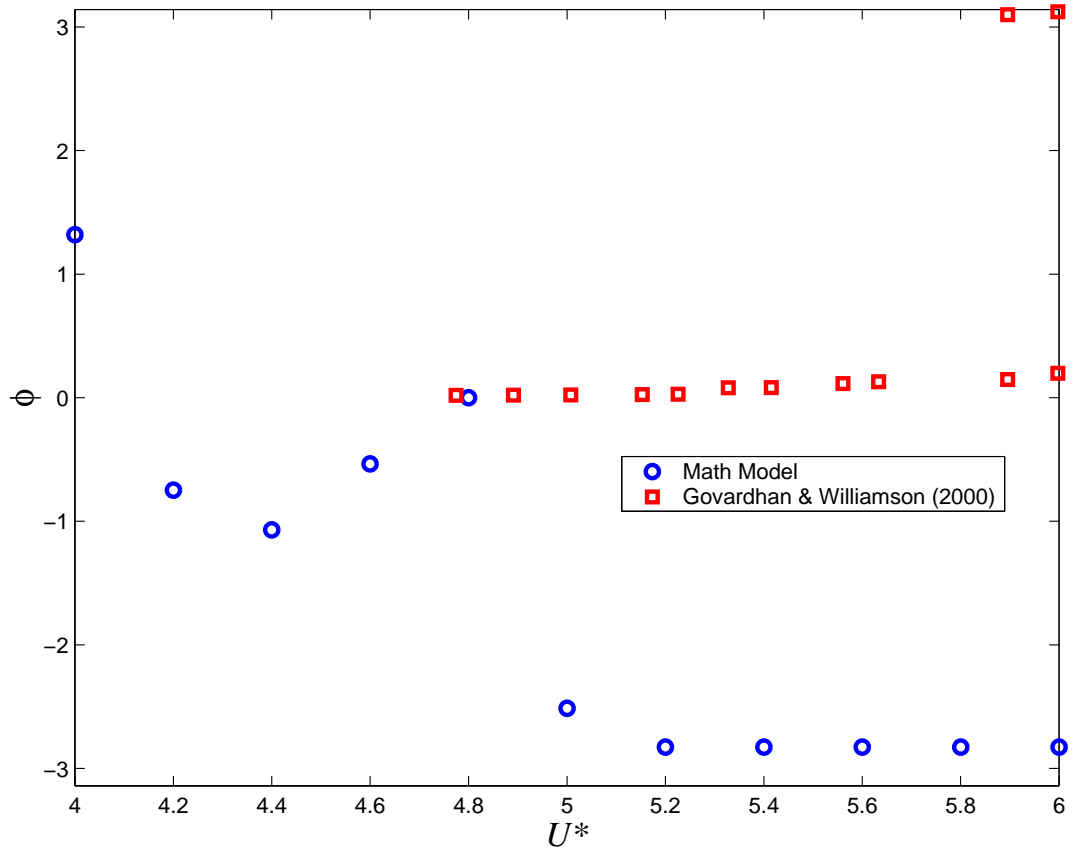


Figure 6.6: Comparison of the phase-shift response of the developed math model to the low mass ratio experimental data set from Govardhan and Williamson (2000), data received via private communication from Williamson.

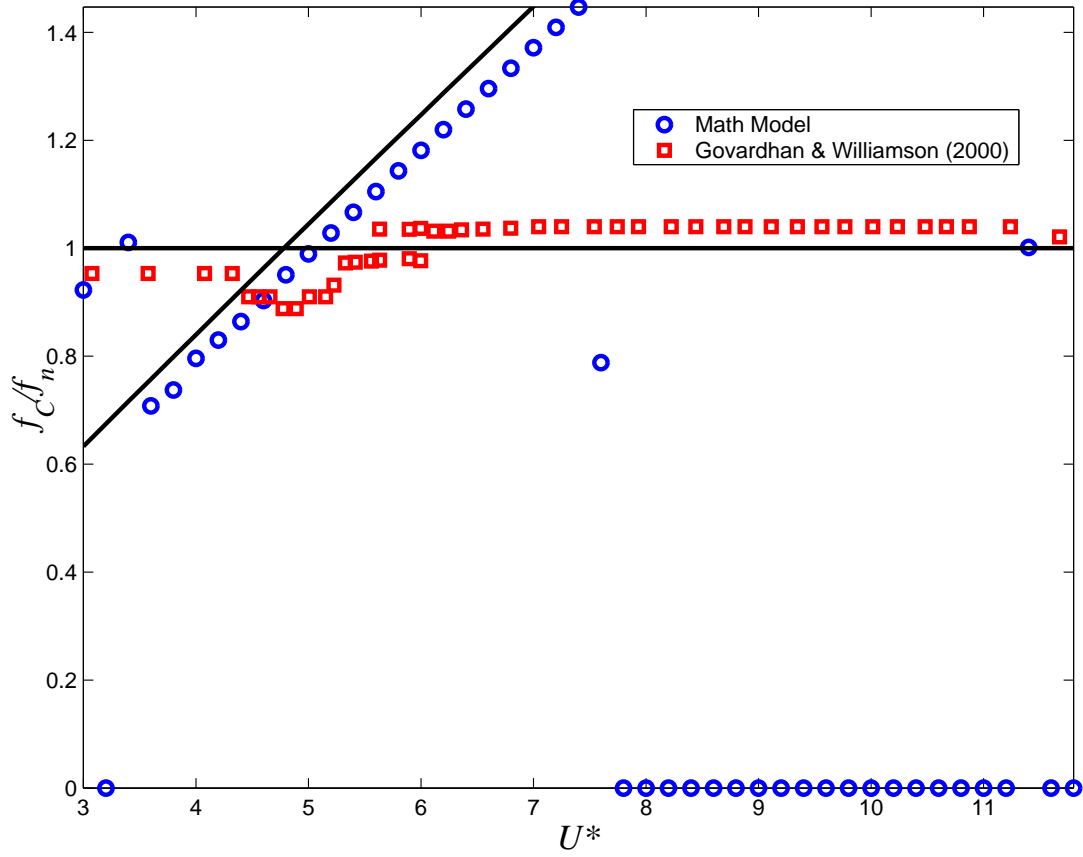


Figure 6.7: Comparison of the cylinder frequency response of the developed math model to the low mass ratio experimental data set from Govardhan and Williamson (2000), data received via private communication from Williamson.

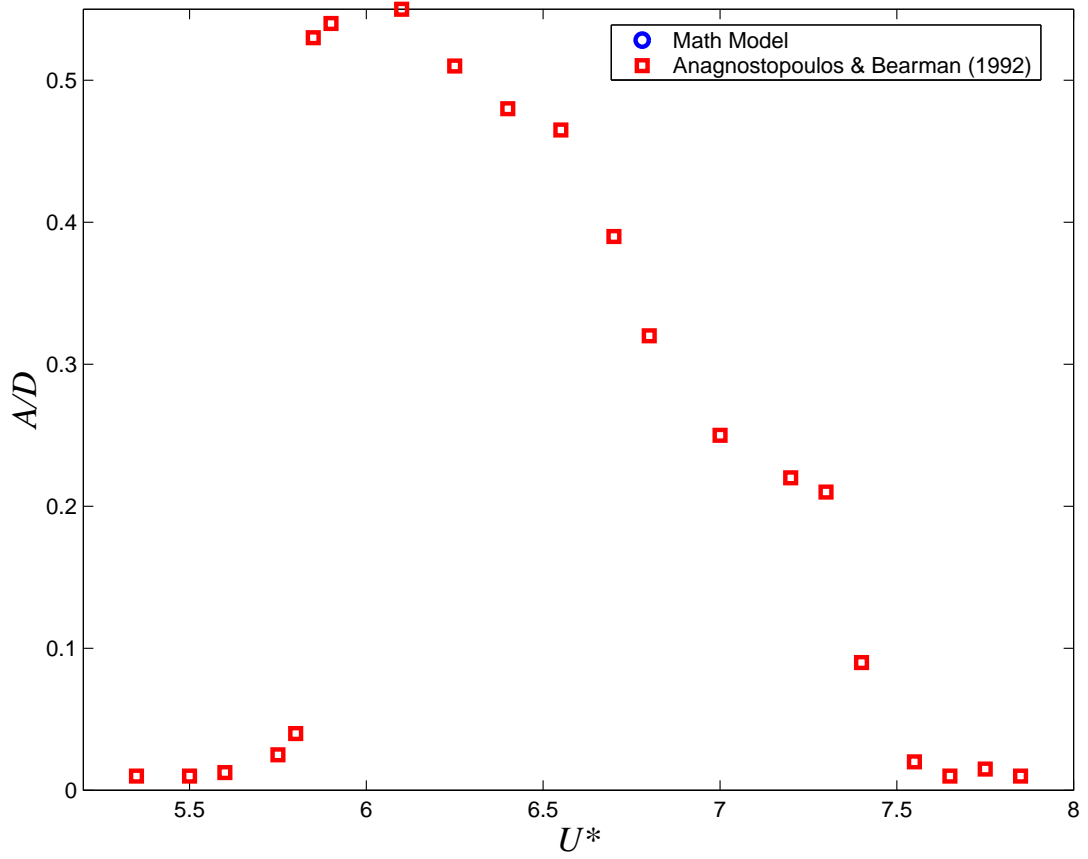


Figure 6.8: Comparison of the amplitude response of the developed math model to the experimental data set from Anagnostopoulos and Bearman (1992), data taken from points on plots.

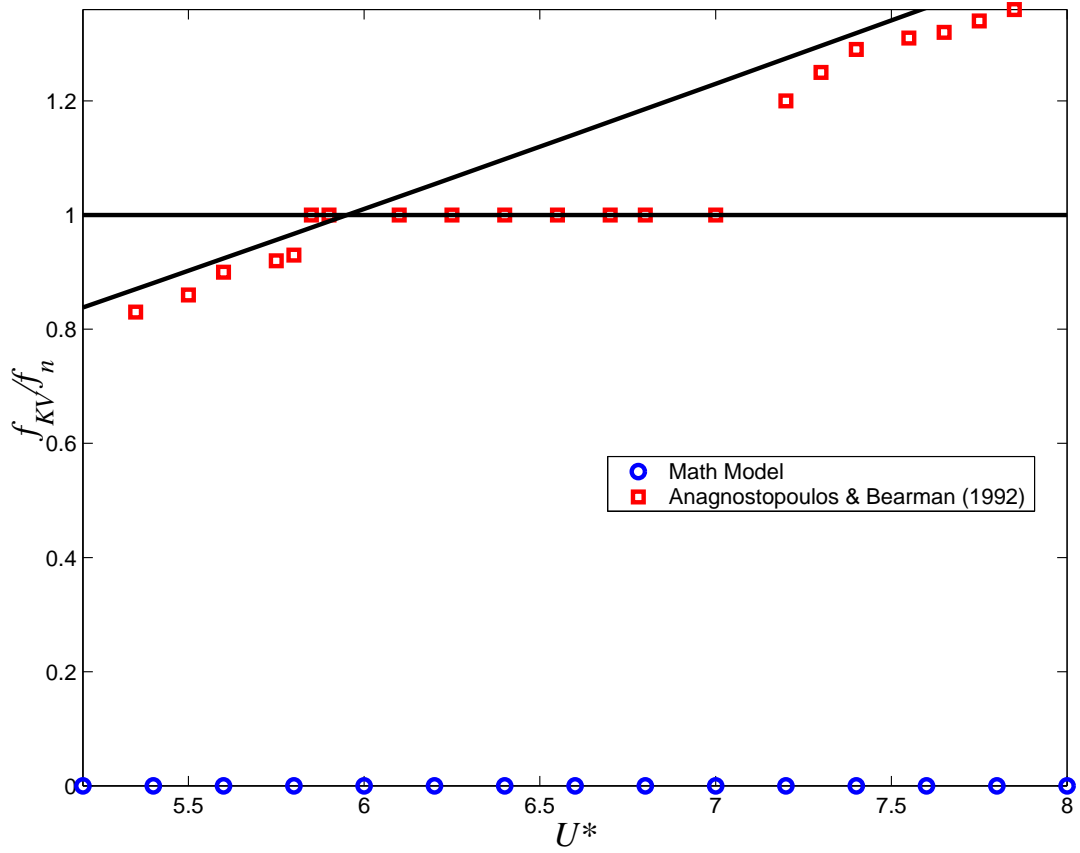


Figure 6.9: Comparison of the vortex-shedding frequency response of the developed math model to the experimental data set from Anagnostopoulos and Bearman (1992), data taken from points on plots.

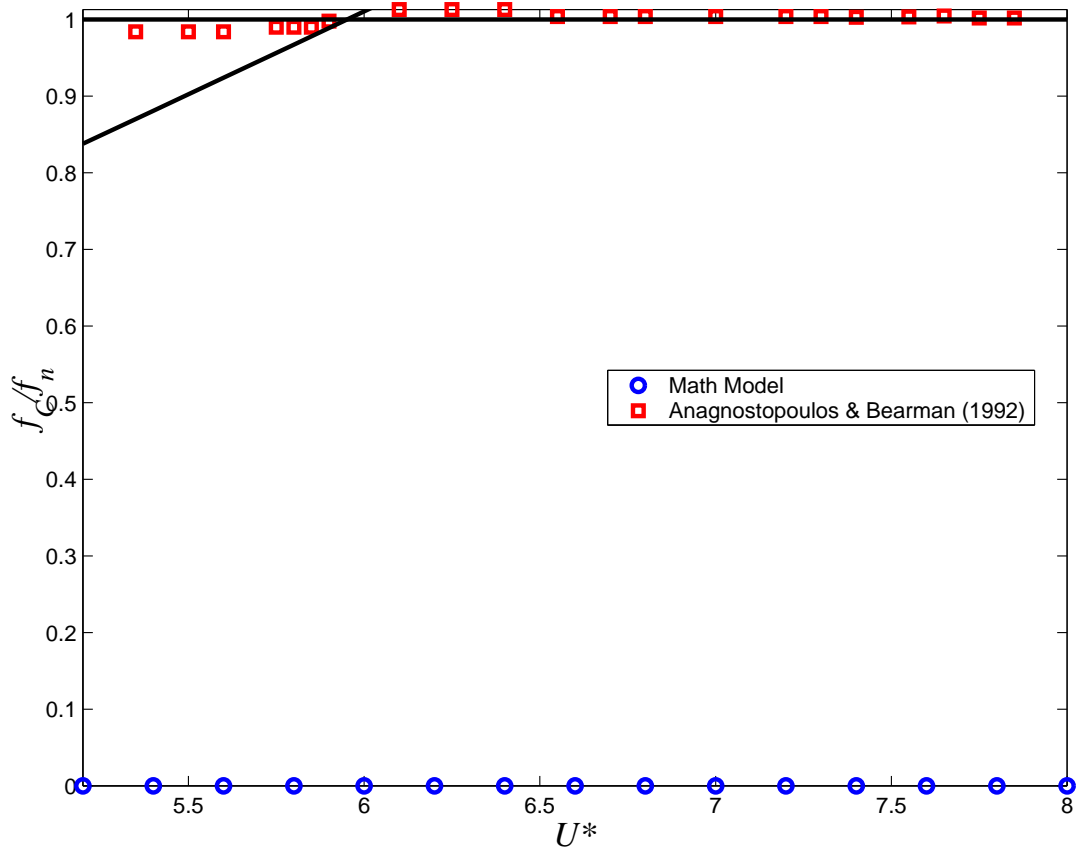


Figure 6.10: Comparison of the cylinder frequency response of the developed math model to the experimental data set from Anagnostopoulos and Bearman (1992), data taken from points on plots.

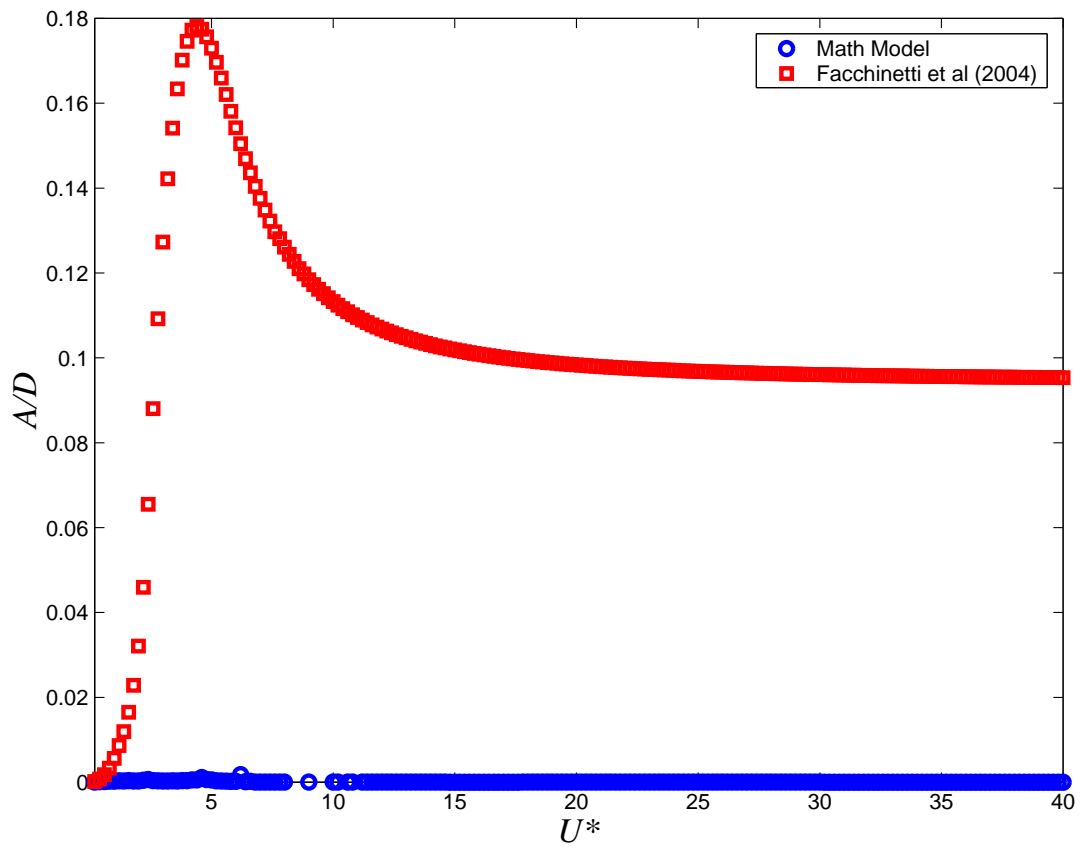


Figure 6.11: Comparison of the amplitude response of the developed math model to the van der Pol oscillator from Facchinetti, de Langre, and Billey (2004) with acceleration coupling.

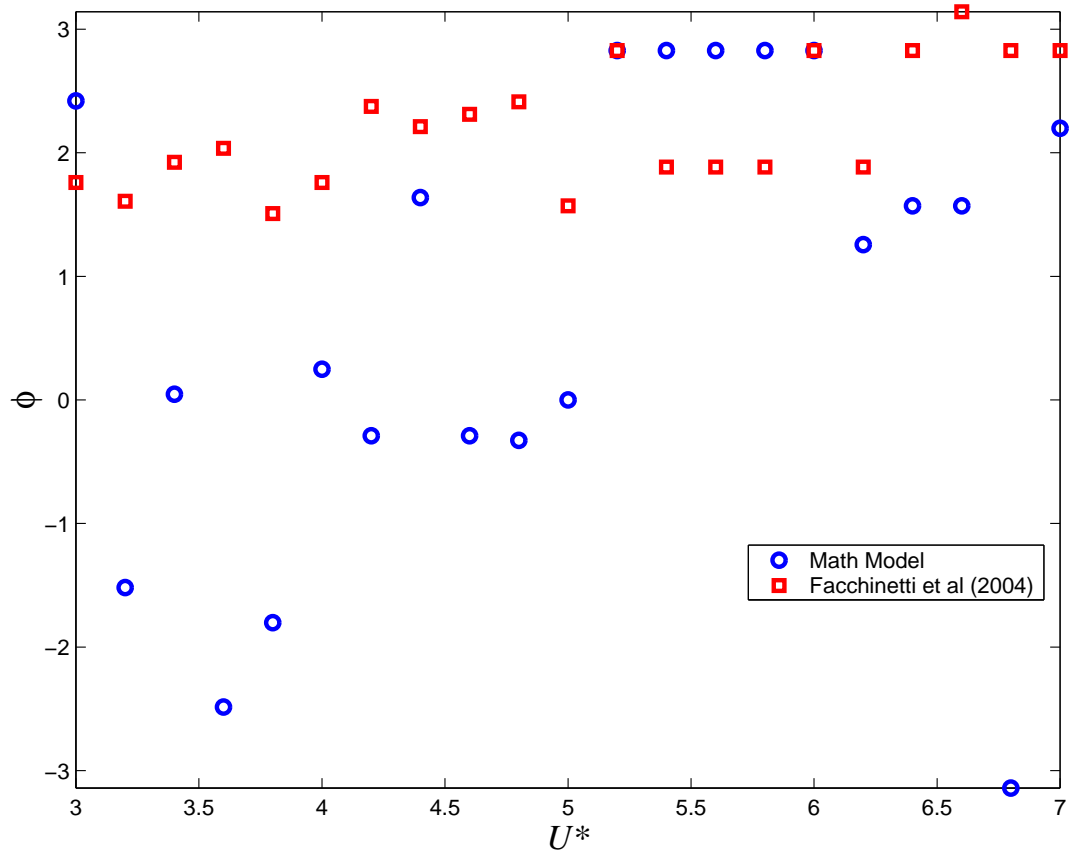


Figure 6.12: Comparison of the phase-shift response of the developed math model to the van der Pol oscillator from Facchinetti, de Langre, and Biolley (2004) with acceleration coupling.

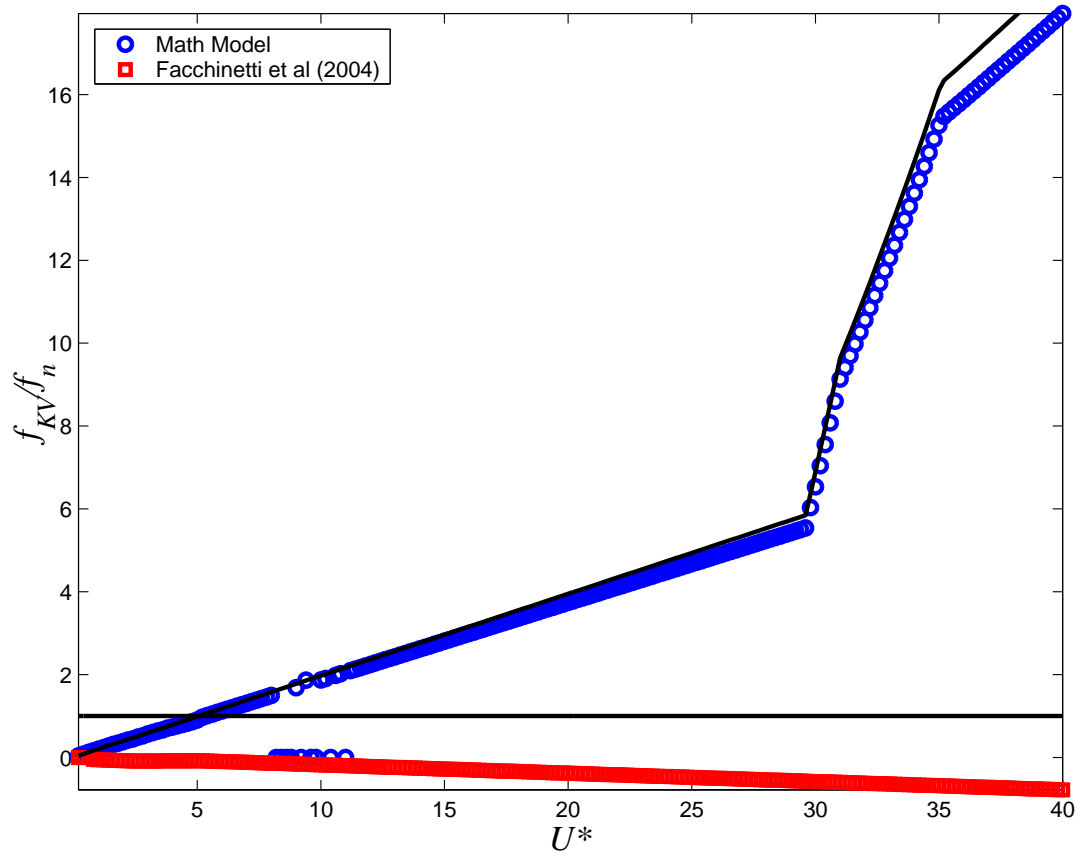


Figure 6.13: Comparison of the vortex-shedding frequency response of the developed math model to the van der Pol oscillator from Facchinetti, de Langre, and Biolley (2004) with acceleration coupling.



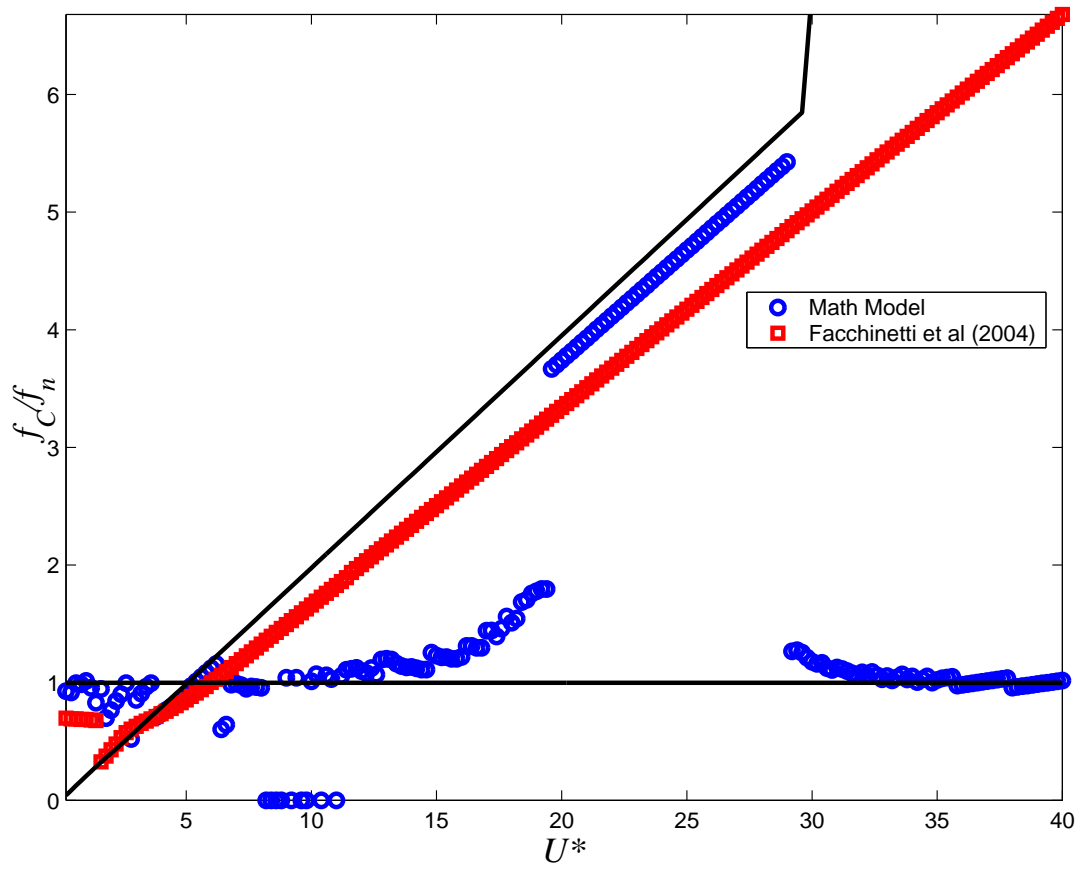


Figure 6.14: Comparison of the cylinder frequency response of the developed math model to the van der Pol oscillator from Facchinetti, de Langre, and Biolley (2004) with acceleration coupling.

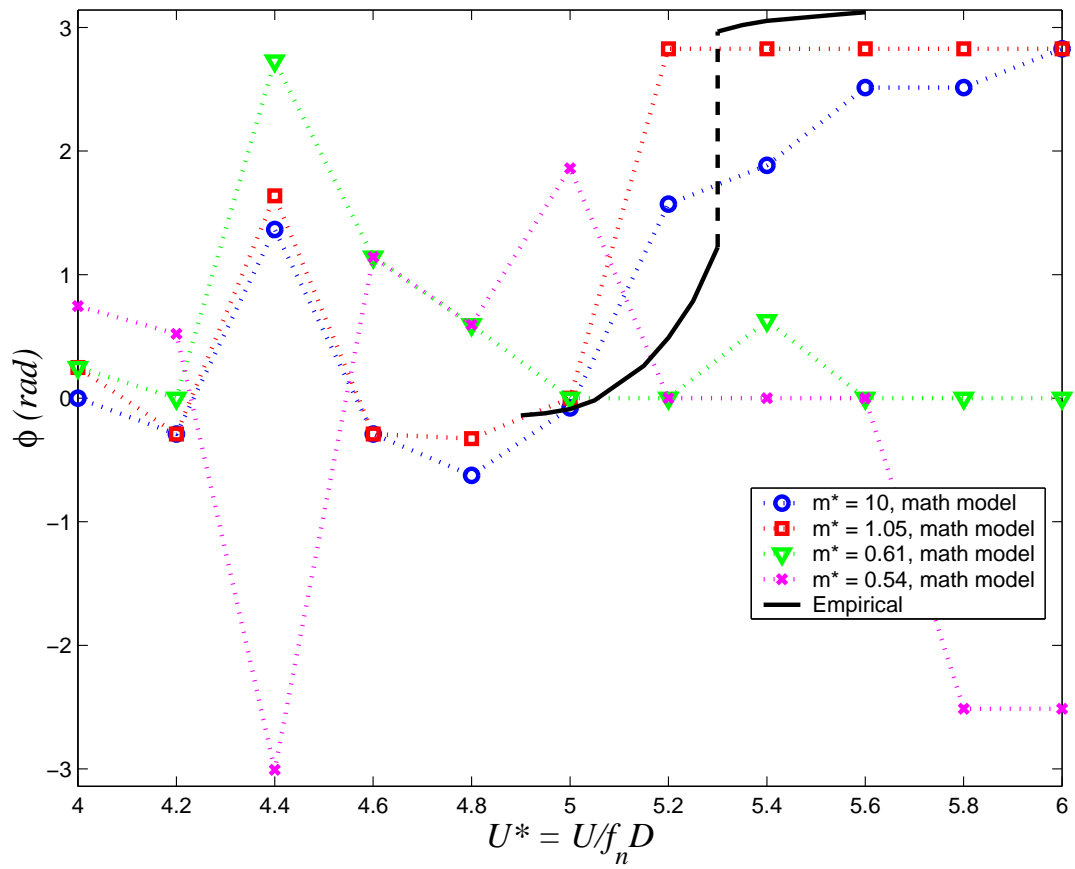


Figure 6.15: Comparison of the phase-shift response of the developed math model to the empirically based results as shown in Sumer and Fredsøe (1997).

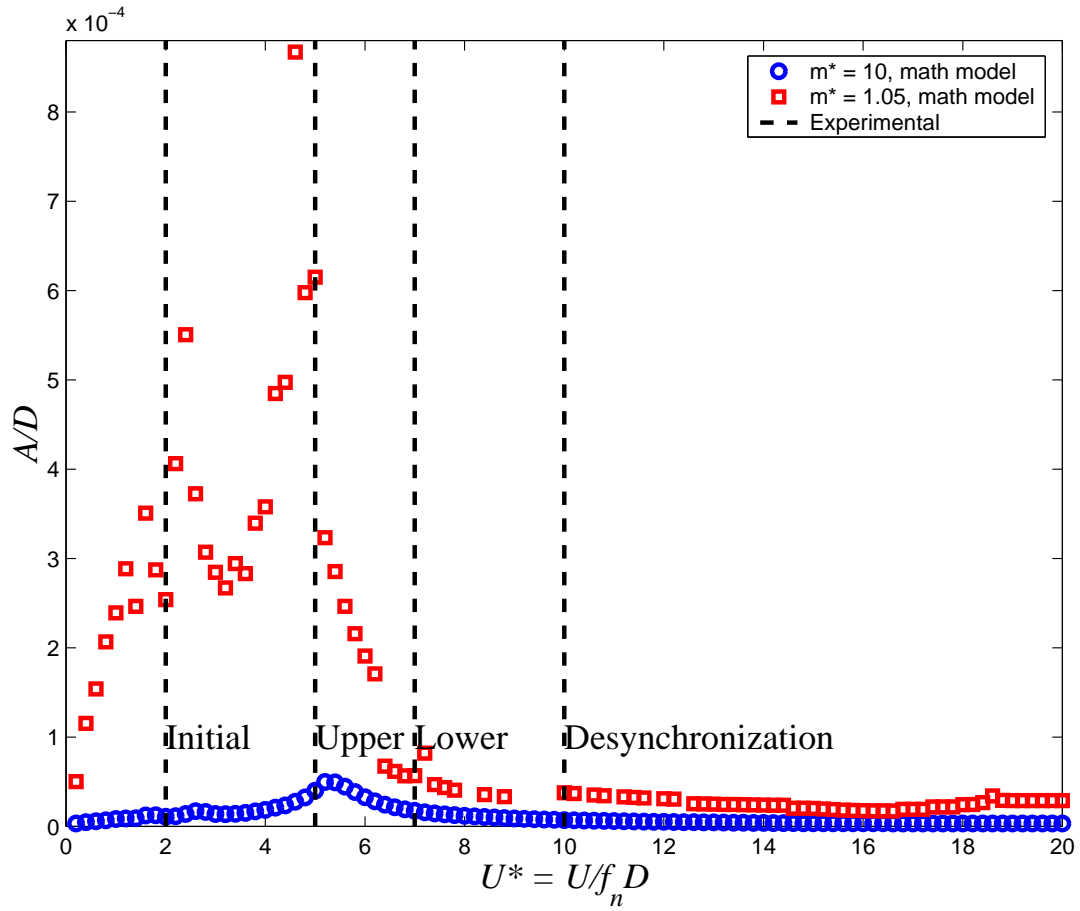


Figure 6.16: Comparison of the amplitude response of the developed math model for high mass ratio to the empirically based range of synchronization as taken from Williamson and Govardhan (2004).

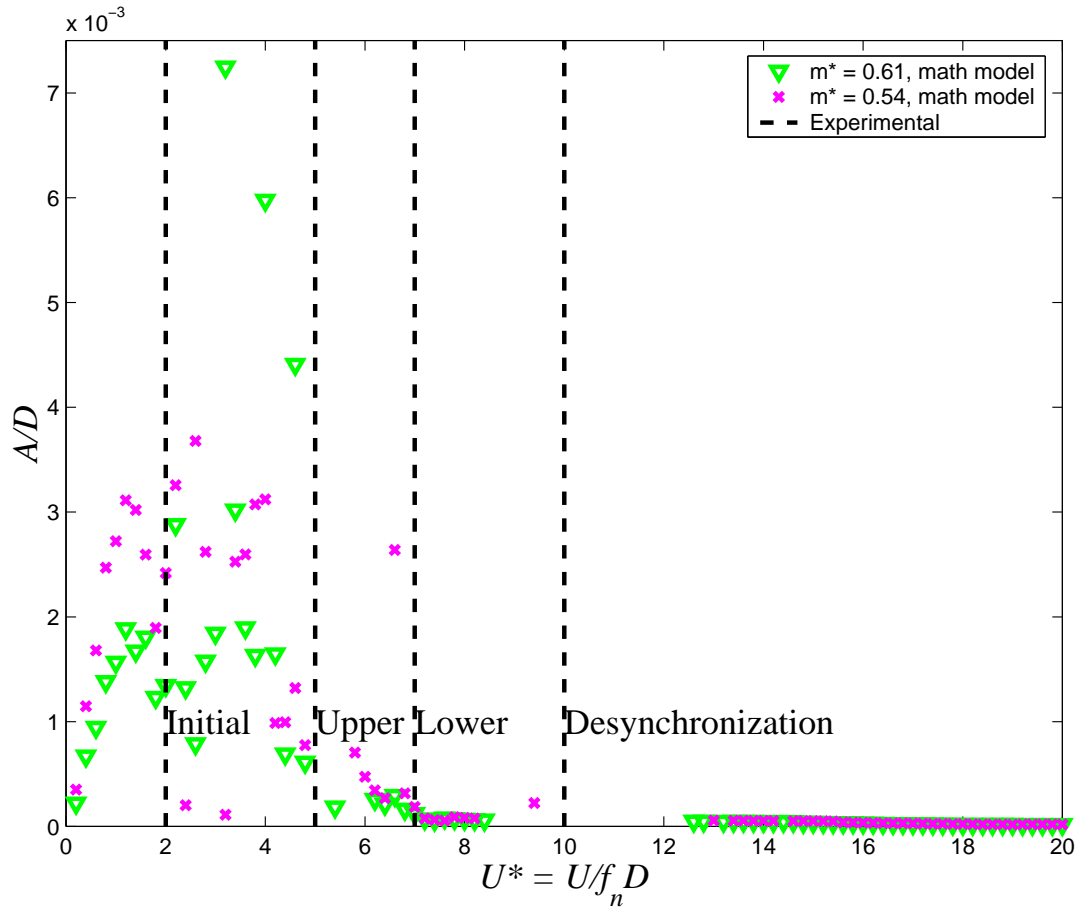


Figure 6.17: Comparison of the amplitude response of the developed math model for low mass ratio to the empirically based range of synchronization as taken from Williamson and Govardhan (2004).

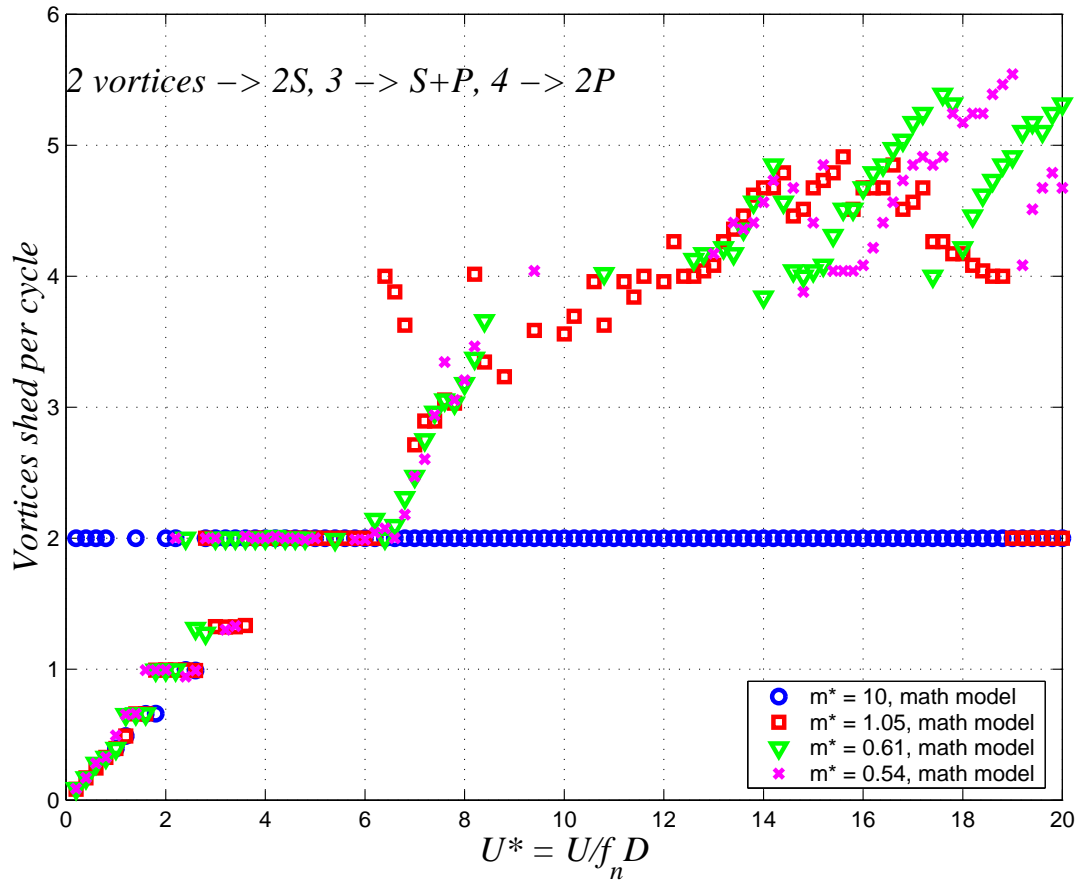


Figure 6.18: Comparison of the approximate number of vortices shed per cycle from the developed math model to the empirically based vortex shedding modes as taken from Williamson and Roshko (1988). Many experimental results show mode  $2S$  present up to around  $U^* = 5$  and then mode  $2P$  takes over.

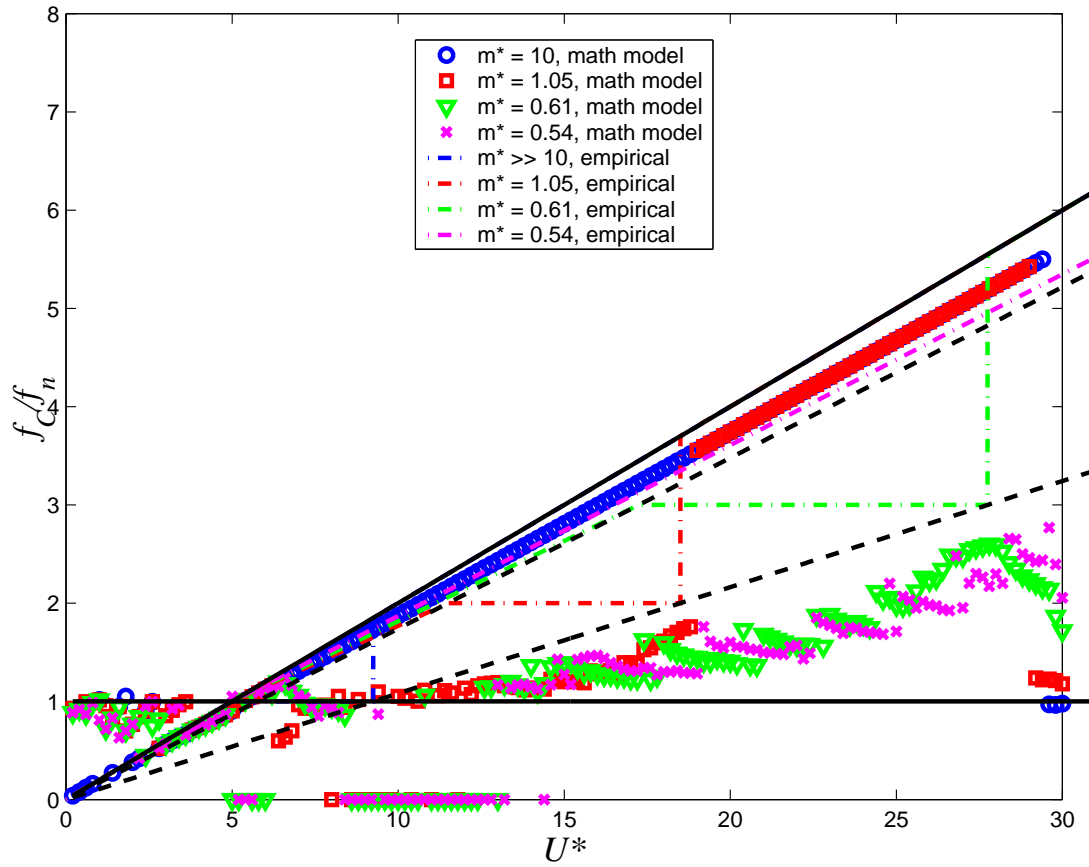


Figure 6.19: Comparison of the cylinder frequency response of the developed math model to the empirically based frequency response for low mass ratios as taken from Govardhan and Williamson (2000).

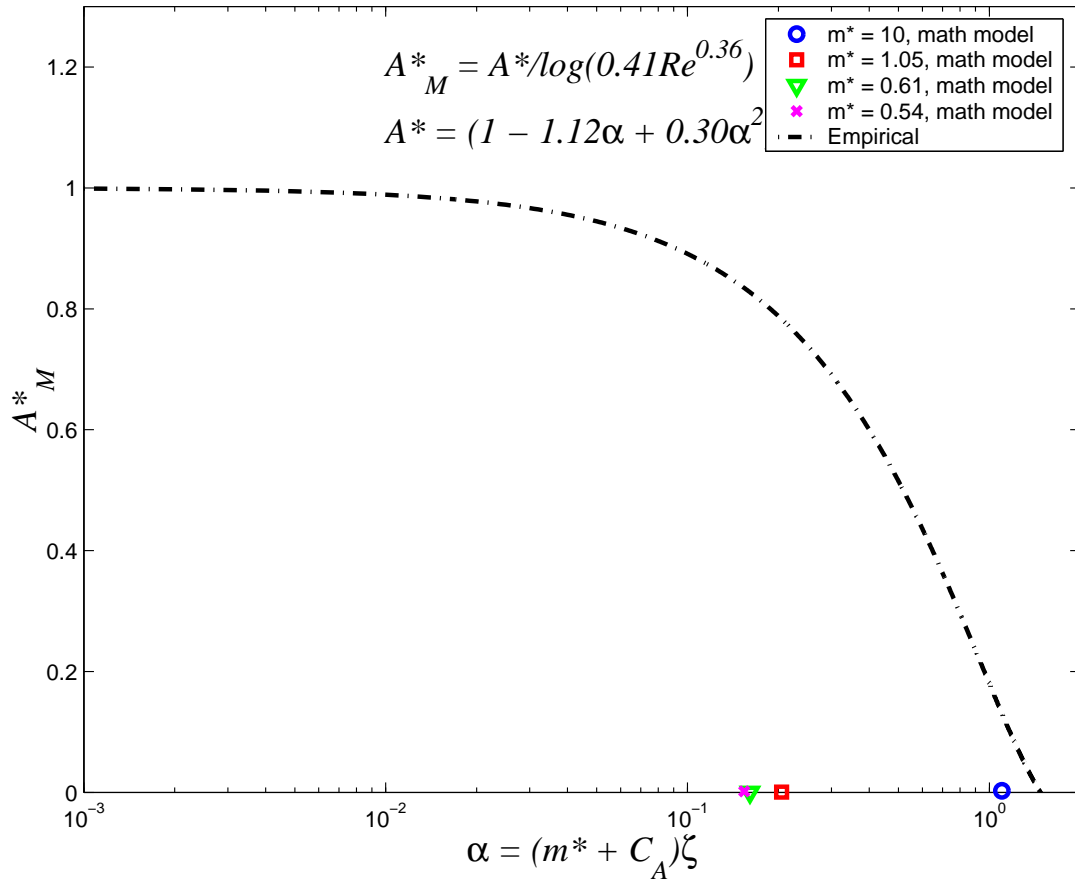


Figure 6.20: Comparison of the modified Griffin amplitude response of the developed math model to the empirically based modified Griffin plot as taken from Govardhan and Williamson (2006).

## CHAPTER 7

### VIVACE Design

This chapter will outline certain considerations that will need to be made once the math model is improved to the level of acceptable error from experimental results. The model can then be used to determine a great many details about the cross-sectional arrangement of multiple cylinders in a given free-stream. This chapter serves only as an outline and should not be taken as a final criterion for design. Basic design constraints must be defined in order to determine the total energy take-off in order to design for site-specific criteria as well as for comparison to other ocean energy extraction devices.

#### 7.1 Cylinder Spacing

Figure 1.2 showed a possible arrangement for multiple cylinders for energy extraction. The spacing of these cylinders will be very important in optimizing the energy take-off. Since the model is currently two-dimensional and assumes a uniform free-stream velocity, there are limitations in optimizing the cylinder spacing. When placed in a body of water, the cylinder's axis is oriented perpendicular to the flow of water and perpendicular to gravity. There are two directions in which the cylinders are spaced, and a third direction defined by the length of the cylinder. The first direction is the downstream direction. The second is the direction of gravity.



The third direction over the length of the cylinder is the axial direction of the current two-dimensional model. See Figures 1.1 and 1.2 for a schematic of the cylinder orientation. Figure 7.2 gives an overview of multiple cylinder arrangements.

It is inappropriate to attempt optimizing cylinder spacing in the downstream direction because the downstream cylinders will be experiencing the wake of the upstream cylinders. This has been shown to result in a combination of the phenomenon of VIV and galloping. A more advanced model could potentially be developed for this purpose, or Computational Fluid Dynamics (CFD) could prove useful for this model.

The cross-stream spacing could be examined with this model once the results are within an acceptable error of observed experiments. For spacing of the cylinders in the direction of gravity, estimates can be obtained for the maximum displacement of each cylinder, and the cylinders can then be placed with spacing for this distance. In the cylinder-axial direction, integration of the two-dimensional model can provide estimates of the energy take-off for a given length cylinder. Optimal aspect ratios of the length to diameter of a cylinder in VIV have already been reviewed in numerous references and will be used as input here.

#### **7.1.1 Length from Aspect Ratio**

Raghavan (2007) discussed the importance of the aspect ratio on maximum lift for the VIVACE system. He reviewed several works and concluded that for the VIVACE system, the aspect ratio should be between 7 and 20, or the length of the cylinder should be between 7 to 20 times the diameter of the cylinder. This was in order to optimize the mechanical power extraction based on the correlation length. The correlation length is the distance in the axial direction of the cylinder over which the vortex shedding is in phase (Sumer and Fredsøe 1997). For longer cylinders,

experiments have revealed that the vortices shed in cells rather than all shedding at the same time. This leads to varying lift over the length of the cylinder. A correlation length divided by the cylinder length equal to 1 would mean that there is only one vortex sheet shedding at the same time. However, if the correlation length is less than the length of the cylinder, vortices will be shedding at different times, canceling some of the lift over the entire length. In the case of VIV, vortices shed over larger correlation lengths due to VIV synchronization.

Since the model presented in this dissertation is two-dimensional and no conclusions can be drawn about the third dimension, the conclusion of Raghavan (2007) is used here. The aspect ratio is selected to be between 7 and 20.

### **7.1.2 Vertical Spacing**

Once parameters such as the mass and the diameter have been determined in order to be operating with maximum lift, a numerical simulation can be run to determine the maximum displacement of the cylinder. If each cylinder is allowed to oscillate freely without fixing its motion to its neighbor, then it is theoretically possible that the top cylinder is in the trough of its cycle while the lower cylinder is in the peak of its cycle, bringing the cylinders the closest they would be expected to get. It would be logical to assume that there is a stopper system to prevent two cylinders from ever touching. However, limiting the stroke of a cylinder is equivalent to limiting the energy the system can absorb. Therefore, the cylinders should be allowed to reach their peak, albeit damped, amplitudes. Once the amplitude of response has been found, each cylinder can be placed twice that amplitude from its neighbor on each side. Figure 7.3 give an overview of the effects on the wakes of the proximity of two cylinders.

## 7.2 Energy Extraction

Bernitsas, Raghavan, Ben-Simon, and Garcia (2006) derived the relationship between the damping of a cylinder in VIV to the power that is taken off from that damping. That relationship is followed herein. However, instead of using the linear, single degree-of-freedom model developed in the reference, the current derived model is used instead. To begin, the model will be written in the following form, where all forcing terms are on the right-hand side and all cylinder motion terms are preserved on the left-hand side of the equation.

$$m\ddot{y} + c\dot{y} + ky = F \quad (7.1)$$

In Bernitsas, Raghavan, Ben-Simon, and Garcia (2006), the force was divided into viscid and inviscid terms. However, the rigorous derivation of the mathematical model derived here cannot be divided this way. All force terms will remain on the right hand side of the equation. The mechanical power within a single VIVACE module can then be derived from the math model in the following way. First, the instantaneous power is found by multiplying the entire left-hand side by the velocity of the cylinder motion.

$$P_{instantaneous} = \dot{y} (m\ddot{y} + c\dot{y} + ky) \quad (7.2)$$

The mechanical power over time can then be found by integrating over at least one period of the cylinder motion, and then dividing by the period. This period can be derived from the frequency that is found from the Fast-Fourier Transform of the numerically-integrated output. Since there is often more than one period present in the transform and the signal is not exactly periodic, it is best to integrate and divide over several periods for the best average power.

$$P = \frac{1}{nT_s} \int_0^{nT_s} \dot{y} (m\ddot{y} + c\dot{y} + ky) dt \quad (7.3)$$

In the above equation,  $n$  represents the number of periods that are taken for the particular integration. If the signal was hypothetically perfectly sinusoidal, the only terms left for power extraction would be the damping term, since it is in phase with the multiply factor  $\dot{y}$ . However, a comparison can easily be made for the numerical integration of the entire equation and just the damping for power extraction.

$$P_{damping} = \frac{1}{nT_s} \int_0^{nT_s} c\dot{y}^2 dt \quad (7.4)$$

The data sets taken from the previous simulations can be used as inputs for the above integrations. This leads to a purely numerical integration. However, the time-stepping was always set to have at least 20 time-steps per smallest time period, be it the Stouhal or the natural. With 20 time-steps per period, an integration can be performed with reasonable output. The output can also be compared to the output had the displacement been perfectly sinusoidal in nature. Bernitsas, Raghavan, Ben-Simon, and Garcia (2006) derived the following expression for the mechanical power of VIVACE.

$$P_{VIVACE} = 8\pi^3(m + m_a)\zeta(y_{max}f_C)^2 f_{n_{water}} = 2\pi^2 c(y_{max}f_C)^2 \quad (7.5)$$

When selecting design criteria for a given sight, it has been shown experimentally to be important to work within the TrSL3 regime as defined by Zdravkovich (1997), since this will be where the lift coefficient is a maximum for the system. With maximum lift should come maximum energy. Therefore, the diameter of the cylinder can be selected so that the Reynolds number regime for a given free-stream velocity coincides with the TrSL3 regime.

### 7.3 Ecological Implications of VIVACE

Many things can effect the ecology of a water system. The flow regime defines the ecosystem. Figure 7.1 shows a flow chart representing how the flow regime

defines the ecosystem. In addition to the large-scale variations that may result from an obstruction in the water column, the smallest scale variations will also have an effect. Rivers are typically turbulent environments (Hart and Finelli 1999). However, the VIVACE converter will introduce a certain amount of turbulence itself on specific scales that may or may not be natural to the flow stream. The scales of the turbulence from VIVACE are defined in the same manner outlined for the argument for direct numerical simulation in Chapter 1. The largest vortices will be the von Kármán type vortices that will shed at the Strouhal frequency. However, there will be vortices of all sizes from this largest size down to the Kolmogorov length scale. As mentioned in Chapter 1, the Kolmogorov length scale is a function of the Reynolds number, and for the case of  $Re = 1 \times 10^5$  for a diameter of about  $0.1m$ , which was the criterion of VIVACE laboratory experiments, the smallest length scales were then approximately  $6 \times 10^{-6}m$ .

$$L \approx 2.9 \frac{R}{Re^{7/8}} \quad (7.6)$$

(Biggs, Nikora, and Snelder 2005) proposed that organisms are affected by turbulence that has a length scale of approximately the same order of magnitude. Therefore, the range of sizes of organisms affected by the above example will be of the sizes of  $6 \times 10^{-6}m$  up to  $0.1m$ . This type of analysis is a good first step when assessing ecological implications of the installation of a VIVACE converter.

As for the temporal effects of a VIVACE installation, the period of oscillations will be on the order of seconds, affecting the mass-transfer of the flow regime. Mass-transfer effects can be expected to have an effect on the oxygen, nutrients, and food uptake of the system, as well as affecting photosynthesis and respiration of the biota (Biggs, Nikora, and Snelder 2005).

### 7.3.1 General Ecological Review of VIVACE

Placing any obstruction within a water channel will have some sort of effect on the system. This section will examine the possible effects on the ecology of the water environment and quantify a few flow regime changes that can be expected based on the length and vertical spacing of the VIVACE cylinders as outlined above. A VIVACE converter array may be installed anywhere where there is a current of substantial velocity ( $> 0.25m/s$ ). This means that the environment in which a converter may be found could be a stream or river, or it could be the open ocean. Much of what is to follow will pertain to river flow regimes. However, the discussion of flow regime change also applies to water motion such as the Gulf Stream, where many of the same characteristics can be defined on a larger scale (Allan and Castillo 2007).

As shown in Figure 7.1, the energy in the water current is important for ecological integrity. Any changes to the water flow regime can affect the water quality, energy sources, physical habitat, and biotic interaction. The impact of taking energy and velocity out of the system and adding turbulence into the system must be considered. Vorticity near the cylinders can also change the flow, but further downstream, viscous dissipation will reduce this effect. However, once the energy is taken out of the water, there is an impact.

The impact of placing a VIVACE installation into a water channel, be it a river or a ocean current or tidal stream, may not be entirely negative. It has been seen that placing offshore installations in the ocean can often encourage biotic diversity in the vicinity of the new structure. In addition, the effect of decreasing the flow velocity while increasing the turbulence can also create a less diverse and less competitive feeding environment for the fish, invertebrates and plants (Hart and Finelli 1999). In

addition, a flow stream already experiences a wide range of natural variability spatially and temporally. These variations define the physical, chemical, and biological conditions of each site. Temporal variations can take place over minutes, hours, days (from storms), seasons, years, decades, or even longer. Therefore, the area of the installation may already be accustomed to the variations introduced or enhanced by the fluid-structure interaction of VIVACE if the variability introduced falls within the natural variability range.

Any stream flow regime can be defined by the following properties. The magnitude of the flow, or the volume of water moving past a point per unit time, is one defining element of stream flow. The frequency, or how often a given flow magnitude occurs, is another defining element. In addition, there are the temporal elements of duration of a given magnitude of flow, the timing of the magnitude, be it daily or seasonal or other, and the rate of change of the flow, where often the magnitude may rise very quickly after a rain storm, but to fall back to its mean flow may take much longer.

Each stream has a natural flow regime that defines its ecology. Every time the flow regime changes, the stream will respond. There are several types of responses that can be expected due to changes in the flow regime. The channel may adjust by changing the geometry, defined by the depth and width at each cross-section. The riparian plants may be disturbed, either from inundation or drought, spawning cues for fish may be disturbed, the general habitat may change, and the water quality may be effected. Overall, there is an alteration to the habitat. This may lead to disruptions in the life processes of organisms. In addition, there may be a loss of connectivity over lengths of the river, perhaps due to human structures or due to lower water flows. Lastly, a flow modification can result in an increased susceptibility to invasive species.

If a stream has naturally widely variable flows, it has been found that the species existing in such an ecological system tend to be generalists, able to adapt to the frequent changes. However, if a stream is fairly stable or predictable, the species in such a system are more specialists. Any variation in flow can alter the habitat, disrupting the life processes of the biota, testing the adaptability of all species. A specialist is less likely to adapt than a generalist. Therefore, determining the natural variability in a flow will be important in determining the effect of an obstruction such as VIVACE in the flow.

Nothing specific will be mentioned about the effects of the change on the flow regime caused by VIVACE. This is partly due to the site-specific nature of the problems, where a stream system must first be classified by its magnitude, frequency, timing, duration, and rate of change and then looked at more specifically. It is also partly due to the fact that it is difficult to quantify the effect of any changes to the flow regime. The topic of water ecology is very heavily researched to this day, and no universal guidelines can be set forth for installations that alter the flow.

In addition to the elements of the flow regime itself, there are characteristics of the water channel. These include the slope, width, and depth of the channel, the velocity profile of the channel, the grain size of sediment within the channel, the roughness of the water bed, and the degree of the meandering of the flow. These characteristics perform a balancing act between each other by mutually adjusting to changes. Any perturbation to the flow will force the water channel system to seek out a new dynamic equilibrium (Allan and Castillo 2007).

Any large structure affects this dynamic equilibrium. Natural structures like boulders or large wood debris can lead to scouring, flow divergence, and sediment accumulation (Allan and Castillo 2007). Scouring has also shown to be an effect of



a cylinder close to the bottom of the water channel (Sumer and Fredsøe 1997), and the hydrodynamics around cylindrical structures is very similar to the obstruction of any large structure in the water channel. In addition to scouring, flow divergence and sediment accumulation can be expected results of placing a VIVACE converter array in the water column. The extent of these effects will depend on the distance from the bottom surface and to total blockage of the water channel. No matter what the blockage is, it will be far less than that of a dam. A dam in a river or tidal stream is nearly a 100 % blockage, with regulating outflow. This regulated outflow results in a decline in the number of species found in the area, as the natural variability of the flow has been stopped.

### **7.3.2 Sediment transport**

One major job of streams, both in rivers and oceans, is to transport sediment. As a stream meanders, it collects sediment from erosion of the banks as well as from the bottom surface. Sediment size and density determines the velocity that a particle needs to experience to be lifted into the flow and carried downstream. A reduction in the velocity, as may be experienced from the energy extraction of VIVACE, may result in less sediment being transported downstream. The question then becomes how much is the velocity reduction.

### **7.3.3 Distance from the free surface**

It is beneficial both to the phenomenon of VIV and to the ecology of the environment that the VIVACE system not disturb the free surface. The free surface is often a delicate interface between the air and the water, carrying contaminants over the surface of the water (Bernitsas, Allan, Webb, and Lyon 2006). From the phenomenological standpoint, interaction with the free surface is an energy draw, sucking away the energy the body could otherwise have absorbed. It also prohibits

the alternating vortex shedding pattern, whereby the edge closest to the surface will no longer experience vortex growth and shedding, and a recirculating bubble will often take over (Raghavan 2007; Sumer and Fredsøe 1997).

In addition to the contaminants and the disruption of the VIV phenomenon, proximity to the free surface can result in what is known as a hydraulic jump. This was seen by the VIVACE research group in the lab on various occasions. The cylinder was relatively close to the surface, based on the Froude number, and the water was forced to rise in level just before the cylinder and then drastically drop downstream of the cylinder. This resulted in a large amount of air becoming entrained into the fluid. More air becoming entrained into an ecological system will affect the flow regime integrity, although it is not expected to have a significant impact on the system ecology. This alteration, although instinctively thought of as beneficial, is in fact changing the environment in which the biological matter is used to surviving. If this balance of air in the water is altered, either the original species will find it difficult to survive, or new invasive species may find it a welcoming habitat and eventually kill off the original species. Therefore, it is crucial to minimize air entrainment so as to not alter the original habitat.

In Raghavan (2007), a literature review shows that for a Froude number based on the gap ratio in the range of 0.40 to 0.54 begins to show a disruption of the free surface by the cylinder. When the Froude number exceeds one, the phenomenon of VIV is expected to stop. The Froude number based on the gap ratio is given in the following equation.

$$Fr_h = \frac{U}{\sqrt{gh}} \quad (7.7)$$

Therefore, it is recommended that the gap be maintained so that the Froude

number is less than 0.4, and always away from 1.

$$h > \frac{1}{g} \left( \frac{U}{Fr} \right)^2 \quad (7.8)$$

#### **7.3.4 Distance from the bottom**

Like with the free surface, proximity to the rigid bottom boundary is also a consideration. Again, there is an issue of contaminants, as the bottom boundary often acts as a natural barrier, collecting settled contaminants out of the water column (Bernitsas, Allan, Webb, and Lyon 2006). Disturbing this bottom boundary could then mix such contaminants back into the water column, disrupting the natural cycle. Benthic biota will also be affected, by disturbance of the bottom boundary, creating a ripple effect through the local biota with the significant role that benthic biota play in the system ecology. The magnitude to which the benthic biota are affected should be on the same order as the change in sediment transport. In addition, scouring of the sediments can also be a problem. Many foundations of marine structures have experienced failures due to the fact that the scouring of the local sediments was so large, the structure itself was undermined. Therefore, ensuring that the motion of the cylinders and the shed vortices do not greatly interfere with the bottom boundary becomes a critical problem of both ecology and engineering once again.

#### **7.3.5 Measures of Regime Change**

There are several ways to examine the effect that an installation of cylinders in VIV would have on the flow regime, thus changing the ecology of the system. One measure is to look at the instantaneous and integral blocked area, knowing that, when expressed as a percentage, an idea of just how large a cross-sectional area will no longer be accessible can be extracted. Another measure is the change in the energy from upstream to downstream of the cylinders. The change in energy also relates to

the change in the velocity from upstream to downstream sides of the cylinder. This is one of the defining factors in the flow regime as shown in Figure 7.1.

With a more comprehensive math model, all of these values could be computed as a percentage. The per cent blocked area (both instantaneous and total) would be calculated as follows, were  $n$  is the number of cylinders in the vertical cross-section.

$$A_{instantaneous} = nD \quad (7.9)$$

$$A_{total} = 2nAD \quad (7.10)$$

$$\%A = \frac{A}{A_{cs}} \times 100 \quad (7.11)$$

There is no downstream measure as this particular math model makes no attempt to model the flow into or out of a cylinder downstream of the first row. Here,  $A_{cs}$  is the area of the cross-section of the stream assumed constant from the front to the back of the system.

The per cent change in energy per unit length of the cross-sectional area can then be found by calculating how much energy there is upstream of VIVACE versus the energy extracted by VIVACE (total energy extracted).

$$E_{out} = E_{in} - E_{VIVACE} \quad (7.12)$$

$$E_{in} = \frac{1}{2}\rho A_{cs}U^2 \quad (7.13)$$

The energy taken out of the system by the VIVACE converter comes from the power extraction calculations above. Power multiplied by unit time gives energy.

$$\%E = \frac{E_{in} - E_{out}}{E_{in}} \times 100 \quad (7.14)$$

The per cent change in velocity can then also be examined once the energy is known, since the energy is computed a purely kinetic at this point.

$$E = \frac{1}{2}\rho A_{cs}v_{avg}^2 \quad (7.15)$$

The energy out has already been computed for the above change in energy. Therefore, the average velocity out the system for the same cross-stream in incompressible flow can be found.

$$v_{avg_{out}} = \sqrt{\frac{2E_{out}}{\rho A_{cs}}} \quad (7.16)$$
$$v_{avg_{in}} = \sqrt{\frac{2E_{in}}{\rho A_{cs}}}$$

$$\%C_v = \frac{v_{in} - v_{out}}{v_{in}} \times 100 \quad (7.17)$$

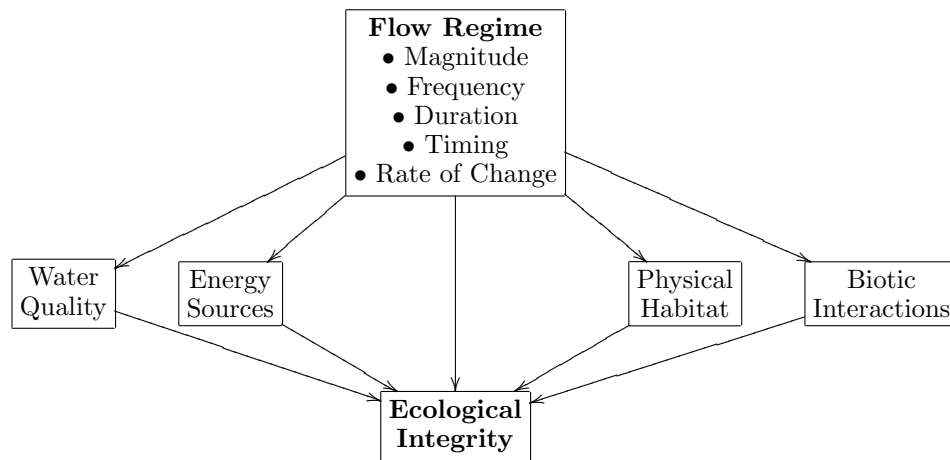


Figure 7.1: Flow chart for the effect of flow regime on ecological integrity (Allan and Castillo 2007).

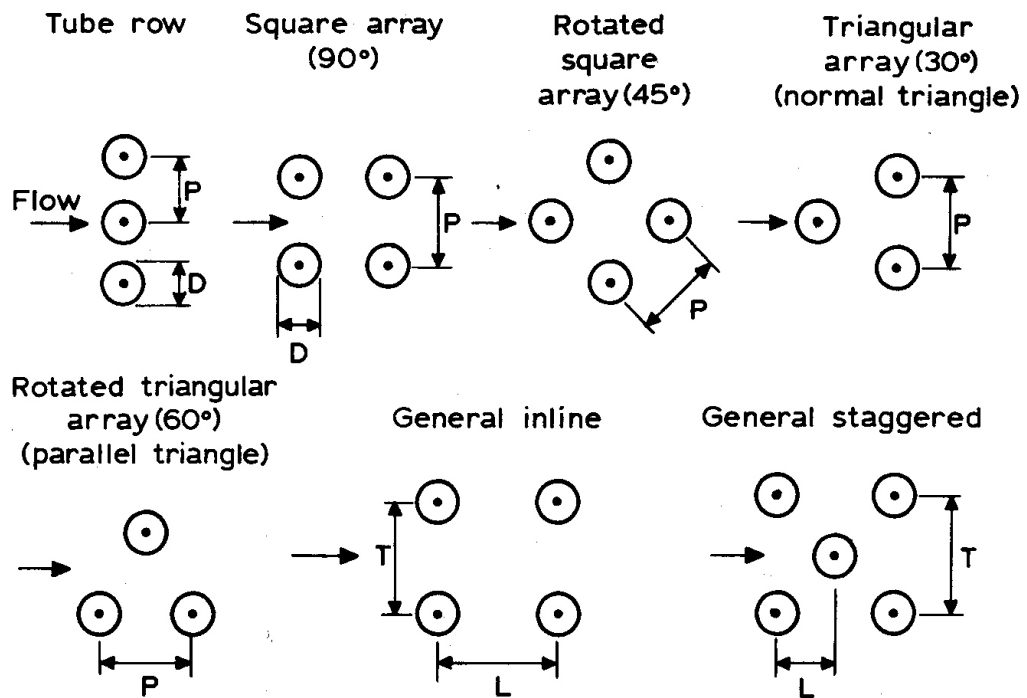


Figure 7.2: Definitions of basic multiple cylinder arrangements (Blevins 1990).

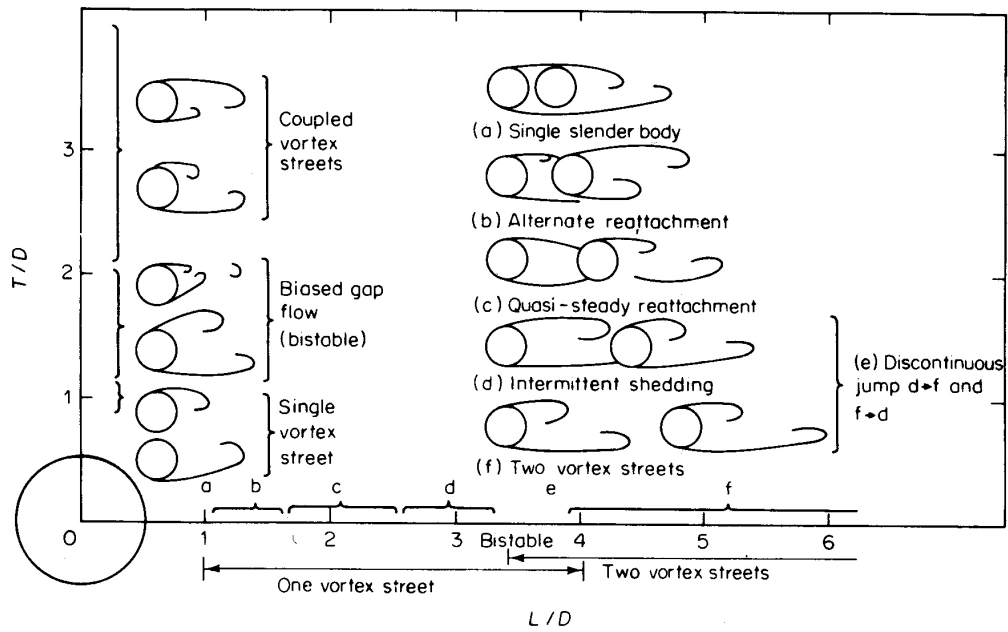


Figure 7.3: Side-by-side and tandem cylinder wakes as a function of separation (Blevins 1990).

## CHAPTER 8

### Conclusion

To complete the thesis, an overview of the problem and the results is provided here along with recommendations for future research.

#### 8.1 Math Model Overview

Already with this first attempt to rigorously derive a mathematical model based on energy phenomenology information about VIV, several key features appear very clearly in the results. With the inclusion of a critical vortex energy parameter, the phase shift at lock-in between the displacement and the forcing was very clearly captured. In addition, the lock-in frequency of the cylinder for very low mass ratios showed the same trend observed in experiments where for mass ratios less than one, the frequency of the cylinder normalized by the cylinder natural frequency rose far above unity, and was shown to even lock in above two, just as shown by Govardhan and Williamson (2000).

In addition, features of the initial, upper, and lower branches were observable from the amplitude of response over the expected reduced velocity range. There was also a clear delineation between the range of synchronization and desynchronization, where desynchronization showed slowly decreasing response, in contrast to the irregular and excitable trend observed at the neighboring lower branch velocities. The term



excitable is used here because although the amplitudes around  $U^* = 10$  are lower than those of the upper branch around resonance, the points that were observed to head to infinity were most noticeable around 10.

It is asserted that the current math model is far superior to any other VIV model yet derived. This is due to the fact that this model attempts to model VIV, and not match VIV observed response to an existing, unrelated mathematical equation. The terms of the model were unforced, unlike other models developed as outlined in Chapter 1. It is further asserted that with a few modifications, it is expected that the current math model will achieve the amplitude response expected in VIV, and as such the other features are expected to align.

#### **8.1.1 Qualitative Overview**

The following discussion draws largely from the qualitative discussion at the end of Chapter 4 as well as the baseline comparison at the end of Chapter 6. Qualitatively, the model has shown an appropriate phase-shift at lock-in for most test cases. In addition, there are noticeable regions that can be associated with the initial, upper, and lower branches within the amplitude response range of synchronization. The desynchronization range is obvious from the tapering off response typical above reduce velocities of 15 or 20.

The vortex-shedding frequency has almost exclusively stayed within range of the Strouhal frequency, even with the critical-energy based shedding criteria. The fact that the vortex-shedding frequency remains around the Strouhal frequency while the cylinder frequency locks in to the natural frequency indicates various vortex shedding modes. This shows that the system does not have to respond at the frequency at which it is excited. In addition, this allows for different vortex shedding modes, and there was evidence of the  $2P$  mode shown in Chapter 6. This has not been captured

by other math models to the authors knowledge. Also within the cylinder frequency response there is clear evidence of lock-in, where the cylinder begins to respond around the natural frequency above  $U^* = 5$ . In addition, lock-out was observed with the improvements to the model in Chapter 5.

There has also been evidence in the model that for low mass ratios, the cylinder frequency response does in fact lock in to higher frequencies than the natural frequency, in agreement with the findings of Govardhan and Williamson (2000). The model is not yet developed to the point of being ready for comparison to the modified Griffin plot (Govardhan and Williamson 2006), because the Griffin plot relies on the amplitude of response.

### **8.1.2 Quantitative Overview**

Quantitative success has been achieved in the phase-shift and in the frequency response. However, quantitative results for the amplitude response of the cylinder are not yet on the proper order of magnitude. Evidence suggests, however, that the development of this math model should arrive to the proper amplitude with further improvements. Very small changes, as were done in Chapter 5, showed disproportionately large changes in the response, where by the same test case was used through-out and nearly two orders of magnitude improvement was achieved.

It is therefore asserted that, while working with this model, it has become evident that this method is appropriate for the development of a VIV model. What is to take place is a more thorough search for additional energy sources . While geometrically simple, the model can quickly become too complex to handle and therefore has little advantage over Computational Fluid Dynamics (CFD). However, with attention to the complexity of the model, a single equation can be easily developed with physically meaningful variables, and the result from a numerical integrator is expected to show

good agreement with VIV. The physically meaningful parameters along with the simplicity to define the system show the properties of this model to capture more VIV features than any other phenomenological model. With more effort, the model is expected to be a proper predictor for VIV, with Reynolds number considerations included.

## **8.2 VIVACE Overview**

Based on what is already known about VIV and the implementation of the derived math model, the cylinder length and cross-flow distribution can be proposed, with a separation of two times the expected maximum amplitude of response. Other characteristics for the design of the full VIVACE system can quickly be arrived at once the math model is further improved and the amplitude response is within the proper order of magnitude while still maintaining the phase-shift and frequency accuracy.

## **8.3 Future Work**

The model derived in this thesis has proved to be fairly successful in the fact that all properties presented can be measured or estimated, making all quantities physically meaningful. The result is a model that captures many basic characteristics of VIV. The range of synchronization is very visible in most all simulations. Cylinder frequency response lock-in to the natural frequency is also visible in simulations, with the fact that higher mass ratios lead to lock-in far above the natural frequency as well. This has been observed experimentally (Govardhan and Williamson 2000). This is particularly promising since the lock-in of the response frequency to the natural frequency is a defining feature of the phenomenon of VIV, and one that separates it from other fluid-structure phenomena. The nonlinearity of the model helps to

exhibit the known phase shift between the forcing and displacement that shifts  $180^\circ$

There are several possibilities for improvement that the author recognizes at this point in time.

- The concept of attached viscous fluid meeting an outer, potential flow fluid indicates that the free-stream velocity is not necessarily the correct choice for the outer velocity of the boundary layer. For potential flow around a cylinder, the velocity is found to be  $2U \sin \theta$ , so that at  $90^\circ$ , the flow velocity is in fact  $2U$ . The boundary layer can be forced to merge with this velocity instead of free-stream velocity  $U$ , and a large quantity of energy would be captured, satisfying the goal of improving the model. In order to determine the outer velocity beyond  $90^\circ$ , a half-body panel method can be used. This is the logical next step for the model.
- The separation point excursion should be a function of the oscillation of the cylinder. Sarpkaya (1992) outlined the difference between a stationary cylinder and a cylinder in oscillatory flow, where a stationary cylinder has a separation point excursion of about  $6^\circ$ , ( $\pm 3^\circ$ ) while a cylinder in oscillatory flow can experience excursions up to  $120^\circ$ . This large variation along with the fact that the flow experienced by the cylinder will be oscillatory indicates that a more dynamic input with feedback would be more physically meaningful.
- The velocity profile within the boundary layer and shear layer may not be properly capturing the energy present. As stated in Chapter 4, it has been observed experimentally that the velocity within the boundary layer often exceeds the free-stream velocity at a point, then decreasing towards the boundary layer

thickness (White 1991). It is thought that using a velocity profile that exhibits such a behavior may contribute to better results, in particular increasing the amplitude of response.

- Separate equations should be derived for the case of the fully turbulent shear layer and fully turbulent boundary layer. Blasius showed that in the case of laminar flow, the boundary layer thickness for a flat plate could be modeled relatively successfully with equation 8.1. However, in the case of turbulent flow, the boundary layer thickness follows a very different profile best approximated by equation 8.2. This would result in different energy and force equations for the boundary layer, shear layer, and attached vortex radius.

$$\delta_{laminar} \approx \frac{5x}{Re_x^{1/2}} \quad (8.1)$$

$$\delta_{turbulent} \approx \frac{0.16x}{Re_x^{1/7}} \quad (8.2)$$

- It has been observed through experimental visualization that the shear layer contains vortices after a point called the shear layer transition point. At low Reynolds numbers it starts with one small vortex and increases up to a very large number. The best analysis of the vortices comes from a frequency analysis, comparing the shear layer vortices to the attached von Kármán vortex in the frequency range. Prasad and Williamson (1997) found a phenomenological relationship between the shear layer frequency and the Strouhal frequency.

$$f_{SL} = f_{KV} \left( \frac{Re}{262} \right)^{0.67} \quad (8.3)$$

The relationship is shown in Figure 8.2. Prasad and Williamson (1997) explained the variation in the frequency of the shear layer and the frequency of the vortex based on the origin of the instability in each. They stated that the

primary instability in the vortex comes from a Hopf bifurcation, and the wavelength is on the order of the diameter of the cylinder,  $D$ . The primary instability in the shear layer, however, is suggested to be a Kelvin-Helmholtz instability, and is on the order of the shear layer thickness. Incorporating another frequency can aid in creating a more full curve, where the response is not solely focused around the point of resonance. However, the current model already shows a response suggestive of a full VIV profile. Therefore the complications of adding this new frequency response to the math model may not be worth the effort and may prove to be a minimal addition to the model.

It goes without saying that with many more additions to the model, the force equations quickly become very complicated and carry many operations per iteration of the model. Even though the model remains conceptually easy, the mathematical equations become complex. For this reason, it is stated that at a certain point, this approach may have to be abandoned for a Computational Fluid Dynamics (CFD) model that can capture some of the basic VIV features. This concept closely follows the development of Vortex Element Methods (VEM). This CFD method was the result of what started as a mathematical model using vortices in the boundary layer. However, the complexity of the development of the VEM model grew so rapidly that it soon became a full-blown CFD method. For this reason, the mathematical model developed here is proposed to be an elegant back-of-the-envelope estimate for the response of a cylinder in VIV, but for more details or to require less input of experimental information, a CFD approach is recommended. A certain amount of consideration must be made, though, for the complexity and time constraints of problem solving. As outlined in Chapter 1, even working at the theoretical fastest speed of computations, a VIV problem at high Reynolds numbers can take a long

time, such as the example worked through in Chapter 1 of 60 million years to complete a single VIV simulation. The fact that the rough estimates obtained in the model each took about one minute suddenly seems more than reasonable despite the imperfections of the model.

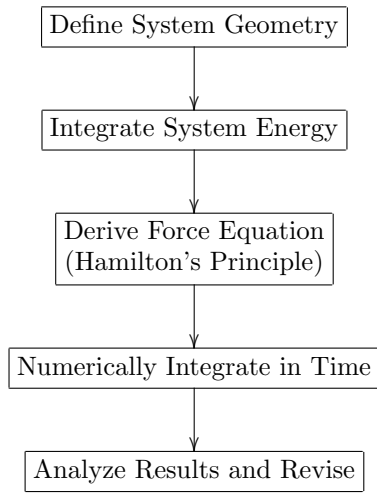


Figure 8.1: Flow chart for derivation of the VIV energy math model.

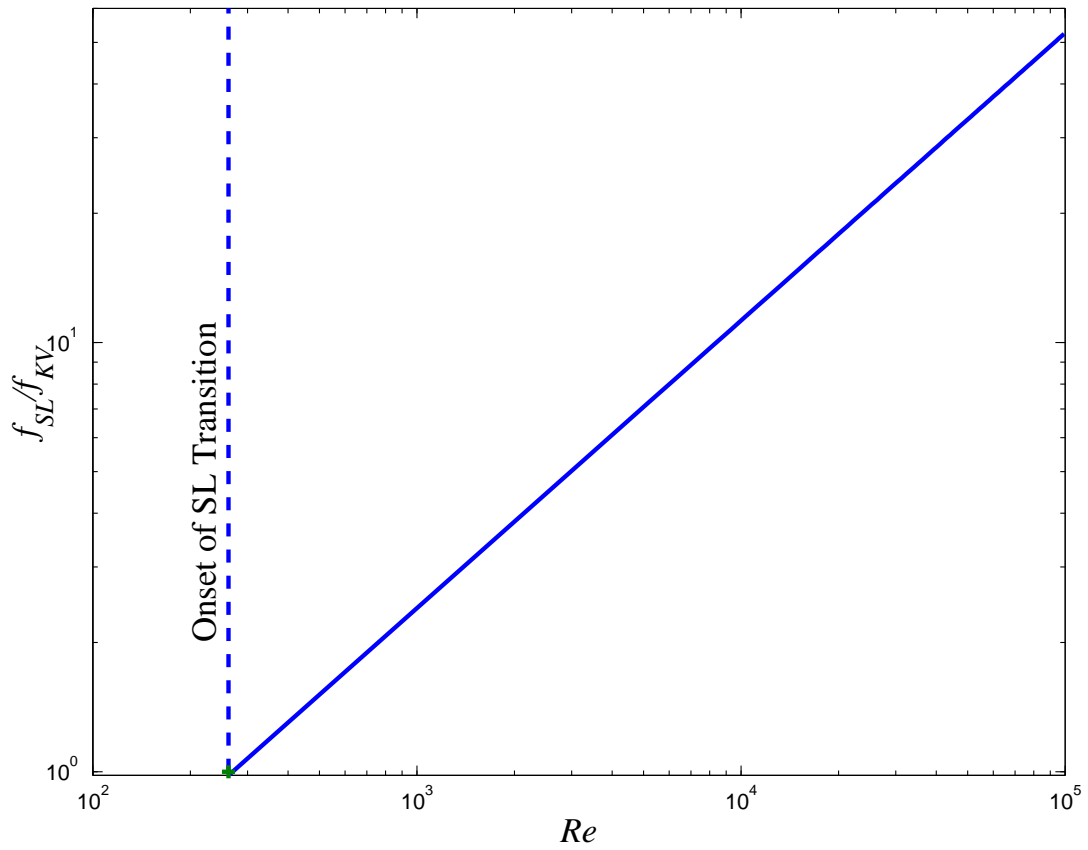


Figure 8.2: Shear layer transition frequency in comparison to von Kármán vortex shedding frequency as a function of Reynolds number (Prasad and Williamson 1997).



## BIBLIOGRAPHY

## Bibliography

- Achenbach, E. (1968). Distribution of local pressure and skin friction around a circular cylinder in cross-flow up to  $re = 5 \times 10^6$ . *Journal of Fluid Mechanics* 34(4), 625–39.
- Achenbach, E. (1971). Influence of surface roughness on the cross-flow around a circular cylinder. *Journal of Fluid Mechanics* 46(2), 321–35.
- Ali, K. H. M. and O. Karim (2002). Simulation of flow around piers. *Journal of Hydraulic Research* 40(2), 161–74.
- Allan, J. D. and M. M. Castillo (2007). *Stream Ecology: Structure and Function of Running Waters* (Second ed.). Springer.
- Anagnostopoulos, P. and P. W. Bearman (1992). Response characteristics of a vortex-excited cylinder at low Reynolds numbers. *Journal of Fluids and Structures* 6, 39–50.
- Aranha, J. A., C. A. Martins, J. R. Meneghini, B. S. Carmo, and L. M. Y. da Silveira (2005). Flow around a circular cylinder: steady solution, stability and Ginzburg-Landau equation. In T. Leweke and C. H. K. Williamson (Eds.), *Fourth Conference on Bluff Body Wakes and Vortex-Induced Vibrations*.
- Balasubramanian, S. (2003). Renewable ocean energy—an overview of the state of the art. *Marine Technology Society Journal* 36(4), 3–4.
- Baranyi, L. and R. I. Lewis (2006, Jan). Comparison of grid-based CFD method and vortex dynamics predictions of low Reynolds number cylinder flows. *The Aeronautical Journal*, 63–71.
- Bearman, P. W. (1984). Vortex shedding from oscillating bluff bodies. *Annual Review of Fluid Mechanics* 16, 195–222.
- Bearman, P. W. and M. M. Zdravkovich (1978). Flow around a circular cylinder near a plane boundary. *Journal of Fluid Mechanics* 89, 33–48.
- Ben Simon, Y. (2005). Highly damped vortex induced vibrations of circular cylinder. Professional degree, University of Michigan.
- Benaroya, H. and T. Wei (2000). Hamilton’s principle for external viscous fluid-structure interaction. *Journal of Sound and Vibration* 238(1), 113–45.
- Benaroya, H., T. Wei, S. Kuchnicki, and P. Dong (2003). Extended hamilton’s principle for fluid-structure interaction. *Proceedings of the Institution of Mechanical Engineers Part K Journal of Multi-body Dynamics* 217, 153–70.
- Berger, E. and R. Wille (1972). Periodic flow phenomena. *Annual Review of Fluid Mechanics*.
- Bernitsas, M. M. (1979). *Contributions Towards the Solution of Marine Riser Design Problem*. Ph. D. thesis, Massachusetts Institute of Technology.
- Bernitsas, M. M. (2008, Mar). Vivace: A new concept for harnessing hydrokinetic energy. presentation, CITRIS and Ocean Enrriengineering Seminar, University of California, Berkeley.
- Bernitsas, M. M., J. D. Allan, P. W. Webb, and T. Lyon (2006, Sep). Feasibility assessment of the vivace ocean/river current energy converter. Technical report, The University of Michigan Graham Environmental Sustainability Institute.

- Bernitsas, M. M., Y. Ben-Simon, K. Raghavan, and E. M. H. Garcia (2006, Jun). The VIVACE converter: model tests at high damping and Reynolds number around  $10^5$ . In *Proceedings of OMAE2006*, Number OMAE06-92652. 25th International OMAE Conference. in press, Journal of Offshore Mechanics and Arctic Engineering, ASME Transactions.
- Bernitsas, M. M. and K. Raghavan (2004). Converter of current/tide/wave energy. Provisional Patent Application 60/628,252, United States Patent and Trademark Office.
- Bernitsas, M. M. and K. Raghavan (2005a). Fluid motion energy converter. Patent Application 11/272,504, United States Patent and Trademark Office.
- Bernitsas, M. M. and K. Raghavan (2005b). Fluid motion energy converter. International provisional patent application, United States Patent and Trademark Office.
- Bernitsas, M. M. and K. Raghavan (2005c). Supplement to the u.s. provisional patent application titled "converter of current, tide, or wave energy". Technical Report 2973, University of Michigan.
- Bernitsas, M. M. and K. Raghavan (2007, Dec). Reduction/suppression of VIV of circular cylinders through roughness distribution at  $8 \times 10^3 < Re < 1.5 \times 10^5$ . In *BBVIV5*.
- Bernitsas, M. M., K. Raghavan, Y. Ben-Simon, and E. M. H. Garcia (2006, Jun). VIVACE (Vortex Induced Vibration Aquatic Clean Energy): a new concept in generation of clean and renewable energy from fluid flow. In *Proceedings of OMAE2006*, Number OMAE06-92652. 25th International OMAE Conference. in press, Journal of Offshore Mechanics and Arctic Engineering, ASME Transactions.
- Bernitsas, M. M., K. Raghavan, and G. Duchene (2007, Dec). Induced separation and vorticity using roughness in VIV of circular cylinders at  $8 \times 10^3 < Re < 1.5 \times 10^5$ . In *BBVIV5*.
- Bernitsas, M. M., K. Raghavan, and D. Maroulis (2007). Effect of free surface on VIV for energy harnessing at  $8 \times 10^3 < Re < 1.5 \times 10^5$ . In *Proceedings of OMAE2007*, Number OMAE07-29726. 26th International OMAE Conference. submitted, Journal of Offshore Mechanics and Arctic Engineering, ASME Transactions.
- Biggs, B. J. F., V. I. Nikora, and T. H. Snelder (2005). Linking scales of flow variability to lotic ecosystem structure and function. *River Research and Applications* 21, 283–98.
- Billah, K. Y. R. (1989, Jun). *A Study of Vortex-Induced Vibrations*. Ph. D. thesis, Princeton University.
- Blevins, R. D. (1974). *Flow Induced Vibration of Bluff Structures*. Ph. D. thesis, California Institute of Technology.
- Blevins, R. D. (1990). *Flow-Induced Vibration* (Second ed.). New York: Van Nostrand Reinhold.
- Bouckaert, F. W. and J. Davis (1998). Microflow regimes and the distribution of macroinvertebrates around stream boulders. *Freshwater Biology* 40, 77–86.
- Braginton-Smith, B. (2003). Offshore wind energy, frontier outposts for sustainable seas. *Marine Technology Society Journal* 36(4), 11–5.
- Brika, D. and A. Lanevill (1993). Vortex-induced vibrations of a long, flexible circular cylinder. *Journal of Fluid Mechanics* 250, 481–508.
- Burnham, L. (Ed.) (1993). *Renewable Energy: Sources for Fuels and Electricity*. Island Press.
- Carberry, J. (2002). *Wake States of a Submerged Oscillating Cylinder and of a Cylinder beneath a Free-Surface*. Ph. D. thesis, Monash University, Melbourne, Australia.
- Carberry, J., J. Sheridan, and D. Rockwell (2003). Controlled oscillations of a cylinder: forces and wake modes. *Journal of Fluids and Structures* 17(2).
- Cerretelli, C. and C. H. K. Williamson (2003). The physical mechanism for vortex merging. *Journal of Fluid Mechanics* 475, 41–77.
- Cham, J. (2006a). *Life is Tough and Then You Graduate: The Second Piled Higher and Deeper Comic Strip Collection*. Piled Higher and Deeper Publishing.

- Cham, J. (2006b). *Piled Higher and Deeper: A Graduate Student Comic Strip Collection*. Piled Higher and Deeper Publishing.
- Cham, J. (2007). *Scooped: The Third Piled Higher and Deeper Comic Strip Collection*. Piled Higher and Deeper Publishing.
- Chandrasekhar, S. (1961). *Hydrodynamic and Hydromagnetic Stability*. Oxford at the Clarendon Press.
- Chaplin, J. R., P. W. Bearman, Y. Cheng, E. Fontaine, J. M. R. Graham, K. Herfjord, F. J. Huera Huarte, M. Isherwood, K. Lambrakos, C. M. Larsen, J. R. Meneghini, G. Moe, R. J. Pattenden, M. S. Triantafyllou, and R. H. J. Willden (2005). Blind predictions of laboratory measurements of vortex-induced vibrations of a tension riser. *Journal of Fluids and Structures* 21, 25–40.
- Charlier, R. H. (2001). Ocean alternative energy: the view from China-’small is beautiful’. *Renewable and Sustainable Energy Reviews* 5, 403–9.
- Charlier, R. H. (2003). A ”sleeper” awakes: tidal current power. *Renewable and Sustainable Energy Reviews* 7, 515–529.
- Chen, S. S. (1987). *Flow-Induced Vibration of Circular Cylindrical Structures*. Hemisphere Publication Corporation.
- Chen, S. S., S. Zhu, and Y. Cai (1995, Jul). An unsteady flow theory for vortex-induced vibration. *Journal of Sound and Vibration* 184(1), 73–92.
- Cotel, A. J., P. W. Webb, and H. Tritico (2006). Do trout choose habitats with reduced turbulence? *Transactions of the American Fisheries Society* 135(610-9).
- Crandall, S. H., D. C. Karnopp, E. F. Kurtz, Jr., and D. C. Pridmore-Brown (1968). *Dynamics of Mechanical and Electromechanical Systems*. McGraw-Hill Book Company.
- Curran, R. (2002, Aug). Productivity of ocean-wave-energy converters: turbine design. *Journal of Energy Engineering*, 13–31.
- Czitrom, S., I. Núñez, and I. Ramírez (2003). Innovative uses of wave power: environmental management of the Port of Ensenada, Mexico. *Marine Technology Society Journal* 36(4).
- Denny, M. W. (1988). *Biology and the Mechanics of the Wave-Swept Environment*. Princeton University Press.
- Ding, J., S. Balasubramanian, R. Lokken, and T. Yung (2004). Lift and damping characteristics of bare and straked cylinders at riser scale Reynolds numbers. In *Offshore Technology Conference*, Number 16341. ExxonMobil Upstream Research Company.
- Dong, P., H. Benaroya, and T. Wei (2004). Integrating experiments into an energy-based reduced-order model for vortex-induced-vibrations of a cylinder mounted as an inverted pendulum. *Journal of Sound and Vibration* 276, 45–68.
- Dong, S. and G. E. Karniadakis (2005). DNS of flow past a stationary and oscillating cylinder at  $Re = 10\,000$ . *Journal of Fluids and Structures* 20, 519–531.
- Dwyer, H. A. and W. J. McCroskey (1973). Oscillating flow over a cylinder at large Reynolds number. *Journal of Fluid Mechanics* 61(4), 753–67.
- El Bassam, N. and P. Maegaard (2004). *Integrated Renewable Energy for Rural Communities: Planning Guidelines, Technologies and Applications*. Elsevier.
- Eldredge, J. D. (2007). Numerical simulation of the fluid dynamics of 2d rigid body motion with the vortex particle method. *Journal of Computational Physics* 221, 626–648.
- EUREC Agency (Ed.) (1996). *The Future for Renewable Energy: Prospects and Directions*. James & James.
- Facchinetti, M. L., E. de Langre, and F. Biolley (2004). Coupling of structure and wake oscillators in vortex-induced vibrations. *Journal of Fluids and Structures* 19, 123–40.

- Falnes, J. and J. Løvseth (1991, Oct). Ocean wave energy. *Energy Policy*, 768–75.
- Feng, C. C. (1968). The measurements of vortex-induced effects in flow past a stationary and oscillating circular and d-section cylinder. Master’s thesis, University of British Columbia, Vancouver, Canada.
- Filon, L. N. G. (1926, Nov). The forces on a cylinder in a stream of viscous fluid. *Proceedings of the Royal Society of London, Series A, Containing Papers of a Mathematical and Physical Character* 113(763), 7–27.
- Filon, L. N. G. (1928). On the second approximation to the ”Oseen” solution for motion of a viscous fluid. *Proceedings of the Royal Society of London, Series A, Containing Papers of a Mathematical and Physical Character* 227, 93–135.
- Fraenkel, P. (2006, Oct). Marine current turbines tap tidal power. *Marine Technology Reporter*, 24–9.
- Gabbai, R. D. and H. Benaroya (2005a, Sep). Hamilton’s principle for fluid-structure interaction and applications to reduced-order modeling. *Proceedings of International Design Technical Conferences and Computers and Information in Engineering Conference*, 1473–81.
- Gabbai, R. D. and H. Benaroya (2005b). An overview of modeling and experiments of vortex-induced vibration of circular cylinders. *Journal of Sound and Vibration* 282, 575–616.
- Garrett, C. and P. Cummins (2005). The power potential of tidal currents in channels. *Proceedings of the Royal Society A* 461, 2563–72.
- Gerrard, J. H. (1966). The mechanics of the formation region of vortices behind bluff bodies. *Journal of Fluid Mechanics* 25(2), 401–13.
- Gharib, M. (1999). *Vortex-Induced Vibration, Absence of Lock-in and Fluid Force Deduction*. Ph. D. thesis, California Institute of Technology.
- Gharib, M. and A. Weigand (1996). Experimental studies of vortex disconnection and connection at free surface. *Journal of Fluid Mechanics* 321, 59–86.
- Gibbs, W. W. (2006, Sep). Plan B for energy. *Scientific American*, 102–14.
- Gill, A. B. (2005). Offshore renewable energy: ecological implications of generating electricity in the coastal zone. *Journal of Applied Ecology* 42, 605–15.
- Goldemberg, J. (Ed.) (2000). *World Energy Assessment: Energy and the Challenge of Sustainability*. <http://www.undp.org/energy/activities/wea/drafts-frame.html>: United Nations Development Programme.
- Golob, R. and E. Brus (1993). *The Almanac of Renewable Energy*. New York: Henry Holt and Company.
- Gopalkrishnan, R. (1993). *Vortex Induced Forces on Oscillating Bluff Cylinders*. Ph. D. thesis, Massachusetts Institute of Technology.
- Gossick, B. R. (1967, Mar). A lagrangian formulation for nonconservative linear systems which satisfies hamilton’s principle. *IEEE Transactions on Education* 10(1), 37–42.
- Goswami, I., R. H. Scanlan, and N. P. Jones (1993a, Nov). Vortex-induced vibration of circular cylinders. I: experimental data. *Journal of Engineering Mechanics* 119(11), 2270–87.
- Goswami, I., R. H. Scanlan, and N. P. Jones (1993b, Nov). Vortex-induced vibration of circular cylinders. II: new model. *Journal of Engineering Mechanics* 119(11), 2288–302.
- Govardhan, R. (2000). *Vortex Induced Vibration of Two and Three Dimensional Bodies*. Ph. D. thesis, Cornell University.
- Govardhan, R. and C. H. K. Williamson (2000). Modes of vortex formation and frequency response of a freely vibrating cylinder. *Journal of Fluid Mechanics* 420, 85–130.
- Govardhan, R. and C. H. K. Williamson (2002). Resonance forever: existence of a critical mass and an infinite regime of resonance in vortex-induced vibration. *Journal of Fluid Mechanics* 473, 147–66.

- Govardhan, R. and C. H. K. Williamson (2005, Jun). Revealing the effect of reynolds number on vortex-induced vibrations using controlled negative and positive damping. In *Bluff Body Wakes and Vortex-Induced Vibrations*, Greece, pp. 21–24. BBVIV4.
- Govardhan, R. N. and C. H. K. Williamson (2006). Defining the 'modified Griffin plot' in vortex-induced vibration: revealing the effect of Reynolds number using controlled damping. *Journal of Fluid Mechanics* 561, 147–80.
- Griffin, O. M. (1978). A universal Strouhal number for the 'locking-on' of vortex shedding to the vibrations of bluff cylinders. *Journal of Fluid Mechanics* 85(3), 591–606.
- Griffin, O. M. and G. H. Koopmann (1977). The vortex-excited lift and reaction forces on resonantly vibrating cylinders. *Journal of Sound Vibration* 54, 435–48.
- Gupta, H., P. P. Sarkar, and K. C. Mehta (1996, Nov). Identification of vortex-induced-response parameters in time domain. *Journal of Engineering Mechanics* 122(11), 1031–7.
- Gupta, H., T. T. Soong, and G. F. Dargush (2000). Active aerodynamic bidirectional control of structures I: modeling and experiments. *Engineering Structures* 22, 379–88.
- Halkyard, J., S. Srinivas, S. Holmes, Y. Constantinides, O. Oakley, and K. Thiagarajan (2005, Jun). Benchmarking of truss spar vortex induced motions derived from CFD with experiments. In *24th International Conference on Offshore Mechanics and Arctic Engineering*, Number OMAE2005-67252, Halkidiki, Greece. OMAE.
- Harrison, H. R. and T. Nettleton (1997). *Advanced Engineering Dynamics*. Arnold, Hodder Headline Group.
- Hart, D. D., B. D. Clark, and A. Jasentuliyana (1996). Fine-scale field measurement of benthic flow environments inhabited by stream invertebrates. *Limnology and Oceanography* 41, 297–308.
- Hart, D. D. and C. M. Finelli (1999). Physical-biological coupling in streams: the pervasive effects of flow on benthic organisms. *Annual Review of Ecology and Systematics* 30, 363–95.
- Hatipoglu, F. and I. Avci (2003). Flow around a partly buried cylinder in a steady current. *Ocean Engineering* 30(2), 239–49.
- Hay, M. (2005, May/June). From blue to green. *International Ocean Systems* 9(3), 6–9.
- Hiemenz, K. (1911). Die grenzschicht an einem in den gleichförmigen flüssigkeitsstrom eingetachten geraden kreiszylinder. *Dinglers Polytechnische Journal* 326, 321–4.
- Higuchi, H., H. J. Kim, and C. Farell (1989). On flow separation and reattachment around a circular cylinder at critical reynolds numbers. *Journal of Fluid Mechanics* 200, 149–71.
- Holtberg, P. D. (Ed.) (2006). *Annual Energy Outlook 2006 With Projections to 2030*. <http://www.eia.doe.gov/oiaf/archive/aeo06/index.html>: Energy Information Administration.
- Homann, F. (1936). Der einfluß großer zähigkeit bei der strömung um den zylinder und um die kugel. *Zeitschrift für Angewandte Mathematik und Mechanik* 16(3), 153–64.
- Imai, I. (1951, Sep). On the asymptotic behaviour of viscous fluid flow at a great distance from a cylindrical body, with special reference to Filon's paradox. *Proceedings of the Royal Society of London. Series A, Mathematical and Physical Sciences* 208(1095), 487–516.
- International Energy Agency (Ed.) (2006). *Renewable Energy: RD&D Priorities: Insights from IEA Technology Programmes*. Organisation for Economic Co-operations and Development/International Energy Agency.
- Ivanova, I. A., H. Bernhoff, O. Ågren, and M. Leijon (2005). Simulated generator for wave energy extraction in deep water. *Ocean Engineering* 32, 1164–78.
- Jafar, M. (2000). Renewable energy in the South Pacific-options and constraints. *Renewable Energy* 19, 305–9.

- Jie, S. and Z. Chao (2006). Numerical analysis of the flow around a circular cylinder using RANS and LES. *International Journal of Computational Fluid Dynamics* 20(4), 301–7.
- Johnstone, C. M., K. Nielsen, T. Lewis, A. Sarmiento, and G. Lemonis (2006). EC FPVI coordinated action on ocean energy: a European platform for sharing technical information and research outcomes in wave and tidal energy. *Renewable Energy* 31, 191–6.
- Jones, A. T. (2005). Ocean energy: nascent, emerging and mature technologies. *Marine Technology Society Journal* 39(3), 116–8.
- Jones, A. T. and W. Rowley (2003). Global perspectives: economic forecast for renewable ocean technologies. *Marine Technology Society Journal* 36(4), 85–90.
- Jordan, D. W. and P. Smith (1999). *Nonlinear Ordinary Differential Equations: An introduction to dynamical systems* (Third ed.). Oxford University Press.
- Jumars, P. A., J. E. Eckman, and E. Koch (2001). *The Benthic Boundary Layer: Transport Processes and Biogeochemistry*, Chapter 13. Macroscopic Animals and Plants in Benthic Flows, pp. 320–47. Oxford University Press.
- Kallinderis, Y. and H. T. Ahn (2005, Jun). Strongly coupled fluid-structure interactions via a new navier-stokes method for prediction of vortex-induced vibrations. In *24th International Conference on Offshore Mechanics and Arctic Engineering*, Number OMAE2005-67352, Halkidiki, Greece. OMAE.
- Kammen, D. M. (2006, Sep). The rise of renewable energy. *Scientific American*, 84–93.
- Kelly, S. G. (1993). *Schaum's Outline of Theory and Problems of Mechanical Vibrations*. McGraw-Hill, Inc.
- Khalak, A. and C. H. K. Williamson (1996). Dynamics of a hydroelastic cylinder with very low mass and damping. *Journal of Fluids and Structures* 10, 455–72.
- Khalak, A. and C. H. K. Williamson (1997). Fluid forces and dynamics of a hydroelastic structure with very low mass and damping. *Journal of Fluids and Structures* 11, 973–82.
- Khalak, A. and C. H. K. Williamson (1999). Motions, forces and mode transitions in vortex-induced vibrations at low mass-damping. *Journal of Fluids and Structures* 13, 813–51.
- Klamo, J. T., A. Leonard, and A. Roshko (2005). On the maximum amplitude for a freely vibrating cylinder in cross-flow. *Journal of Fluids and Structures* 21, 429–34.
- Kreyszig, E. (1999). *Advanced Engineering Mathematics* (Eighth ed.). John Wiley & Sons.
- Krishnamoorthy, S., S. J. Price, and M. P. Paidoussis (2001). Cross-flow past an oscillating circular cylinder: synchronization phenomena in the near wake. *Journal of Fluids and Structures* 15, 955–80.
- Kristiansen, T., R. Baarholm, G. J. Rørtveit, E. W. Hansen, and C. T. Stansberg (2005, Jun). Kinematics in a diffracted wave field: particle image velocimetry (PIV) and numerical models. In *24th International Conference on Offshore Mechanics and Arctic Engineering*, Number OMAE2005-67176, Halkidiki, Greece. OMAE.
- Kundu, P. K. and I. M. Cohen (2002). *Fluid Mechanics* (Second ed.). Academic Press.
- Lam, K. (1987). Potential flow calculation by surface vorticity method and computer graphics. *Computing & Graphics* 11(1), 35–47.
- Lam, K., G. D. Jiang, Y. Liu, and R. M. C. So (2004). Grid-free surface vorticity method applied to flow induced vibration of flexible cylinders. *International Journal for Numerical Methods in Fluids* 46, 289–313.
- Lam, K., G. D. Jiang, Y. Liu, and R. M. C. So (2006). Simulation of cross-flow-induced vibration of cylinder arrays by surface vorticity method. *Journal of Fluids and Structures* 22, 1113–31.
- Lamb, S. H. (1945). *Hydrodynamics* (Sixth ed.). Dover Publications.
- Landau, L. D. and E. M. Lifshitz (1995). *Fluid Mechanics* (Second ed.). Pergamon Press.

- Laneville, A. and D. Brika (1999). The fluid and mechanical coupling between two circular cylinders in tandem arrangement. *Journal of Fluids and Structures* 13, 967–86.
- Langhaar, H. L. (1989). *Energy Methods in Applied Mechanics*. Krieger Publishing Company.
- Laughton, M. A. (Ed.) (1990). *Renewable Energy Sources*. Elsevier Applied Science.
- Lavie, A. M. (1975). The extended Kutta-Joukowski theorem for a two dimensional cylinder in a viscous stream. *Israel Journal of Technology* 13, 237–45.
- Le Gal, P., A. Nadim, and M. Thompson (2001). Hysteresis in the forced Stuart-Landau equation: application to vortex shedding from an oscillating cylinder. *Journal of Fluids and Structures* 15, 445–57.
- Leweke, T. and C. H. K. Williamson (Eds.) (2005, Jun). *Fourth Conference on Bluff Body Wakes and Vortex-Induced Vibrations*, Santorini, Greece. BBVIV4.
- Liao, J. C., D. N. Beal, G. V. Lauder, and M. S. Trianyafyllou (2003a). Fish exploiting vortices decrease muscle activity. *Science* 302, 1566–9.
- Liao, J. C., D. N. Beal, G. V. Lauder, and M. S. Trianyafyllou (2003b). The Kármán gait: novel body kinematics of rainbow trout swimming in a vortex street. *Journal of Experimental Biology* 206.
- Lin, J. C., J. Towfighi, and D. Rockwell (1995). Instantaneous structure of the near wake of a circular cylinder: on the effect of Reynolds number. *Journal of Fluids and Structures* 9, 409–18.
- Lu, X. Y. and C. Dalton (1996). Calculation of the timing of vortex formation from an oscillating cylinder. *Journal of Fluids and Structures* 10(5), 527–41.
- Maplesoft (2007, Feb). *Maple 11.00*. 277223. Maplesoft.
- Mathews, J. H. and K. D. Fink (2004). *Numerical Methods Using MATLAB*. Peason Prentice Hall.
- MathWorks (2006, Jan). *MATLAB R2006a* (7.2.0.232 ed.). <http://www.mathworks.com>: The MathWorks, Inc.
- McCormick, M. E. and D. R. B. Kraemer (2003). Ocean wave energy utilization. *Marine Technology Society Journal* 36(4), 52–8.
- McNutt, M. K. (2002). Developing the ocean: opportunities and responsibilities. *The Futurist* 36(1), 38–43.
- Merrill, M. L. (2007, Jun). The prospects for the subsea market in offshore wind power. *Marine Technology Reporter*, 24–9.
- Meyer, R. (2005, Jul). Looking around the corner or is it time to plan ahead. *Sea Technology* 46(7), 77.
- Morton, T. S. (2006). An estimate of the circulation generated by a bluff body. *European Journal of Mechanics B/Fluids*.
- Mustto, A. A., G. C. R. Bodstein, and M. H. Hirata (2000). Vortex method simulation of the flow around a circular cylinder. *AIAA Journal* 38(6), 1100–2.
- Nakamura, H. and T. Igarashi (2004). Variation of Nusselt number with flow regime behind a circular cylinder for Reynolds numbers from 70 to 30 000. *International Journal of Heat and Mass Transfer* 47, 5169–73.
- Neelamani, S. (2003). A decade of wave power development in india-the challenges. *Marine Technology Society Journal* 36(4), 59–73.
- Nikora, V. I., D. G. Goring, and B. J. F. Biggs (2002). Some observations of the effects of micro-organisms growing on the bed of an open channel on the turbulence properties. *Journal of Fluid Mechanics* 450, 317–41.



- Norberg, C. (1987a). Effects of reynolds number and a low-intensity freestream turbulence on the flow around a circular cylinder. Technical Report NR 87/2, Chalmers University, Goteberg, Sweden.
- Norberg, C. (1987b). *Reynolds number and freestream turbulence effects on the flow and fluid forces for a circular cylinder in cross flow*. Ph. D. thesis, Chalmers University, Sweden.
- Norberg, C. (1994). An experimental investigation of the flow around a circular cylinder: influence of aspect ratio. *Journal of Fluid Mechanics* 258, 287–316.
- Oakley, Jr., O. H., Y. Constantinides, C. Navarro, and S. Holmes (2005, Jun). Modeling vortex induced motions of spars in uniform and stratified flows. In *24th International Conference on Offshore Mechanics and Arctic Engineering*, Number OMAE2005-67238, Halkidiki, Greece. OMAE.
- Odeh, M., J. F. Noreika, A. Haro, A. Maynard, T. Castro-Santos, and G. F. Cada (2002). Evaluation of the effects of turbulence on the behavior of migratory fish. Contract 00000022 200005700, Bonneville Power Administration, Portland, Oregon.
- OECD (1988). *Environmental Impacts of Renewable Energy: The OECD Compass Project*. Organisation for Economic Co-Operation and Development.
- Papaioannou, G. V., D. K. P. Yue, M. S. Triantafyllou, and G. E. Karniadakis (2006). Three-dimensionality effects in flow around two tandem cylinders. *Journal of Fluid Mechanics* 558, 387–413.
- Parfit, M. Future power: where will the world get its next energy fix? *National Geographic*, 2–7,17–31.
- Parsons, M. G. (1984). NA420 Ship Resistance and Propulsion II. Informal Notes.
- Pavlov, D. S., A. I. Lupandin, and M. A. Skorobogatov (2000). The effects of flow turbulence on the behavior and distribution of fish. *Journal of Ichthyology* 40(Supplement 2), S232–61.
- Pelc, R. and R. M. Fujita (2002). Renewable energy from the ocean. *Marine Policy* 26, 471–9.
- Pikovsky, A., M. Rosenblum, and J. Kurths (2003). *Synchronization: A universal concept in nonlinear sciences*. Cambridge University Press.
- Poff, N. L., J. D. Allan, M. B. Bain, J. R. Karr, K. L. Prestegard, B. D. Richter, R. E. Sparks, and J. C. Stromberg (1997, Dec). The natural flow regime: a paradigm for river conservation and restoration. *BioScience* 47(11), 769–84.
- Ponta, F. L. (2006). Effect of shear-layer thickness on the Strouhal-Reynolds number relationship for bluff-body wakes. *Journal of Fluids and Structures* 22, 1133–8.
- Ponta, F. L. and H. Aref (2004, Aug). Strouhal-Reynolds number relationship for vortex streets. *Physical Review Letters* 93(8).
- Pontes, M. T., L. Cavaleri, and D. Mollison (2003). Ocean waves: energy resource assessment. *Marine Technology Society Journal* 36(4), 42–51.
- Porthouse, D. T. C. and R. I. Lewis (1981). Simulation of viscous diffusion for extension of the surface vorticity method to boundary layer and separated flows. *Journal Mechanical Engineering Science* 23(3), 157–67.
- Prasad, A. and C. H. K. Williamson (1997). The instability of the shear layer separation from a bluff body. *Journal of Fluid Mechanics* 333, 375–402.
- Previsic, M. (2003, Jul). The state of the art in wave energy conversion. *Sea Technology* 44(7), 15–8.
- Previsic, M., R. Bedard, and G. Hagerman (2004, Jun). E2i epr assessment: Offshore wave energy conversion devices. Technical Report WP-004-US-Rev 1, Electricity Innovation Institute, EPRI.
- Raghavan, K. (2007). *Energy Extraction from a Steady Flow Using Vortex Induced Vibration*. Ph. D. thesis, The University of Michigan.

- Raghavan, K. and M. M. Bernitsas (2007, Dec). Enhancement of high damping VIV through roughness distribution for energy harnessing at  $8 \times 10^3 < Re < 1.5 \times 10^5$ . In *BBVIV5*.
- Raghavan, K., M. M. Bernitsas, and D. Maroulis (2007, Jun). Effect of bottom boundary on VIV for energy harnessing at  $8 \times 10^3 < Re < 1.5 \times 10^5$ . In *Proceedings of OMAE2007*, Number OMAE07-29727. 26th International OMAE Conference. submitted, Journal of Offshore Mechanics and Arctic Engineering, ASME Transactions.
- Raghavan, K., B. M. M., and D. Maroulis (2007). Effect of Reynolds number on vortex induced vibrations. In *IUTAM Symposium*, Hamburg, Germany. invited paper.
- Rakshit, T., S. Atluri, and C. Dalton (2005, Jun). VIV of a composite riser at moderate Reynolds number using CFD. In *24th International Conference on Offshore Mechanics and Arctic Engineering*, Number OMAE2005-67206, Halkidiki, Greece. OMAE.
- Ravindran, M. and R. Abraham (2003). The Indian 1 MW demonstration OTEC plant and the pre-commissioning tests. *Marine Technology Society Journal* 36(4), 36–41.
- Reichl, P. (2001). *Flow Past a Cylinder Close to a Free Surface*. Ph. D. thesis, Monash University.
- Rocchi, D. and A. Zasso (2002). Vortex shedding from a circular cylinder in a smooth and wired configuration: comparison between 3D LES simulation and experimental analysis. *Journal of Wind Engineering and Industrial Aerodynamics* 90, 475–89.
- Rosenhead, L. (1931, Nov). The formation of vortices from a surface of discontinuity. *Proceedings of the Royal Society of London. Series A, Containing Papers of a Mathematical and Physical Character* 134(823), 170–92.
- Roshko, A. (1961). Experiments on the flow past a circular cylinder at very high Reynolds number. *Journal of Fluid Mechanics* 10, 345–56.
- Saltara, F., J. R. Meneghini, and R. A. Fregonesi (2003, Jun). Numerical simulation of flow around elastically mounted cylinder. *International Journal of Offshore and Polar Engineering* 13(2), 99–104.
- Sarpkaya, T. (1979, Jun). Vortex-induced oscillations. *Journal of Applied Mechanics* 46, 241–58.
- Sarpkaya, T. (1989, Mar). Computational methods with vortices—the 1988 Freeman scholar lecture. *Journal of Fluids Engineering* 111, 5–52.
- Sarpkaya, T. (1992, Sep). Brief reviews of some time-dependent flows. *Journal of Fluids Engineering* 114, 283–98.
- Sarpkaya, T. (1995). Hydrodynamic damping, flow-induced oscillations, and biharmonic response. *Journal of Offshore Mechanics and Arctic Engineering* 117, 232–8.
- Sarpkaya, T. (2001). On the force decompositions of Lighthill and Morison. *Journal of Fluids and Structures* 15, 227–33.
- Sarpkaya, T. (2004). A critical review of the intrinsic nature of vortex induced vibrations. *Journal of Fluids and Structures* 19, 389–447.
- Schewe, G. (1983). On the force fluctuations acting on a circular cylinder in cross-flow from subcritical up to transcritical reynolds numbers. *Journal of Fluid Mechanics* 133, 265–285.
- Schlichting, H. (1968). *Boundary-Layer Theory*, Volume Sixth. McGraw-Hill Book Company.
- Shao, J. and C. Zhang (2006, Jun). Numerical analysis of the flow around a circular cylinder using RANS and LES. *International Journal of Computational Fluid Dynamics* 20(5), 301–7.
- Shea, K. (2007, Jun). Tidal turbines: power up in NYC. *Marine Technology Reporter*, 30–1.
- Simonic, A. (2006). *WinEdt 5* (5.5 ed.). <http://www.winedt.com>: WinEdt, Inc. 20061213.
- Sims, R. E. H. (2004). Renewable energy: a response to climate change. *Solar Energy* 76, 9–17.
- Skop, R. A. and O. M. Griffin (1973). A model for the vortex-excited resonant response of bluff cylinders. *Journal of Sound and Vibration* 27(2), 225–33.

- Statzner, B., J. A. Gore, and V. H. Resh (1988). Hydraulic stream ecology: observed patterns and potential applications. *Journal of the North American Benthological Society* 7, 307–60.
- Strogatz, S. H. (2000). *Nonlinear Dynamics and Chaos: With Applications to Physics, Biology, Chemistry, and Engineering*. Perseus Books.
- Struble, R. A. (1962). *Nonlinear Differential Equations*. McGraw-Hill Book Company, Inc.
- Subramaniam, S. (1996). *A New Mesh-Free Vortex Method*. Ph. D. thesis, Florida State University.
- Sumer, B. M. and J. Fredsøe (1997). *Hydrodynamics Around Cylindrical Structures*. World Scientific Publishing.
- Szepessy, S. (1993). On the control of circular cylinder flow by end plates. *European Journal of Mechanics B-Fluids* 12, 217–44.
- Szepessy, S. and P. W. Bearman (1992). Aspect ratio and end plate effects on vortex shedding from a circular cylinder. *Journal of Fluid Mechanics* 234, 191–218.
- Tait, R. V. and R. S. De Santo (1972). *Elements of Marine Ecology*. Springer-Verlag.
- Takada, H. (1975). Determination of the position of separation for the free-streamline flow past a circular cylinder. *Journal of the Physical Society of Japan* 39(1), 247–52.
- Thiagarajan, K. P., Y. Constantinides, and L. Finn (2005, Jun). CFD analysis of vortex-induced motions of bare and straked cylinders in currents. In *24th International OMAE Conference*, Greece. OMAE.
- Tietjens, O. G. (1934). *Applied Hydro- and Aeromechanics*. Dover Publications, Inc.
- Ullman, P. W. (2003). Offshore tidal power generation—a new approach to power conversion of the oceans’ tides. *Marine Technology Society Journal* 36(4), 16–24.
- Unal, M. F. and D. Rockwell (1988a). On vortex formation from a cylinder. part 1. the initial instability. *Journal of Fluid Mechanics* 190, 491–512.
- Unal, M. F. and D. Rockwell (1988b). On vortex formation from a cylinder. part 2. control by splitter-plate interference. *Journal of Fluid Mechanics* 190, 513–529.
- Ünal, U. O. and O. Gören (2005). Vortex shedding from a circular cylinder at high Reynolds number. *Maritime Transportation and Exploitation of Ocean and Coastal Resources*, 301–7.
- Ushiyama, I. (1999). Renewable energy in Japan. *Renewable Energy* 16, 1174–9.
- Vadus, J. R. (2003). Renewable ocean energy technologies & economics—a commentary. *Marine Technology Society Journal* 36(4), 5–7.
- Vega, L. A. (2003). Ocean thermal energy conversion primer. *Marine Technology Society Journal* 36(4), 25–35.
- Vikestad, K. (1998, Apr). *Multi-Frequency Response of a Cylinder Subjected to Vortex Shedding and Support Motions*. Ph. D. thesis, Norwegian University of Science and Technology, Trondheim, Norway.
- Vikestad, K., J. K. Vandiver, and C. M. Larsen (2000). Added mass and oscillation frequency for a circular cylinder subjected to vortex-induced vibrations and external disturbance. *Journal of Fluids and Structures* 14, 1071–88.
- Vogel, S. (1994). *Life in Moving Fluid* (Second ed.). Princeton, New Jersey: Princeton University Press.
- Walker, D. (2003). Testimony before the president’s commission on ocean policy in Chicago, Illinois on September 24, 2002. *Marine Technology Society Journal* 36(4), 91–6.
- Walker, D. T., D. R. Lyzenga, E. A. Ericson, and D. E. Lund (1996, Sep). Radar backscatter and surface roughness measurements for stationary breaking waves. In *Mathematical, Physical, and Engineering Sciences*, Volume 452, pp. 1953–84. The Royal Society.

- Watson, I. T. and T. J. Barber (2006). Validation of numerical and experimental results using the Kriging estimator. *AIAA* (3301).
- Webb, P. W. (1998). Entrainment by river chub, *Nocomis micropogon*, and smallmouth bass, *Micropterus dolomieu*, on cylinders. *Journal of Experimental Biology* 201, 2403–12.
- Webb, P. W. (2006). Use of fine-scale current refuges by fishes in a temperate warm-water stream. *Canadian Journal of Zoology* 84, 1071–8.
- White, F. M. (1991). *Viscous Fluid Flow* (Second ed.). McGraw-Hill.
- White, F. M. (1994). *Fluid Mechanics* (Third ed.). McGraw-Hill, Inc.
- Willden, R. H. J. and J. M. R. Graham (2005, Jun). CFD simulations of the vortex-induced vibrations of model riser pipes. In *24th International Conference on Offshore Mechanics and Arctic Engineering*, Number OMAE2005-67197, Halkidiki, Greece. OMAE.
- Willden, R. H. J., T. E. Kendon, and J. M. R. Graham (2005, Jun). Aspects of the transverse vortex-induced vibrations of low mass ratio elastically supported circular cylinders. In *Bluff Body Wakes and Vortex-Induced Vibrations*, Greece. BBVIV4.
- Williamson, C. H. K. (1989). Oblique and parallel modes of vortex shedding in the wake of a circular cylinder at low Reynolds numbers. *Journal of Fluid Mechanics* 206, 579–627.
- Williamson, C. H. K. (1996). Vortex dynamics in the cylinder wake. *Annual Review of Fluid Mechanics* 28, 477–539.
- Williamson, C. H. K. and G. L. Brown (1998). A series in  $1/\sqrt{Re}$  to represent the strouhal-reynolds number relationship of the cylinder wake. *Journal of Fluids and Structures* 12, 1073–85.
- Williamson, C. H. K. and R. Govardhan (2004). Vortex-induced vibrations. *Annual Review of Fluid Mechanics* 36, 413–55.
- Williamson, C. H. K. and A. Roshko (1988). Vortex formation in the wake of an oscillating cylinder. *Journal of Fluids and Structures* 2, 355–81.
- Wiltshire, J. C. (2003). Methane hydrates: a future ocean energy resource? *Marine Technology Society Journal* 36(4), 8–10.
- Yamamoto, C. T., J. R. Meneghini, F. Saltara, R. A. Fregonesi, and J. A. Ferrari, Jr. (2004). Numerical simulations of vortex-induced vibration on flexible cylinders. *Journal of Fluids and Structures* 19, 467–89.
- Yang, W. J. (Ed.) (2001). *Handbook of Flow Visualization* (Second ed.). Taylor & Francis.
- Young, W. J. (1992). Clarification of the criteria used to identify near-bed flow regimes. *Fresh-water Biology* 28, 383–91.
- Zdravkovich, M. M. (1990). Conceptual overview of laminar and turbulent flows past smooth and rough circular cylinders. *Journal of Wind Engineering and Industrial Aerodynamics* 33, 53–62.
- Zdravkovich, M. M. (1996, Jul). Different modes of vortex shedding: an overview. *Journal of Fluids and Structures* 10(5), 427–37.
- Zdravkovich, M. M. (1997). *Flow Around Circular Cylinders*, Volume 1: Fundamentals. Oxford University Press.
- Zdravkovich, M. M. (2003). *Flow Around Circular Cylinders*, Volume 2: Applications. Oxford University Press.
- Zhu, Q., J. C. Lin, M. F. Unal, and D. Rockwell (2000). Motion of a cylinder adjacent to a free-surface: flow patterns and loading. *Experiments in Fluids* 28, 559–75.